Linear Beam Dynamics
and
Ampere Class Superconducting RF Cavities
@RHIC

A Dissertation Presented

by

Rama R. Calaga

to

The Graduate School

in Partial Fulfillment of the Requirements

for the Degree of

Doctor of Philosophy

in

Physics and Astronomy

Stony Brook University

March 2006

Copyright © by
Rama R. Calaga
2006

Stony Brook University

The Graduate School

Rama R. Calaga

We, the dissertation committee for the above candidate for the Doctor of Philosophy degree, hereby recommend acceptance of the dissertation.

Dr. Ilan Ben-Zvi (Advisor)
Adjunct Professor of Physics and Astronomy
Stony Brook University

Dr. Stephen Peggs (Co-Advisor)
Adjunct Professor of Physics and Astronomy
Stony Brook University

Dr. Thomas Hemmick (Chairperson)
Professor of Physics and Astronomy
Stony Brook University

Dr. George Sterman
Distinguished Professor of Physics and Astronomy
Stony Brook University

Dr. Thomas Roser
Accelerator Division Head
Brookhaven National Laboratory

This dissertation is accepted by the Graduate School.

Dean of the Graduate School

Abstract of the Dissertation

Linear Beam Dynamics and Ampere Class Superconducting RF Cavities @RHIC

by

Rama R. Calaga

Doctor of Philosophy

in

Physics and Astronomy

State University of New York at Stony Brook

2006

The Relativistic Heavy Ion Collider (RHIC) is a hadron collider designed to collide a range of ions from protons to gold. RHIC operations began in 2000 and has successfully completed five physics runs with several species including gold, deuteron, copper, and polarized protons. Linear optics and coupling are fundamental issues affecting the collider performance. Measurement and correction of optics and coupling are important to maximize the luminosity and sustain stable operation. A numerical approach, first developed at SLAC, was implemented to measure linear optics from coherent betatron oscillations generated by ac dipoles and recorded at multiple beam position monitors (BPMs) distributed around the collider. The approach is extended to a fully coupled 2D case and equivalence relationships between Hamiltonian and matrix formalisms are

derived. Detailed measurements of the transverse coupling terms are carried out at RHIC and correction strategies are applied to compensate coupling both locally and globally. A statistical approach to determine BPM reliability and performance over the past three runs and future improvements also discussed.

Aiming at a ten-fold increase in the average heavy-ion luminosity, electron cooling is the enabling technology for the next luminosity upgrade (RHIC II). Cooling gold ion beams at 100 GeV/nucleon requires an electron beam energy of approximately 54 MeV and a high average current in the range of 50-200 mA. All existing e^- coolers are based on low energy DC accelerators. The only viable option to generate high current, high energy, low emittance CW electron beam is through a superconducting energy-recovery linac (SC-ERL). In this option, an electron beam from a superconducting injector gun is accelerated using a high gradient ($\sim$ 20 MV/m) superconducting RF (SRF) cavity. The electrons are returned back to the cavity with a 180° phase shift to recover the energy back into the cavity before being dumped. A design and development of a half-cell electron gun and a five-cell SRF linac cavity are presented. Several RF and beam dynamics issues ultimately resulting in an optimum cavity design are discussed in detail.

Dedicated To My Mother

Contents

List of Figures **x**

List of Tables **xv**

Acknowledgements **xviii**

1 Introduction **1**
1.1 The Relativistic Heavy Ion Collider, RHIC 1
1.2 Linear Beam Dynamics 2
1.2.1 Transverse Betatron Motion 3
1.2.2 Emittance 5
1.2.3 Dispersion 6
1.2.4 Betatron Tune and Chromaticity 7
1.2.5 Linear Magnetic Field Errors 8
1.3 RHIC Instrumentation 8
1.3.1 Beam Position Monitors 9
1.3.2 Beam Loss Monitors 10
1.3.3 Profile Monitors 10
1.3.4 Wall Current Monitors 10
1.3.5 Transverse Kickers 11
1.3.6 AC Dipoles 11

2 Principle Component Analysis and Linear Optics **15**
2.1 Introduction 15
2.2 Singular Value Decomposition 16
2.3 Linear Optics: Formalism 17
2.4 RHIC Linear Optics: Measurements 19
2.5 Error source identification 22
2.5.1 Global Correction 22
2.5.2 Local Correction 24
2.6 Summary 25

3 Statistical analysis of RHIC beam position monitors performance 28
3.1 Introduction . . . 28
3.2 FFT TECHNIQUE . . . 28
3.3 SVD Technique . . . 30
3.4 Analysis . . . 32
3.4.1 Hardware Cut . . . 32
3.4.2 Peak-to-Peak Thresholds . . . 32
3.4.3 FFT Analysis . . . 35
3.4.4 SVD Analysis . . . 36
3.4.5 SVD & FFT Comparison . . . 40
3.5 Observation of System Improvements . . . 40
3.6 Conclusion . . . 42

4 Betatron coupling: Merging Formalisms and Localization of Sources 46
4.1 Introduction . . . 46
4.2 Hamiltonian terms and coupling matrix . . . 47
4.2.1 Matrix formalism . . . 48
4.2.2 Resonance driving terms . . . 49
4.2.3 Relating the $\mathbf{C}$ matrix to RDT's . . . 49
4.2.4 Simulations . . . 50
4.3 Determinant of $\overline{\mathbf{C}}$ . . . 54
4.3.1 Calculation of $\overline{C}_{12}/\gamma$ using SVD . . . 54
4.3.2 Calculation of $|\overline{C}|/\gamma^2$ from Tracking Data . . . 56
4.3.3 Calculation of $|\overline{\mathbf{C}}|/\gamma^2$ for RHIC Lattice . . . 58
4.3.4 Calculation of skew quadrupole strengths . . . 60
4.4 The closest tune approach . . . 61
4.5 Conclusions . . . 63

5 Betatron Coupling: Measurements at RHIC with AC Dipoles 65
5.1 Introduction . . . 65
5.2 Baseline Measurements of coupling RDT's and $|\overline{\mathbf{C}}|/\gamma^{\mathbf{2}}$ . . . 66
5.2.1 Injection Energy . . . 66
5.2.2 Top Energy (Store) . . . 68
5.3 A Possible Correction Strategy . . . 68
5.3.1 IR Corrector Scan: Injection . . . 69
5.3.2 Vertical Orbit Bump at 2.858 km . . . 72
5.3.3 IR Corrector Scan: Store . . . 72
5.4 Global Coupling, Correction, and Optimization . . . 73

5.5 Conclusion 74

6 Electron Cooling at RHIC **88**
6.1 Intra-Beam Scattering 88
6.2 Electron Cooling 90

7 Radio Frequency Basics and Superconductivity **93**
7.1 Introduction 93
7.2 Pill-Box Cavity 94
7.3 Characteristic Parameters 96
7.3.1 Accelerating Voltage 96
7.3.2 Stored Energy 96
7.3.3 Surface Resistance and Power Dissipation 96
7.3.4 Quality Factor 97
7.3.5 Geometric Factor and Shunt Impedance 97
7.4 RF Superconductivity 98
7.4.1 Superconductivity 98
7.4.2 Surface Resistance of Superconductor 99
7.4.3 Critical Fields 99
7.4.4 Elliptical Multi-cell Cavities 100

8 Ampere Class Energy-Recovery SRF Cavities **101**
8.1 Introduction 101
8.2 Cavity Design 102
8.2.1 Frequency 102
8.2.2 Cavity Geometry 103
8.2.3 Number of Cells 106
8.2.4 Beam Pipe Ferrite Absorbers 108
8.2.5 HOM Loop Couplers 109
8.2.6 Beam Pipe Geometry 109
8.2.7 Final Design 111
8.3 Higher Order Modes 112
8.3.1 Shunt Impedance and Quality Factor 113
8.3.2 HOMs: Frequency Domain 117
8.3.3 HOMs: Time Domain Method 121
8.4 Single Bunch Effects 124
8.5 Multipass Multibunch Instabilities 128
8.6 Power Coupler Kick 130
8.7 Multipacting 134
8.8 Lorentz Force Detuning 135

8.9 Conclusion 137

9 High Current Superconducting $\frac{1}{2}$-Cell Gun 139
9.1 Introduction 139
9.2 SRF Gun Design 139
9.2.1 Cavity Shape 140
9.2.2 HOM Power 141
9.2.3 Multipacting 143
9.3 Beam Dynamics 145
9.3.1 Longitudinal Focusing 145
9.3.2 Transverse Emittance 147
9.4 Final Design and Issues 148
9.4.1 Transition Section 149
9.4.2 Fundamental Power Coupler 153
9.4.3 Cathode Isolation & Design Issues 158
9.5 Ideas for a $1\frac{1}{2}$-Cell Gun for e^- Cooling 159
9.6 Conclusion 160

10 Conclusions 166
10.1 Part I: Linear Optics and Coupling 166
10.2 Part II: SRF Cavities 166

A Perturbative View of BPM data Decomposition 168

B Geometric view of coupled SVD modes 169

C Coupling Matrix 171
C.1 Propagation of the $\overline{\mathbf{C}}$ matrix 171
C.2 Normalized momenta 171
C.3 $\overline{C}_{21}$ in coupler free region 172
C.4 Skew quadrupole strength from two BPMs 173

D Five-Cell SRF Cavity 174
D.1 Bead Pull for Fundamental Mode 174
D.2 BNL II - Alternate Design 175
D.3 Bellow Shielding 176

E $\frac{1}{2}$-Cell SRF Gun 178
E.1 Loss Factor Correction for $\beta < 1$ 178
E.2 Amplitude and Phase Modulation 178
E.3 Voltage Estimates for Parasitic Modes 182

Bibliography **184**

List of Figures

1.1 The hadron collider complex at BNL. 2
1.2 Nucleon-pair luminosity A_1A_2L 4
1.3 Frenet-Serret (curvilinear) coordinate system to describe particle motion in an accelerator. 5
1.4 The Courant-Snyder invariant ellipse with an area of $\pi\epsilon$. . . . 6
1.5 Stripline BPM graphic and prototype 9
1.6 Tranverse profiles recorded by RHIC IPM's 10
1.7 Longitudinal profile recorded by RHIC WCM 11
1.8 Beam response seen by a BPM due to transverse kick 12
1.9 Graphic of the ramp up, flat top, and ramp down of an AC dipole field. 12

2.1 The 6 o'clock IR final-focus region 20
2.2 β functions and dispersion functions at the 8'O clock IR region. 21
2.3 Phase advance and beta function for Au-Au injection optics using AC dipoles. 22
2.4 Phase advance and beta function for p-p injection optics using AC dipoles. 23
2.5 RMS relative differences of phase and β functions between model and measured values. 24

3.1 Fourier spectrum of a good RHIC BPM signal 29
3.2 Spatial vectors and FFT of temporal vectors of the dominant modes 30
3.3 Spatial and temporal vectors of modes corresponding to two noisy BPMs with correlation. 31
3.4 Percentage of occurrences of system failure per BPM 33
3.5 Peak-to-peak values for all BPMs in all data files. 34
3.6 Histograms of the rms observable for the two rings and two planes. The total number of signals used in the histograms are shown. 35

3.7 Comparison between two different rms cuts showing qualitatively similar results. 36
3.8 Average rms observable versus longitudinal position of the BPM. 37
3.9 Histogram of largest peak amplitudes of all spatial modes . . . 38
3.10 Histograms of the norm of n largest peak values of spatial modes 39
3.11 Comparison between two SVD thresholds (0.85 and 0.95) for Blue ring-horizontal plane. 40
3.12 Comparison of the FFT and SVD techniques 41
3.13 Percentage of occurrences of system failure per BPM 43
3.14 Average rms observable versus longitudinal position of the BPM for Run 2004. 44
3.15 Histogram showing number of occurrences of faulty BPMs around the ring 45

4.1 Comparison of coupling terms f_{1001} and $\overline{\mathbf{C}}$ 51
4.2 Mean of the ratio of the coupling terms as a function of skew quadrupole strength 52
4.3 Stop-band limits and coupling terms behavior near sum and difference resonances 53
4.4 Comparison $|C|/\gamma^2$ between model and numerical calculations 57
4.5 Effect of noise on $|C|/\gamma^2$ 58
4.6 Comparison of $|\overline{\mathbf{C}}|/\gamma^2$ between model and numerical calculations using tracking data 59
4.7 Schematic view of a skew quad and the neighbor BPMs 60
4.8 Skew quadrupole strengths calculated from RDT's and $\overline{\mathbf{C}}$ . . . 62
4.9 ΔQ_{min} calculated using RDT's or $|\overline{\mathbf{C}}|$ 63

5.1 Baseline injection measurements of $4|f_{1001}|$ and $|\overline{\mathbf{C}}|/\gamma^{\mathbf{2}}$ in yellow ring 75
5.2 Baseline injection measurements of $4|f_{1001}|$ and $|\overline{\mathbf{C}}|/\gamma^{\mathbf{2}}$ in blue ring 76
5.3 Baseline injection measurements in yellow ring without skew families 77
5.4 Baseline top energy measurements of $4|f_{1001}|$ and $|\overline{\mathbf{C}}|/\gamma^{\mathbf{2}}$ in yellow ring 78
5.5 Baseline top energy measurements of $4|f_{1001}|$ and $|\overline{\mathbf{C}}|/\gamma^{\mathbf{2}}$ in blue ring 79
5.6 Scan of YO9 corrector in IR-10 region 80
5.7 Scan of YI3 and YO4 correctors in IR-4 region 81
5.8 Scan of YO5 and YI6 correctors in IR-6 region 82

5.9 Scan of YO-8 corrector in IR-8 region 83
5.10 Scan of YI11 corrector in IR-12 region 84
5.11 Scan of YO1 corrector in IR-2 region 85
5.12 $|\overline{\mathbf{C}}|/\gamma^{\mathbf{2}}$ (top) as a function the vertical orbit bump amplitude . 86
5.13 Coupling vectors of the three skew quadrupole families of RHIC 87
5.14 f_{1001} from model for a set of different skew families configurations 87

6.1 Typical RHIC stores and refill times with gold ions 89
6.2 Graphical Representation of IBS with and without e^- cooling. 90
6.3 Electron cooling schematic for RHIC II upgrade 92

7.1 Mode frequencies as a function of cavity dimension for a pill box resonator. 95
7.2 Schematic of an elliptical cavity with field lines of TM_{010} mode. 95

8.1 Average power dissipated due to single bunch losses in existing and future SERLs 102
8.2 3D cut away model of the five-cell cyromodule 103
8.3 BCS surface resistance as a function of temperature for different operating frequencies 104
8.4 Parametrization of elliptical cavities. 105
8.5 Optimization of some RF parameters using cavity geometry . 106
8.6 Final middle-cell and end-cell designs for five-cell cavity and an alternate design option, BNL II. 107
8.7 Effect of the number of cells on HOM propogation 108
8.8 Ferrite absorber assembly 109
8.9 Cut away view of 3D model of the HOM loop coupler 110
8.10 Cutoff frequencies of different types of modes in a cylindrical waveguide 111
8.11 Beam pipe transition section consisting of two ellipses 112
8.12 Graphic of the final design of the five-cell cavity, beam pipe transition and the coaxial FPC. 112
8.13 Field flatness of the fundamental mode peak-peak 96.5%. . . . 113
8.14 Trapping of an HOM due to large frequency difference between middle and end cells 115
8.15 Shunt impedance (R/Q) calculated using MAFIA for monopole and dipole modes upto 2.5 GHz. 116
8.16 A coupling parameter κ shows the influence of the BC on the frequency of the mode 118
8.17 Dispersion curves of monopole and dipole modes 119

8.18 Full scale copper prototype 121
8.19 Comparison of calculated and measured values of Q_{ext} 122
8.20 Impedance spectrum and wake function for azimuthally symmetric modes 124
8.21 Impedance spectrum and wake function for transverse dipole modes 127
8.22 Integrated loss factor for BNL I geometry 127
8.23 Logitudinal and transverse loss factors as a function of bunch length. 128
8.24 A computation of complex eigenvalues for each frequency sample from 0.8 to 1.8 GHz. 130
8.25 Time domain beam breakup simulations for e^--cooling scenario 131
8.26 Frequency domain beam breakup simulations for e^--cooling scenario 132
8.27 Q_{ext} as a function of the tip penetration 133
8.28 Longitudinal and transverse fields on-axis of the SRF cavity due to transverse coaxial coupler 134
8.29 Electron counter function and impact energy of surviving electrons 135
8.30 Enhanced counter function as a function of peak field 136
8.31 Multipacting electron trajectories 137
8.32 Surface electric and magnetic fields on the five-cell cavity and corresponding radiation pressure 138
8.33 Deformation of the cavity walls due to Lorentz forces 138

9.1 Conceptual 3D Graphic of $\frac{1}{2}$ cell SRF gun at 703.75 MHz . . . 140
9.2 Six different cavity shapes used for comparison to optimize the final gun design 142
9.3 Integrated longitudinal loss factor calculated by ABCI for the six different designs under consideration. 143
9.4 Electron counter function and final impact energy of the surviving electrons 144
9.5 Enhanced counter function as a function of peak electric field . 145
9.6 Multipacting electron trajectories in the gun 146
9.7 Energy-phase curves for the six different designs 147
9.8 Energy spread in the prototype system with six different gun shapes 148
9.9 Recessed and non-recessed cathode 149
9.10 Longitudinal electric field for recessed and non-recessed cathodes 150
9.11 Vertical emittance for the prototype ERL for six different gun designs 151

9.12 Longitudinal and transverse emittances as a function of cathode position 153
9.13 Broadband impedance spectrum for monopole and dipole modes 154
9.14 Beam pipe transition section for the SRF gun 155
9.15 Frequency spectrum of the beam harmonics with amplitude and time modulations 156
9.16 3D graphic of the 703.75 MHz SRF gun with the dual FPCs with an optimized "pringle" tip. 157
9.17 FPC outer conductor and beam pipe blending to increase coupling 161
9.18 cross section of the SRF gun and the coupler showing the pringle contour and dimensions 162
9.19 Q_{ext} as a function of the transverse pringle dimensions 162
9.20 Q_{ext} as a function of the pringle tip thickness 163
9.21 Q_{ext} as a function of the tip penetration 163
9.22 Longitudinal and transverse fields on-axis of the SRF gun due to FPC 164
9.23 Initial design of $1\frac{1}{2}$-cell gun for e^--cooler 165

B.1 Parametric plots of SVD modes of BPM data from each plane (x-red, y-blue). Data taken using ac dipoles during Run-2004. 169

D.1 Broadband impedance for monopole and dipole modes computed by ABCI for BNL I, I-A, and II designs. 175
D.2 A simple shielding mechanism for the bellows in the 5 K helium region. 176
D.3 A simple shielding mechanism for the bellows in the 5 K helium region. 177

E.1 Longitudinal loss factors computed for the first nine monopole modes in the gun using Eq. E.1 for both $\beta = 1$ and $\beta = 0.5$. The analytical calculation is also compared to the numerical calculation using ABCI. 179

List of Tables

1.1 Ion performance evolution for the RHIC collider. 3
1.2 RHIC parameters for Au-Au, p-p, and Cu-Cu during Runs IV and V. 14

2.1 Injection optics at different working points 26
2.2 Tope energy optics at different working points 27

3.1 Thresholds for peak-to-peak values 34

4.1 FODO Lattice Parameters (NA: Not applicable) 50

5.1 Design tunes and AC dipole drive tunes along with drive amplitude settings at injection energy 67
5.2 Design tunes and AC dipole drive tunes along with drive amplitude settings at top energy settings 68
5.3 Skew quadrupole maximum strengths, and nominal settings at store and injection for the yellow ring. 69
5.4 Skew quadrupole maximum strengths, and nominal settings at store and injection for the yellow ring 70

6.1 Parameters for the prototype SC-ERL 92

7.1 AC power required to operate 500 MHz superconducting and normal conducting cavities at 1 MV/m 98

8.1 Cavity geometrical parameters 107
8.2 RF Parameters for final design of BNL I cavity compared to an alternate BNL II, TESLA, and CEBAF cavities. NE - Not estimated. 114
8.3 Measurement of R_a/Q_0 using spherical beads. R/Q determined from MAFIA calculation is **403.5** Ω. 114
8.4 Lossy properties of ferrrite-50, C-48, and those used in simulation 120

8.5 Longitudinal and transverse loss factors for BNL I, BNL II, TESLA, and CEBAF designs 126
8.6 Transverse kick and normalized emittance growth for a single coupler,dual coupler with 1 mm asymmetry, and a single coupler with a symmetrizing stub, both with a $Q_{ext} \approx 3 \times 10^7$. 133

9.1 Parameters for the prototype SC-ERL 141
9.2 Comparison of RF parameters for the six different cavity shapes 141
9.3 Beam dynamics parameters for the six designs 152
9.4 Cavity geometrical parameters using elliptical parametrization 152
9.5 Transverse kick and normalized emittance growth due to FPC asymmetry 158

E.1 Frequencies and R/Q values (accelerator definition) for the first few monopole and dipole modes in the SRF gun. 180

Acknowledgements

Three women come ahead of everyone else. Fate or not I am her grandson, son, and brother for which I am forever grateful. Their support and trust without which this thesis would simply be a ridiculous thought.

If I can describe my adviser Ilan in one word, OUTSTANDING comes to mind. His patience, vision, committment, and care is simply something to strive for. I owe a lot Steve Peggs who through countless esoteric discussions manages to kindle new thoughts and interesting avenues.

A special thanks to Rogelio who can probably take credit for a good part of this thesis. In the course of the past few years, he has become one of my closest friends. The infinite number of conversations about everything life and work has gotten me through this tempest called "graduate school". I owe you man!! I would also like to thank a mutual friend and collaborator Andrea. I wish this team will go strong for many years to come.

The three years at the collider accelerator department was exceptional and I can only attribute this experience to some of the nicest and most professional colleagues some of who have become good friends.

T. Roser, V. Litvenenko, W. Fischer, J. Sekutowicz and M. Blaskeiwicz have helped me a great in making this thesis a reality and I am grateful for the numerous illuminating discussions.

Todd Satogata needs a special mention, I cannot thank him enough for the infinite number of times he has helped through almost every aspect of this thesis.

There are a number of people I would to thank from the Accelerator Physics group who have helped me a great deal to learn about the complex RHIC machine. In particular, M. Bai, V.Ptitsyn, S. Tepikian, W. Mckay, N. Malitsky, Y. Luo, D. Kayran, D.Trbojevic, F. Pilat, A. Drees, J. DeLong, K. Smith, M. Brennan and others. I would also like to sincerely thank G. McIntyre, D. Pate, A. Burill, S.Seiberg, R.Anderson and the rest of the engineering and machine shop crew have gone out of their way to help me and accommodate my requests.

I owe a lot to the administrative staff both at Stony Brook and BNL who

made my graduate career an easy sail. I would to mention a few names, Pat, Diane, Sara from Stony Brook and Ana, Marion, Gladys, Ann who made sure that immigration doesn't kick me out.

Last but not the least, I would also like thank all my collaborators and friends from a number of National Labs and Universities whose help and friendship was invaluable. It is inevitable that I forgot to mention someone, but I would like assure that your contribution to this thesis will not be forgotten.

Chapter 1

Introduction

1.1 The Relativistic Heavy Ion Collider, RHIC

RHIC consists of two six-fold symmetric superconducting rings with a circumference of 3.833 km. The two rings (blue and yellow) consist of six arcs intersecting at six interaction regions (IRs) and provide collisions to 2-4 concurrent experiments. The main goal of RHIC is to provide collisions at energies up to 100 GeV/u per beam for heavy ions ($^{197}Au^{79}$). The accelerator is also designed for colliding lighter ions all the way down to protons (250 GeV), including polarized protons [1, 2]. RHIC currently offers a unique feature to collide different ion species, for example deuteron-gold collisions in 2002. A sketch of the BNL accelerator complex, showing the RHIC injectors, beamlines, and location of the interaction regions is shown in Fig 1.1.

An important figure of merit for colliders is luminosity which defines the number of interactions produced per unit cross section given by the convolution integral [3]

$$\mathcal{L} = \int_A N_1\rho_1(x,y)N_2\rho_2(x,y)\ da \tag{1.1}$$

where $N_{1,2}$ are the number of particles per beam, and $\rho_{1,2}(x,y)$ are the transverse particle distributions [1]. For Gaussian beams with equal beam sizes, Eq. 1.1 becomes [5]

$$\mathcal{L} = n\frac{f_{rev}N_1N_2}{4\pi\sigma_x^*\sigma_y^*} \tag{1.2}$$

where n is the number of bunches, f_{rev} is the revolution frequency, and $\sigma_{x,y}^*$ are the RMS widths of the Gaussian beam. For experiments the integrated

[1]Note that this integral holds for head on collision and short bunches. For bunches with $\sigma_z < \beta^*$, a luminosity reduction due to hourglass effect [4] is non-negligible like in p-p collisions at RHIC.

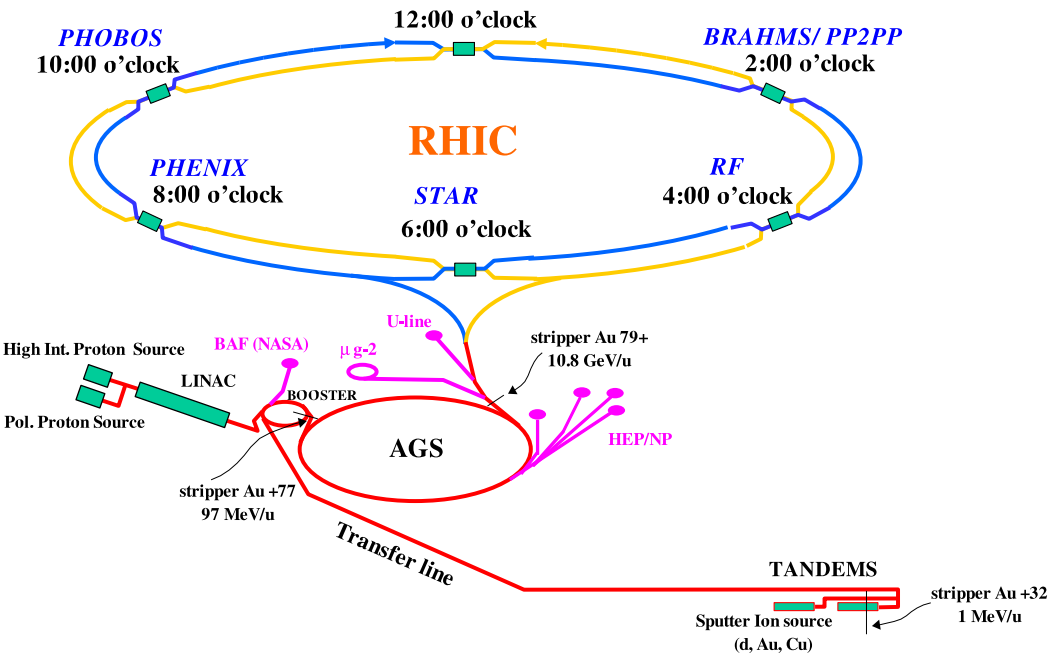

Figure 1.1: The hadron collider complex at Brookhaven National Laboratory. The path of a Au ion can be traced from its creation at the Tandem until its injection into RHIC. The polarized protons are injected from the LINAC into the booster ring, AGS, and finally into RHIC.

luminosity is a better figure of merit than the instantaneous luminosity given in Eq. 1.2. RHIC was commissioned in 1999 and has successfully completed five physics runs with heavy-ions and polarized protons. Table 1.1 shows design, achieved, and upgrade machine parameters. Fig. 1.2 shows an evolution of the nucleon-pair luminosity ($A_1 A_2 L$) indicative of the length of the runs as delivered to the PHENIX experiment.

Future luminosity upgrades involve electron cooling of the ion beams which is discussed in Part II of this thesis.

1.2 Linear Beam Dynamics

In a circular accelerator, the motion of a particle can be expressed as oscillations around a momentum dependent closed orbit [2] commonly know as

[2]The average particle trajectory closes on itself after one complete revolution

Table 1.1: Ion performance evolution and Run-# parameters shown for the RHIC collider. Note that some runs have collisions with different energies and the integrated luminosity listed is summed up over the different modes. The flexibility of different collision energies is an important aspect of RHIC. Enhanced luminosity numbers are facility goals c. 2008, before electron cooling [6].

Run	Species	No of bunches	Ions/bunch [10^9]	$\beta^\star$ [m]	Emittance [$\pi\mu$rad]	$\mathcal{L}_{int}$
Design	Au-Au	56	1.0	2	-	-
Run-1	Au-Au	56	0.5	3	15	20 μb^{-1}
Run-2	Au-Au	55	0.6	1-3	15-40	258.4 μb^{-1}
	p-p	55	70	3	25	1.4 pb^{-1}
Run-3	d-Au	55/110	120d/0.7Au	2	15-25	73 nb^{-1}
	p-p	55	70	1	20	5.5 pb^{-}1
Run-4	Au-Au	45	1.1	1-3	15-40	3.80 nb^{-1}
	p-p	56	70	1	20	7.1 pb^{-1}
Run-5	Cu-Cu	35-56	3.1-4.5	0.85-3	15-30	43.6 nb^{-1}
	p-p	56-106	60-90	1-2	25-50	29.6 pb^{-1}
Enhanced	Au-Au	112	1.1	0.9	15-40	-
Enhanced	p-p	112	2.0	1	25-50	-

betatron motion. The transverse motion can be expressed as

$$x(s) = x_0(s) + x_\beta(s) + D_x(s)\delta \tag{1.3}$$

where, $x_0(s)$ is the reference closed orbit, x_β is the betatron amplitude, and $\delta \equiv \Delta p/p_0$ is the momentum deviation from the ideal particle with momentum p_0 and D_x is the dispersion function.

1.2.1 Transverse Betatron Motion

Assuming no dispersion and small amplitude betatron oscillation around the closed orbit, the motion of the particles are governed by second order homogeous differential equations also know as Hill's equations

$$x^{''} + K_x(s)x(s) = 0 \tag{1.4}$$

$$y^{''} + K_y(s)y(s) = 0 \tag{1.5}$$

where,

$$K_x \equiv \frac{1}{\rho^2} - \frac{\partial B_y}{\partial x}\frac{1}{B\rho}, \quad K_y \equiv \frac{\partial B_y}{\partial x}\frac{1}{B\rho}$$

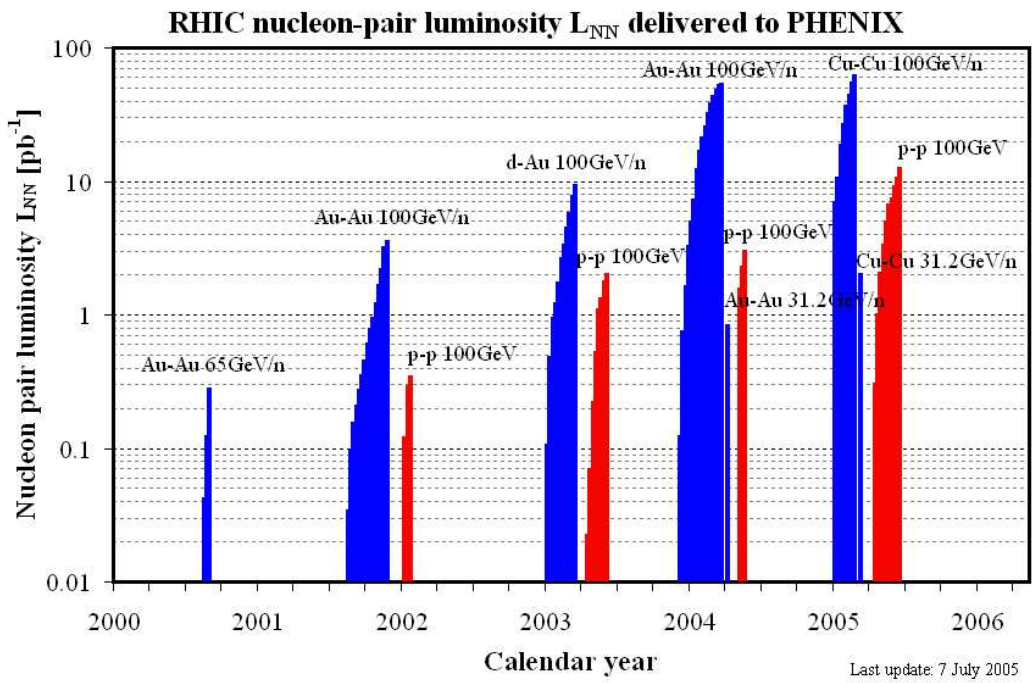

Figure 1.2: Nucleon-pair luminosity A_1A_2L delivered to the PHENIX experiment (courtesy RHIC operations).

The solution to the 2nd order differential equations are

$$x(s) = \sqrt{2J\beta(s)}\cos\left(\psi(s)+\phi\right) \tag{1.6}$$

$$x'(s) = \sqrt{\frac{2J}{\beta(s)}}\left[\sin\left(\psi(s)+\phi\right)+\alpha(s)\cos\left(\psi(s)+\phi\right)\right] \tag{1.7}$$

where J and ϕ are action angle invariants of motion, $\beta(s)$ is the betatron function, $\alpha(s) \equiv -\beta'(s)/2$, and $\psi(s)$ is the phase advance given by

$$\psi(s_1 \rightarrow s_2) = \int_{s_1}^{s_2} \frac{1}{\beta(s)}\, ds \tag{1.8}$$

Assuming that the motion of the particle is linear motion, the evolution of the transverse coordinates of the particle motion in one turn can be conveniently expressed through a linear matrix

$$\begin{bmatrix} x \\ x' \end{bmatrix}_2 = \mathcal{M}_C \begin{bmatrix} x \\ x' \end{bmatrix}_1 \tag{1.9}$$

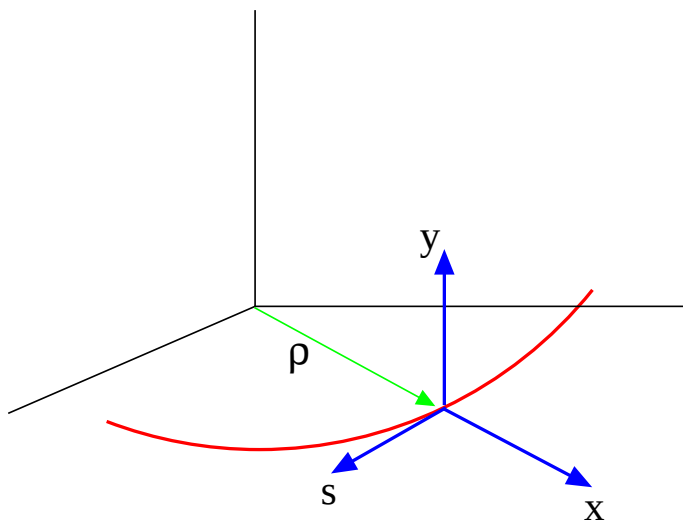

Figure 1.3: Frenet-Serret (curvilinear) coordinate system to describe particle motion in an accelerator.

where C is the circumference of the accelerator and

$$\mathcal{M}_C = \mathbf{I}\cos(\psi_C) + \mathbf{J}\sin(\psi_C). \tag{1.10}$$

Here, $\mathbf{I}$ is the 2×2 identity matrix, and

$$\mathbf{J} = \begin{bmatrix} \alpha & \beta \\ -\gamma & -\alpha \end{bmatrix} \tag{1.11}$$

where $\gamma \equiv (1+\alpha^2)/\beta$ and stable motion of the particle requires

$$|tr\mathcal{M}_C| \leq 2. \tag{1.12}$$

1.2.2 Emittance

The action variable J can be expressed in terms of x and x' to yield the Courant-Snyder invariant given by [8]

$$2J = \gamma x^2 + 2\alpha x x' + \beta x'^2 = \epsilon \tag{1.13}$$

The trajectory of the particle in the (x, x') frame follows an ellipse with an area of $2\pi J$ as shown in Fig. 1.4. When particles are subject to acceleration, it is useful to define a normalized emittance

$$\epsilon_N = \beta_r \gamma_r \epsilon \tag{1.14}$$

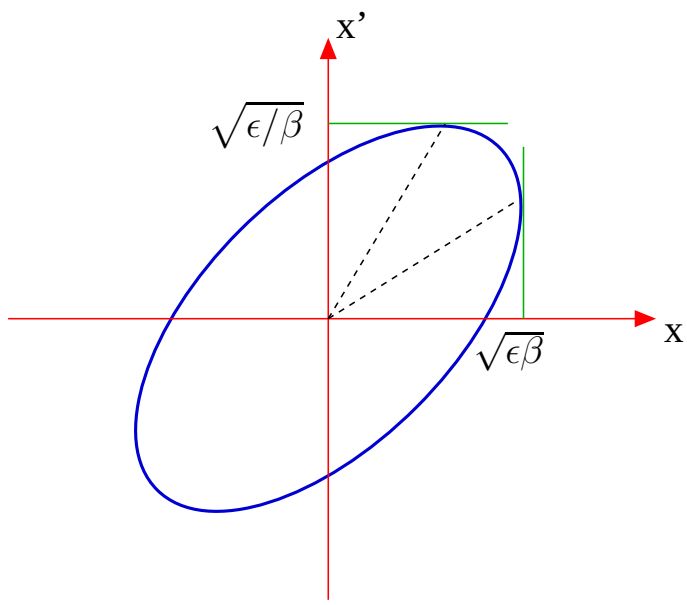

Figure 1.4: The Courant-Snyder invariant ellipse with an area of $\pi\epsilon$.

which is generally conserved. Here, β_r and γ_r are relativistic factors.

Given a distribution of particles, each tracing an ellipse, the rms beam emittance can be defined as [9]

$$\epsilon_{rms} = \sqrt{\sigma_x^2 \sigma_{x'}^2 - \sigma_{xx'}^2} \tag{1.15}$$

where

$$\sigma_x^2 = \int [x - \langle x \rangle]^2 \ \rho(x, x') \ dx \ dx' \tag{1.16}$$

is the transverse beam size, and $\rho(x, x')$ is the normalized distribution function. Therefore, the rms beam size is given by $\sqrt{\beta(s)\epsilon_{rms}}$.

1.2.3 Dispersion

The position of a particle with a momentum deviation Δp with respect to the reference particle with momentum p_0 can be expressed in terms of periodic dispersion function given by

$$x(s) = D(s)\delta \tag{1.17}$$

where $\delta \equiv \Delta p / p_0$ is the fractional momentum deviation. The Hill's equation of motion can be written as [9]

$$x''_\beta + (K_x(s) + \Delta K_x) x_\beta = 0 \tag{1.18}$$

where, to first order

$$\Delta K_x = \left[-\frac{2}{\rho^2} + K(s) \right] \delta \tag{1.19}$$

and $K_x = (1/\rho^2) - K(s)$ and $K(s) = \frac{1}{B\rho}(\partial B_y/\partial x)$. The 2×2 Courant-Snyder matrix can be enlarged to include the dispersion terms as

$$\begin{bmatrix} x \\ x' \\ \delta \end{bmatrix}_2 = \mathcal{M}_C \begin{bmatrix} x \\ x' \\ \delta \end{bmatrix}_1 + \mathcal{M}_C \begin{bmatrix} D(s)\delta \\ D'(s)\delta \\ \delta \end{bmatrix}_1 \tag{1.20}$$

Here, $\mathcal{M}_\mathcal{C}$ is an extended version of Eq. 1.10 with

$$\mathbf{J} = \begin{bmatrix} \alpha & \beta & 0 \\ -\gamma & -\alpha & 0 \\ 0 & 0 & 1 \end{bmatrix} \tag{1.21}$$

1.2.4 Betatron Tune and Chromaticity

An important parameter in colliders is the number of betatron oscillations in one turn which is commonly refered to as *tune* given by

$$Q = \frac{1}{2\pi}\Delta\psi_C = \frac{1}{2\pi}\oint \frac{ds}{\beta} \tag{1.22}$$

The particles with different momenta are focused differently. This effect of momentum dependent focusing is known as chromatic aberration and results in a tune shift given by

$$\Delta Q = \xi\delta \tag{1.23}$$

where the natural chromaticity from quadrupoles is given by

$$\xi = -\frac{1}{4\pi}\oint K\beta ds \tag{1.24}$$

A large chromaticity can result in an overlap of betatron tunes with resonances due to magnet imperfections and lead to beam losses. Furthermore, chromaticity can result in instabilities (head-tail) depending on its sign. Chromaticity correction is usually achieved from non-linear elements like sextupoles. These elements are sources of non-linearities and drive higher order resonances and affect beam stability. They also result in a reduction of the dynamic aperture, the available phase space area sustaining stable motion.

1.2.5 Linear Magnetic Field Errors

The presence of dipole field errors gives an additional transverse orbit displacement. The displacement at a location "s" due to the integrated effect of N deflections θ_i is [10]

$$\Delta x(s) = \frac{\sqrt{\beta}}{2\sin(\pi Q)} \sum_{i=1}^{N} \theta_i \sqrt{\beta_i}\ \cos\left[|\psi(s) - \psi(s_i)| - \pi Q\right]. \tag{1.25}$$

where $\theta_i = \Delta B \Delta s/(B\rho)$ for a dipole, and $\theta_i = (Kl)_i \delta x_i$ for a horizontal displacement of δx_i of a quadrupole. The corresponding change in the length of the closed orbit is given by

$$\Delta L = \sum_{i=1}^{N} \theta_i D(s_i) \tag{1.26}$$

where $D(s)$ is the dispersion function. It can be seen from Eq. 1.25 that dipole perturbations can lead to integer resonances and the closed orbit becomes unstable if the betatron tunes are close to an integer. A large orbit distortion also reduces the available aperture for betatron oscillations.

Similarly, the presence of quadrupole errors results in a perturbation of the β function. The integrated effect on the β function from N quadrupole errors is given by [10]

$$\frac{\Delta\beta}{\beta} = \frac{1}{2\sin(2\pi Q)} \sum_{i=1}^{N} (\Delta Kl)_i \beta(s_i)\ \cos\left[2|\psi(s) - \psi(s_i)| - 2\pi Q\right] \tag{1.27}$$

The corresponding tune shift due to gradient is given by

$$\Delta Q = -\frac{\beta(s_i)}{4\pi}(\Delta Kl)_i \tag{1.28}$$

A second resonance condition at the $\frac{1}{2}$-integer is encountered from quadrupole perturbations which is seen from Eq. 1.27. Therefore, a betatron tune near the $\frac{1}{2}$-integer leads to a diverging solution.

1.3 RHIC Instrumentation

Like most accelerators, RHIC is equipped with a variety of instruments that monitor the beam coordinates, intensities, losses and other beam properties. These instruments not only establish stable circulating beam but also protect the sensitive superconducting elements and electronics crucial for successful operation. Some of the instruments are briefly decribed in the section.

1.3.1 Beam Position Monitors

Beam position monitors (BPMs) are usually stripline or button type monitors used to measure the transverse position of the beam centroid. The transverse beam position is given by

$$x \approx \frac{w}{2}\left[\frac{U_+ - U_-}{U_+ + U_-}\right] \tag{1.29}$$

where $U_\pm$ is either the current or voltage signal from the electrode and $w/2$ is the effective width of the stripline. Fig. 1.5 shows a graphic of a stripline BPM and a cutaway view of a prototype of a RHIC BPM. BPMs are typically

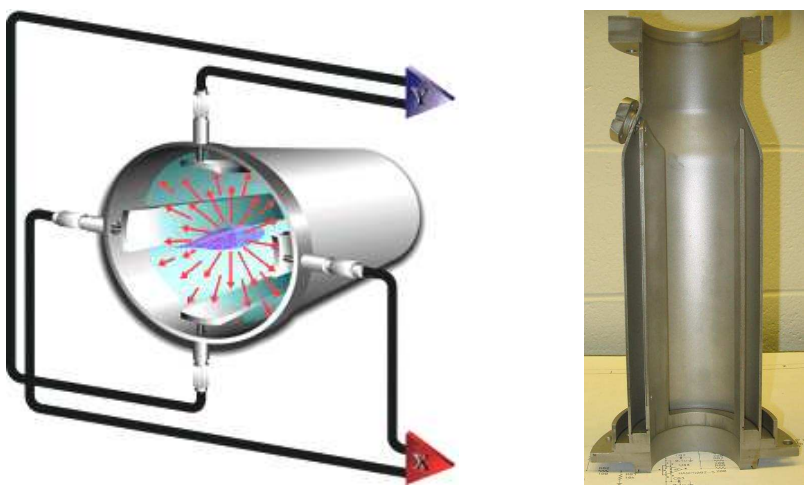

Figure 1.5: Left: A graphic of a stripline beam position monitor [11]. Right: A cutaway view of the RHIC BPM (Courtesy J. Cupolo) designed for cryogenic temperatures.

used to measure the closed orbit averaged over several turns ($\sim 10^4$ or larger). This mode is usually robust and offers a good resolution due to the statistical benefits ($\leq$ 10 μm in RHIC). They are also used to measure turn-by-turn (TBT) beam orbits which contain both position and phase information which is of great interest for the measurement of several linear and non-linear aspects of the lattice. However, issues relating noise, resolution, timing, and fast data acquisition often limit the quality of the data. Part I (chapter 2- 5) of this thesis will focus on bpm reliability, measurement and correction of linear optics and coupling based on TBT data.

1.3.2 Beam Loss Monitors

The beam loss monitors (BLMs) are critical for the protection of the superconducting magnets in RHIC. The RHIC BLMs are ion chambers with an electrode in a cylindrical glass container enclosed in a metal chamber. The chamber is typically filled with dry pressurized gas for sensitivity (Argon in RHIC BLMs). A DC voltage is applied between the outer can and the center electrode to create an electric field. Ionizing radiation passing through the chamber collides with gas molecules producing ion pairs. The primaries and secondaries are swept to the oppositely charged electrode by the electric field. This results in a net current which is then passed through various electronics to amplify and measure the amount beam loss. Pin diodes are also employed in RHIC for fast and sensitive measurement of losses [12].

1.3.3 Profile Monitors

Ionization beam profile monitors (IPM's) measure the beam profile by collecting electrons from background gas ionization [12, 13]. IPM's are primarily used to measure beam emittance and injection matching. RHIC is equipped with four IPM's to measure horizontal and vertical profiles in each ring.

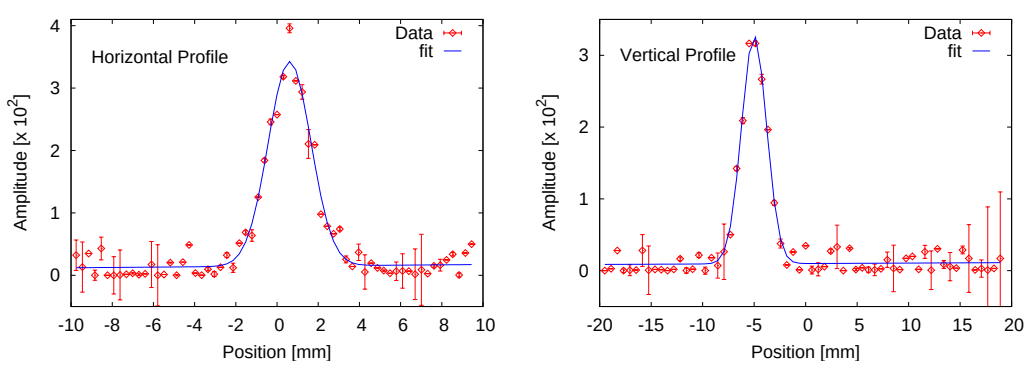

Figure 1.6: A typical plot of the transverse profiles recorded by RHIC IPM's. The data points are averaged over 100 samples. They were taken during Run 2006, p-p collisons at 100 GeV (Fill # 7655). The transverse normalized emittances are estimated to be $\epsilon_x \sim 21\pi$ mm·mrad, $\epsilon_y \sim 15\pi$ mm·mrad.

1.3.4 Wall Current Monitors

A wall current monitor (WCM) is a ceramic break in the beam pipe with several parallel resistors spanning the break [12, 14]. The enclosure is damped

by ferrites to extend the bandwidth from 3kHz out to 6GHz. The voltage induced in the resistors due to image currents of the beam is measured to determine both the beam current and longitudinal profile. RHIC is also equipped with direct current transducers (DCCTs) to measure the average current by balancing primary and secondary currents through a transformer.

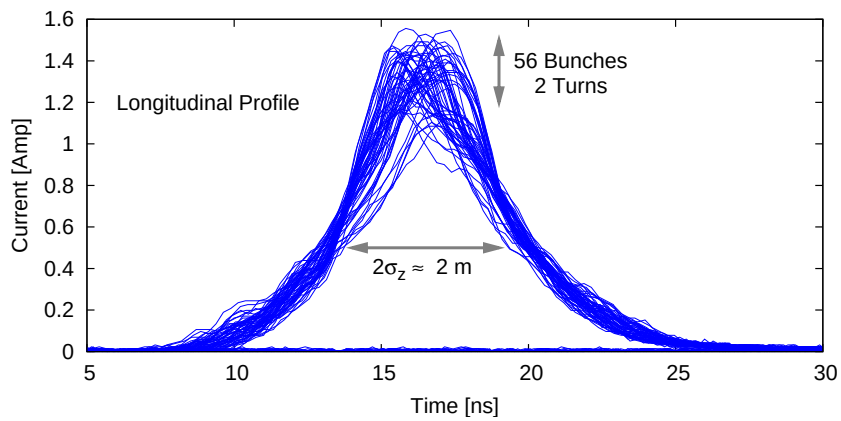

Figure 1.7: A typical longitudinal profile recorded by the RHIC WCM. This data was acquired during Run 2004, p-p collisons with 56 bunches.

1.3.5 Transverse Kickers

RHIC is equipped with fast kicker magnets for injection, beam abort, and tune measurements. Two transverse kicker magnets are available for tune measurements in each ring, capable of generating single turn kick pulses of approximately 140 ns by fast switches [12]. Dedicated dual plane BPMs in each ring are used to measure the beam response (TBT) from a succesion of kicks and calculate tunes which are very useful for machine developement and operation. A typical beam response seen on a BPM due to a transverse kick is shown in Fig. 1.8

1.3.6 AC Dipoles

Unlike a kicker magnet which imparts a impulse kick to the beam, an AC dipole has an oscillating field to induce coherent large amplitude oscillations in the beam when driven close to a resonance. The amplitude of the oscillations is given by [15]

$$x(s) \approx \frac{1}{4\pi|\delta Q|}\frac{B_d l}{B\rho}\sqrt{\beta(s)\beta_d} \tag{1.30}$$

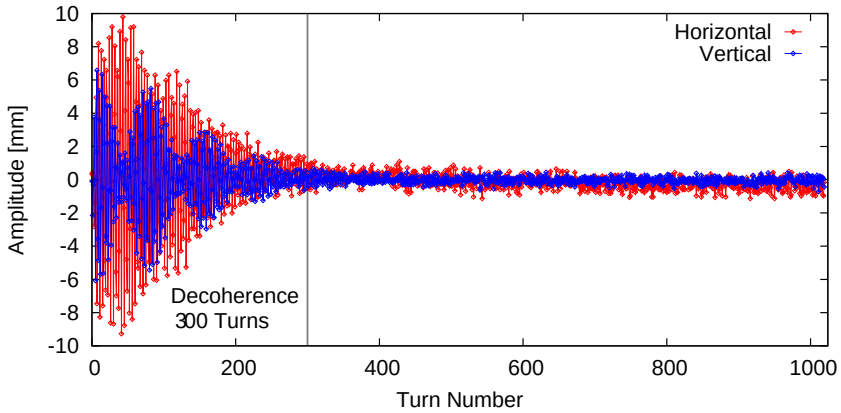

Figure 1.8: Typical beam response as seen on a BPM due to transverse kick in both planes. The decoherence time is in this case is approximately 300 turns which is mainly dominated by linear chromaticity and also some non-linear de-tuning.

where d is the location of the AC dipole, and $\delta Q = Q_0 - Q_d$ is the tune separation between the drive frequency and the betatron frequency. An AC dipole can be ramped adiabatically and has the advantage of preserving the beam emittance unlike an impulse kick. Coherent betatron oscillations overcome the

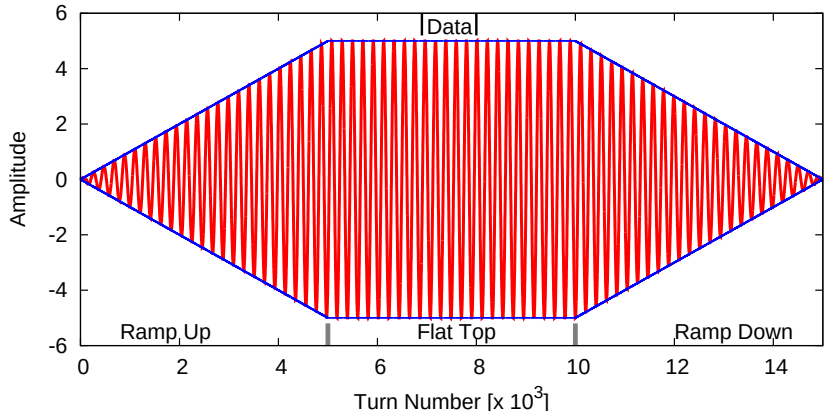

Figure 1.9: Graphic of the ramp up, flat top, and ramp down of an AC dipole field.

difficulties associated with decohered oscillations to measure beam properties with known numerical techniques (for example broadening of the Fourier spectrum) [16]. In principle, the length of the AC dipole excitation is limited by the data acquisition capability. In Part I of this thesis, AC dipole data is ex-

tensively used to measure linear optics and coupling. Several other uses like accelerating through depolarizing resonances [17] and non-linear studies [18, 19] make the AC dipole an unique and invaluable device.

Table 1.2: RHIC parameters for Au-Au, p-p, and Cu-Cu during Runs IV and V. Tune scan simulations and experiments found betatron tunes at $Q_x = 28.72$, $Q_y = 29.73$ to provide better dynamic aperture and fewer spin resonances for polarized protons [7].

			Gold	**Protons**	**Copper**
parameter	symbol	unit	value	value	value
Mass number	A	-	197	1	63
Atomic number	Z	-	79	1	29
Number of ions/bunch	N_b	10^9	1	100	4.5
Number of bunches/ring	-	-	*variable, from 28 to 110*		
Circumference	C	m	3833.85		
Energy per beam injection	E	GeV/n	10.8	28.3	12.6
Energy per beam store	E	GeV/n	100	100 & 190	100
Transition energy	γ_t	-	22.89		
Magnetic rigidity injection	$B\rho$	T m	81.1	81.1	81.1
Magnetic rigidity store	$B\rho$	T m	839.5	339.5	724.6
Dipole field injection	B	T	??	0.33	???
Dipole field store	B	T	??	1.37	???
Betatron tune horizontal	Q_x	-	28.23		29.72
Betatron tune vertical	Q_y	-	28.22		29.73
β^* at IP injection	β^*	m	10		
β^* at IP store	β^*	m	1-3		
Quadrupole gradient	-	T/m	≈71		
Operating temp, ^{4}He	T	K	4		
Harmonic number injection	h	-	360	360	360
Harmonic number store	h	-	2520	360	2520
RF voltage injection	V	MV	0.3	0.1	0.3
RF voltage store	V	MV	2-4	0.3	2-4
RF frequency injection	$\omega_{\rm rf}$	MHz	28.15	28.15	28.15
RF frequency store	$\omega_{\rm rf}$	MHz	198	28.15	198
Synchrotron freq. injection	Q_s	Hz	120	25	145
Synchrotron freq. store	Q_s	Hz	333	43	270
Energy spread injection	$\Delta E/E$	10^{-3}	±1.49	±1.26	??
Energy spread store	$\Delta E/E$	10^{-3}	±1.49	±0	??
Bunch area injection	$S_{95\%}$	eV s/u	0.5	0.5	0.7
Bunch area store	$S_{95\%}$	eV s/u	1.1	1.2	1.0
Normalized emittance	ϵ_n	mm mrad	10π	20π	10π

Chapter 2

Principle Component Analysis and Linear Optics

2.1 Introduction

Principle component analysis (PCA) is a widely used technique in multivariate statistics to identify dominant patterns in a given dataset. This is accomplished by a transformation to pick a coordinate axis that maximizes the variance of all data points along that axis [20, 21, 22]. For a given dataset X, the unit length basis vectors $\mathbf{v} = [v_1, v_2, \ldots, v_n] \in \mathcal{R}^M$ that maximize the variance is evaluated as

$$\frac{v^T C_{ij} v}{v^T v} = max \tag{2.1}$$

where

$$C_{ij} = \frac{1}{n-1} \sum_{i,j=0}^{n} (X_i - \overline{X})(X_j - \overline{X}) \tag{2.2}$$

is the covariance matrix ($cov\{X_i, X_j\}$). Subsequent orthogonal axes can be computed to form a set of basis vectors that completely define the dataset with a reduced dimensionality. Using this transformation, the original data matrix $X_{n\times m}$ can be decomposed as

$$X = WV^T \tag{2.3}$$

where $W_{n\times m}$ and $V_{m\times m}$ comprise of orthogonal vectors describing the spatial[1] and temporal[2] behavior of the leading principle components. This decomposition is mathematically equivalent to a singular value decomposition (SVD).

[1]Behavior of the principle components at the each monitor position.

[2]Time evolution of a principle component.

2.2 Singular Value Decomposition

Any $n \times m$ real or complex matrix X can be factorized into the form

$$X = U\Sigma V^\dagger \tag{2.4}$$

where U is an $n \times n$ unitary matrix, Σ is a $n \times m$ diagonal matrix, and $V^\dagger$ is the Hermitian conjugate of an $m \times m$ unitary matrix [23]. Both U and V are hermitian, such that

$$XX^\dagger = U\Sigma^2 U^\dagger, \quad X^\dagger X = V\Sigma^2 V^\dagger \tag{2.5}$$

The diagonal elements of Σ represent the square roots of the eigenvalues of covariance matrix $X^\dagger X$ or $XX^\dagger$ and are referred to as singular values. The number of non-zero singular values reveals the dimensionality of the data set. Since U and V are unitary matrices, the vectors of $\{u_1, u_2, \ldots, u_n\}$ and $\{v_1, v_2, \ldots, v_m\}$ form an orthonormal basis of X.

SVD has found many applications, especially in data processing and numerical problems. The most direct application of SVD is the computation of eigenvalues of $cov\{X_i, X_j\}$. Unlike the computation of eigenvalues using traditional algorithms, SVD is robust against perturbations and roundoff errors [24]. A perturbation in the data matrix can be decomposed as

$$A + \delta A = U(\Sigma + \delta\Sigma)V^\dagger \tag{2.6}$$

Since U and V are unitary, they have a unit norm, and $||\delta A|| = ||\delta\Sigma||$. Therefore, perturbations in the data matrix manifest themselves as perturbations in singular values of the same order. Given a rectangular matrix, the SVD essentially computes a pseudo-inverse which naturally lends itself to least square problems extensively used in physics. The rank of the matrix is easily estimated from the number of non-zero singular values which determines the minimum number of modes to completely the describe the system. Since the factorization groups the data into basis vectors, the reduced dimensionality is very useful for data and image compression schemes.

The distribution of multiple BPMs along the beam trajectory and their capability to acquire several sequential TBT data is ideal for multivariate time series analysis to understand the underlying structure of the lattice. Since the BPM data is a collection of space-time series, SVD factorizes the information into

$$B(\mathbf{x}, t) = \sum_n \sigma_n U_n(t) V_n(\mathbf{x}) \tag{2.7}$$

where, U_n and V_n are the eigenmodes of the "spatial" and "temporal" correlation matrices

$$C(x_i, x_j) = \sum_t B(x_i, t) B(x_j, t) \tag{2.8}$$

$$C(t_i, t_j) = \sum_x B(x, t_i) B(x, t_j) \tag{2.9}$$

In this chapter we focus on the application of SVD on TBT data from the BPMs to infer beam phase space and corresponding lattice parameters. This numerical technique was first applied to beam physics by J. Irwin and group [25]. A detailed treatment of transverse beam dynamics in 1D (no transverse coupling) using PCA-SVD formalism can be found in Refs. [26, 27]. Independent component analysis, another numerical approach (similar to PCA) using a blind source separation technique has also been applied to study BPM signals of interest [28]. We outline the application of SVD on BPM data and present measurements of RHIC optics using this formalism and betatron oscillations excited by ac dipoles.

2.3 Linear Optics: Formalism

Assuming, the motion is dominated by betatron motion without coupling, the data from m BPMs recording t turns each can be represented in a matrix form. This BPM matrix can be factorized as

$$\underbrace{\begin{pmatrix} b_1^1 & b_2^1 & \dots \\ b_1^2 & \ddots & \\ b_1^3 & & \\ \vdots & & \end{pmatrix}}_{B_{t\times m}} = \underbrace{\begin{pmatrix} u_1^+ & u_1^- & \dots \\ \vdots & \vdots & \\ \vdots & \vdots & \\ u_t^+ & u_t^- & \dots \end{pmatrix}}_{U_{t\times m}} \underbrace{\begin{bmatrix} \sigma_+ & 0 & \dots & \dots \\ 0 & \sigma_- & & \\ \vdots & & \ddots & \\ \vdots & & & \sigma_m \end{bmatrix}}_{\Sigma_{m\times m}} \underbrace{\begin{bmatrix} v_1^+ & v_1^- & \dots \\ \vdots & \vdots & \\ \vdots & \vdots & \\ v_m^+ & v_m^- & \dots \end{bmatrix}^T}_{V^T_{m\times m}} \tag{2.10}$$

where "+" and "-" represent the orthogonal vectors representing a betatron mode. $\Sigma_{m\times m} = [\sigma^+, \sigma^-, \dots]$, $V_{m\times m} = [v^+, v^-, \dots]$, and $U_{t\times m} = [u^+, u^-, \dots]$, are the corresponding non-negative singular values, eigenvectors representing the spatial variation of betatron function, and temporal eigenvectors representing the time evolution of the betatron mode respectively.

The TBT data in the mth BPM can be expressed as

$$b_t^m = \sqrt{2J_t\beta_m}\cos(\phi_t + \psi_m) \tag{2.11}$$

The BPM matrix is normalized by the number of turns $B = b_t^m/\sqrt{T}$, therefore the covariance matrix is given by

$$C_B^{mn} = \frac{1}{T}\sum_{t=1}^{T} b_t^m b_t^n \tag{2.12}$$

$$= \sum_{t=1}^{T} \frac{J}{T}\sqrt{\beta_m\beta_n}[\cos(\psi_m - \psi_n) + \cos(2\phi_t + \psi_m + \psi_n)] \tag{2.13}$$

$$= \langle J\rangle\sqrt{\beta_m\beta_n}\cos(\psi_m - \psi_n) \tag{2.14}$$

To find the eigenvalues and eigenvectors, we need to solve

$$C_B v = \lambda v \tag{2.15}$$

where $v = \sqrt{2J\beta_m}\cos(\phi_0 + \psi_m)$. From the mth component of the secular equation we have the condition that

$$\sum_{n=1}^{M} \beta_n \sin 2(\phi_0 + \psi_n) = 0. \tag{2.16}$$

The two solutions for Eq. 2.16 are

$$\phi_0 = -\frac{1}{2}\tan^{-1}\left(\frac{\sum_n \beta_n \sin 2\psi_n}{\sum_n \beta_n \cos 2\psi_n}\right) \tag{2.17}$$

and $\phi_0 + \pi/2$ corresponding to the two eigenvalues

$$\lambda_\pm = \frac{1}{2}\langle J\rangle\left[\sum_{n=1}^{M}\beta_n \pm \sum_{n=1}^{M}\beta_n\cos 2(\phi_0 + \psi_n)\right]. \tag{2.18}$$

The normalized eigenvectors (spatial) are given by

$$v_+ = \frac{1}{\sqrt{\lambda_+}}\left[\sqrt{\langle J\rangle\beta_m}\cos(\phi_0 + \psi_m)\right] \tag{2.19}$$

$$v_- = \frac{1}{\sqrt{\lambda_-}}\left[\sqrt{\langle J\rangle\beta_m}\sin(\phi_0 + \psi_m)\right] \tag{2.20}$$

and the corresponding, normalized temporal vectors are given by

$$u_+ = \sqrt{\frac{2J_t}{T\langle J\rangle}}\cos(\phi_t - \phi_0) \tag{2.21}$$

$$u_- = -\sqrt{\frac{2J_t}{T\langle J\rangle}}\sin(\phi_t - \phi_0) \tag{2.22}$$

Therefore, the Twiss functions[3] can be derived from the betatron vectors

$$\psi = \tan^{-1}\left(\frac{\sigma_- v_-}{\sigma_+ v_+}\right) \tag{2.23}$$

$$\beta = \langle J\rangle^{-1}(\sigma_+^2 v_+^2 + \sigma_-^2 v_-^2) \tag{2.24}$$

Error bounds in the Twiss functions are

$$\sigma_\psi = \sqrt{\left(\frac{\partial\psi}{\partial\sigma_+}\right)^2\sigma_+^2 + \left(\frac{\partial\psi}{\partial\sigma_-}\right)^2\sigma_-^2} \approx \frac{1}{\sqrt{T}}\frac{\sigma_r}{\sigma_s}\sqrt{\frac{\langle\beta\rangle}{2\beta}} \tag{2.25}$$

$$\sigma_{\frac{\Delta\beta}{\beta}} = \sqrt{\left(\frac{\partial\beta}{\partial\sigma_+}\right)^2\sigma_+^2 + \left(\frac{\partial\beta}{\partial\sigma_-}\right)^2\sigma_-^2} \approx 2\beta\sigma_\psi \tag{2.26}$$

2.4 RHIC Linear Optics: Measurements

The RHIC lattice consists of 6 arcs, each with 11 FODO[4] cells with approximately 80° phase advance. Parameters of the arc dipoles and quadrupoles are shown in Table 1.2. Each of the six interaction region (IRs) consists of a triplet quadrupole scheme to focus the beams at the collision point, and a pair of $D0$ and DX dipole magnets to bring the beams in and out of collision. A schematic of the final focus IR (6 o'clock) is shown Fig. 2.1. A section between the final focus and arc consists of FODO cells similar to the arc with a few dipoles for dispersion suppression. The "ideal" β functions and dispersion functions near an IR are plotted a function of longitudinal position in Fig. 2.2. Optics in Fig. 2.1 are for proton-proton collisions with $\beta^* = 1m$ at the collision point.

Limitations in measuring Twiss functions are primarily related to the quality and availability of reliable BPM data. At RHIC, a significant number of BPMs exhibit failures related to radiation, electronics and low level software issues which are discussed in chapter 3 and Ref. [30]. These BPMs are excluded from the calculation of Twiss parameters. It was also found that a few BPMs show turn mismatch due to timing problems in the electronics which is corrected for 1-2 turns mismatch because the phase advance between two consecutive BPMs are usually smaller than $\pi/2$. Beyond three turns, this correction can lead to ambigous results and the only remedy is to fix the timing

[3]The parameters β, α, and γ are also called Twiss functions [29]

[4]A pair of focusing and defocusing quadrupoles inter-spaced by a bending dipole magnet or a drift space

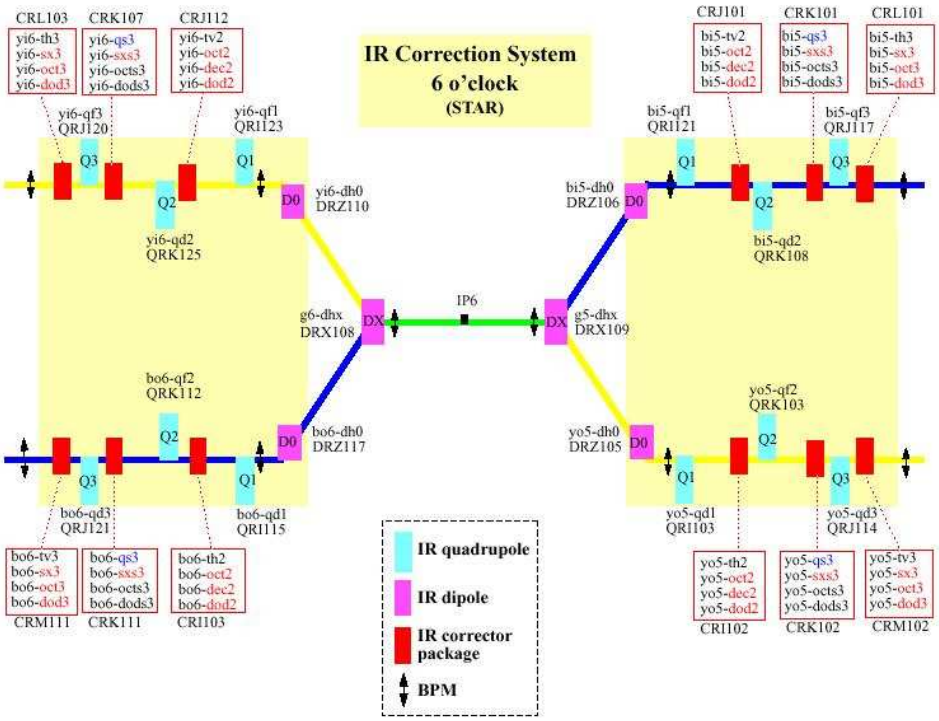

Figure 2.1: The 6 o'clock IR final-focus region with triplet quadrupoles, $D0$ and DX bending dipoles, and linear and non-linear correctors (courtsey F. Pilat).

at the hardware level using simulated beam signals or with a circulating beam with a single injected bunch.

Optics measurements were taken at injection during a working point scan during Run 2004 [7]. Figs. 2.3 and 2.4 show a comparison between model and measured Twiss functions for Au-Au injection ($\gamma = 10.25$) and p-p injection ($\gamma = 25.94$). The rms of the phase advance difference, ($\psi_m^{model} - \psi_m^{measured}$) and the rms of relative difference in β function, $(\beta_m^{model} - \beta_m^{meas})/\beta^{model}$ were calculated to understand the sensitivity of optics measurements to the working point and β^*. Some measurements show a large deviation from the model mainly due to BPM failures. Data files with very large deviation are not included in this analysis. The measurements for Yellow and Blue ring were not separated because we assume that the instrumentation in both rings were similar.

Tables 2.1 and 2.2 show a detailed list of rms differences for the different working points at injection and store. Note that the model tunes are not exactly matched to measured tunes [31]. Fig. 2.5 shows a plot of average

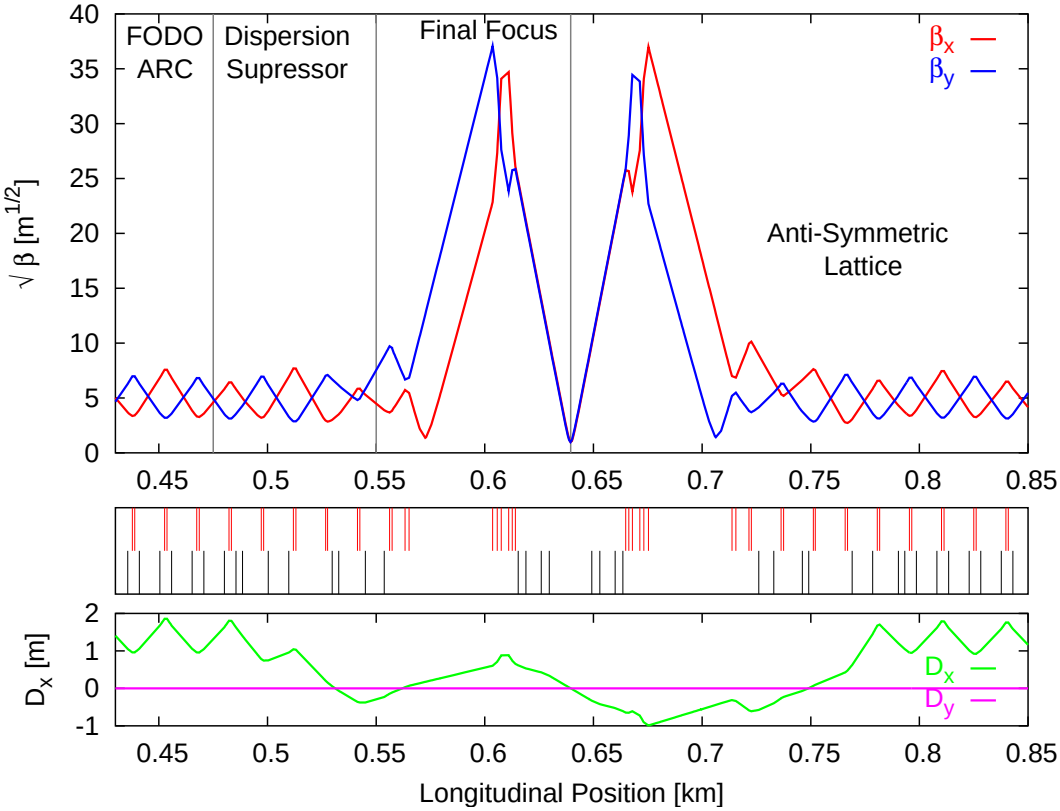

Figure 2.2: β functions (top) and dispersion functions (bottom) at the 6 o'clock IR region. A representation of the lattice (dipoles in black and quadrupoles in red) is shown in the middle. The betatron tunes are $Q_x = 28.23$ and $Q_y = 28.22$, and the horizontal dispersion at the collision point is zero.

values and their standard deviations of $(\Delta\beta/\beta)^{rms}$ and $\Delta\psi^{rms}$ only for Au-Au and p-p injection and store conditions. The other working points are not plotted because of large systematic errors. It is clear from Fig. 2.5 that large deviation from the mean values are mainly due to systematic errors. A number of systematic measurements and improvements in BPM reliability will reduce these deviations significantly. One can notice that the rms phase advance difference for $Q \sim 0.2$ region appears to be slightly better than $Q \sim 0.7$ region. One can also notice that for $Q \sim 0.2$ region, the $(\Delta\beta/\beta)^{rms}$ is smaller for injection optics ($\beta^* = 10$m) than store optics ($\beta^* = 1$m) as expected. However, the region near $Q \sim 0.7$ shows contrary results which needs to be verified. A large number of statistics are needed to arrive at a definitive conclusion.

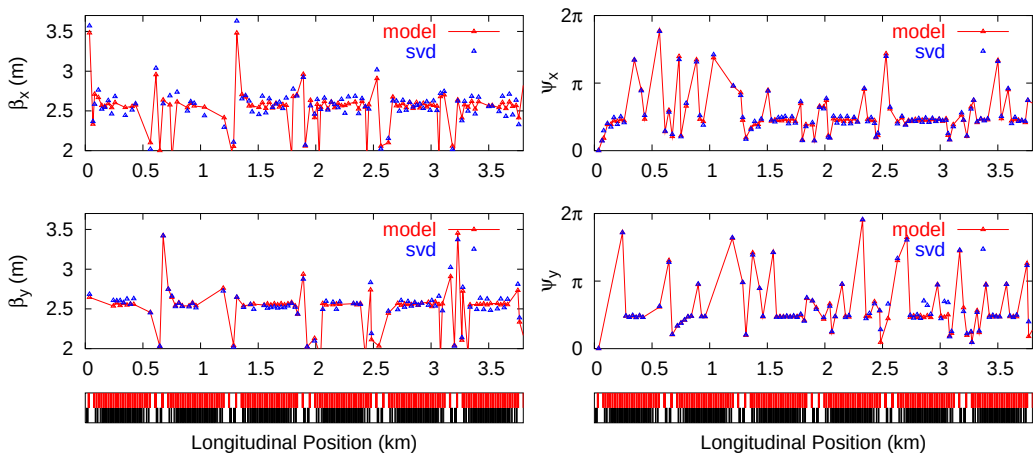

Figure 2.3: Phase advance and beta function for Au-Au injection optics using AC dipoles.

2.5 Error source identification

Closed orbit correction due to random dipole errors has been extensively studied [32, 33]. Global techniques using linear least square algorithms and local orbit bumps are routinely used in most accelerators to correct the particle orbit. A thin horizontal focusing error of Δq [m^{-1}] causes a horizontal perturbation wave that propagates (β-beat) downstream to first order in Δq like

$$\frac{\Delta\beta}{\beta} \approx -\Delta q\, \beta_0 \sin(2(\phi - \phi_0)) \tag{2.27}$$

where β_0 is the design horizontal beta function at the quadrupole error source. The close analogy between particle trajectory and beta wave pertubation indicates a close connection between the problems of closed orbit correction and quadrupole error source identification.

2.5.1 Global Correction

The effect of the β function perturbation at m BPMs due to change in strength of n correctors can be formulated into a $m \times n$ response matrix (similar to closed orbit response matrix)

$$\mathcal{A}\Delta\vec{q} = \left[\frac{\Delta\vec{\beta}}{\vec{\beta}}\right] \tag{2.28}$$

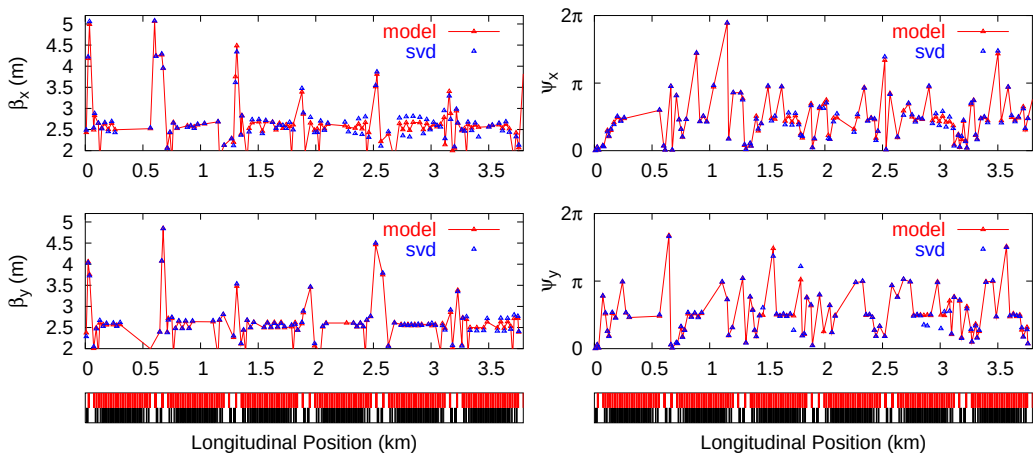

Figure 2.4: Phase advance and beta function for p-p injection optics using AC dipoles.

where

$$\mathcal{A}_{mn} = \frac{\beta_n}{2\sin(2\pi Q)} \cos\left(2|\psi_m - \psi_n| - 2\pi Q\right). \tag{2.29}$$

The model and measured β-functions at m BPMs can be expressed into a β-beat vector

$$\left[\frac{\Delta\vec{\beta}}{\vec{\beta}}\right] = \left[\left(\frac{\Delta\beta}{\beta}\right)_1, \left(\frac{\Delta\beta}{\beta}\right)_2, \ldots, \left(\frac{\Delta\beta}{\beta}\right)_m\right] \tag{2.30}$$

The goal is to minimize the quadratic residual β-beat at all the BPMs

$$\left\|\mathcal{A}\Delta\vec{q} - \frac{\Delta\vec{\beta}}{\vec{\beta}}\right\|^2 = min. \tag{2.31}$$

For $m = n$, the solution for this linear equation is unique and is given by

$$\Delta\vec{q} = (\mathcal{A}^T\mathcal{A})^{-1}\mathcal{A}^T\left[\frac{\Delta\vec{\beta}}{\vec{\beta}}\right] \tag{2.32}$$

and for

$$\begin{array}{lcll} m > n & : & \text{over-determined} & \{\text{minimum residual}\} \\ m < n & : & \text{over-constrained} & \{\|\Delta\vec{q}\| \rightarrow \text{min}\} \end{array}. \tag{2.33}$$

which can be easily solved using numerical techniques like SVD.

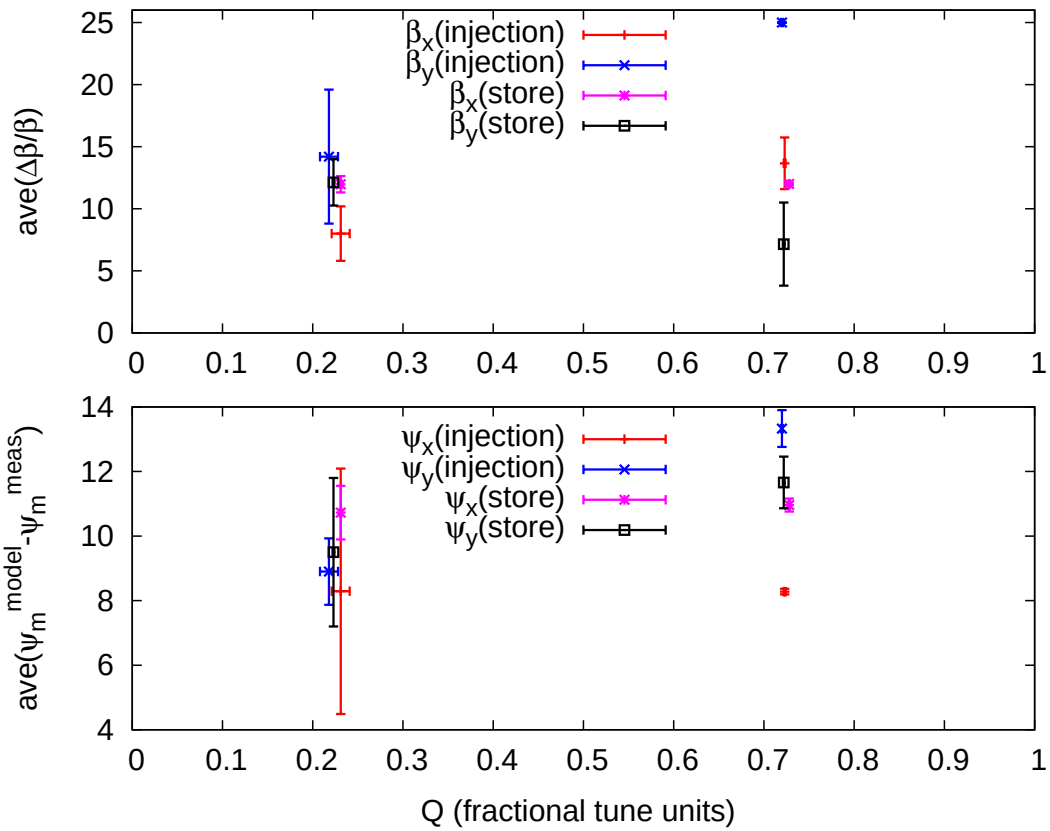

Figure 2.5: RMS relative differences of phase and β functions between model and measured values. The data points represent the different working points for Au-Au and p-p beams at both injection and store.

2.5.2 Local Correction

Just as 3 dipole correctors can be powered to create a closed orbit "three-bump", so also can 3 quadrupoles create a local β-bump. The local β perturbation by three quadrupoles require

$$\beta_1 \Delta q_1 C(\psi_{31} - 2\pi Q) + \beta_2 \Delta q_2 C(\psi_{32} - 2\pi Q) + \beta_3 \Delta q_3 C(2\pi Q) = 0 \quad (2.34)$$

$$\beta_1 \Delta q_1 C(2\pi Q) + \beta_2 \Delta q_2 C(\psi_{21} - 2\pi Q) + \beta_3 \Delta q_3 C(\psi_{13} - 2\pi Q) = 0 \quad (2.35)$$

where "C" is the cosine function. Therefore, the strengths of the three quadrupoles to make a closed β-bump are

$$\begin{aligned}
\Delta q_1 &= -\frac{\Delta\beta_2}{\beta_2}\,\frac{1}{\beta_1}\,\frac{1}{\sin(2\psi_{21})} \\
\Delta q_2 &= +\frac{\Delta\beta_2}{\beta_2}\,\frac{1}{\beta_2}\,\frac{\sin(2\psi_{31})}{\sin(2\psi_{32})\,\sin(2\psi_{21})} \\
\Delta q_3 &= -\frac{\Delta\beta_2}{\beta_2}\,\frac{1}{\beta_3}\,\frac{1}{\sin(2\psi_{32})}
\end{aligned} \tag{2.36}$$

and where, for example,

$$\psi_{21} = \psi_2 - \psi_1 \tag{2.37}$$

It should be noted that the β-bump is not closed in the other (vertical) plane. The "sliding 3-bump" algorithm can take the measured $\Delta\beta/\beta$ at many BPMs vector as input, generating a suggested quadrupole correction vector (with elements at every lattice quadrupole) as output. It is often more practical to interpret this output vector as a set of quadrupole error sources, especially if the quadrupoles are powered in families (as in RHIC). If independent horizontal and vertical optics error measurements are available, then both measurements should identify the same quadrupole error sources. An off-line code **β-beat** is developed to automate source identification. Simulations to predict quadrupole errors in LHC and correct β-beat below the 20% level[5] in this fashion is under study [34].

2.6 Summary

An outline of PCA, SVD and their applications to linear optics in colliders is discussed. The measurement of linear optics using AC dipole data was demonstrated reliably in Run 2003-04. Optics were measured for different working point tunes and a comparison for each working point was done to understand the effect of tune. Although the region near $Q \sim 0.2$ shows slightly better results than the region near $Q \sim 0.7$, no significant difference was found between the working points. The effect of β^* on the magnitude of β-beat is consistent for data near $Q \sim 0.2$ region. The region near $Q \sim 0.7$ needs to be revisited and more systematic studies will help develop a more accurate model. For all measurements faulty BPMs were removed based on criteria explained in the chapter 3.

[5]LHC aperture constraint for maximum allowable β-beat.

Table 2.1: Working point optics at Injection($\gamma_{Au} - 10.52$, $\gamma_{pp} - 25.94$). β^* @ 6 IPs (10,10,10,10,10,10) [m]. NE - Not Estimated due to excitation of AC dipole in only one plane or large systematic errors.

Ring	Q_x	Q_y	$\Delta\psi_x^{rms}$	$\frac{\Delta\beta_x}{\beta_x}^{rms}$	$\Delta\psi_y^{rms}$	$\frac{\Delta\beta_y}{\beta_x}^{rms}$
RHIC Tunes: Au-Au						
B	0.237	0.222	11.9	8 %	NE	NE
B	0.237	0.222	11.31	7 %	9.4	12 %
Y	0.21	0.22	10.9	NE	10.4	14 %
B	0.238	0.20	6.7	10 %	8.27	8 %
B	0.238	0.20	5.9	11 %	8.6	18 %
Y	0.219	0.232	2.5	5 %	8.6	17 %
B	0.238	0.224	11.46	7 %	10.1	23 %
B	0.238	0.224	NE	NE	7.5	8 %
RHIC Tunes: p-p						
Y	0.723	0.720	8.19	12 %	14	25 %
Y	0.723	0.720	8.3	13 %	13	NE
Y	0.723	0.720	8.36	16 %	13	NE
RHIC Design Tunes: Au-Au						
Y	0.168	0.182	16.1	48 %	9.57	NE
Y	0.168	0.182	4.79	33 %	NE	NE
Y	0.201	0.187	2.13	19 %	9.8	32 %
Y	0.201	0.187	15.4	39 %	6.5	12 %
ISR Tunes (Au-Au)						
B	0.1025	0.11	10.9	13 %	22.3	52 %
B	0.1025	0.11	NE	NE	22.4	31 %
B	0.1025	0.11	NE	NE	15	8 %
SPS Tunes (Au-Au)						
B	0.705	0.695	13.3	25 %	20.07	39 %
B	0.705	0.695	17.0	23 %	17.7	36 %
B	0.705	0.695	NE	NE	14.5	9 %
B	0.705	0.695	NE	NE	12.3	9 %

Table 2.2: Working Point Optics at Store with ($\gamma_{Au} - 10.52$, $\gamma_{pp} - 106.58$).

Ring	Q_x	Q_y	$\Delta\psi_x^{rms}$	$\frac{\Delta\beta_x}{\beta_x}^{rms}$	$\Delta\psi_y^{rms}$	$\frac{\Delta\beta_y}{\beta_x}^{rms}$
RHIC Tunes Au-Au β^*(3,5,1,1,3,5) [m], $\gamma - 107.76$						
B	0.231	0.223	10.3	12 %	8.0	11 %
B	0.231	0.223	10.7	13 %	7.0	11 %
B	0.231	0.223	10.0	13 %	11.2	12 %
B	0.231	0.223	11.9	12 %	11.9	15 %
RHIC Tunes p-p β^*(3,10,2,2,3,10) [m], $\gamma - 106.58$						
Y	0.728	0.722	10.8	12 %	10.7	11 %
Y	0.728	0.722	10.9	12 %	11.93	6 %
Y	0.728	0.722	11.19	12 %	12.36	5 %

Chapter 3

Statistical analysis of RHIC beam position monitors performance

3.1 Introduction

BPMs are used in accelerators to record the average orbit and transverse turn-by-turn displacements of the bunch centroid motion. RHIC consists of two six-fold symmetric rings with six interaction regions. There are 160 BPMs per plane per ring (yellow & blue): 72 dual-plane BPMs distributed through the IRs, and 176 single-plane BPMs distributed in the arcs [35]. Each BPM channel acquires 1024 consecutive turn-by-turn positions.

It is imperative to understand the functioning of each BPM to obtain reliable and consistent data for any beam dynamics analysis. In this chapter we perform a first detailed statistical analysis to evaluate the performance of the RHIC BPM system with the aid of numerical tools. A large set of data files recorded after applying a horizontal kick during RUN 2002-03 were analyzed using SVD and FFT techniques [25, 36]. Both techniques were independently employed to identify malfunctioning BPMs from available data sets. Statistical behavior of BPM performance was extracted to characterize each pick-up and make a comparison between the two methods. A comparison between two different operation years is also presented and improvements in the BPM system is evident.

3.2 FFT TECHNIQUE

The Fourier spectrum of turn–by–turn data has already been used to determine faulty BPM signals from the Super Proton Synchrotron of CERN [36]. This technique relies on the fact that the Fourier spectrum of an ideal signal has well localized peaks while noisy or faulty signals show a randomly popu-

lated Fourier spectrum. A priori two observables seem to provide information on this regard: the average and the rms of the background of the Fourier spectrum. The average background depends on other parameters apart from the noise of the signal, therefore it is discarded for our purposes. The rms of the background of the Fourier spectrum is larger for noisier BPMs and its dependence with other parameters is negligible. This observable is therefore used to identify the noisy pick–ups. It is estimated by computing the rms of the amplitudes of the spectral lines within one or several spectral windows. These windows are chosen in such a way that an ideal pick–up would not show any peak within them. It is important to avoid including the zero frequency and the betatron tunes in any window. An illustration of a typical configuration for RHIC is shown in Fig. 3.1, using a good signal.

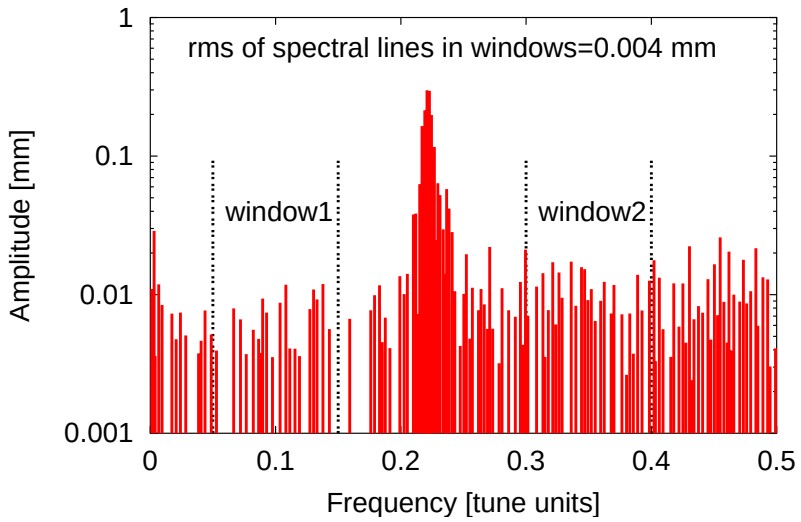

Figure 3.1: Fourier spectrum of a good RHIC BPM signal. The spectral lines within the windows are used to determine the rms noise observable.

A signal is considered faulty if its rms noise observable is larger than a certain threshold. The value of the threshold is extracted from statistics over a large number of signals. A histogram of rms observables from all signals is constructed. Typically a large peak containing the largest percentage of the data is observed in the low rms values of the histogram. This peak contains the set of physical signals, while its long tail with larger rms values contains the faulty signals. A suitable threshold is chosen towards the end of the tail. It will be shown in section 3.4 that particular choices of the cut do not give qualitatively different results.

3.3 SVD Technique

SVD has proved to be a powerful numerical tool in a wide variety of disciplines and has been recently applied to beam dynamics under the name "Model Independent Analysis" [25]. SVD is used to identify the principle components by maximizing the cross-covariance between time-dependent data. The number of non-zero singular values gives the effective rank of the matrix. For a matrix containing turn-by-turn data from several BPMs, the dominant singular vectors represent the temporal and spatial variation of physical modes characterizing the motion of the beam.

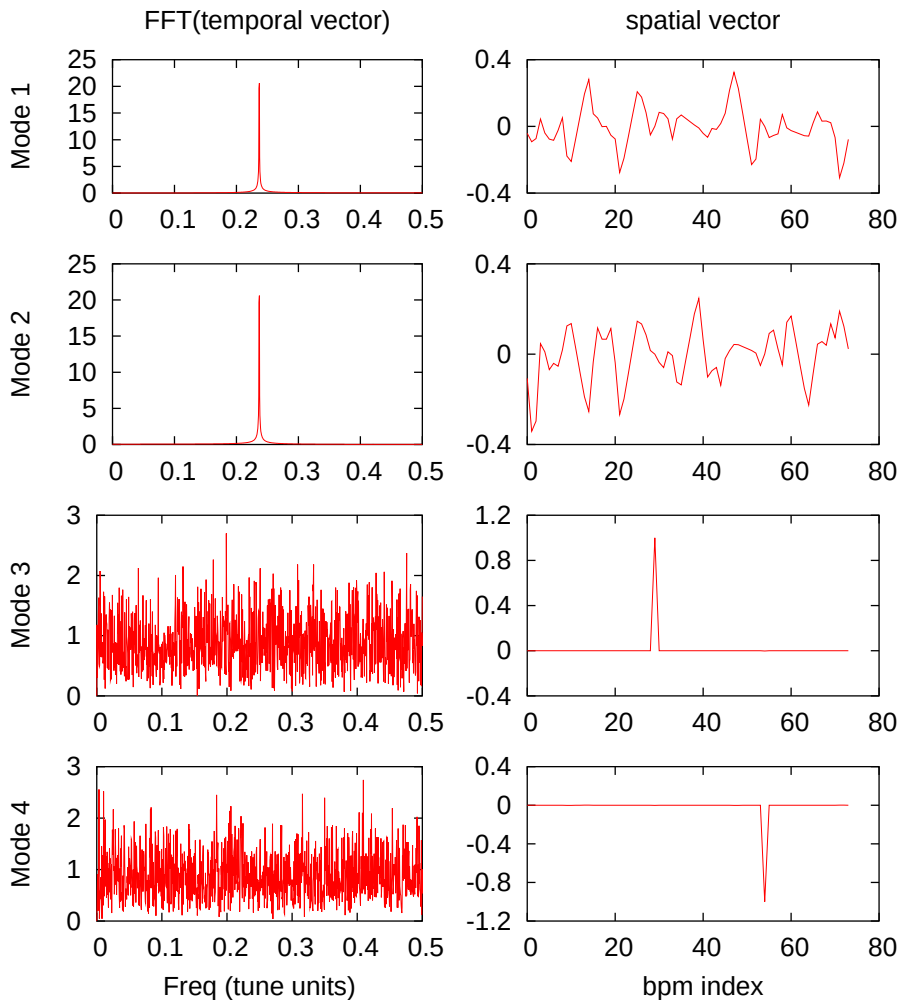

Figure 3.2: Spatial vectors and FFT of temporal vectors of the 4 dominant modes from simulation data. Note that singular vectors are normalized.

The potential scope of SVD analysis in accelerators runs deep. This chapter attempts to exploit one facet that aids in identifying malfunctioning BPMs. Fig. 3.2 shows typical plots from the application of SVD to simulated BPM data (after subtracting the average orbit), with only linear elements and two noisy BPMs at arbitrary locations. The singular value spectrum shows two dominant modes ("Mode 1" and "Mode 2") corresponding to the betatron oscillation in the plane of observation. The Fourier transform of the temporal mode yields the betatron tune. "Mode 3" and "Mode 4" show sharp spikes in their spatial vectors. The signal manifested in this mode is localized to a particular BPM location indicating a potentially noisy BPM. The Fourier transform of their temporal modes yields all frequencies, confirming that these are noisy BPMs. In this situation of relatively ideal conditions, we find distinct peaks localized at corresponding noisy BPM locations and a flat signal elsewhere. However, from real data, we observe multiple peaks in the spatial vectors, due to random correlations between the noisy BPMs. One such possibility was simulated by setting the noise amplitudes in the two pickups to be approximately equal. We observe two dominant modes as above, but the spatial vectors now contain two peaks in each mode, as shown in Fig. 3.3.

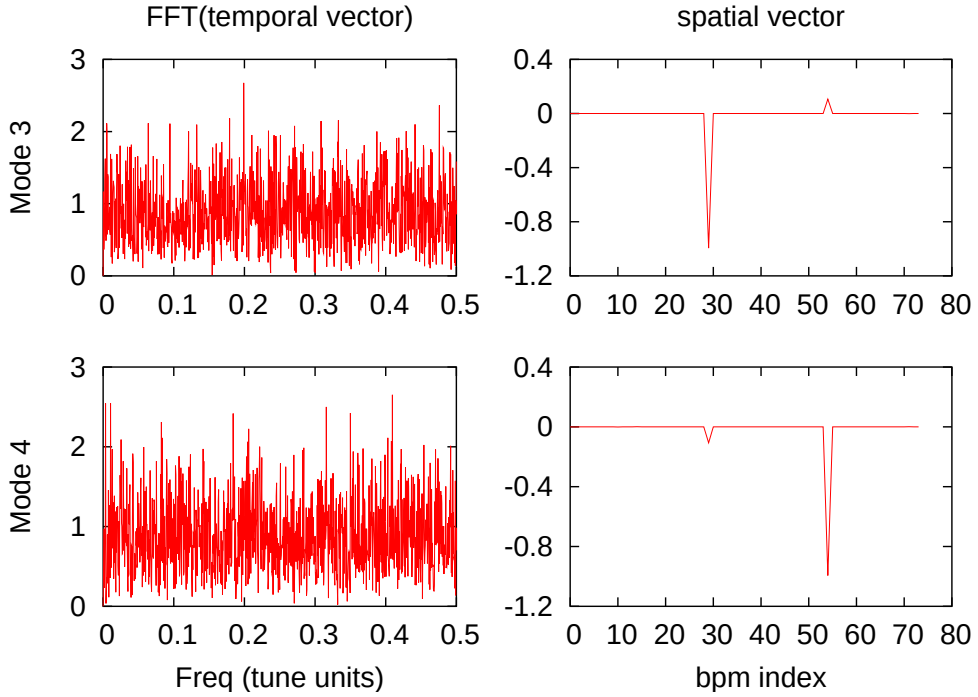

Figure 3.3: Spatial and temporal vectors of modes corresponding to two noisy BPMs with correlation.

A simple approach to identify faulty BPMs would entail finding modes with spatial vectors consisting only of localized peaks. A localized peak threshold value of 0.7 or greater might be sufficient to tag them as noisy BPMs [37]. However, we explore a statistical approach to understand the characteristics of BPM signals from which we choose the appropriate thresholds. A histogram of the largest peaks in each spatial mode for a large set of data is constructed to determine these thresholds. It will also be shown from statistics that an alternate approach using the norm of n largest peaks in each mode is a more accurate procedure to determine threshold values. One should note that the SVD method is insensitive to flat signals. Some preprocessing of BPM data, using peak-to-peak signal information, will be effective before applying such techniques. This is discussed below.

3.4 Analysis

About 2000 data sets (1000 for each ring) taken during Run 2003 of deuteron-gold collisions were used in this statistical approach. Statistical cuts were applied during data preprocessing before using the two techniques. This data is then used to determine independent thresholds for each technique, to identify noisy BPMs. We discuss each statistical cut in detail to explore the advantages and limitations of such an approach.

3.4.1 Hardware Cut

RHIC BPM hardware internally determines the status for each turn-by-turn measurement in a data set. Status bit information acquired in this way allows us to identify obvious hardware failures. We make a simple histogram of all BPMs that fail (status = 0), as shown in Fig. 3.4. BPMs failing this cut are removed from the data and are not included in further analysis. This histogram also helps us identify any consistent hardware problems. We also find a number of files in which fewer than 30 BPMs were present, and these files were excluded for this analysis separately for each plane.

3.4.2 Peak-to-Peak Thresholds

A peak-to-peak cut is necessary because both techniques become less sensitive as signal oscillations become small. Peak-to-peak signal values for all BPMs in all data sets were calculated, and plotted in a histogram in Fig. 3.5. One has to be careful to choose an appropriate cut. If optics and machine

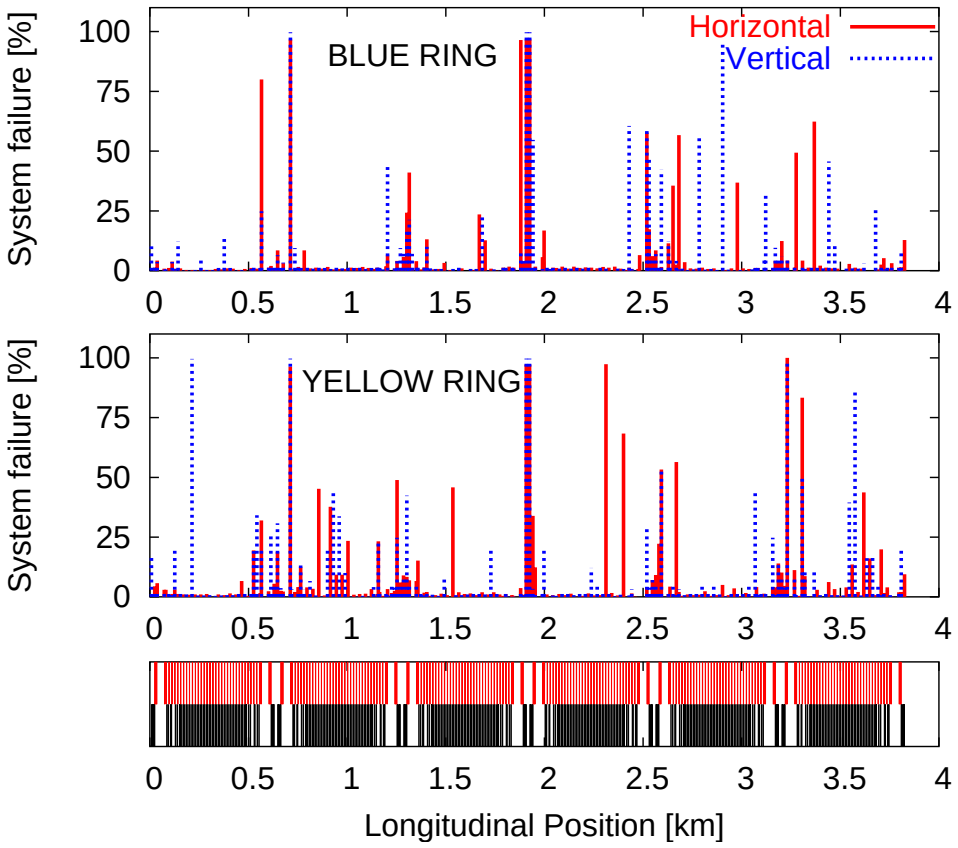

Figure 3.4: Percentage of occurrences of system failure per BPM versus longitudinal location. A representation of the lattice (dipoles in black and quadrupoles in red) is shown in the bottom graph.

conditions were static, it would be easier to determine the best threshold. However, this is not true in regular operation. A very low cut might help retain good BPMs with small signal, but it will also retain BPMs that are faulty. A large cut removes faulty BPMs, but will also identify many good BPMs as faulty.

The data sets being analyzed are mostly horizontally kicked data, hence we will discuss horizontal plane features in detail. There is a distinct minimum at 0.3 mm and a peak below that value which we believe are BPMs that do not respond to beam current. If a 0.3 mm cut removes good BPMs for a specific set of unexcited data, they will appear as background in the final identification, and will not be tagged as faulty BPMs. We observe a large peak around 1 mm

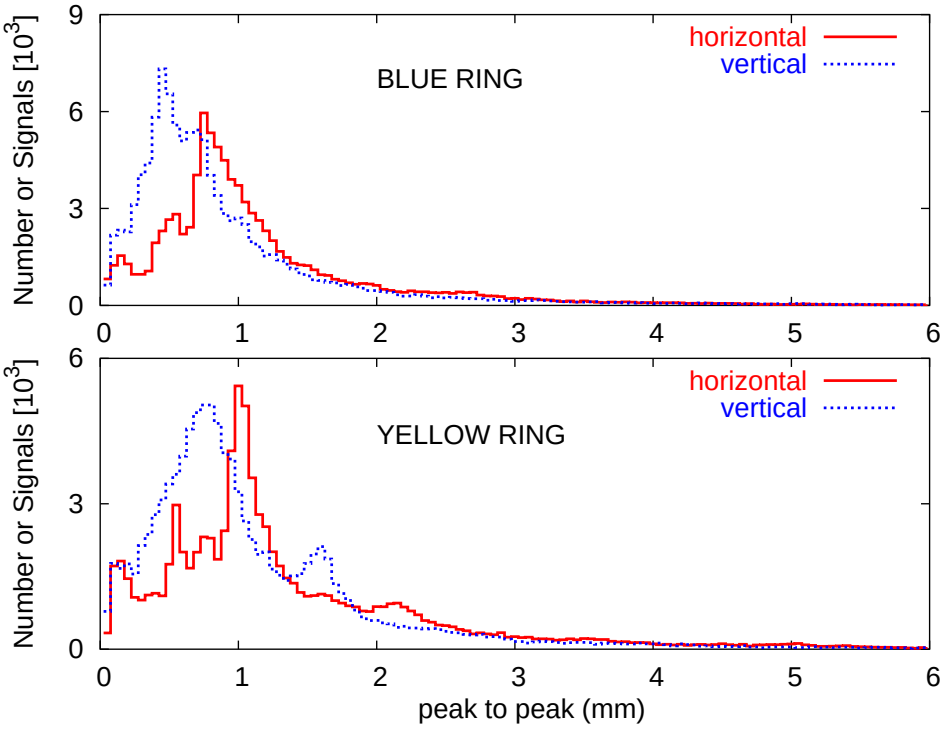

Figure 3.5: Peak-to-peak values for all BPMs in all data files.

indicating the typical oscillation amplitude for most pick-ups. Two smaller peaks are also observed between 1.5 mm and 2.2 mm, and two more between 0.5 mm and 1 mm, possibly indicating signals from different sets of optics or different kick amplitudes.

The vertical plane signals appear at smaller amplitudes because the data analyzed are mostly kicked in the horizontal plane. In such cases smaller peak-to-peak thresholds must be chosen. A summary of thresholds and files analyzed are given in Table 3.1.

Table 3.1: Thresholds for peak-to-peak values

Plane	Ring	peak-to-peak	# of files analyzed
H	yellow	0.3	678
V	yellow	0.15	815
H	blue	0.3	708
V	blue	0.15	833

3.4.3 FFT Analysis

The histograms of the FFT rms observable for the two rings and two planes are shown in Fig. 3.6. It is remarkable that the four peaks show almost identical features. This confirms the fact that the hardware system of the pick-ups is very similar for the two rings and planes. From these plots it is concluded that suitable cuts lie in the range between 1.5 μm and 3 μm. Signals with rms noise above the cut are labeled faulty.

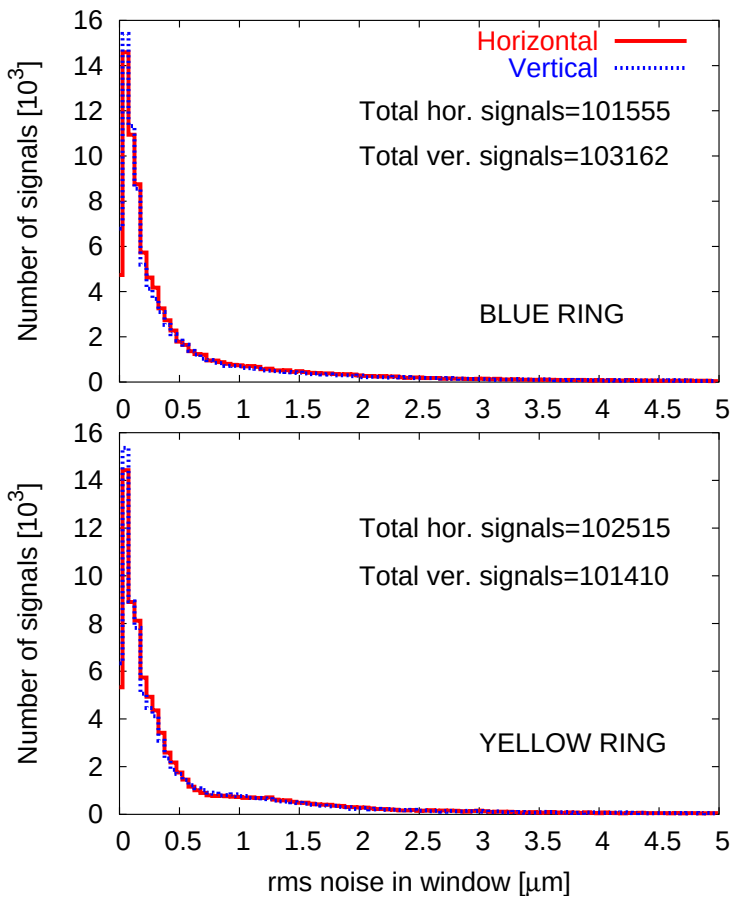

Figure 3.6: Histograms of the rms observable for the two rings and two planes. The total number of signals used in the histograms are shown.

To study the performance of particular BPMs, we record the number of faulty signals provided by each pick-up. Fig. 3.7 shows these occurrences plotted versus longitudinal location for two different cuts (1.5 μm and 2.7

μm). Pick-ups that perform worse than the others are clearly identified from either cut.

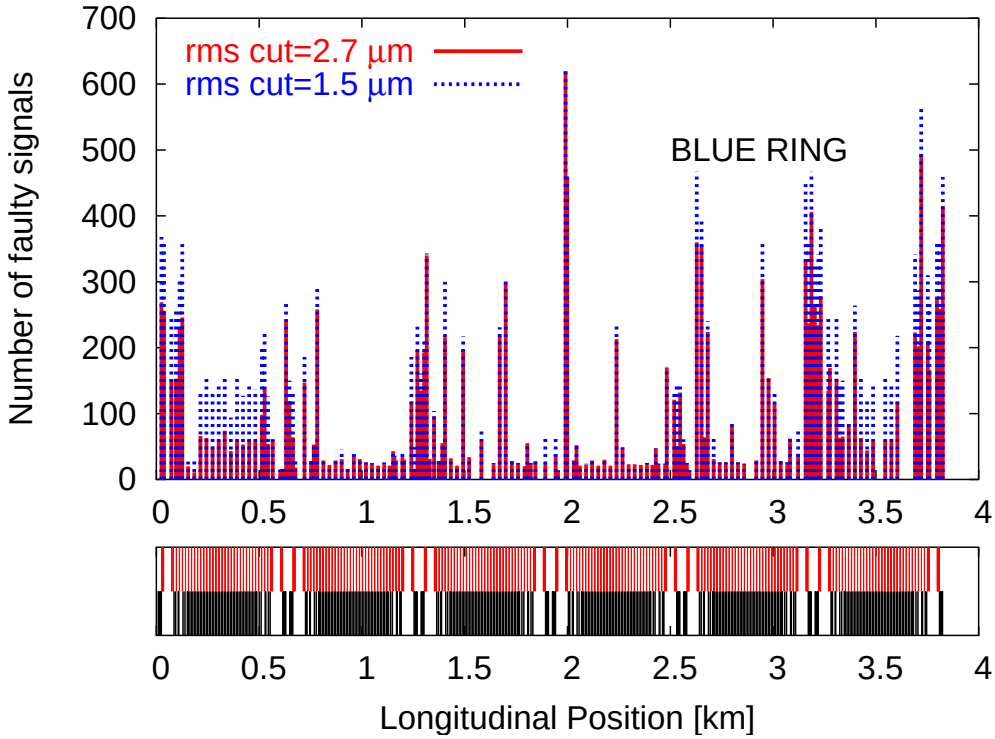

Figure 3.7: Comparison between two different rms cuts showing qualitatively similar results.

To obtain more information on the performance of particular BPMs, the average of the rms noise observables coming from each pick-up is computed and plotted in Fig. 3.8 versus the longitudinal location of the pick-up. The picture shows few spikes that correspond to those systematically bad pick-ups. These spikes happen to be dense in the interaction regions. Fig. 3.8 also shows that the BPMs within certain sextants of the machine have consistently larger rms noise than in the rest of the ring. This will be discussed in section 3.5.

3.4.4 SVD Analysis

The SVD of BPM data with oscillations above the peak-to-peak threshold can be processed to determine spatial modes with localized peaks as shown in

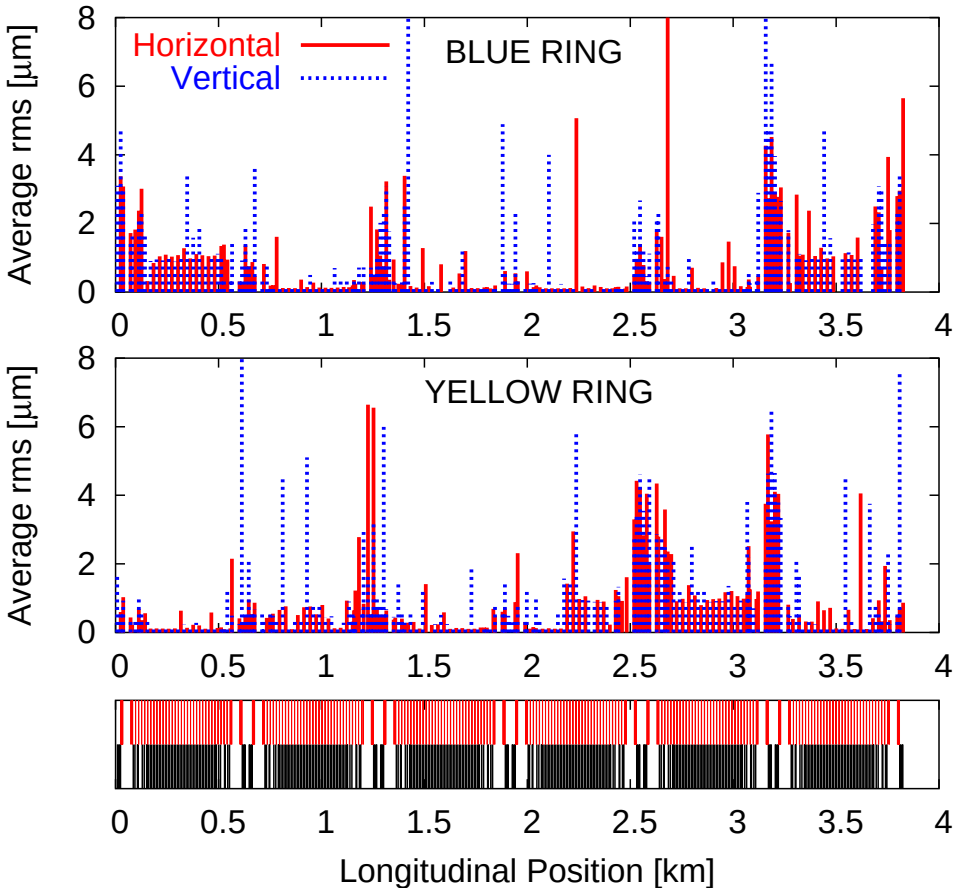

Figure 3.8: Average rms observable versus longitudinal position of the BPM.

Fig. 3.3. The largest peak values of all modes were determined for a large set of data and plotted in the histogram shown in Fig. 3.9. This figure shows a Gaussian-like distribution representing coherent signal in good BPMs and a sharp peak close to one indicating obviously faulty BPMs. In the absence of any correlations between noisy BPMs, the second peak unambiguously identifies the complete set of faulty BPMs. However, for machine data we observe multiple peaks in each mode due to correlations between noisy BPMs. There are many faulty BPMs between 0.6 and 1. Fig. 3.9 does not provide a clear way to determine a good threshold value. A large threshold might be too pessimistic, leaving unidentified faulty BPMs, while a smaller threshold might risk losing good data.

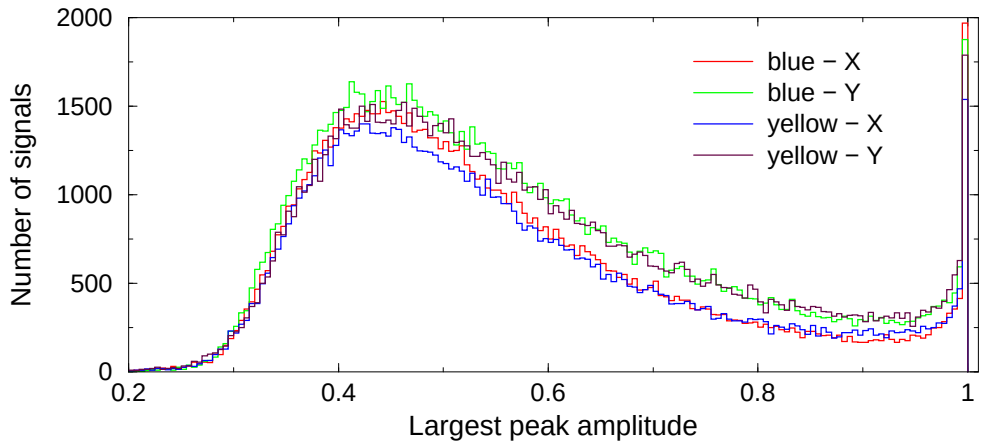

Figure 3.9: Histogram of largest peak amplitudes of all spatial modes for both planes in both rings. The Gaussian like distributions represent coherent signal from good BPMs and peaks at 1 represent faulty BPMs.

Since the singular vectors are normalized, we explore an alternate approach taking advantage of the unit norm of spatial vectors. In the presence of multiple peaks, the norm of the n largest peaks for noisy BPMs,

$$\|V\|_{1\to n} = \sqrt{\sum_{j=1}^{n} v_{ij}^2} \ , \tag{3.1}$$

is approximately equal to 1, where $2 \geq n \geq 5$. However, a mode consisting of coherent signals usually have a norm < 0.85 for the same n. Thus, the range of the choice of threshold values is considerably smaller than in the largest peak approach. The norms of each mode using the n largest peaks were calculated for all data sets and plotted in the histograms shown in Fig. 3.10. As we increase n, a clear minimum becomes apparent, helping to determine the threshold values more accurately. Thus, this approach is more reliable than using the largest peak approach, where the optimum threshold value is ambiguous. One can determine a suitable threshold value from inspection. For the horizontal plane in the yellow ring, we find the threshold value lies between 0.85 and 1. It is important to note that signals from all four peaks contribute to fail a chosen cut, but we only tag the BPM with the largest amplitude in the norm as faulty to exclude degeneracies. The other correlated BPMs will appear dominant in subsequent modes and will be identified. A similar analysis for both planes and both rings was performed.

These threshold values and the peak-to-peak cut presented earlier are ap-

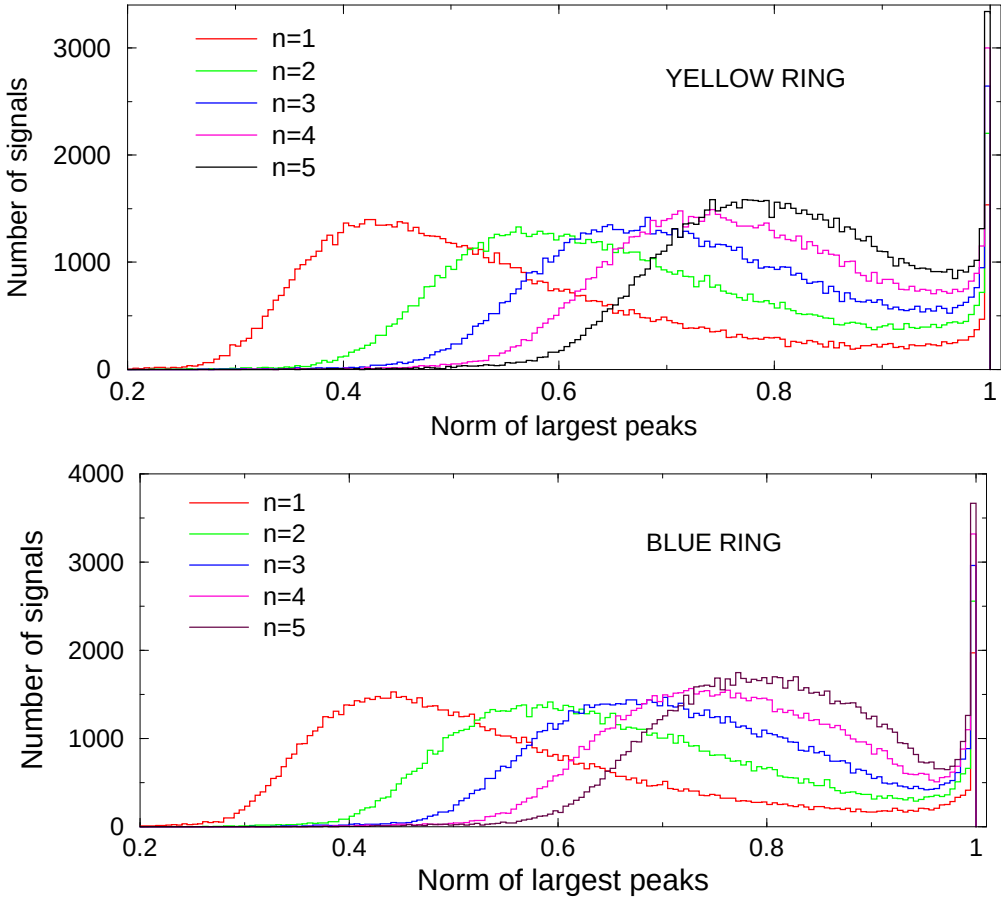

Figure 3.10: Histograms of the norm of n largest peak values in each mode of the spatial modes in the horizontal plane. Gaussian like distributions represent coherent signal from good BPMs and peaks at 1 represent faulty BPMs.

plied to data to construct a final histogram showing the number of occurrences of BPMs failing these cuts. Fig. 3.11 shows such a histogram with two different SVD thresholds (0.85 and 0.95) for the blue ring horizontal data. This comparison allows us to understand the sensitivity of the SVD cut and hence determine an optimum range. It is clear from Fig. 3.11 that the regions corresponding to more noisy BPMs (mostly interactions regions) are significantly enhanced with a lower threshold compared to that of the arc regions. However, certain arc regions show different behavior from the others. This disagreement will be discussed in section 3.5.

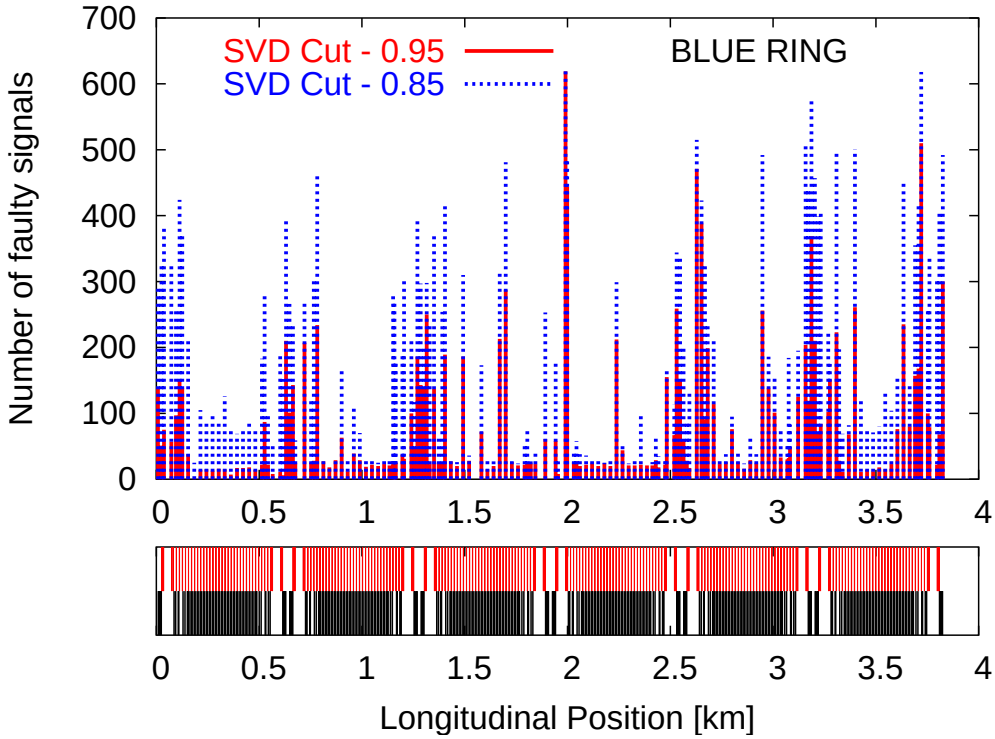

Figure 3.11: Comparison between two SVD thresholds (0.85 and 0.95) for Blue ring-horizontal plane.

3.4.5 SVD & FFT Comparison

To compare the SVD and FFT techniques, the number of identified faulty signals provided by each BPM is plotted versus its location, in Fig. 3.12. This plot contains the horizontal BPMs of the Yellow ring. The reader can also compare the results for horizontal BPMs of the Blue ring from Figs. 3.7 and 3.11. For a set of optimized cuts, the agreement is excellent between the two different techniques. This confirms the feasibility of identifying non-physical signals provided by beam position monitors.

3.5 Observation of System Improvements

As seen in Figs. 3.7, 3.8 and 3.11, BPMs in the arc regions between 0-0.5 km and 3.2-3.8 km have a strikingly larger background than the rest of the arcs. It was found that BPMs in these arcs were exhibiting sporadic noise ("hairs") of ten to thousands of μm on BPM position data. This effect was caused due

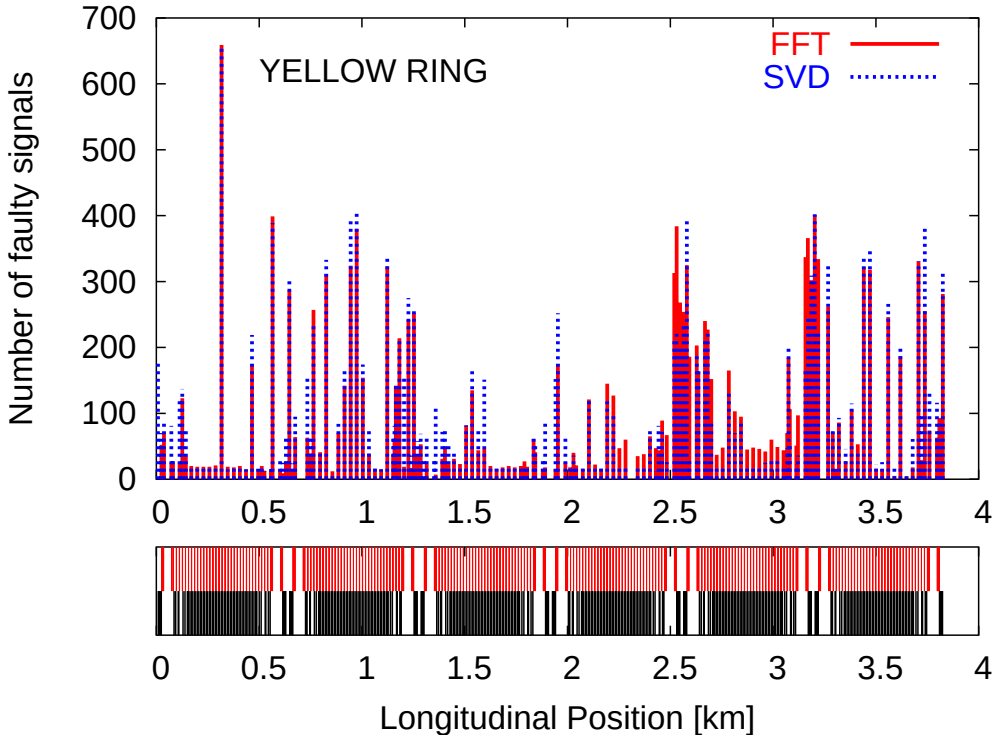

Figure 3.12: Comparison of the FFT and SVD techniques for 678 files from the yellow ring showing a good agreement. The number of times a BPM provides a faulty signal is plotted versus its location.

to unforeseen and untested conditions in low-level DSP code leading to noise jumps on some raw sampled data [38].

Low level software upgrades were implemented as a part of BPM system improvement during the commissioning period of Run 2004. A change of DSP timing parameters was particularly important in resolving the phenomena of "hairs". Kicked data during Run 2004 were regularly recorded for analysis of BPM performance. A large set of data similar to the one from 2003 was analyzed using the above numerical techniques to understand the behavior of the BPMs after system improvements. Fig. 3.13 shows the percentage of occurrences of system failure per BPM versus longitudinal location for Run 2004. These percentages of system failure are in general larger than those observed in the previous year as seen in Fig. 3.4. This is partly due to the fact that the system improvements lead to a better recognition of system failures. The abnormal abundance of system failures at the location of 3 km is presently under investigation. A collective failure of several BPMs is

most likely due to a failure of the front-end computer system responsible for managing the data flow from those BPMs and not due to individual BPM hardware failure. Fig. 3.14 shows the average of the rms noise observables coming from each BPM plotted versus the longitudinal location of the BPM for Run 2004. This figure is to be compared to Fig. 3.8 from the previous year. We observe a clear improvement in BPM resolutions. The larger background at particular sextants has disappeared yielding a consistent BPM performance in all the arcs. This confirms that the problem of "hairs" has been resolved. Nevertheless BPMs located within the interaction regions still show a poorer performance than the rest. Run 2004. The background in PP run is smaller than in Au run, which seems to indicate failure rate of good BPMs are lower.

Peak-to-peak signals in PP run show a smaller occurrence close to zero amplitude than the Au-Au run indicating fewer BPMs with flat signals possibly contributing to the lower background. However, we find more faulty BPMs in IR8 (0.5 km) in PP run as seen in Fig. 3.15 which might point to possible damage of BPMs due to radiation or other operation conditions. Also, BPMs located within the interaction regions in all runs show poorer performance than the rest of the ring despite similar BPM electronics around the ring.

3.6 Conclusion

Two numerical algorithms, the Fourier transform and the Singular Value Decomposition, have been used to identify faulty BPM signals. Appropriate observables characterizing the noise content of a BPM signal have been defined for both techniques. The observables' thresholds above which a signal is identified as faulty are obtained from statistics over a large set of RHIC BPM data. These cuts are used to assess the global performance of every BPM, thus identifying those BPMs that systematically provide faulty data. A comparison between the results from both independent techniques has been presented showing an excellent agreement. Analysis of run 2004 data shows clear improvements in the BPM system and successful elimination of "hairs".

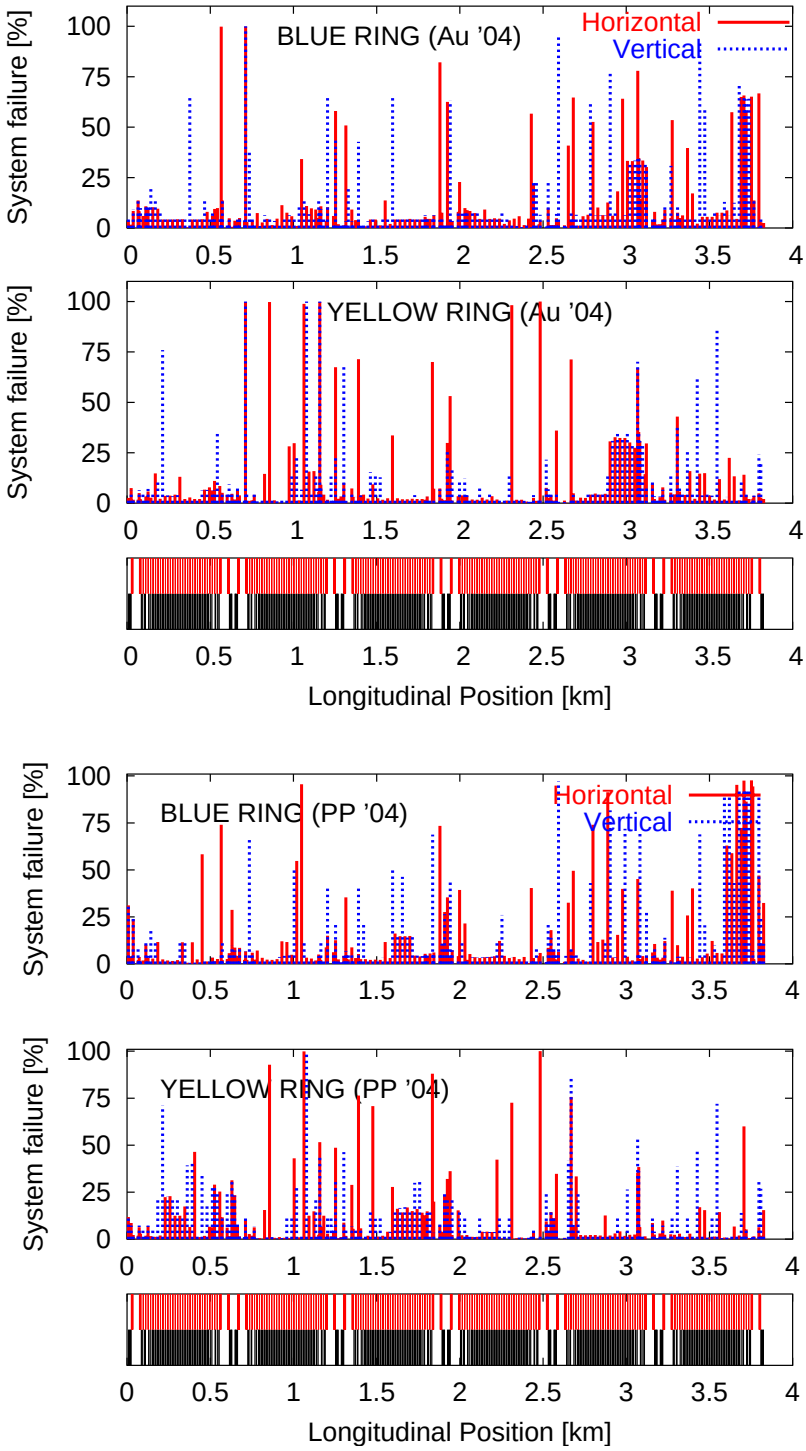

Figure 3.13: Percentage of occurrences of system failure per BPM versus longitudinal location. Run 2004 (Au-Au), and Run 2004 (PP). A representation of the lattice (dipoles in black and quadrupoles in red) in the bottom.

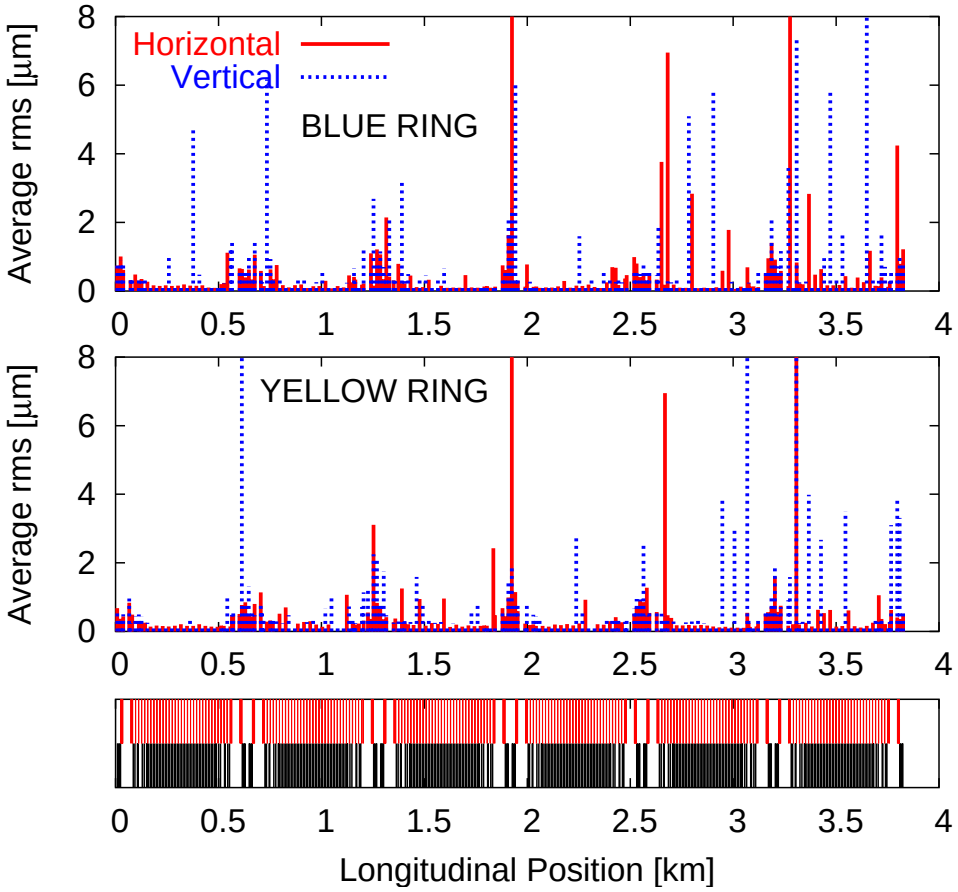

Figure 3.14: Average rms observable versus longitudinal position of the BPM for Run 2004.

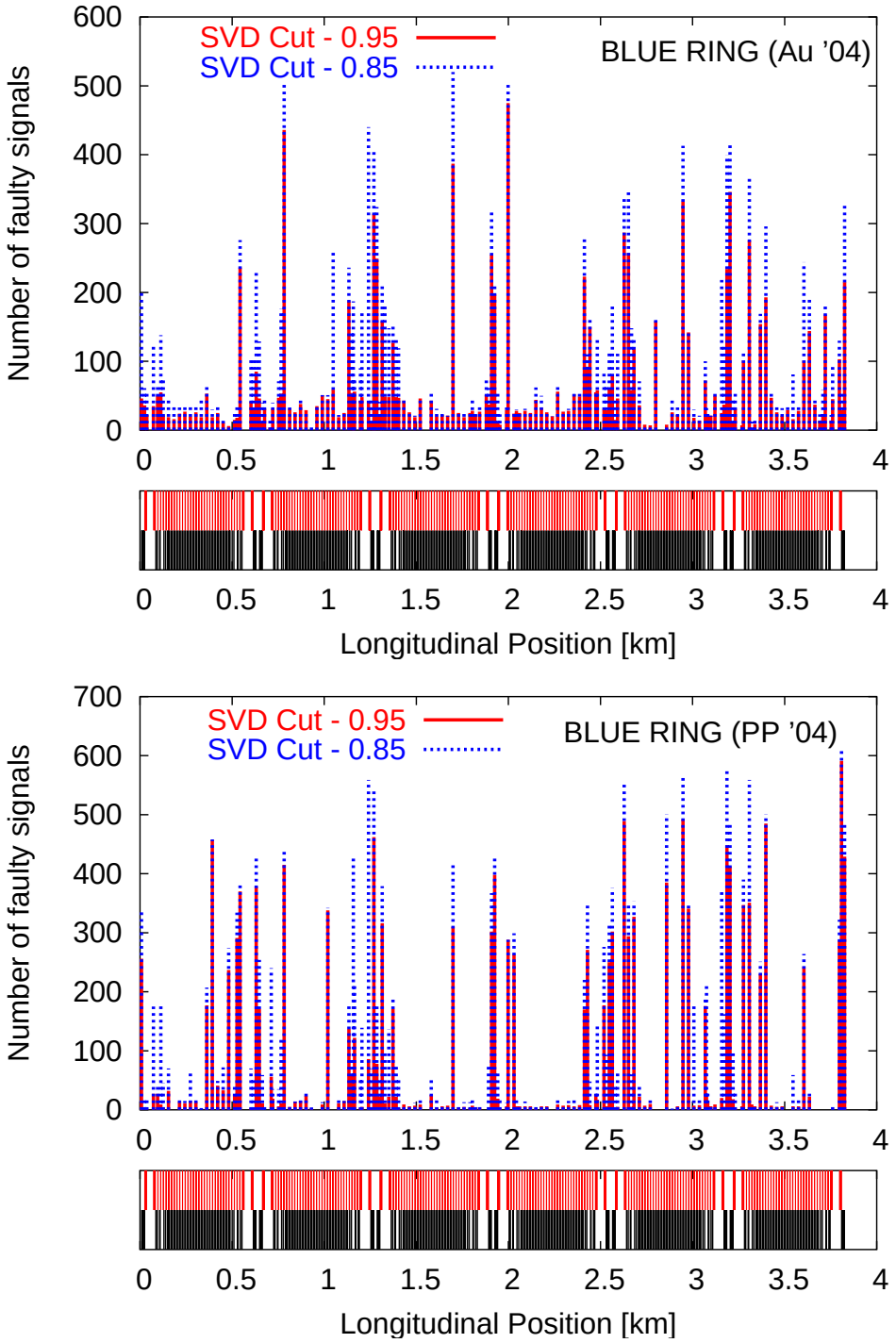

Figure 3.15: Histogram showing number of occurrences of faulty BPMs around the ring. Top to bottom: Run 2003, Run 2004 (Au-Au), and Run 2004 (PP). A representation of the lattice (dipoles in black and quadrupoles in red) in the bottom.

Chapter 4

Betatron coupling: Merging Formalisms and Localization of Sources

4.1 Introduction

Betatron coupling in circular accelerators has been widely studied using both matrix formalism and Hamiltonian perturbation theory. In the matrix formalism the transverse beam motion is represented by a 4×4 one-turn matrix $\mathbf{T}$ which can be factorized into a block diagonal normal mode form [39, 40]

$$\mathbf{T} = \begin{pmatrix} \mathbf{M} & \mathbf{m} \\ \mathbf{n} & \mathbf{N} \end{pmatrix} = \mathbf{V}\mathbf{U}\mathbf{V}^{-1} \tag{4.1}$$

by means of the similarity transformation. The symplectic 4×4 matrices $\mathbf{U}$ and $\mathbf{V}$ of the form

$$\mathbf{U} = \begin{pmatrix} \mathbf{A} & \mathbf{0} \\ \mathbf{0} & \mathbf{B} \end{pmatrix} , \quad \mathbf{V} = \begin{pmatrix} \gamma\mathbf{I} & \mathbf{C} \\ -\mathbf{C}^{\dagger} & \gamma\mathbf{I} \end{pmatrix} , \tag{4.2}$$

consisting of the transverse Twiss functions and a 2×2 coupling matrix ($\mathbf{C}$ matrix) respectively. $\mathbf{I}$ is the 2×2 identity matrix, $\mathbf{C}$ is the 2×2 coupling matrix, and $\mathbf{C}^{\dagger}$ is its symplectic conjugate requiring

$$|\mathbf{C}| + \gamma^2 = 1. \tag{4.3}$$

Therefore, the parameters γ and $\mathbf{C}$ are given

$$\gamma = \sqrt{\frac{1}{2} + \frac{1}{2}\sqrt{\frac{\mathrm{Tr}[\mathbf{M}-\mathbf{N}]^2}{\mathrm{Tr}[\mathbf{M}-\mathbf{N}]^2 + 4|\mathbf{H}|}}} \tag{4.4}$$

$$\mathbf{C} = \frac{-\mathbf{H}\ \mathrm{sgn}\{\mathrm{Tr}[\mathbf{M}-\mathbf{N}]\}}{\mathrm{Tr}[\mathbf{M}-\mathbf{N}]^2 + 4|\mathbf{H}|} \tag{4.5}$$

where,

$$\mathbf{H} = \mathbf{m} + \mathbf{n}^{\dagger} \tag{4.6}$$

For stable motion, it can be shown that

$$\mathrm{Tr}[\mathbf{M} - \mathbf{N}]^2 + 4|\mathbf{H}| > 0. \tag{4.7}$$

In the Hamiltonian approach the coupling elements are considered to be a perturbation to the uncoupled lattice. The perturbed Hamiltonian is given by

$$\mathcal{H} = \mathcal{H}_0 + \mathcal{H}_1 = \frac{1}{2}\left[p_x^2 + p_y^2 + k_x(s)x^2 + k_y(s)y^2\right] + p(s)xy \tag{4.8}$$

where $k_x(s) = \rho^2 - \frac{1}{B\rho}\frac{\partial B_x}{\partial y}$, $k_y(s) = \rho^2 - \frac{1}{B\rho}\frac{\partial B_y}{\partial x}$, and $p(s) = \frac{1}{B\rho}\left(\frac{\partial B_x}{\partial x} - \frac{\partial B_y}{\partial y}\right)$. The equations of motion are expanded up to the first order in those perturbations. Direct relations between the two approaches are derived and discussed in detail and their applicability to localize and measure transverse coupling sources are presented.

Numerical methods such as Fourier Transform and Singular Value Decomposition (SVD) have been demonstrated to be effective in measuring relevant quantities in both formalisms [41, 42, 43, 36]. However, in the matrix formalism, measurements have been constrained to three of the four elements in the coupling matrix [42, 43]. The individual elements of the coupling matrix usually have complicated behavior around the ring. One often has to rely on fitting techniques to identify sources of local coupling [42]. An approach to extend the existing methods to measure the complete $\mathbf{C}$ matrix and hence the determinant is presented. The behavior of the determinant in the presence of coupling sources is discussed in detail and its advantage of localizing these coupling sources is transparent. The applicability of the expression relating closest tune approach (ΔQ_{min}) and $\overline{\mathbf{C}}$ matrix given in Refs. [44] and [45] is also studied.

4.2 Hamiltonian terms and coupling matrix

To relate the coupling matrix to the Hamiltonian terms the expressions describing the turn-by-turn motion from both formalisms are compared. This is achieved by introducing the canonical momentum in the matrix framework and constructing a complex variable. Prior to this the two approaches in terms of particle motion are briefly discussed.

4.2.1 Matrix formalism

Since the Twiss parameters are dependent on choice of axis, it is useful to normalize the normal modes with

$$\begin{bmatrix} a \\ a' \\ b \\ b' \end{bmatrix} = \begin{bmatrix} G_a & 0 \\ 0 & G_b \end{bmatrix} \begin{bmatrix} x \\ x' \\ y \\ y' \end{bmatrix} \tag{4.9}$$

By means of this similarity transformation the β dependence is normalized out of $\mathbf{C}$,

$$\overline{\mathbf{C}} = \mathbf{G_a C G_b^{-1}} \tag{4.10}$$

where

$$\mathbf{G_{a,b}} = \begin{bmatrix} \frac{1}{\sqrt{\beta_{a,b}}} & 0 \\ \frac{\alpha_{a,b}}{\sqrt{\beta_{a,b}}} & \sqrt{\beta_{a,b}} \end{bmatrix} \tag{4.11}$$

are the normalization matrices for the a and b modes [40]. Note that $|\overline{\mathbf{C}}| = |\mathbf{C}|$. The normalized motion in the horizontal and vertical planes can be expressed as

$$\begin{bmatrix} \hat{x} \\ \hat{p}_x \\ \hat{y} \\ \hat{p}_y \end{bmatrix} = \begin{bmatrix} \gamma & 0 & \overline{C}_{11} & \overline{C}_{12} \\ 0 & \gamma & \overline{C}_{21} & \overline{C}_{22} \\ -\overline{C}_{22} & \overline{C}_{12} & \gamma & 0 \\ \overline{C}_{21} & -\overline{C}_{11} & 0 & \gamma \end{bmatrix} \begin{bmatrix} A_x C\psi_x \\ A_x S\psi_x \\ A_y C\psi_y \\ A_y S\psi_y \end{bmatrix} \tag{4.12}$$

where "C" and "S" are the cosine and sine functions respectively. Using the above expressions for normalized positions and momenta, the complex variables are given by

$$\begin{aligned} \hat{x} + i\hat{p}_x &= \gamma A_x e^{i\psi_x} \\ &\quad + \frac{A_y}{2}\Big((\overline{C}_{11} + i\overline{C}_{12} + i\overline{C}_{21} - \overline{C}_{22}) e^{-i\psi_y} \\ &\quad + (\overline{C}_{11} - i\overline{C}_{12} + i\overline{C}_{21} + \overline{C}_{22}) e^{i\psi_y} \Big) , \end{aligned} \tag{4.13}$$

$$\begin{aligned} \hat{y} + i\hat{p}_y &= \gamma A_y e^{i\psi_y} \\ &\quad + \frac{A_x}{2}\Big((\overline{C}_{11} + i\overline{C}_{12} + i\overline{C}_{21} - \overline{C}_{22}) e^{-i\psi_x} \\ &\quad + (-\overline{C}_{11} - i\overline{C}_{12} + i\overline{C}_{21} - \overline{C}_{22}) e^{i\psi_x} \Big) . \end{aligned} \tag{4.14}$$

Note that the convention for momenta used in Hamiltonian theory described in [46] is the negative of that used in matrix formalism described in Ref. [47] ($\hat{p_x^h} = -\hat{p}_x$).

4.2.2 Resonance driving terms

Using Hamiltonian and Normal Form theory a weakly coupled lattice is treated as a perturbation to the uncoupled lattice. The turn-by-turn normalized particle positions and momenta at a location s are described as [46],

$$\begin{aligned} \hat{x} - i\hat{p}_x^h &= \sqrt{2I_x}e^{i\psi_x} - 2if_{1001}\sqrt{2I_y}e^{i\psi_y} \\ &\quad -2if_{1010}\sqrt{2I_y}e^{-i\psi_y} \ , \end{aligned} \tag{4.15}$$

$$\begin{aligned} \hat{y} - i\hat{p}_y^h &= \sqrt{2I_y}e^{i\psi_y} - 2if_{1001}^*\sqrt{2I_x}e^{i\psi_x} \\ &\quad -2if_{1010}\sqrt{2I_x}e^{-i\psi_x} \ , \end{aligned} \tag{4.16}$$

where $I_{x,y}$ are the horizontal and the vertical invariants. The phases of the oscillations, $\psi_{x,y}$ are expressed as function of the natural tunes $Q_{x,y}$, the turn number N and the initial phases $\phi_{x0,y0}$ as $\psi_{x,y} = 2\pi Q_{x,y}N + \phi_{x0,y0}$. The resonance driving terms (RDT's) f_{1001} and f_{1010} are proportional to the Hamiltonian terms [46] and drive the difference and the sum resonances respectively. These terms are functions of the uncoupled lattice parameters at the location of both the coupling elements and the observation point s given by

$$f(s)_{\substack{1001\\1010}} = -\frac{1}{4(1-e^{2\pi i(Q_x \mp Q_y)})}\sum_l k_l\sqrt{\beta_x^l\beta_y^l}e^{i(\Delta\phi_x^{sl} \mp \Delta\phi_y^{sl})} \tag{4.17}$$

where k_l is the lth integrated skew quadrupole strength, $\beta_{x,y}^l$ are the Twiss functions at the location of the lth skew quadrupole, $\Delta\phi_{x,y}^{sl}$ are the phase advances between the observation point s and the lth skew quadrupole and $Q_{x,y}$ are the horizontal and vertical tunes.

4.2.3 Relating the C matrix to RDT's

The relation to the Hamiltonian formalism can now be established by directly comparing Eqs. (4.15) and (4.16) to Eqs. (4.13) and (4.14) obtaining,

$$f_{1001} = \frac{1}{4\gamma}(\overline{C}_{12} - \overline{C}_{21} + i\overline{C}_{11} + i\overline{C}_{22}) \ , \tag{4.18}$$

$$f_{1010} = \frac{1}{4\gamma}(-\overline{C}_{12} - \overline{C}_{21} + i\overline{C}_{11} - i\overline{C}_{22}) \ , \tag{4.19}$$

or, equivalently expressing $\overline{\mathbf{C}}$ as function of the RDT's,

$$\frac{1}{2\gamma}\overline{C}_{\substack{12\\21}} = -\mathcal{R}e\{f_{1010} \mp f_{1001}\} \ , \tag{4.20}$$

$$\frac{1}{2\gamma}\overline{C}_{\substack{11\\22}} = \mathcal{I}m\{f_{1001} \pm f_{1010}\} \ , \tag{4.21}$$

where $\mathcal{R}$ and $\mathcal{I}$ stand for real and imaginary parts respectively. The determinant of $\overline{\mathbf{C}}$ can also be related to the RDT's as

$$\frac{|\overline{\mathbf{C}}|}{4\gamma^2} = |f_{1001}|^2 - |f_{1010}|^2 \ , \tag{4.22}$$

and using $|\overline{\mathbf{C}}| + \gamma^2 = 1$ yields,

$$|\overline{\mathbf{C}}| = 1 - \frac{1}{1 + 4(|f_{1001}|^2 - |f_{1010}|^2)} \ , \tag{4.23}$$

$$\gamma^2 = \frac{1}{1 + 4(|f_{1001}|^2 - |f_{1010}|^2)} \tag{4.24}$$

These expressions have a direct interpretation: if $|\overline{\mathbf{C}}|$ is positive the difference resonance (f_{1001}) dominates, and if it is negative the sum resonance (f_{1010}) dominates. From these expressions it is also observed that a null $|\overline{\mathbf{C}}|$ does not imply null coupling, but $|f_{1001}| = |f_{1010}|$. If $|f_{1010}|^2 > (\frac{1}{4} + |f_{1001}|)$, then $\gamma^2 < 0$ and the particle motion is unstable (see discussion in [40] after Eq. (12)).

In [36] it was demonstrated that the amplitude of the RDT's remains constant along sections free of coupling sources and experiences abrupt jumps at locations with couplers. In [36] it is also shown that the relative longitudinal variations of the RDT's become smaller as the tunes approach the resonance. On the resonance, the amplitude of the RDT's becomes invariant around the ring. Thus, by virtue of Eq. (4.22), the determinant of $\overline{\mathbf{C}}$ also tends to be invariant around the ring as the tunes approach the resonance.

4.2.4 Simulations

To confirm the relations derived above, simulations were carried out with the aid of MAD-X [48]. A simple ring consisting of 80 FODO cells is constructed using parameters shown in Table 4.1. Three skew quadrupoles of

Table 4.1: FODO Lattice Parameters (NA: Not applicable)

Species	Length (m)	Strength
Dipoles	6.5	0.039 rad
Quadrupoles	0.5	0.1 m^{-2}
Skew Quadrupoles	0.2	4.3×10^{-3} m^{-2}
Drifts	0.25	NA

different strengths were placed at arbitrary locations to introduce transverse coupling in the lattice.

$\mathbf{f_{1001}}$ and $\overline{\mathbf{C}}$ matrix

Twiss functions and coupling matrix elements in the form of **R** matrix (Edwards-Teng parameterization [39]) are directly available from MAD-X. The **C** matrix is determined by a simple transformation of the **R** matrix given by

$$\mathbf{C} = \frac{\mathbf{1}}{\mathbf{1} + |\mathbf{R}|}\mathbf{J^{-1}RJ} \tag{4.25}$$

where $\mathbf{J} = \begin{bmatrix} 0 & 1 \\ -1 & 0 \end{bmatrix}$. $\overline{\mathbf{C}}$ is obtained from Eq. (4.10) by normalizing out the beta dependence from **C** . To calculate the RDT's f_{1001} and f_{1010} from MAD-X, the first order approximation given by Eq. (4.17) is used. Fig. 4.1

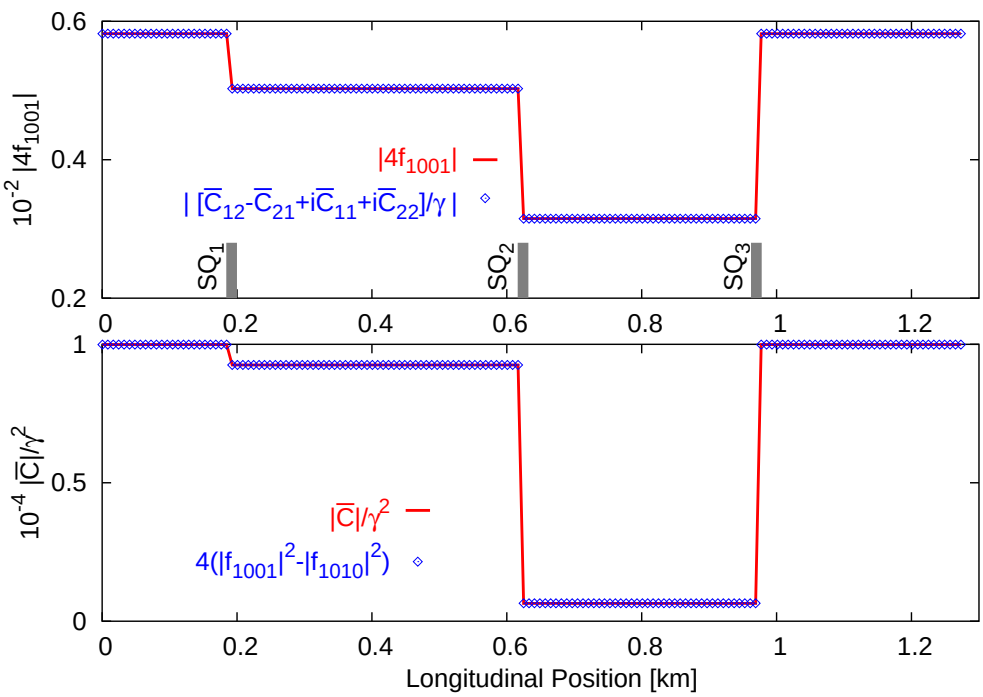

Figure 4.1: Top: $4|f_{1001}|$ and $|[(\overline{C}_{12} - \overline{C}_{21}) + i(\overline{C}_{11} + \overline{C}_{22})]/\gamma|$ plotted as a function of the longitudinal position. Bottom: $|\overline{\mathbf{C}}|/\gamma^{\mathbf{2}}$ and $4(|f_{1001}|^2 - |f_{1010}|^2)$ plotted as a function of longitudinal position. Horizontal and vertical tunes are $Q_x = 18.226$ and $Q_y = 17.257$ respectively and $\Delta Q_{min} = 6.45 \times 10^{-3}$.

shows a comparison between the RDT's and $\overline{\mathbf{C}}$ matrix elements as derived in Eqs. (4.18) and (4.22). The RMS of the differences between the compared quantities are smaller than 10^{-6} thus numerically validating the relations.

Dependence on skew quadrupole strengths

The relations between $|\overline{\mathbf{C}}|$ and the RDT's are first order approximations. To investigate the accuracy of these relations, the mean of the ratio of the quantities compared in Fig. 4.1 are computed for increasing skew quadrupole strengths. The horizontal and vertical tunes are fixed at $Q_x = 18.226$ and $Q_y = 17.232$ respectively. Fig. 4.2 shows a plot of this mean ratio along with the standard deviation of the ratio as a function of closest tune approach (ΔQ_{min}) produced by the three skew quadrupoles. For this particular case, the quantities compared agree in the percent level for a ΔQ_{min} lower than 3×10^{-3}.

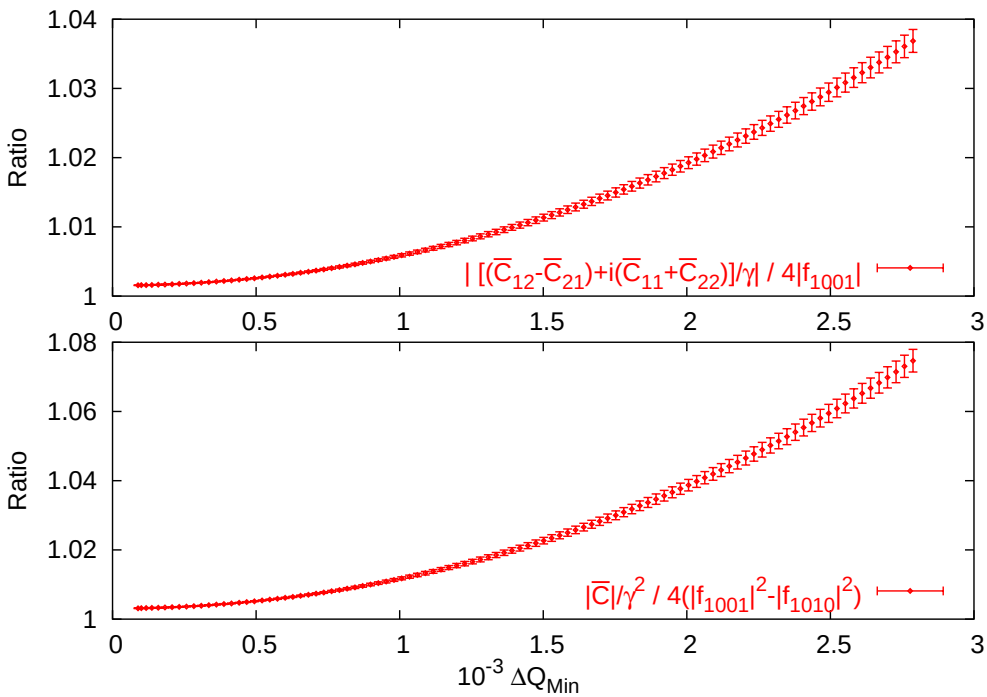

Figure 4.2: Top: Mean of the ratio of $|[(\overline{C}_{12} - \overline{C}_{21}) + i(\overline{C}_{11} + \overline{C}_{22})]/\gamma|$ and $4|f_{1001}|$. Bottom: Mean of the ratio of $|\overline{\mathbf{C}}|/\gamma^{\mathbf{2}}$ and $4(|f_{1001}|^2 - |f_{1010}|^2)$. The error bars represent the standard deviation of the ratio of the respective quantities. The horizontal and vertical tunes are $Q_x = 18.226$ and $Q_y = 17.232$ and $\Delta Q_{min} = 6.45 \times 10^{-3}$.

Stop-Band Limits

To explore the behavior of Eq. (4.22), a scan of horizontal tune (Q_x) is performed with the vertical tune fixed at $Q_y = 0.228$. Fig. 4.3 shows the driving terms, $|f_{1001}|^2$ and $|f_{1010}|^2$ as well as $|\overline{\mathbf{C}}|/\gamma^2$ plotted as a function Q_x for the FODO lattice described above. The dominance of f_{1001} or f_{1010} is seen in Fig. 4.3 depending on the proximity to either the difference or sum resonance respectively. This transition is also evident from the behavior of

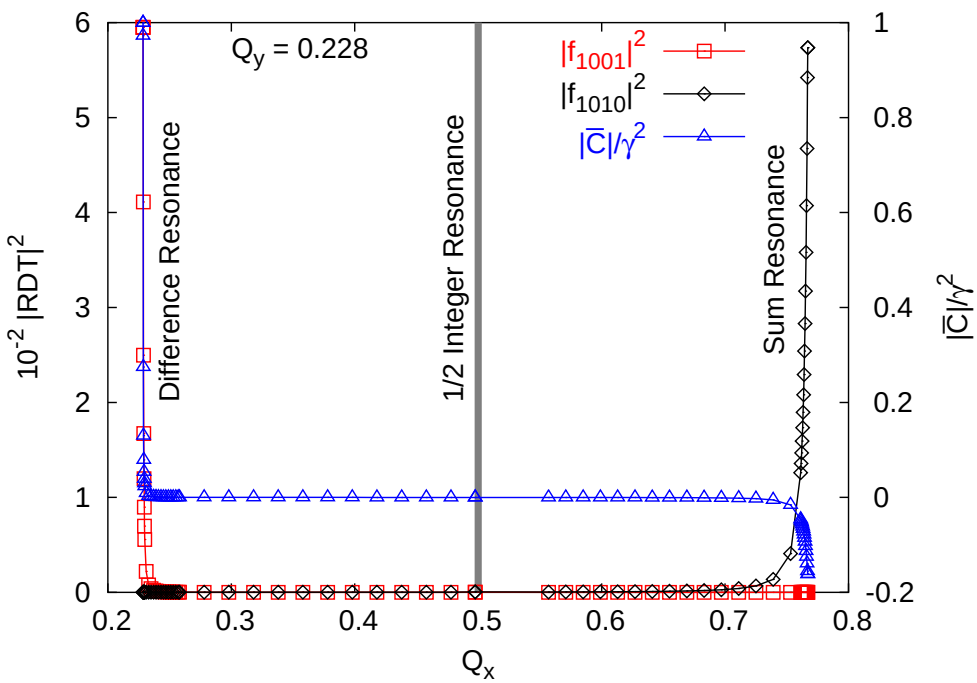

Figure 4.3: $|f_{1001}|^2$, $|f_{1010}|^2$ and $|\overline{\mathbf{C}}|/\gamma^2$ plotted as a function of Q_x ($Q_y = 0.228$). The stop-bands at the sum and the difference resonance show the dramatic increase in these functions. 1/2 integer resonance line is plotted as a reference.

$|\overline{\mathbf{C}}|/\gamma^2$ as it switches sign when we move from difference to the sum resonance in accordance with Eq. (4.22). There are missing data points at $Q_x = 0.5$ due the 1/2 integer resonance.

4.3 Determinant of $\overline{\mathbf{C}}$

It has been demonstrated that $\overline{C}_{12}/\gamma$, $\overline{C}_{11}/\gamma$, $\overline{C}_{22}/\gamma$ are measured using turn-by-turn data from beam position monitors (BPMs) [42, 43]. From $\overline{C}_{12}/\gamma$, one relies on fitting techniques to determine the location of coupler and estimate its strength to correct local coupling [42, 47]. However, the $|\overline{\mathbf{C}}|$ like the RDT's is a constant in coupler free regions and exhibits abrupt jumps at the locations of couplers. These discontinuities are intuitive and can be identified simply by visual inspection to the nearest BPM as seen in Fig. 4.1. The $|\overline{\mathbf{C}}|$ also allows one to easily estimate global quantities like ΔQ_{min} and local quantities like the strength and polarity of the coupler which are useful during machine operation. However, it will be seen that $\overline{C}_{12}/\gamma$ has a better signal-to-noise ratio. Additionally it has better resolution to locate an isolated coupler more accurately using appropriate fitting techniques, while $|\overline{\mathbf{C}}|$ has a resolution to within a region between the two nearest BPMs.

To calculate the determinant, we propose a method to calculate $\overline{C}_{21}$ given $\overline{C}_{12}$, $\overline{C}_{11}$, and $\overline{C}_{22}$ at two locations with an arbitrary phase advance in both normal modes. Given two locations (1) and (2) in a coupler free region, $\overline{C}_{21}^{(1)}$ is given (see appendix C.3) by,

$$\begin{aligned}\overline{C}_{21}^{(1)} &= \Big(-\overline{C}_{11}^{(1)} \cos\phi_a \sin\phi_b + \overline{C}_{12}^{(1)} \cos\phi_a \sin\phi_b \\ &\quad + \overline{C}_{22}^{(1)} \sin\phi_a \cos\phi_b - \overline{C}_{12}^{(2)} \Big) / (\sin\phi_a \sin\phi_b) \end{aligned} \tag{4.26}$$

where ϕ_a and ϕ_b are the phase advances between the two observation locations of the normal modes. We will demonstrate the effectiveness of such a calculation in a simple FODO lattice as well as in a complicated lattice such as RHIC where the coupling sources are mainly localized in the interaction regions with little or no coupling in the arcs.

It is also important to note that RDT's calculated using FFT techniques in [36] can be extended to compute $\overline{\mathbf{C}}$ matrix and hence the determinant according to Eqs. (4.20)- (4.24). The approach of N-turn map presented in [45] could also be extended to calculate both γ and $|\overline{\mathbf{C}}|$.

4.3.1 Calculation of $\overline{C}_{12}/\gamma$ using SVD

An extension to the SVD based technique described in chapter 2 is used to infer the eigenmodes (a and b) of the beam. The knowledge of beam oscillations in '$a-b$" plane can be used to calculate the $|\overline{\mathbf{C}}|$ matrix. This technique is briefly introduced to show the computation of $\overline{\mathbf{C}}$ matrix and its determinant.

A more detailed discussion can be found in Ref. [43, 49]. The betatron motion observed in the BPMs $(x-y)$ plane can be expressed as

$$x_a = \sqrt{2J_a\beta_a}\gamma\cos(\phi_a+\psi_a) \tag{4.27}$$
$$x_b = \sqrt{2J_b\beta_a}c_b\cos(\phi_b+\psi_b+\Delta\psi_b) \tag{4.28}$$

and corresponding motion in the y plane ($x \to y$, $a \to b$). Here, $J_{a,b}$ and $\phi_{a,b}$ are the action and angle variables. $\beta_{a,b}$ and $\psi_{a,b}$ are the Twiss functions and $c_{a,b}$ and $\Delta\psi_{a,b}$ are related to the coupling matrix

$$c_{a,b} = \sqrt{C_{22,11}^2 + C_{12}^2} \tag{4.29}$$
$$\Delta\psi_{a,b} = \mp\arctan\left(\frac{C_{12}}{C_{22,11}}\right) \tag{4.30}$$

A data matrix $[B_x, B_y]$ consisting of t columns of turn-by-turn data at all BPM is decomposed using SVD [25] given by

$$\mathbf{B} = \hat{\mathbf{U}}\mathbf{\Sigma}\hat{\mathbf{V}}^T \tag{4.31}$$

Assume that the beam motion is dominated by betatron oscillations with transverse coupling. The SVD modes do not directly yield the eigenmodes of beam as in the case of uncoupled motion. However, the rank of the matrix is equal to the rank of sum of the physical eigenmodes. Therefore the SVD modes are simply linear combinations of the eigenmodes. A 4×4 orthogonal rotation matrix O is sufficient to transform the SVD modes into the eigenmodes. The inner product of two vectors

$$\langle\cos(\omega_m t),\ \cos(\omega_n t)\rangle = 0, \quad m \neq n \tag{4.32}$$
$$\langle\sin(\omega_m t),\ \sin(\omega_n t)\rangle = 0, \quad m \neq n. \tag{4.33}$$

Therefore, the knowledge of the Fourier spectrum from the "x-y" planes allows us to numerically compute the rotation matrix via projecting the sine-cosine terms at respective tunes onto the corresponding SVD modes

$$O = S\hat{V}^T\left(\sqrt{\bar{J}^*}V^T\right) \tag{4.34}$$

where "*" represents the operation of a transpose, pseudo-inverse, and a transpose. For small mixing of SVD modes, the rotation matrix can be constructed using linearized infinitesimal rotations prescribed in Ref. [49]

$$O = I + \sum\theta_{ij}L_{ij} \tag{4.35}$$

where θ_{ij} are the rotation angles and

$$L_{ij} = (\delta_{ik}\delta_{jl} - \delta_{il}\delta_{jk}); \quad \{k, l = 1 \ldots 4\}. \tag{4.36}$$

A geometric view of constructing the rotation matrix in the phase space of spatial vectors is shown in Appendix B.

Using the rotation matrix, the normal modes are reconstructed from SVD modes as

$$\mathbf{O}^T\mathbf{S}\hat{\mathbf{V}}^T = \begin{pmatrix} \sqrt{\bar{J}_a\beta_a}\gamma\cos(\psi_a - \psi_a^0), & \sqrt{\bar{J}_a\beta_b}c_b\cos(\psi_a + \psi_{cb} - \psi_a^0) \\ \sqrt{\bar{J}_a\beta_a}\gamma\sin(\psi_a - \psi_a^0), & \sqrt{\bar{J}_a\beta_b}c_b\sin(\psi_a + \psi_{cb} - \psi_a^0) \\ \sqrt{\bar{J}_b\beta_a}c_a\cos(\psi_b + \psi_{ca} - \psi_b^0), & \sqrt{\bar{J}_b\beta_b}\gamma\cos(\psi_b - \psi_b^0) \\ \sqrt{\bar{J}_b\beta_a}c_a\sin(\psi_b + \psi_{ca} - \psi_b^0), & \sqrt{\bar{J}_b\beta_b}\gamma\sin(\psi_b - \psi_b^0) \end{pmatrix} \tag{4.37}$$

and the corresponding temporal vectors $\hat{\mathbf{U}}\mathbf{O}$. Note that the matrix $\mathbf{O}^T\mathbf{S}\hat{\mathbf{V}}^T$ is a $4 \times 2m$ matrix where m is the number of BPMs in each plane. Using the computed eigenvectors, $\overline{C}_{12}/\gamma$ can be determined as

$$\frac{\overline{C}_{12}}{\gamma} = \mathrm{sgn}(\sin\Delta\psi_a)\sqrt{\frac{\tilde{A}_a\tilde{A}_b}{A_aA_b}\sin\Delta\psi_a\sin\Delta\psi_b}. \tag{4.38}$$

Here $A_{a,b}^2 \equiv \bar{J}_{a,b}\beta_{a,b}\gamma^2$ and $\tilde{A}_{a,b}^2 \equiv \bar{J}_{a,b}\beta_{b,a}c_{a,b}^2$, where $\bar{J}_{a,b}$ are the average actions. Therefore,

$$\frac{\overline{C}_{11}}{\gamma} = \frac{\overline{C}_{12}}{\gamma}\cot\Delta\psi_b \tag{4.39}$$

$$\frac{\overline{C}_{22}}{\gamma} = -\frac{\overline{C}_{12}}{\gamma}\cot\Delta\psi_a \tag{4.40}$$

4.3.2 Calculation of $|\overline{C}|/\gamma^2$ from Tracking Data

Using Eqs. (4.26), (4.38), (4.39), and (4.40), $|\overline{\mathbf{C}}|/\gamma^{\mathbf{2}}$ can now be calculated from turn-by-turn BPM data. Single-particle tracking is performed using MAD-X on the FODO lattice described earlier to generate turn-by-turn data at a large number of BPM locations. For all simulations, we assume dual plane BPMs capable of measuring transverse positions in both planes, unless otherwise mentioned. The location of BPMs (1) and (2) in Eq. 4.26 to calculate $\overline{C}_{21}/\gamma$ is arbitrary and only requires that there are no coupling sources present between them. For the purpose of the simulations BPM (2) is chosen to be the next upstream detector from location (1). Fig. 4.4 shows

a comparison of MAD-X model and SVD computed values of $|\overline{\mathbf{C}}|/\gamma^{\mathbf{2}}$. The overall discrepancy is smaller than 0.01% and increases up to 1% in the coupler regions. To minimize the discrepancy in the coupler region, $\overline{C}_{21}/\gamma$ at the BPM location just before the coupler, can be calculated using the previous BPM (downstream) instead of the BPM upstream. This maintains the region between the two BPMs to be coupler free and the calculation of $\overline{C}_{21}/\gamma$ exact.

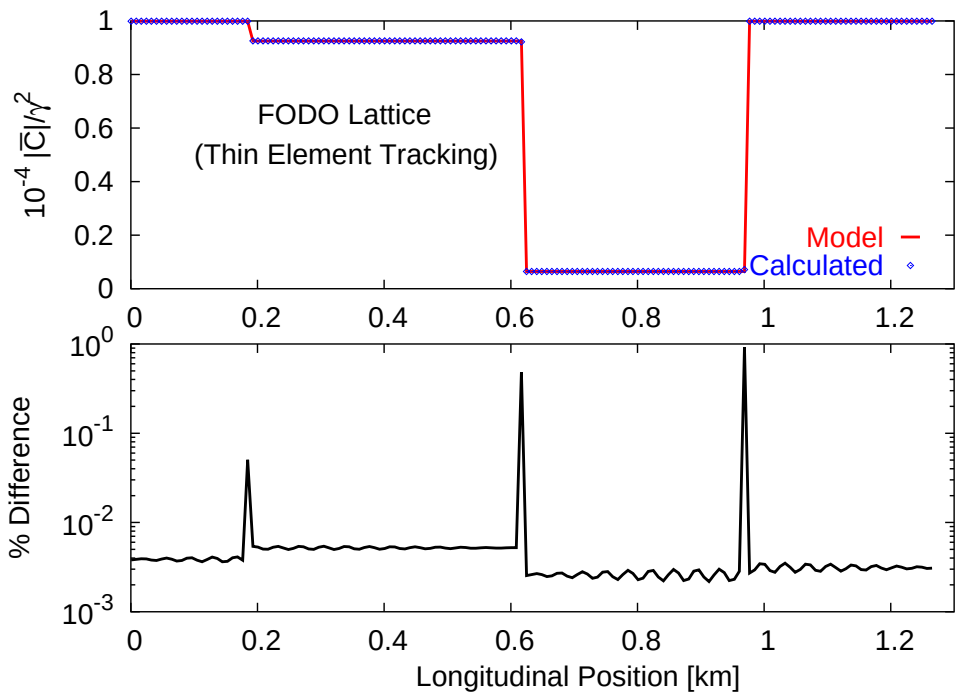

Figure 4.4: Top: Comparison of $|C|/\gamma^2$ between MAD-X model and SVD computed values from tracking data. Bottom: Difference between model and calculated values of $|C|/\gamma^2$. Horizontal and vertical design tunes are $Q_x = 18.226$ and $Q_y = 17.257$ respectively and $\Delta Q_{min} = 6.45 \times 10^{-3}$.

To investigate the effect of noise in BPMs, different levels of Gaussian noise were introduced into turn-by-turn tracking data used to compute $\overline{\mathbf{C}}$ matrix. Fig. 4.5 shows the normalized RMS of the difference for $|C|/\gamma^2$ and $\overline{\mathbf{C}}$ matrix elements between model and calculated values as a function of σ_{noise}/signal amplitude. It is clear that noise deteriorates the measurements. We observe that $\overline{C}_{12}/\gamma$ is more robust against noise than the other elements of the $\mathbf{C}$ matrix. The discrepancy of the effect of noise between $\overline{C}_{12}/\gamma$ and $\overline{C}_{\substack{11\\22}}$ can be attributed to the calculation of $\Delta\psi_{b,a}$ and is under study. $\overline{C}_{21}/\gamma$ inherently has large errors since Eq. 4.26 is only exact in a coupler free region. This

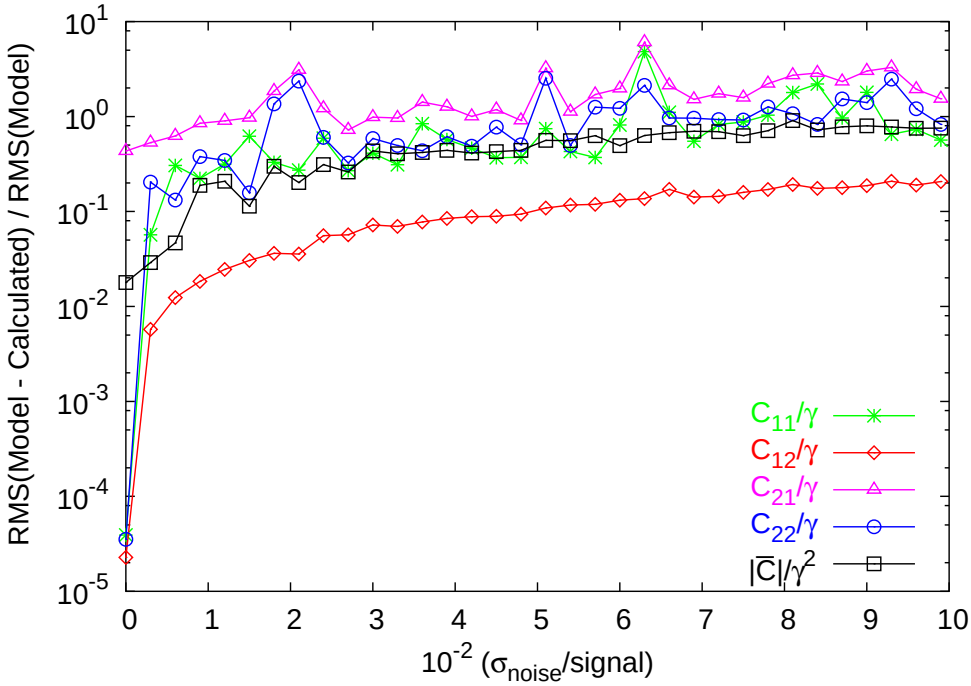

Figure 4.5: Normalized RMS of the difference of $|C|/\gamma^2$ between MAD-X model and SVD computed values for increasing amount of Gaussian noise in turn-by-turn data. Horizontal and vertical tunes are $Q_x = 18.226$ and $Q_y = 17.257$ respectively and $\Delta Q_{min} = 6.45 \times 10^{-3}$.

can be improved by the choice of appropriate BPMs for the calculation as explained above. It was shown that the choice of number of turns in tracking affects the computation of $\overline{\mathbf{C}}$ matrix due to the periodicity effect caused by the number of significant digits in the tune [43]. In real data $\overline{C}_{\substack{11\\22}}$ unlike $\overline{C}_{12}/\gamma$ were shown to be susceptible to large errors due to signal "leaks" in BPMs and their corresponding electronics [41, 47].

4.3.3 Calculation of $|\overline{\mathbf{C}}|/\gamma^2$ for RHIC Lattice

Single particle tracking using the RHIC lattice was performed to verify the applicability of this approach for a more realistic operating accelerator with several coupling sources. RHIC consists of two three-fold symmetric rings with six interaction regions. Each arc is made of 11 FODO cells with 80^0 phase advance, and interaction regions consist of almost the same FODO cells without the dipoles [1]. A model of RHIC containing realistic but uncorrected

errors is used to track a single particle for 2000 turns with $Q_x = 28.266$ and $Q_y = 29.212$. The ΔQ_{min} for this lattice is 4.37×10^{-2}. Fig. 4.6 shows a calculation of $|\overline{\mathbf{C}}|/\gamma^2$ from turn-by-turn data compared to model values from MAD-X. One can clearly see that the coupling sources (for example rolled quadrupoles) are quite strong and mainly located in interaction regions. The

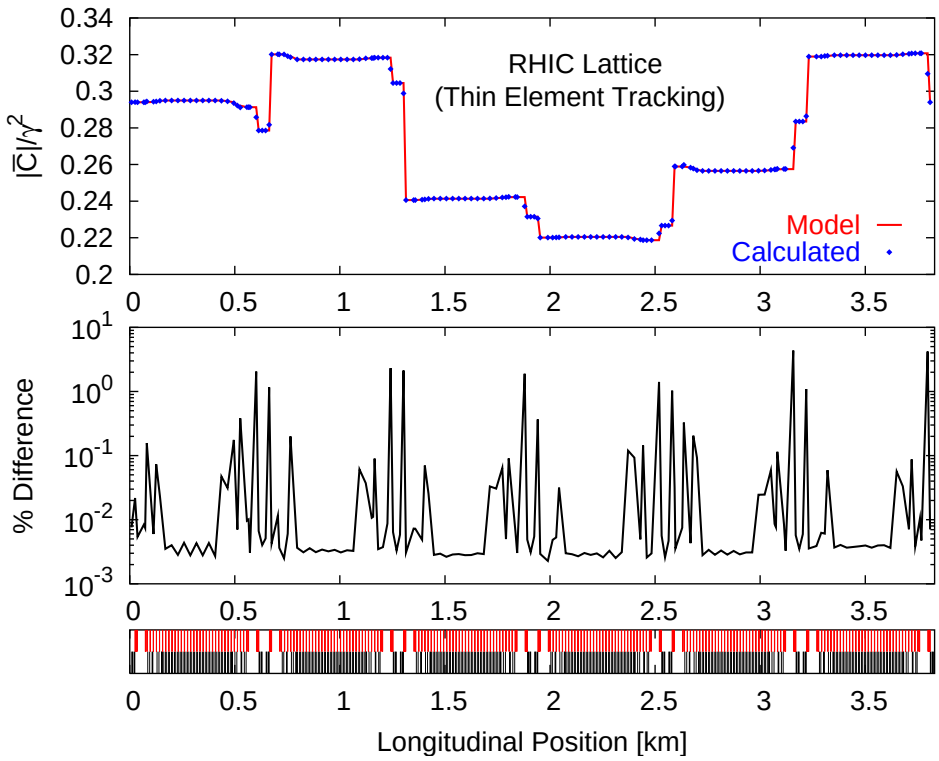

Figure 4.6: Top: Comparison of $|\overline{\mathbf{C}}|/\gamma^2$ between MAD-X model and SVD computed values from tracking data. Middle: Difference between model and calculated values of $|\overline{\mathbf{C}}|/\gamma^2$. Bottom: A representation of the lattice (dipoles in black and quadrupoles in red) is shown in the bottom graph. The horizontal and vertical tunes were $Q_x = 28.266$ and $Q_y = 29.212$ respectively and $\Delta Q_{min} = 4.37 \times 10^{-2}$.

agreement between model and calculated values of $|\overline{\mathbf{C}}|/\gamma^2$ is better in the arcs than in the interaction regions (IR's). The larger discrepancies arising in the IR's are due to the presence of strong coupling sources. However, even in a complicated lattice like RHIC, the sources are clearly identified and errors in $|\overline{\mathbf{C}}|/\gamma^2$ are below 5 %.

For the above simulation, we assumed dual plane BPMs in the lattice. However, this is not true for RHIC and most operating hadron colliders. RHIC

consists of 160 BPMs per plane per ring: 72 dual-plane BPMs distributed through the IR's, and 176 single-plane BPMs distributed in the arcs capable of acquiring 1024 turns. The single plane BPMs in RHIC are confined to the arc regions where coupling sources are minimal. A more sophisticated algorithm to estimate $|\overline{\mathbf{C}}|/\gamma^2$ with lattices consisting of both single and double plane BPMs is under investigation. In real accelerators, many BPMs routinely fail resulting in unreliable data. It has been shown that preprocessing of BPM data is usually effective in removing faulty BPMs and maintain data integrity [30] to obtain reliable measurements.

4.3.4 Calculation of skew quadrupole strengths

In [50] and [51] a method to obtain multipole strengths from the measurement of RDT's was proposed. Skew quadrupole strengths are equivalently obtained from the measurement of the $\overline{\mathbf{C}}$ matrix by use of the above relations. According to fig. 4.7 we assume that only one skew quadrupole of integrated

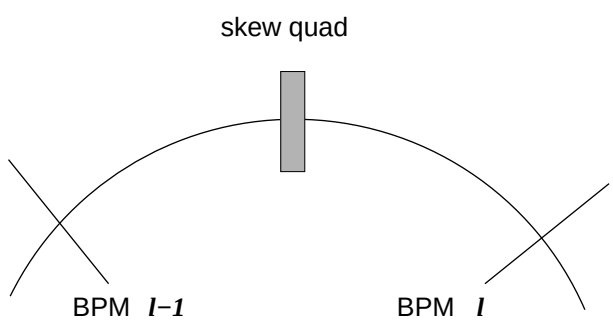

Figure 4.7: Schematic view of a skew quad and the neighbor BPMs

strength k exists between the two BPMs where the $\overline{\mathbf{C}}$ matrices have been measured. From [50] and [51] the integrated strength $\bar{k}$ is given by:

$$\begin{aligned} \bar{k} &= -4e^{-i(\phi_x^{skew}-\phi_y^{skew})} \\ &\quad \times\left(f_{1001}^{(l)}e^{i(\phi_x^l-\phi_y^l)} - f_{1001}^{(l-1)}e^{i(\phi_x^{l-1}-\phi_y^{l-1})}\right), \end{aligned} \tag{4.41}$$

with $\bar{k} = k\sqrt{\beta_x^{skew}\beta_y^{skew}}$. Here k is the strength of coupler, $\beta_{x,y}^{skew}$ and $\phi_{x,y}^{skew}$ are the Twiss functions at the location of the skew quadrupole. $\phi_{x,y}^l$ and $\phi_{x,y}^{l-1}$ are the betatron phases at the lth and $(l-1)^{th}$ BPMs respectively and $f_{1001}^{(l)}$ and $f_{1001}^{(l-1)}$ are the corresponding RDT's. These terms are given by Eq. (4.18) as a function of the measured $\overline{\mathbf{C}}$ matrix. The RDT f_{1010} can also be used

leading to a similar equation. It is also interesting to relate the change of the determinant of $\overline{\mathbf{C}}$ to the strength of the skew quadrupole. By manipulating the above expressions (see alternate derivation in appendix C.4),

$$\bar{k} = -\frac{1}{\chi}\left(\frac{|C^{(l)}|}{\gamma^{(l)^2}} - \frac{|C^{(l-1)}|}{\gamma^{(l-1)^2}}\right) , \tag{4.42}$$

where χ is given by

$$\begin{aligned}\chi &= \frac{1}{\gamma^{(l)}}\Big(-\sin\delta\phi_x \sin\delta\phi_y \overline{C}^{(l)}_{21} + \cos\delta\phi_x \cos\delta\phi_y \overline{C}^{(l)}_{12} \\ &\quad + \sin\delta\phi_x \cos\delta\phi_y \overline{C}^{(l)}_{22} - \cos\delta\phi_x \sin\delta\phi_y \overline{C}^{(l)}_{11}\Big) ,\end{aligned} \tag{4.43}$$

where $\delta\phi_{x,y} = \phi^{skew}_{x,y} - \phi^{l}_{x,y}$ are the phase advances between the skew quadrupole and the second location of observation. Using Eq. (C.7), Eq. (4.43) can also be expressed as

$$\chi = \frac{C^{skew}_{12}}{\gamma^l} \tag{4.44}$$

To determine the applicability of the above expressions, a simulation using strongly coupled RHIC lattice is performed. The ΔQ_{min} for this lattice is 4.37×10^{-2}. Fig. 4.8 shows skew quadrupole strengths determined from Eq. (4.42) for the RHIC lattice. The presence of large coupling sources lead to relative errors of calculated strengths in the 20% level. This is due to fact that these expressions are first order approximations, and deviate with large coupling as illustrated in section 4.2.4.

4.4 The closest tune approach

The following expression relating the closest tune approach and the determinant of $\overline{\mathbf{C}}$ is given in [44] and [45],

$$\Delta Q_{min} = \frac{2\gamma(\cos 2\pi Q_x - \cos 2\pi Q_y)}{\pi(\sin 2\pi Q_x + \sin 2\pi Q_y)}\sqrt{|\overline{\mathbf{C}}|} . \tag{4.45}$$

This equation cannot hold true in general since its l.h.s. is invariant around the ring but the r.h.s. is not, as explained in section 4.2.3. Only close to the difference resonance the determinant of $\overline{\mathbf{C}}$ tends to be invariant and Eq. (4.45)

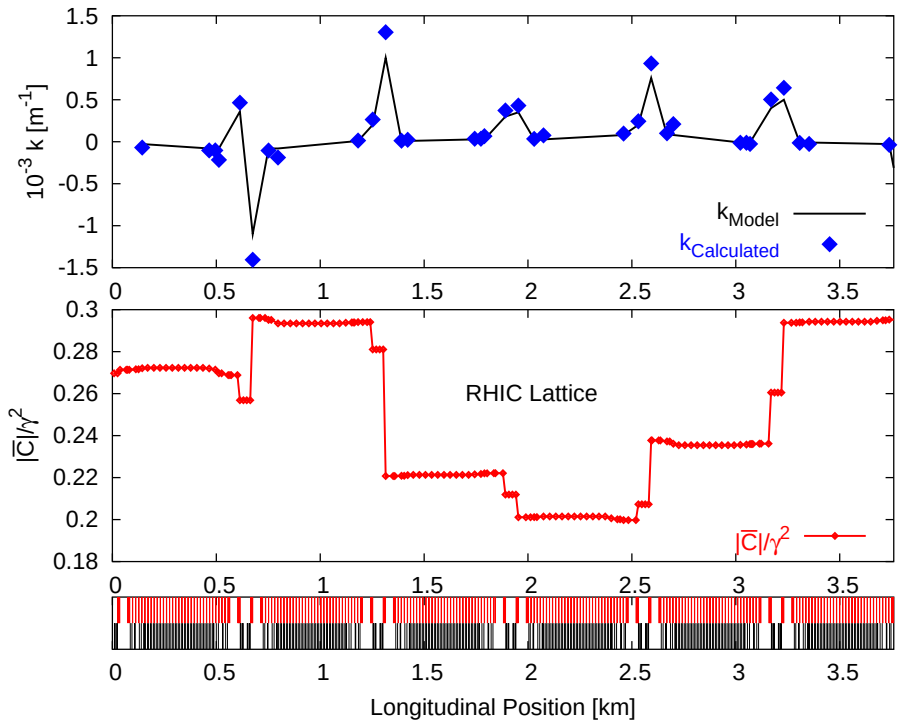

Figure 4.8: Top: Skew quadrupole strengths calculated from RDT's and $\overline{\mathbf{C}}$ matrix are compared to MAD-X model values. Note that RDT's are calculated from $\overline{\mathbf{C}}$ matrix using Eqs. (4.18) and (4.19). Middle: $|\overline{\mathbf{C}}|/\gamma^{\mathbf{2}}$ is plotted as a function of longitudinal position. A representation of the lattice (dipoles in black and quadrupoles in red) is shown in the bottom graph. The horizontal and vertical tunes are $Q_x = 28.266$ and $Q_y = 29.212$ respectively and $\Delta Q_{min} = 4.37 \times 10^{-2}$.

is considered to be a good approximation. Under this assumption the closest tune approach can also be related to the resonance terms,

$$\Delta Q_{min} = \frac{\cos 2\pi Q_x - \cos 2\pi Q_y}{\pi(\sin 2\pi Q_x + \sin 2\pi Q_y)} \times \left(\frac{4\sqrt{|f_{1001}|^2 - |f_{1010}|^2}}{1 + 4(|f_{1001}|^2 - |f_{1010}|^2)} \right) \tag{4.46}$$

and since we assume the tunes to be close to the difference resonance the approximation $|f_{1001}| >> |f_{1010}|$ might also be used [44, 45]. A computer simulation is performed to investigate the validity of Eqs. (4.45) and (4.46). The same FODO lattice with three skew quadrupoles were used with horizontal

and vertical tunes $Q_x = 18.226$ and $Q_y = 17.239$ respectively. Since $|\overline{\mathbf{C}}|$ varies around the ring, ΔQ_{min} is calculated with the three values of $|\overline{\mathbf{C}}|$ at the three locations of skew quadrupoles and plotted as a function of increasing skew quadrupole strengths as shown in Fig. 4.9. We observe a dispersion in the

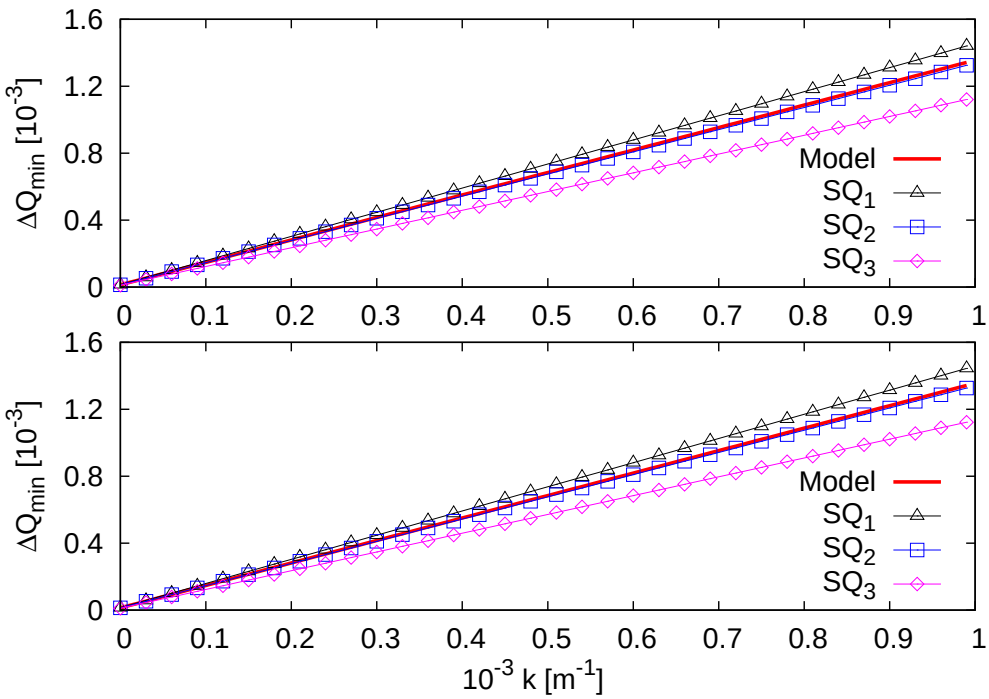

Figure 4.9: Top: ΔQ_{min} calculated using the three different values of RDT's at respective locations of skew quadrupoles as a function of their strength. Bottom: ΔQ_{min} calculated using three different values of $|\overline{\mathbf{C}}|$ at respective locations of skew quadrupoles as a function of their strength ($Q_x = 18.226$, $Q_y = 17.239$).

ΔQ_{min} curves depending on choice of the $|\overline{\mathbf{C}}|$ value used to calculate ΔQ_{min}. If the tunes are closer to the coupling resonance, the relative longitudinal variation in $|\overline{\mathbf{C}}|$ around the ring is smaller, hence reducing this dispersion.

4.5 Conclusions

Direct relations are established between the coupling matrix and the RDT's. This allows reinterpretation of the coupling matrix in terms of resonances and using results from both formalisms indistinctly. Numerical simulations are car-

ried out to confirm these relations and explore their scope of application to real accelerators. The determinant of $\overline{\mathbf{C}}$ and the RDT's ($f_{\substack{1001\\1010}}$) have been demonstrated to exhibit distinct behavior that unambiguously reveals the region of the coupling sources.

A new approach to compute the full $\overline{\mathbf{C}}$ matrix and hence the determinant from turn-by-turn data is presented and comparison to model shows excellent agreement. An approach to extract the skew quadrupole strengths previously using RDT's is also extended to $\overline{\mathbf{C}}$ matrix. The applicability of the expression for ΔQ_{min} from the $|\overline{\mathbf{C}}|$ has been discussed.

Chapter 5

Betatron Coupling: Measurements at RHIC with AC Dipoles

5.1 Introduction

RHIC operates very close to the difference coupling resonance $Q_x = 28.685$, $Q_y = 29.695$ at top energy[1]. This region helps maximize the available "tune space" and avoid any overlap with lattice and spin resonances. It is favorable to operate near the difference resonance to alleviate beam-beam effects and maximize the dynamic aperture. The ability to operate near the difference resonance depends on minimizing the ΔQ_{min}. Therefore, it is important to identify the coupling sources in RHIC and compensate them with available skew quadrupoles, both locally and globally. RHIC has the following relevant sources of transverse coupling:

- Skew quadrupole errors in the interaction region (IR) magnets
- Rolls in the triplet and arc quadrupoles
- Skew quadrupole families in the arc
- IR skew quadrupole correctors
- Sextupole feed-down to skew quadrupole field at the chromaticity sextupoles and at all the dipoles due to vertical closed orbit offsets.
- Experimental Solenoids

[1]The operating tunes Q_x, Q_y have been changed from 28.23, 29.22 to 28.685, 29.695 during Run 2004.

The major sources of the coupling are expected from triplet rolls where the β functions are the largest. Independently powered IR skew quadrupoles are used to compensate individual triplet rolls. This chapter aims at localizing any uncompensated coupling errors in the RHIC lattice using the techniques described in chapter 4 and optimize the IR skew quadrupole settings. The residual coupling from the rest of the lattice is expected to be corrected using three skew quadrupole families which is discussed in section 5.4.

5.2 Baseline Measurements of coupling RDT's and $|\overline{\mathbf{C}}|/\gamma^{\mathbf{2}}$

A variety of techniques to measure RDT's and the **C** matrix exist. Equivalence relations between the RDT's and **C** matrix were derived together with extensions to the existing techniques of measurement using BPM turn-by-turn data in chapter 4 and in Ref. [54]. RHIC is uniquely equipped with two AC dipoles to excite coherent betatron oscillations in transverse planes which are routinely used to measure RHIC optics [55, 56]. An analytical formalism to measure RDT's in the presence of an ac dipole was proposed in Ref. [18] and the measurements of local and global sextupole RDT's using BPM data generated from ac dipole excitation have been demonstrated at RHIC [19]. Detailed measurements of $f_{\substack{1001\\1010}}$ and $|\overline{\mathbf{C}}|/\gamma^{\mathbf{2}}$ at RHIC during the 2005 Cu-Cu run follows.

5.2.1 Injection Energy

Beam experiments were performed during the 2005 polarized proton run to measure f_{1001} and $|\overline{\mathbf{C}}|/\gamma^{\mathbf{2}}$. The goal of these experiments was to identify and measure the magnitude the local coupling sources [2]. Global coupling was initially corrected using the skew quadrupole families to minimize the tune split ($\Delta Q_{min} < 5 \times 10^{-3}$) using a skew quadrupole modulation technique [53]. Coherent betatron oscillations in both transverse planes were driven using two ac dipoles and BPM data are simultaneously recorded. The natural betatron tunes along with the ac dipole drive tunes and amplitudes are shown in Table 5.1. The data are initially processed to remove faulty BPMs according to criteria discussed in chapter 3 and Ref. [30]. Approximately 10-15% of the

[2]It must be noted that beam experiment time is extremely limited and only a few configurations of skew quadrupoles were possible with the given beam time constraints.

Table 5.1: Design tunes and AC dipole drive tunes along with drive amplitude settings at injection energy

	Yellow		Blue	
Parameter	H	V	H	V
Tunes	0.731	0.723	0.735	0.721
Drive Tune	0.74	0.719	0.745	0.712
Drive Amp [mm]	0.05	0.05	0.05	0.05
Tunes	0.735	0.706	-	-
Drive Tune	0.745	0.697	-	-
Drive Amp [mm]	3.0	3.0	-	-

BPMs were found to be consistently faulty which were not used in this analysis. Fig. 5.1 shows four measurements of f_{1001} and $|\overline{\mathbf{C}}|/\gamma^{\mathbf{2}}$ as a function of longitudinal position in the yellow ring.

Although globally decoupled, the f_{1001} and $|\overline{\mathbf{C}}|/\gamma^{\mathbf{2}}$ in the yellow ring (Fig. 5.1) shows significant variations in the ring indicating uncorrected local coupling sources. f_{1001} and $|\overline{\mathbf{C}}|/\gamma^{\mathbf{2}}$ in the blue ring (Fig. 5.2) look relatively flat and also globally well decoupled. Since, the yellow ring at injection exhibits substantial features, data sets were also taken with the global skew families turned off to capture the effects of natural skew error sources without external compensation. The coupling terms with the global families are shown in Fig. 5.3 This is to be compared with Fig. 5.1. Despite the missing BPMs, both scenarios consistently exhibit positive or negative slopes in the $|f_{1001}|$ and $|\overline{\mathbf{C}}|/\gamma^{\mathbf{2}}$ behavior in the the arc regions. This is counter intuitive to the original assumption that the coupling sources are mainly confined to IR regions. Possible reasons for the slope can be attributed to

- A systematic roll of quadrupoles (or skew quadrupole component in dipole ends) in an entire arc region. This is unlikely because any roll in the quadrupoles around the ring is likely to be random and uncorrelated and will not yield a slope behavior.

- A systematic vertical orbit displacement in the arc sextupoles. This is also unlikely because the orbit recorded by the BPMs is usually centered and any small orbit displacements maybe random in nature.

An experiment with a closed three-bump orbit displacement and its effect on the coupling terms is discussed in section 5.3.2. Simulations are also underway to use the quadrupole roll and/or sextupole orbit displacement as input

variables to fit the data and identify the possible sources of slopes via fitting techniques.

5.2.2 Top Energy (Store)

An experiment similar to injection was performed at top energy for the blue and yellow rings to measure f_{1001} and $|\overline{\mathbf{C}}|/\gamma^{\mathbf{2}}$. Global coupling was initially compensated similar to injection energy and the skew families were set at nominal operating values[3]. The settings for the tunes and amplitudes for top energy in the blue ring are shown in Table 5.2.

Table 5.2: Design tunes and AC dipole drive tunes along with drive amplitude settings at top energy settings

	Blue		Yellow	
Parameter	H	V	H	V
Tune	0.684	0.694	0.697	0.685
Drive Tune	0.675	0.703	0.705	0.675
Drive Amp [mm]	2	2	3	3

The data was processed to remove faulty BPMs similar to the injection data. However, the BPMs between IR4 - IR6 (3.5 - 3.85 km) in blue ring yield a $f_{1001} = 0$ which is being investigated. Fig. 5.4 shows a measurement of f_{1001} at top energy for the blue ring. A large discontinuity in f_{1001} is observed at IR12 (2 km) and smaller ones at IR8 (0.5 km) and IR4 (3 km) which indicate local skew sources.

The yellow ring exhibits large discontinuities at IR8 (0.5 km) and IR2 (2.5 km) as shown Fig. 5.5. The slope behavior is also evident at store in the yellow ring.

5.3 A Possible Correction Strategy

RHIC is equipped with skew quadrupole correctors on either side of the IR with individual power supplies located approximately with zero phase advance to the triplet quadrupoles. The main function of these individual correctors is to compensate for roll in the triplet quadrupoles. Although the corrector

[3]It is almost impossible to operate without global skew families at store without beam losses due to overlap of lattice resonaces

pair affects global coupling, they are most effective for compensating triplet magnets in that IR.

Although the slope behavior is not well understood with an additional constraint of several missing BPMs, a possible correction strategy using individually powered IR skew correctors was explored. The procedure involved a systematic scan of IR skew correctors and simultaneous measurement of $4|f_{1001}|$ and $|\overline{\mathbf{C}}|/\gamma^{\mathbf{2}}$. The goal of the scan was to minimize all local jumps and also reduce the overall amplitude of the coupling terms. Any residual coupling will be further compensated with global skew families that yields the minimum f_{1001} for the minimum achievable ΔQ_{min}. Table 5.3 shows the available IR correctors with their current settings for nominal operation.

Table 5.3: Skew quadrupole maximum strengths, and nominal settings at store and injection for the yellow ring. Note that the longitudinal location specified for the IRs are approximate.

Location	**Skew Quad Name**	**Max. Strength** kl $[m^{-1}]$	I (Amp)	**Injection** kl $[m^{-1}]$	**Store** kl $[m^{-1}]$
IR-6: 0.0 km	YO-5	0.00153	50	-0.26	-0.26
	YI-6	0.00153	50	0.07	0.07
IR-8: 0.6 km	YI-7	0.00153	50	0.36	0.36
	YO-8	0.00153	50	-1.1	-1.1
IR-10: 1.3 km	Y0-9	0.00153	50	0.7	0.7
	YI-10	0.00153	50	1.0	1.0
IR-12: 1.9 km	YI-11	0.00153	50	0.3	0.3
	YO-12	0.00153	50	0.35	0.35
IR-2: 2.5 km	YO-1	0.00153	50	0.2	0.2
	YI-2	0.00153	50	0.76	0.76
IR-4: 3.2 km	YI-3	0.00153	50	0.4	0.4
	YO-4	0.00153	50	0.5	0.5

5.3.1 IR Corrector Scan: Injection

A systematic scan of a local corrector in IR-10 (YO9) was performed as an initial experiment and f_{1001} and $|\overline{\mathbf{C}}|/\gamma^{\mathbf{2}}$ were measured as shown in Fig. 5.6. Both positive and negative deviations from its nominal value increases the global coupling which is evident from the increase in f_{1001}. Since the absolute

Table 5.4: Skew quadrupole maximum strengths, and nominal settings at store and injection for the blue ring. Note that the longitudinal location specified for the IRs are approximate.

Location	**Skew Quad Name**	**Max. Strength** Setting	I (Amp)	**Injection Setting**	**Store Setting**
IR-6: 0.0 km	BI-5	0.00153	50	0.0	0.0
	BO-6	0.00153	50	-0.1	-0.1
IR-8: 0.6 km	BO-7	0.00153	50	-0.9	-0.9
	BI-8	0.00168	55	1.4	1.4
IR-10: 1.3 km	BI-9	0.00168	55	0.35	0.35
	BO-10	0.00168	55	0.65	0.65
IR-12: 1.9 km	BO-11	0.00153	50	0.5	0.5
	BI-12	0.00153	50	-0.32	-0.32
IR-2: 2.5 km	BI-1	0.00168	55	-0.2	-0.2
	BO-2	0.00168	55	1.2	1.2
IR-4: 3.2 km	BO-3	0.00153	50	0.32	0.32
	BI-4	0.00153	50	0.32	0.32

value of the coupling term is quite large, discontinuities are not clearly visible. Therefore an effective local correction would also entail a simultaneous global family correction for each local scan value which is difficult and maybe impossible given the time available for experiments. Hence the following scans were performed with global families turned off and tunes well separated. For the following scans only the $|\overline{\mathbf{C}}|/\gamma^{\mathbf{2}}$ is shown since the corresponding $4|f_{1001}|$ shows similar behavior.

IR-4 Scan

Both correctors on either side of the IR in the 4 o'clock region (YI3 and YO4) were also scanned systematically. The coupling terms and the corresponding mean values of $|\overline{\mathbf{C}}|/\gamma^{\mathbf{2}}$ and $4|f_{1001}|$ as a function of skew corrector strength is plotted in Fig. 5.7. Similar to IR-6, the red curve in Fig. 5.7 (top) appears to have the least excursion near IR-4 region which is also close to the global minimum. The nominal value seems to be close to the optimum setting, and a small decrease in both corrector values may be of further help.

IR-6 Scan

In the 6 o'clock two correctors on either side of the IR, Y05 and YI6 were scanned systematically. The coupling terms and the corresponding mean values of $|\overline{\mathbf{C}}|/\gamma^{\mathbf{2}}$ and $4|f_{1001}|$ as a function of skew corrector strength is plotted in Fig. 5.8. Although an optimum setting is not conclusive, the red curve in Fig. 5.8 (top) appears to have the least excursion near IR-6 region. The global minimum also occurs closer to the positive side of the corrector value spectrum.

IR-8 Scan

In the 8 o'clock region a single corrector (YO-8) was scanned systematically to investigate its effect on the locally. The coupling terms and the corresponding mean values of $|\overline{\mathbf{C}}|/\gamma^{\mathbf{2}}$ and $4|f_{1001}|$ as a function of skew corrector strength is shown in Fig. 5.9. In IR-8, the nominal value of the YO-8, similar to the red curve in Fig. 5.9 (top) seems to have the least excursion near the IR-8 region and also a relatively flat distribution elsewhere. Unfortunately, this corrector is already close to its maximum strength, and further increase might have to be accomplished from the opposite side corrector (YI-7) [4].

IR-12 Scan

A scan of a single corrector (YI11) in the 12 o'clock region was performed. The coupling terms and the corresponding mean values of $|\overline{\mathbf{C}}|/\gamma^{\mathbf{2}}$ and $4|f_{1001}|$ as a function of skew corrector strength is shown in Fig. 5.10. The YI11 corrector, although located near 2 km, seems to have a significant effect in the first part of the ring (0-1.5 km). The cyan or blue curves in Fig. 5.10 (top) has a relatively flat distribution with the least excursion in the IR-10 region. The nominal value is insufficient to compensate this IR, and an increase in the correctors (YI11, YO12, or both) should improve the coupling situation in IR-12[5].

IR-2 Scan

Similar to IR-12, a single corrector (YO1) in the 2 o'clock region was also systematically scanned. The coupling terms and the corresponding mean values of $|\overline{\mathbf{C}}|/\gamma^{\mathbf{2}}$ and $4|f_{1001}|$ as a function of skew corrector strength is shown in Fig. 5.11. The behavior near IR-2 is rather inconclusive but the nominal

[4]Note that YI-7 corrector was not scanned for IR-8

[5]Note that YO12 corrector was not scanned for IR-12

setting appears to a show a larger excursion. A increase in the corrector (YO1, YO2, or both) may improve the local coupling in IR-2 and will bring the machine closer to the global minimum.

5.3.2 Vertical Orbit Bump at 2.858 km

An experiment to investigate the effect of a vertical orbit bump on the behavior of the coupling terms was performed. A closed 3-bump was inserted in the middle of an arc between the IR-2 and IR-4 region of RHIC (2.858 km). AC dipole data with increasing amplitude of the orbit bump was taken and Fig. 5.12 shows $|\overline{\mathbf{C}}|/\gamma^{\mathbf{2}}$ and its average value as a function of orbit bump amplitude.

Although small slopes exist in the baseline measurements as shown in Fig. 5.3, the slope behavior becomes prominent with the introduction of the vertical orbit bump. Additionally, the increase in the bump amplitude only seems to increase the average value of the coupling terms with changing the behavior or the magnitude of the slope around the ring. The increase in the coupling can be attributed to the coupling induced by a vertical offset in chromaticity sextupoles located in the arcs. However, the distinct slopes cannot be directly attributed to the sextupoles because of two possible reasons:

- The vertical orbit displacements in the arcs are generally random in nature
- The polarities of the chromaticity sextupoles are alternating, which would lead one to expect an oscillating behavior rather than a consistent slope.

Simulations are being performed to investigate the effect of vertical offsets in sextupoles as variables to fit to measured data. Also, the location of the slope is far from the location of the bump pointing to a more global effect than local. Therefore, vertical offsets are not likely to be a source of the slopes but merely amplify the feature. The average value of the coupling term at nominal settings in every scan (including the orbit bump) were offset from the other values in the scan. This is most likely due to hysteresis.

5.3.3 IR Corrector Scan: Store

Additional to beam time constraints, measurements at top energy (100 GeV/n) are fairly complicated due to:

- The ramping process from injection to top energy and back is approximately 1 hr. This requires that we sustain beam at top energy for the

entire beam experiment. Therefore, careful placement of betatron tunes all times is necessary to avoid any overlap with resonances which may dump the beam.

- The rigidity of the beam is quite large at 100 GeV (Au ions) requiring a sufficiently large kick when using transverse dipole kickers. This leads to large emittance dilution.

- Operating an AC dipole is tricky because of resonant excitation of the beam requiring careful choice of tunes. Although this maybe the only viable option, scanning skew correctors can easily change the tunes and possibly overlap with dangerous resonances.

Therefore, compensation of local coupling sources will be optimized at injection energy and possibly extrapolated to top energy. Future measurements will determine if further optimization of the local correctors are necessary.

5.4 Global Coupling, Correction, and Optimization

The RHIC lattice has to be globally decoupled in order to operate close to the difference betatron coupling resonance. RHIC is equipped with three families of skew quadrupoles in the arcs to compensate global coupling. The coupling vectors of these families are represented in Fig. 5.13. In addition, RHIC is also equipped with two local skew correctors in each interaction region (IR). Global coupling is routinely corrected at RHIC by minimizing ΔQ_{min} using skew families either by a tune scan, a skew quadrupole modulation technique [53], or at injection using N-turn maps [45]. Two families are enough to construct a unique coupling vector and minimize the closest tune approach. The RHIC coupling correction system consists of three families with a phase of 60° between them. Therefore, there exists an infinite number of settings for three families that minimize the closest tune approach. Assuming that the setting given by the vector (f_1, f_2, f_3) minimizes the tune split, then any other setting of the form $(f_1 - \Delta, f_2 + \Delta, f_3 + \Delta)$ with arbitrary Δ is also a local minimum of the tune split. This feature can lead to situations in which the tune split is minimum (globally decoupled) but the machine is highly coupled locally. Fig. 5.14 shows an illustration by plotting the RDT, $|f_{1001}|$ around RHIC lattice (yellow ring) for different configurations of the three families, all yielding a ΔQ_{min} of about 0.001. Although different configurations all yield a minimum tune split, $|f_{1001}|$ varies significantly for each setting. The best

setting should have the lowest values without large spikes. A good recipe is to minimize the average and the standard deviation at the same time. Situations as in Fig. 5.14 may have an impact on the machine optics and must be avoided. The measurement of the coupling RDTs and **C** matrix around the ring is the only way to ensure an optimum correction of coupling.

5.5 Conclusion

Detailed measurements of RDT's and **C** matrix elements were accomplished during the RHIC Run-2005. A systematic scan of IR skew correctors was performed for each individual IR as a possible strategy to minimize local jumps in the coupling terms. A consistent slope behavior was observed and the source of the slopes is under investigation. A vertical offset experiment helps rule out the arc sextupoles as possible sources for the slopes. It is clear that the nominal settings at injection can be improved using the information from these corrector scans to reduce the excursions and overall amplitude in the yellow ring. Appropriate extrapolation and possibly more experiments can help improve the settings at top energy. A technique using RDT's or **C** matrix to optimize the global family settings was also outlined with possible experiments during Run-2006.

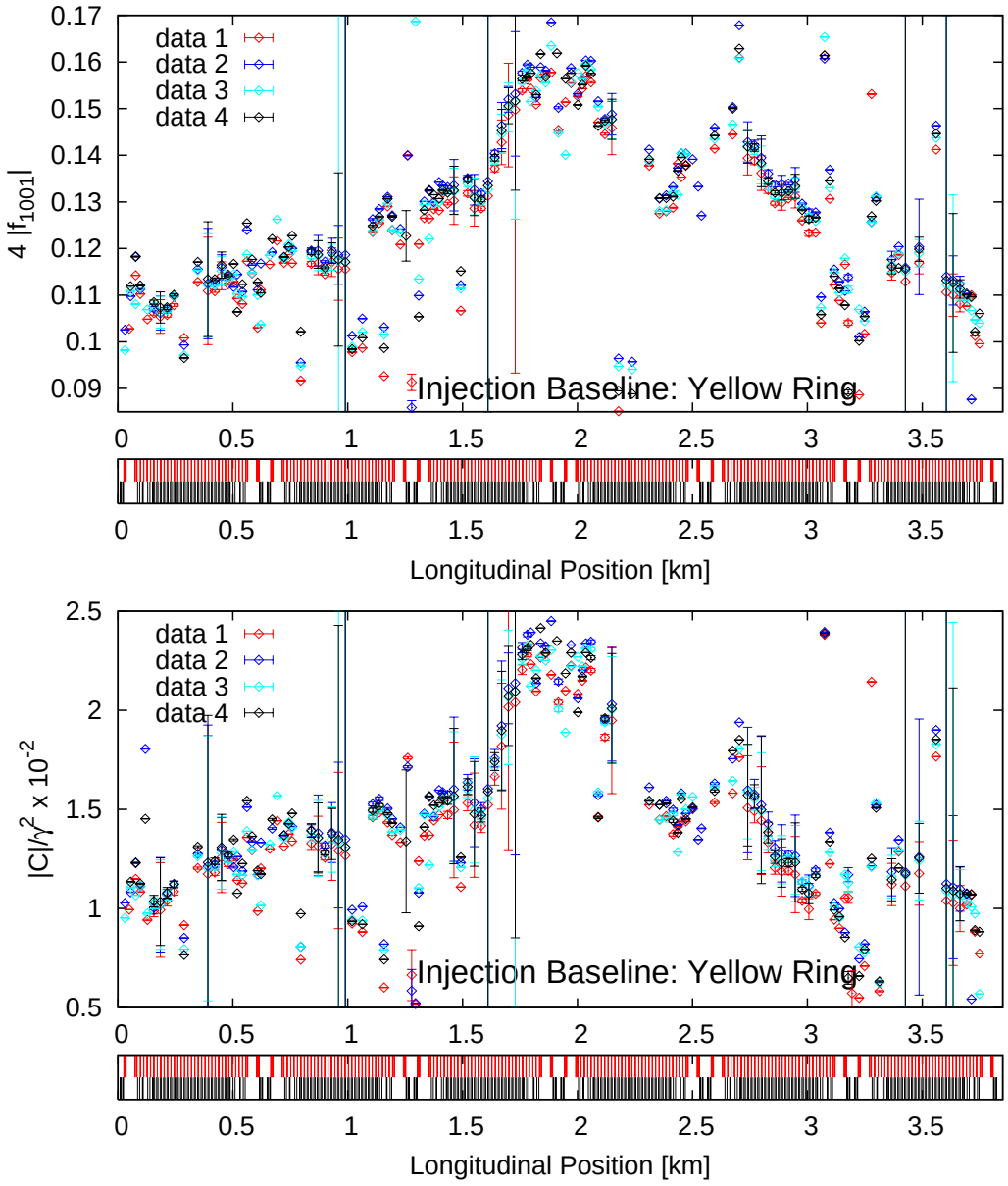

Figure 5.1: Baseline injection measurements of $4|f_{1001}|$ (top) and $|\overline{\mathbf{C}}|/\gamma^{\mathbf{2}}$ (bottom) plotted as a function of longitudinal position along the yellow ring. A representation of the lattice (dipoles in black and quadrupoles in red) is shown in the bottom graph.

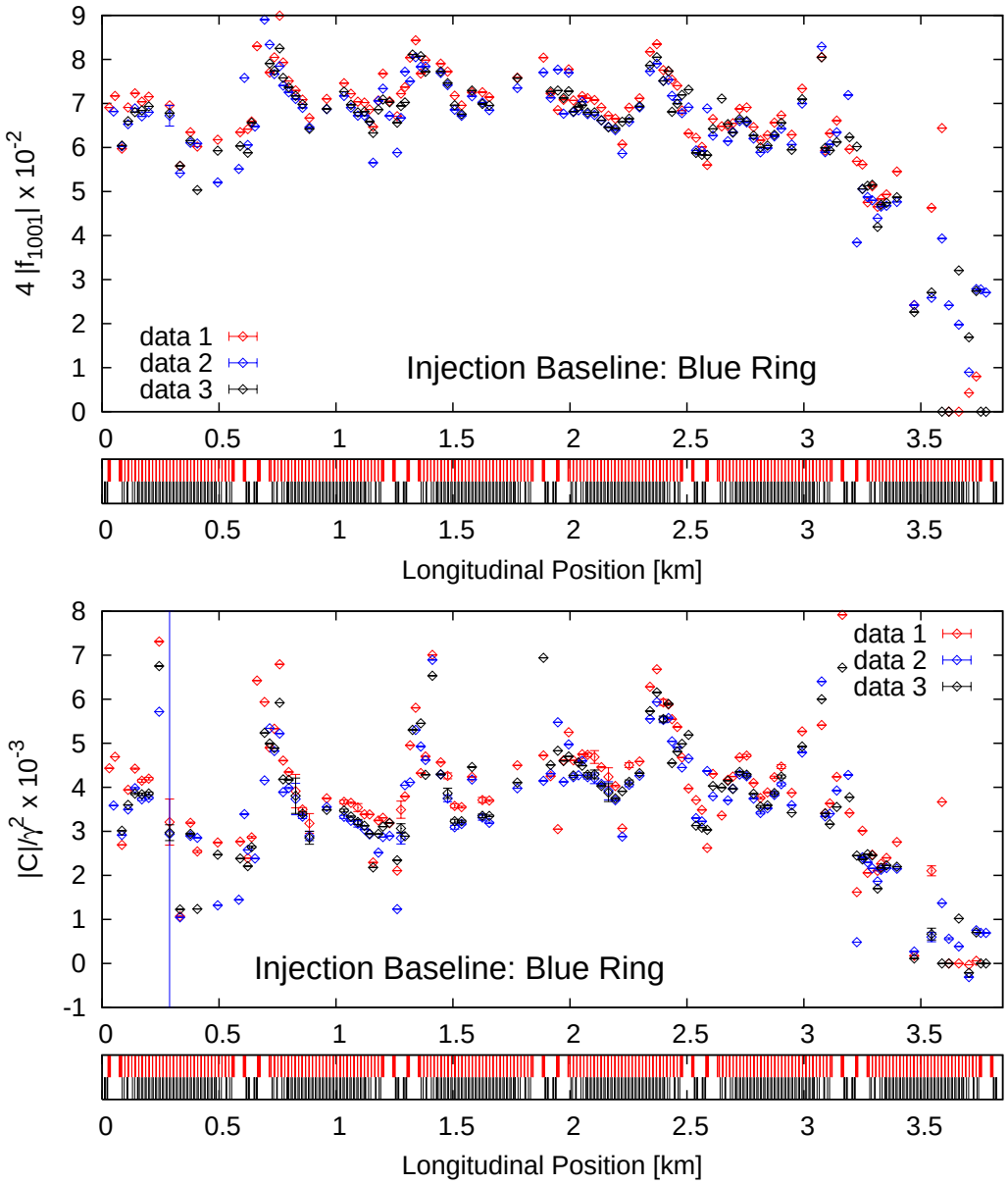

Figure 5.2: Baseline injection measurements of $4|f_{1001}|$ (top) and $|\overline{\mathbf{C}}|/\gamma^{\mathbf{2}}$ (bottom) plotted as a function of longitudinal position along the blue ring. A representation of the lattice (dipoles in black and quadrupoles in red) is shown in the bottom graph.

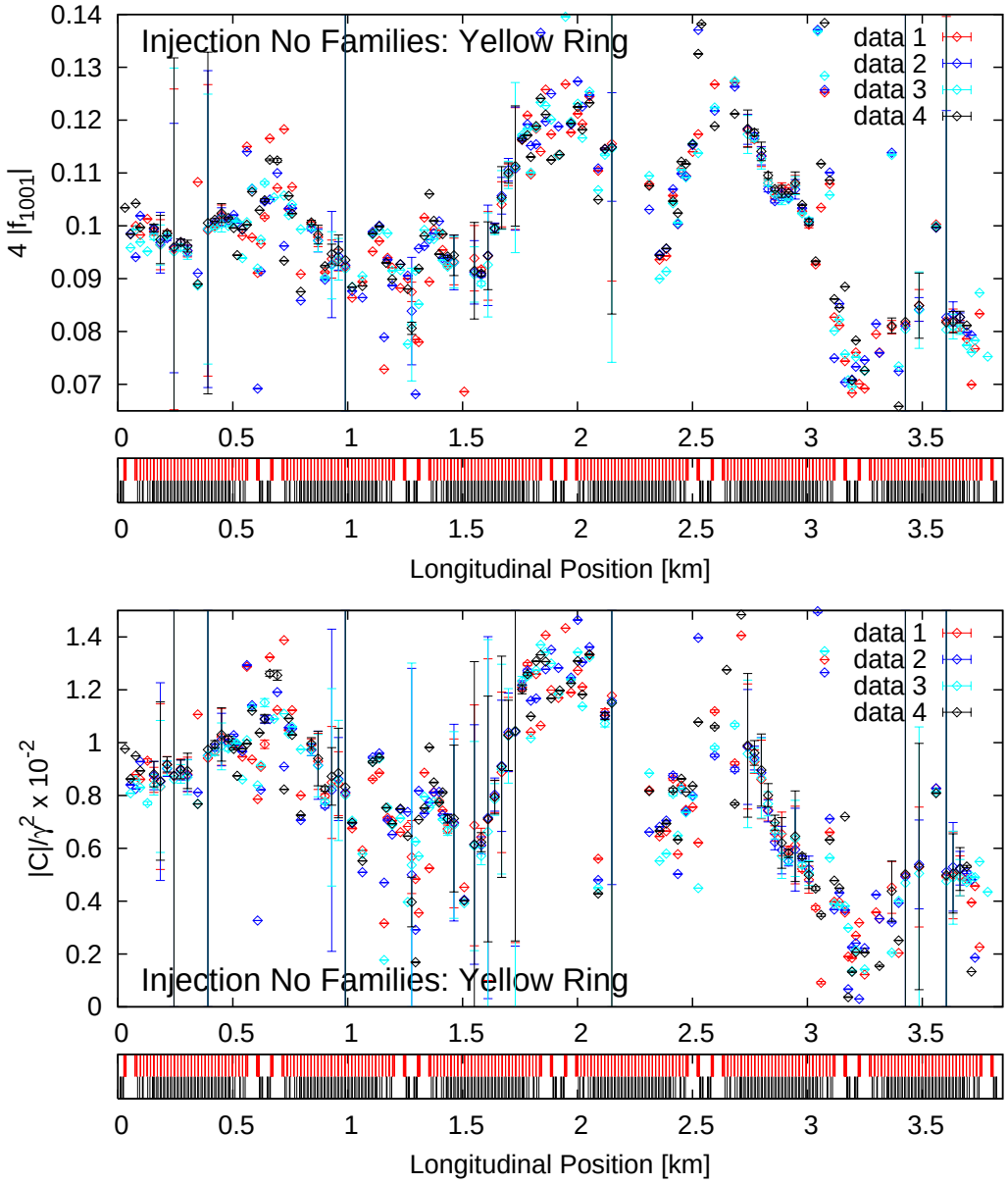

Figure 5.3: Baseline injection measurements of $4|f_{1001}|$ (top) and $|\overline{\mathbf{C}}|/\gamma^{\mathbf{2}}$ (bottom) without global skew quadrupole families plotted as a function of longitudinal position along the yellow ring. A representation of the lattice (dipoles in black and quadrupoles in red) is shown in the bottom graph.

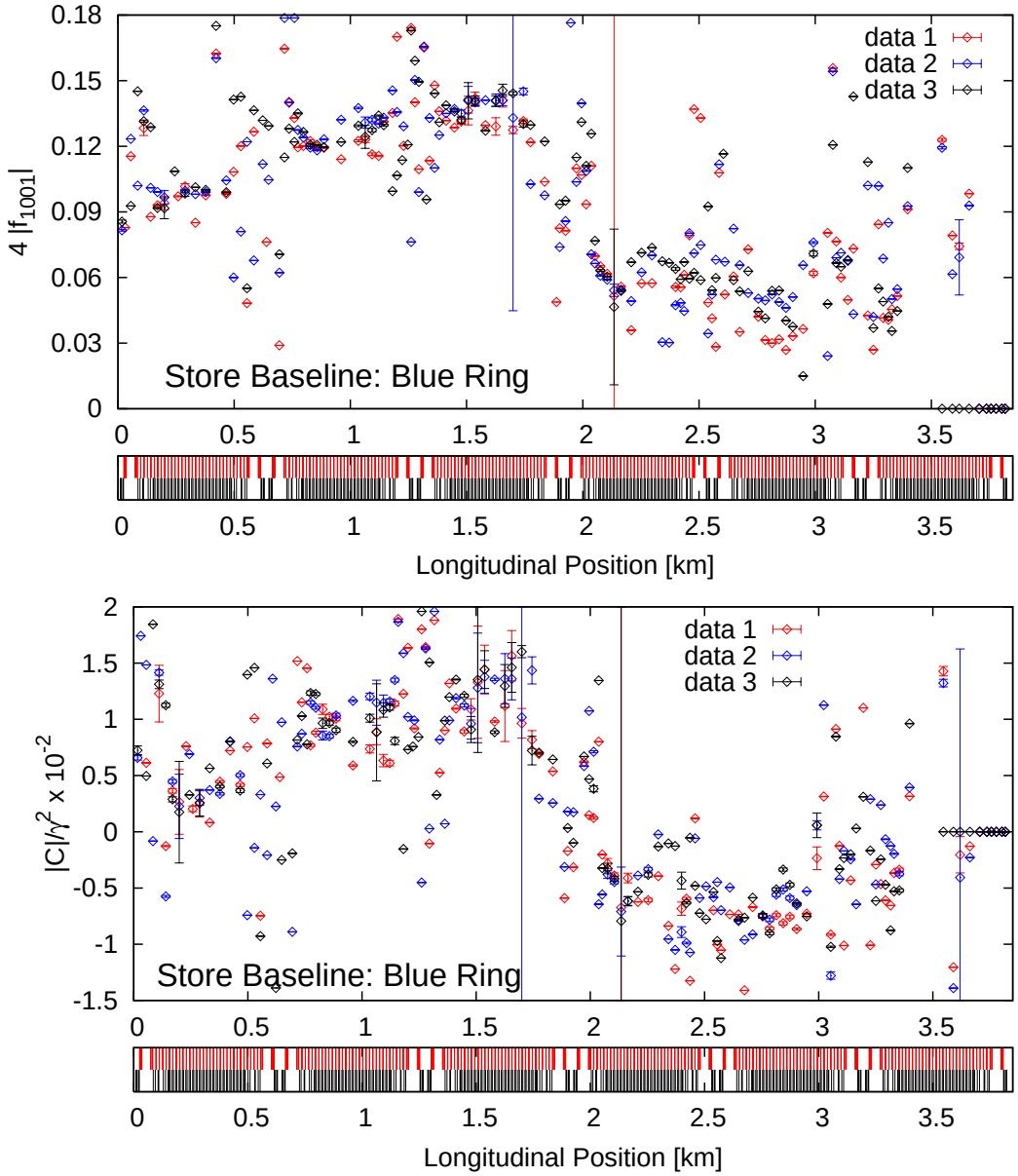

Figure 5.4: Baseline injection measurements of $4|f_{1001}|$ (top) and $|\overline{\mathbf{C}}|/\gamma^{\mathbf{2}}$ (bottom) plotted as a function of longitudinal position along the blue ring at top energy. Four data sets were taken with the same settings shown in Table 5.2. A representation of the lattice (dipoles in black and quadrupoles in red) is shown in the bottom graph.

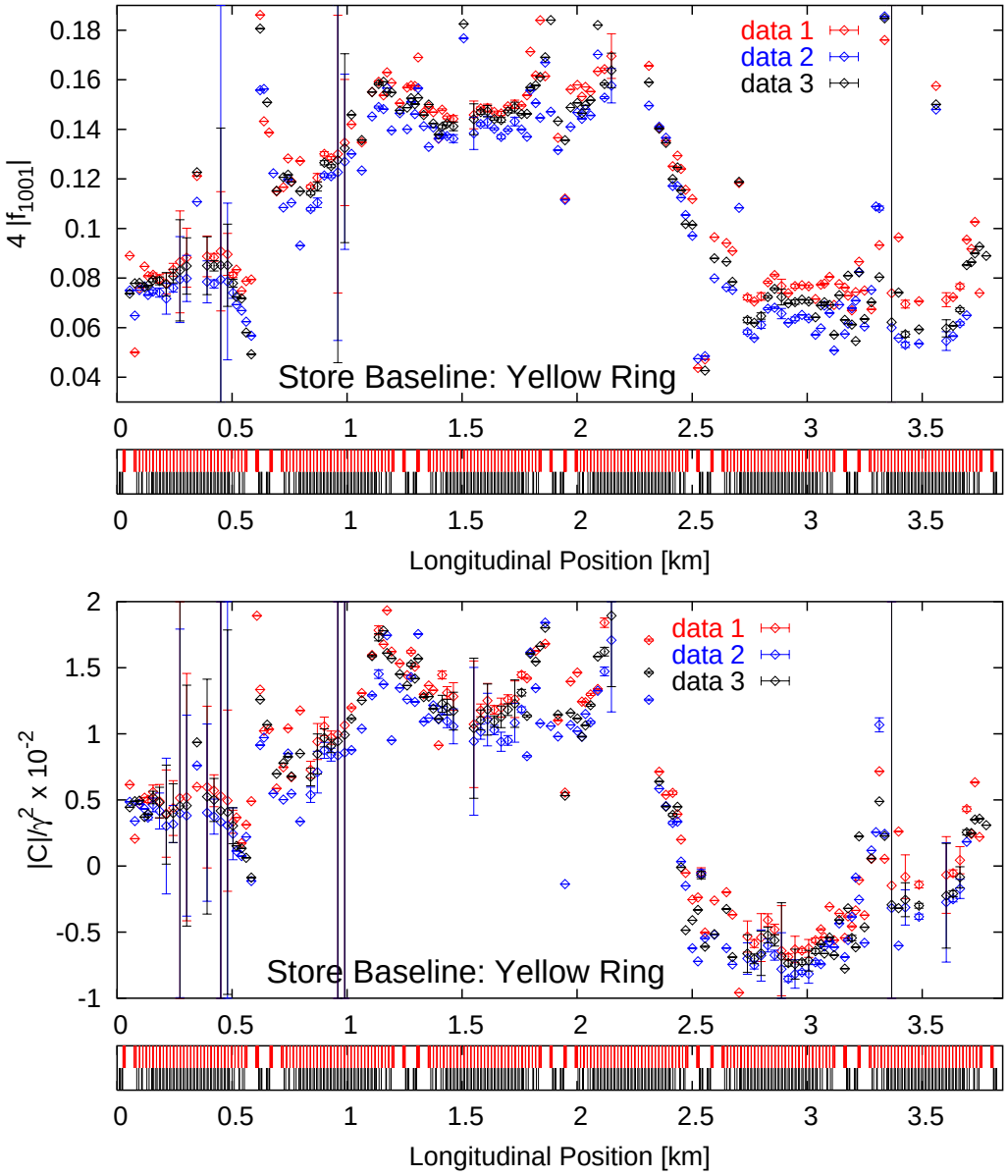

Figure 5.5: Baseline injection measurements of $4|f_{1001}|$ (top) and $|\overline{\mathbf{C}}|/\gamma^{\mathbf{2}}$ (bottom) plotted as a function of longitudinal position along the yellow ring at top energy. All four data sets were taken with the same settings shown in Table 5.2 A representation of the lattice (dipoles in black and quadrupoles in red) is shown in the bottom graph.

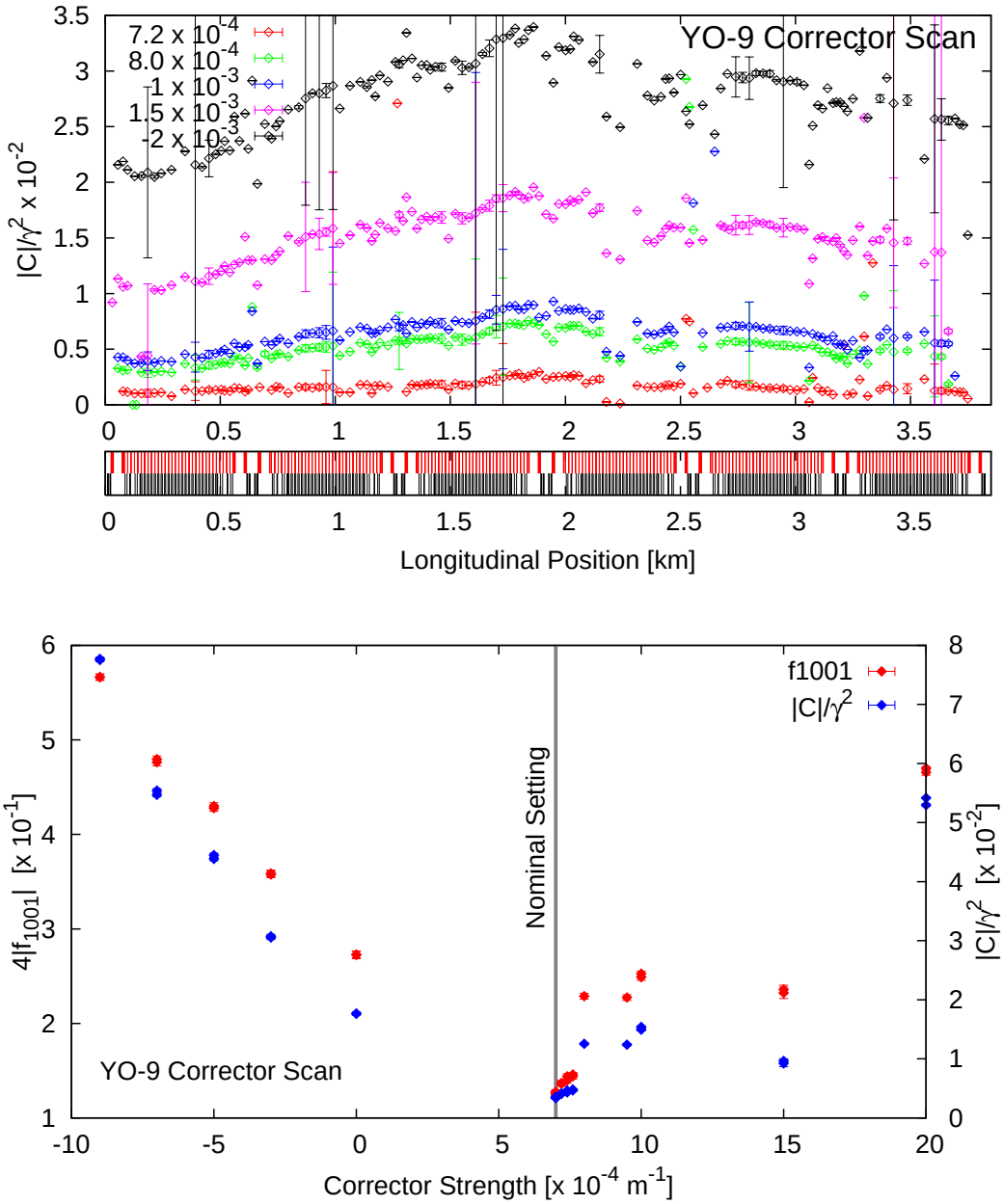

Figure 5.6: Top: $|\overline{\mathbf{C}}|/\gamma^{\mathbf{2}}$ during a positive and negative scan of YO9 corrector in IR-10 region from its nominal value as a function of longitudinal position. Bottom: The average value of $4f_{1001}$ and $|\overline{\mathbf{C}}|/\gamma^{\mathbf{2}}$ plotted as a function of the skew corrector strength. The error bars are calculated from the standard deviation of the coupling terms around the ring. Global families were compensated before the scan and drive tunes $Q_{x,y}$ and $Q^d_{x,y}$ were adjusted accordingly.

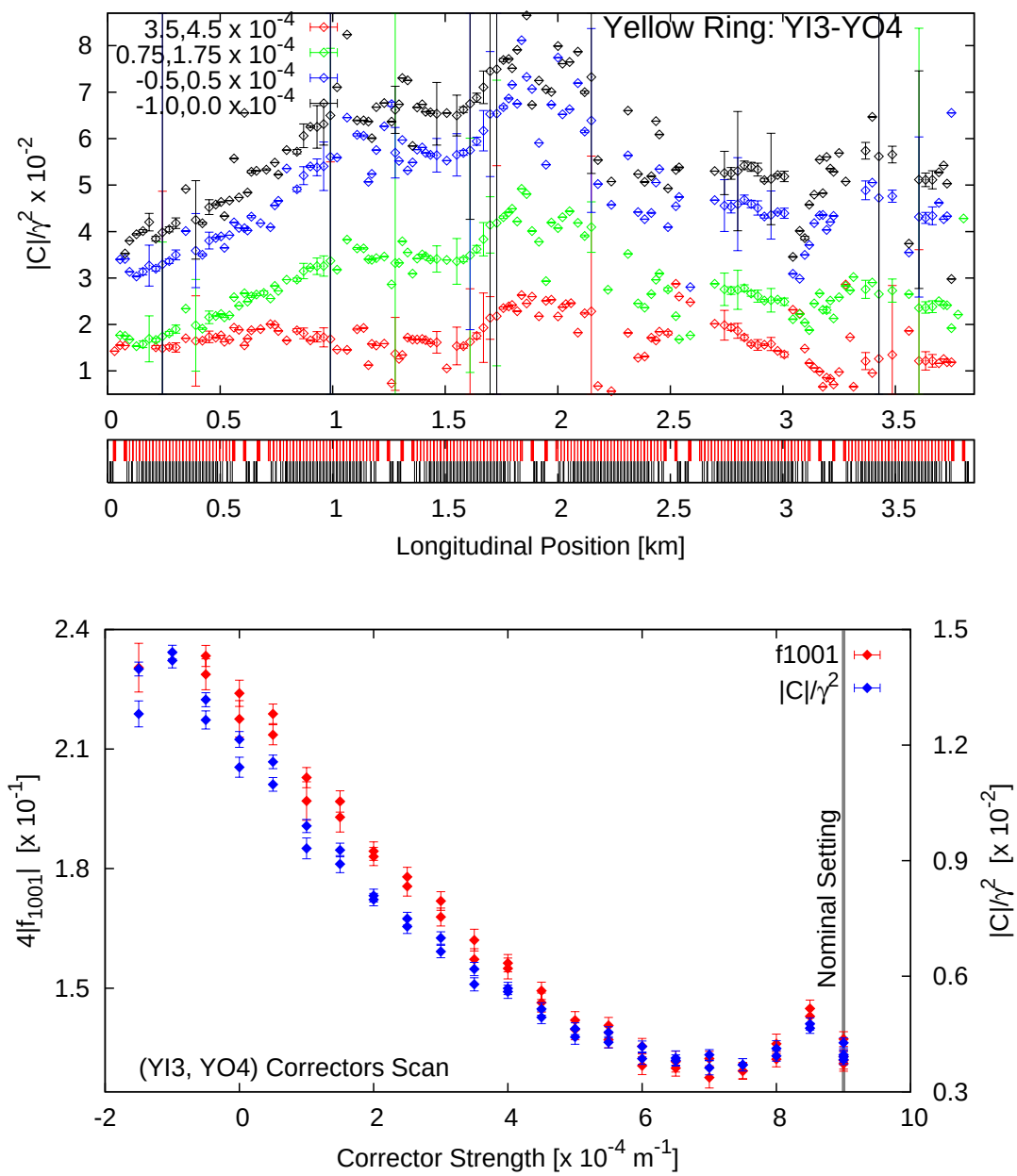

Figure 5.7: Top: $|\overline{\mathbf{C}}|/\gamma^{\mathbf{2}}$ during a scan of YI3 and YO4 correctors in IR-4 region from its nominal value as a function of longitudinal position. Bottom: The average value of $4f_{1001}$ and $|\overline{\mathbf{C}}|/\gamma^{\mathbf{2}}$ plotted as a function of the skew corrector strength. The error bars are calculated from the standard deviation of the coupling terms around the ring. Global families were turned off and t he natural and drive tunes $Q_{x,y}$ and $Q^d_{x,y}$ were adjusted accordingly.

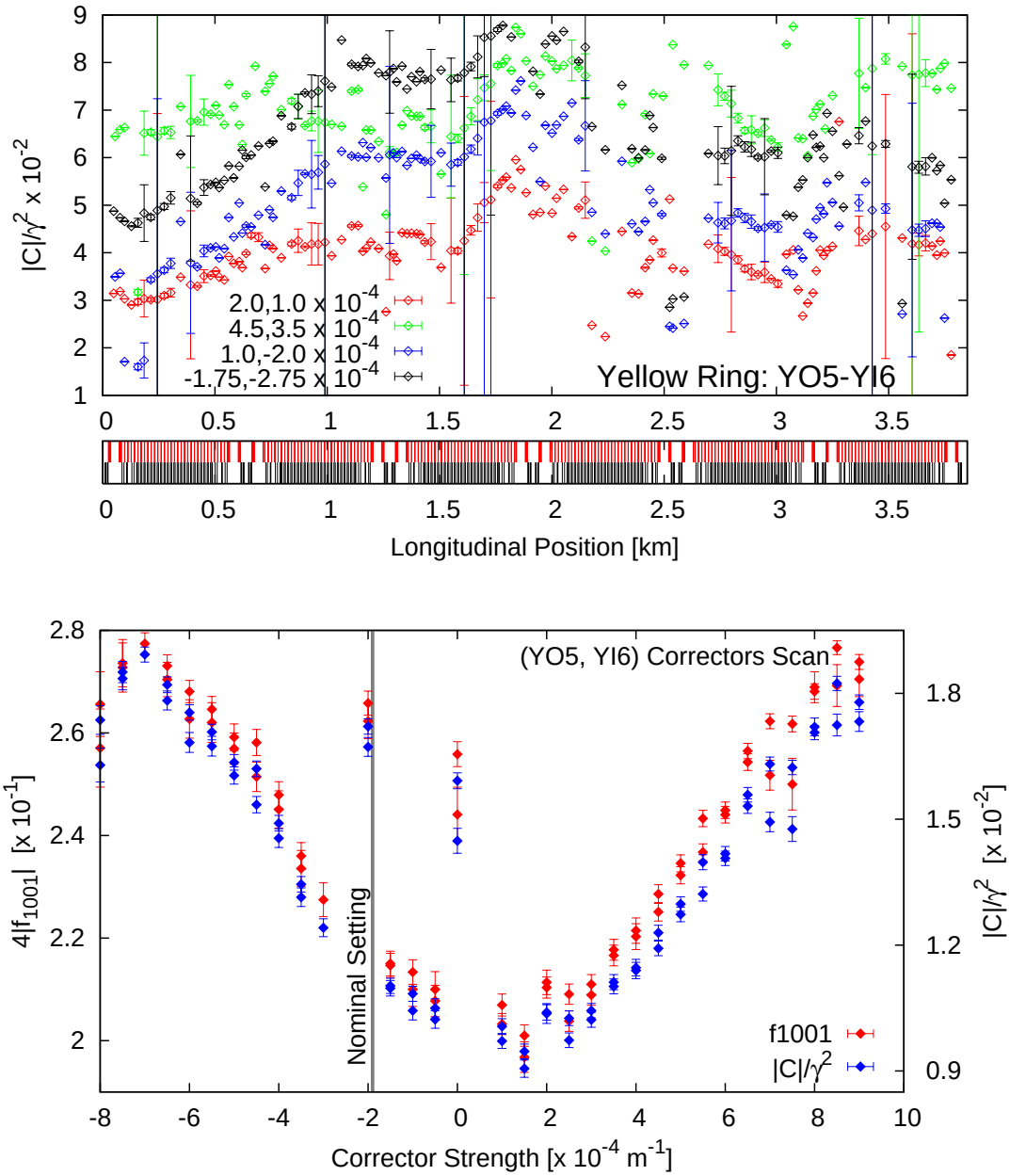

Figure 5.8: Top: $|\overline{\mathbf{C}}|/\gamma^{\mathbf{2}}$ during a positive and negative scan of YO5 and YI6 correctors in IR-6 region from its nominal value as a function of longitudinal position. Bottom: The average value of $4f_{1001}$ and $|\overline{\mathbf{C}}|/\gamma^{\mathbf{2}}$ plotted as a function of the skew corrector strength. The error bars are calculated from the standard deviation of the coupling terms around the ring. Global families were turned off and the natural and drive tunes $Q_{x,y}$ and $Q^d_{x,y}$ were adjusted accordingly.

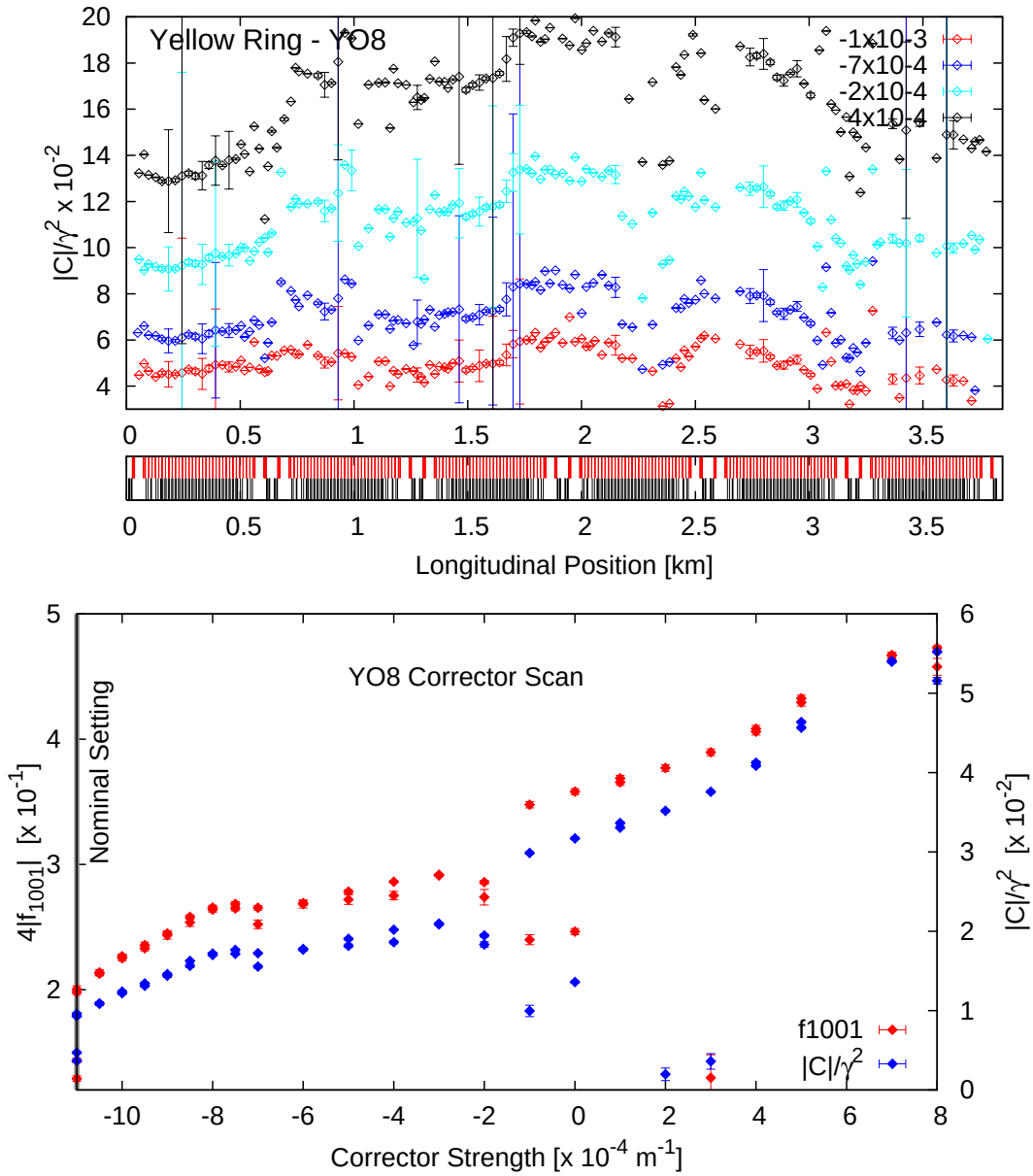

Figure 5.9: Top: $|\overline{\mathbf{C}}|/\gamma^{\mathbf{2}}$ during a scan of YO-8 corrector in IR-8 region from its nominal value. Bottom: The average value of $4f_{1001}$ and $|\overline{\mathbf{C}}|/\gamma^{\mathbf{2}}$ plotted as a function of the skew corrector strength. The error bars are calculated from the standard deviation of the coupling terms around the ring. Global families were turned off and the natural and drive tunes $Q_{x,y}$ and $Q^d_{x,y}$ were adjusted accordingly.

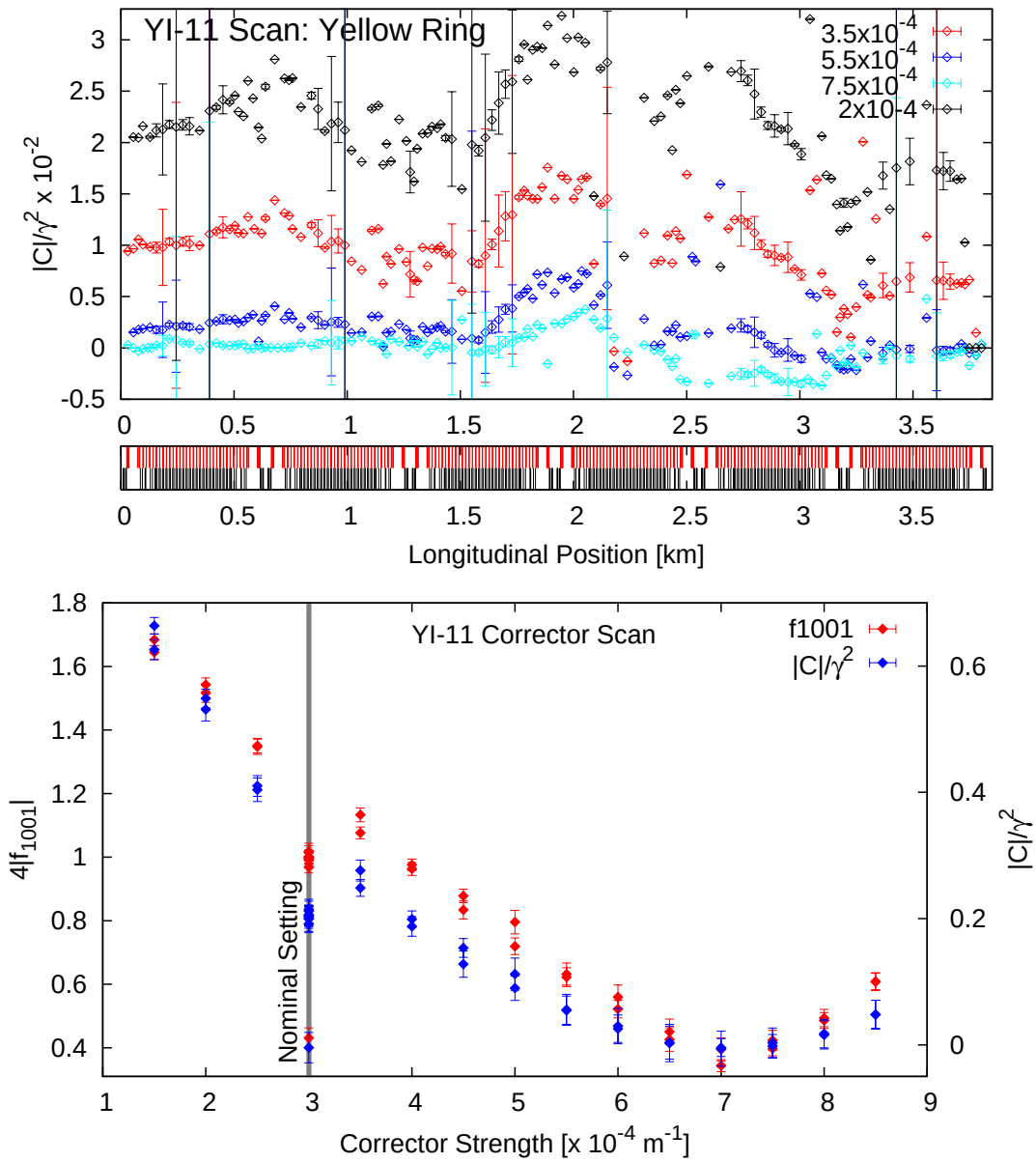

Figure 5.10: Top: $|\overline{\mathbf{C}}|/\gamma^{\mathbf{2}}$ during a scan of YI11 corrector in IR-12 region from its nominal value. Bottom: The average value of $4f_{1001}$ and $|\overline{\mathbf{C}}|/\gamma^{\mathbf{2}}$ plotted as a function of the skew corrector strength. The error bars are calculated from the standard deviation of the coupling terms around the ring. Global families were turned off and the natural and drive tunes $Q_{x,y}$ and $Q^d_{x,y}$ were adjusted accordingly.

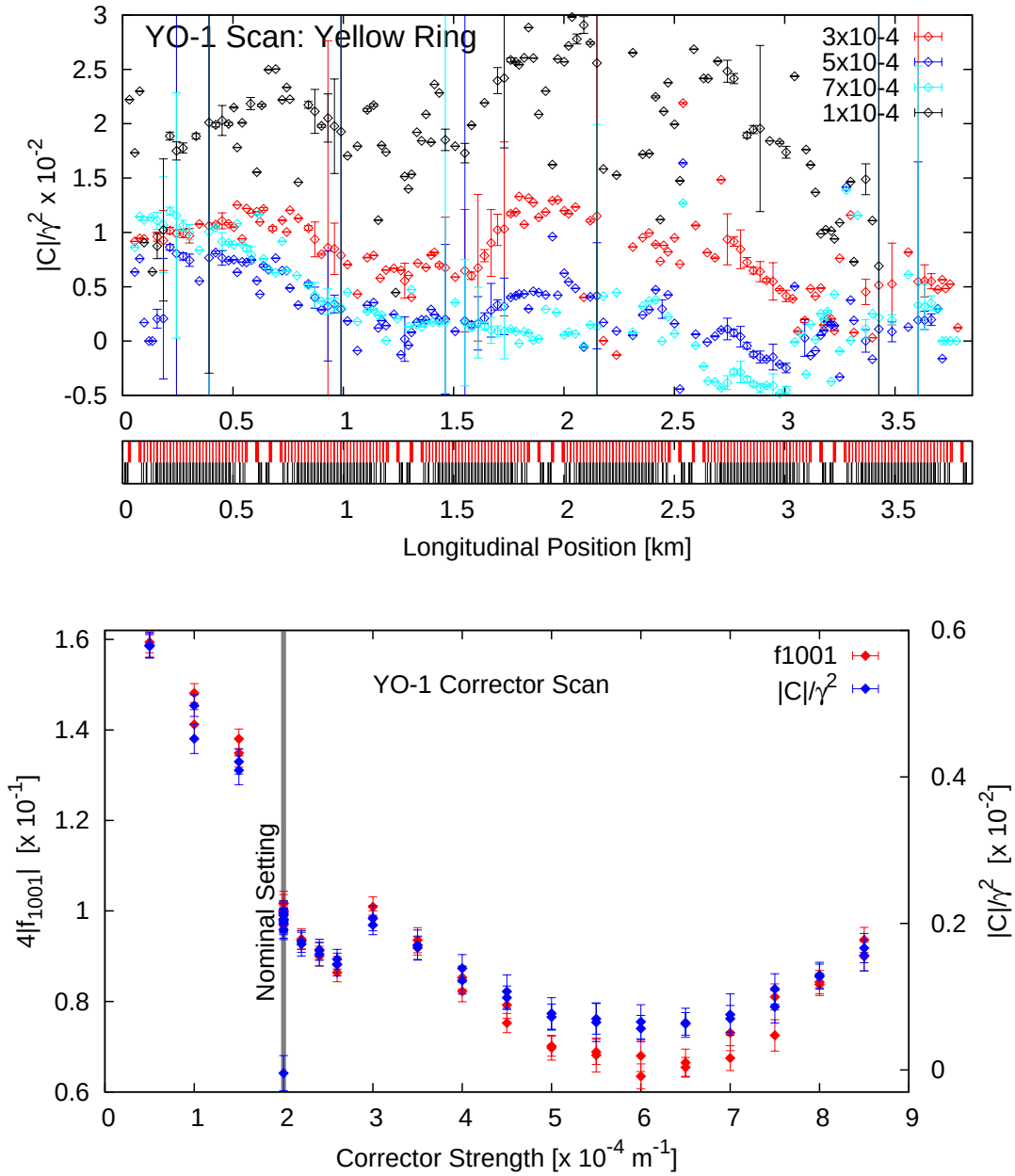

Figure 5.11: Top: $|\overline{\mathbf{C}}|/\gamma^{\mathbf{2}}$ during a scan of YO1 corrector in IR-2 region from its nominal value as a function of longitudinal position. Bottom: The average value of $4f_{1001}$ and $|\overline{\mathbf{C}}|/\gamma^{\mathbf{2}}$ plotted as a function of the skew corrector strength. The error bars are calculated from the standard deviation of the coupling terms around the ring. Global families were turned off and the natural and drive tunes $Q_{x,y}$ and $Q^d_{x,y}$ were adjusted accordingly.

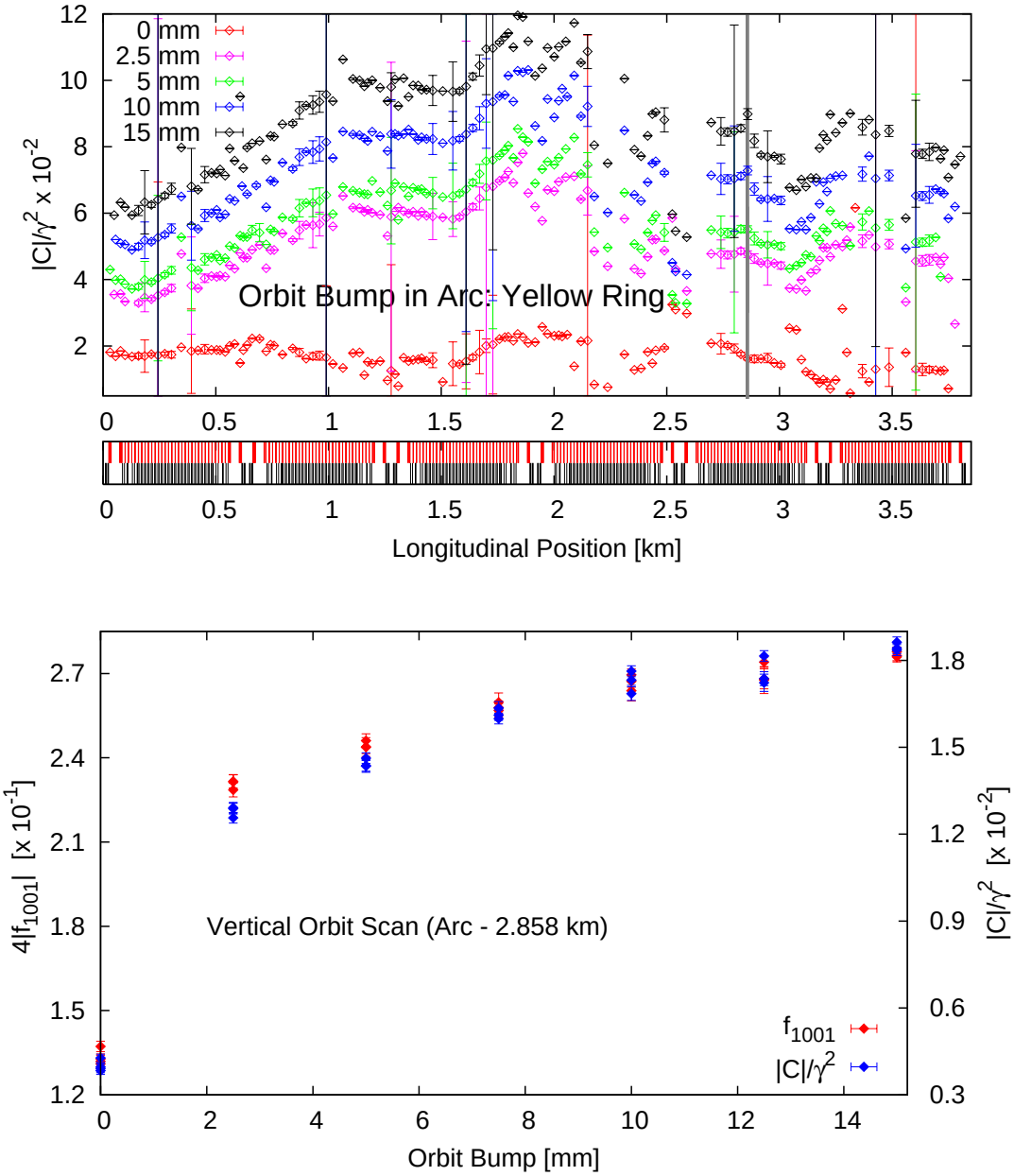

Figure 5.12: $|\overline{\mathbf{C}}|/\gamma^{\mathbf{2}}$ (top) and it's mean value (bottom) as a function the vertical orbit bump amplitude. The vertical bump was placed at 2.858 km (middle of the arc). Global families were turned off and the natural and drive tunes $Q_{x,y}$ and $Q^d_{x,y}$ were adjusted accordingly.

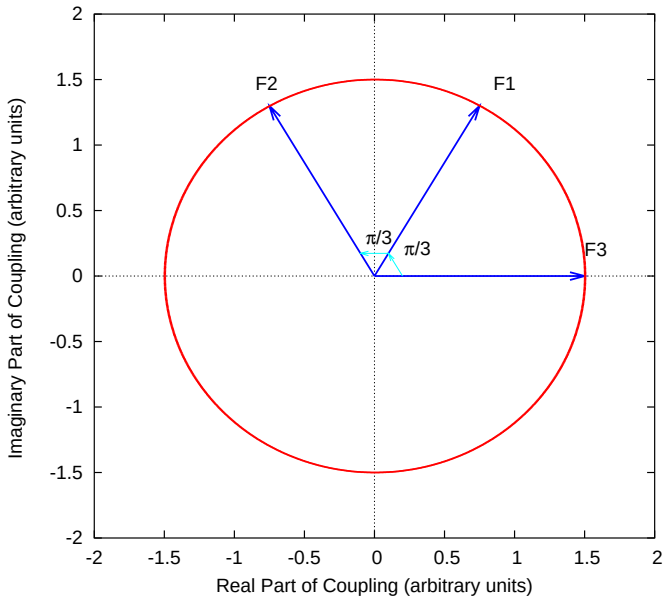

Figure 5.13: Coupling vectors of the three skew quadrupole families of RHIC (Courtesy Y. Luo).

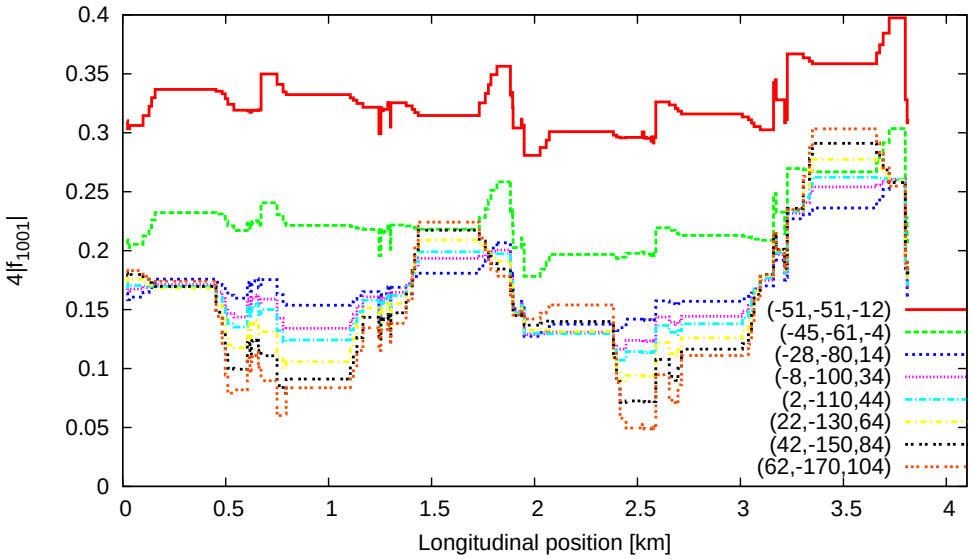

Figure 5.14: f_{1001} from model for a set of different skew families configurations. All of them have a tune split close to 0.001. The numbers in brackets represent the strength of the families in units of 10^{-5} m^{-1} (Courtesy R. Tomás).

Chapter 6

Electron Cooling at RHIC

6.1 Intra-Beam Scattering

The recent advances in nuclear physics experimental research demand high density particle beams with low emittances. Multiple small-angle Coulomb scattering or intra-beam scattering (IBS) is one of main limitations of luminosity and lifetime at the RHIC due to diffusion in both transverse and longitudinal planes. The presence of non-linear elements also results in the increase of the normalized emittance of the ion beam. Fig. 6.1 shows a typical RHIC store with Au-Au collisions at a top energy of 100 GeV/nucleon. Several analytical treatments have been developed to describe the effect of the IBS [58, 59, 60]. The growth rate due IBS either using a classical two body scattering or gas diffusion representation for round beams at high energies scales approximately as [61]

$$\frac{1}{\tau_{||}} \sim \frac{1}{(\beta_r\gamma_r)^3\epsilon_x^{3/2}\langle\beta_\perp^{1/2}\rangle} \tag{6.1}$$

where $\beta_r\gamma_r$ is the relativistic factor, ϵ_x is the transverse emittance, and $\beta_\perp$ is the average transverse beta function of the lattice. The transverse growth can be expressed as function of the longitudinal growth time as

$$\frac{1}{\tau_\perp} \sim \frac{1}{\epsilon_x}\left\langle\frac{D_x^2}{\beta_x}\right\rangle\frac{1}{\tau_{||}} \tag{6.2}$$

where, D_x and β_x are the average dispersion function and the beta function over the lattice. Note that the terms with derivatives of the dispersion and the β function have been neglected due to their weak contribution.

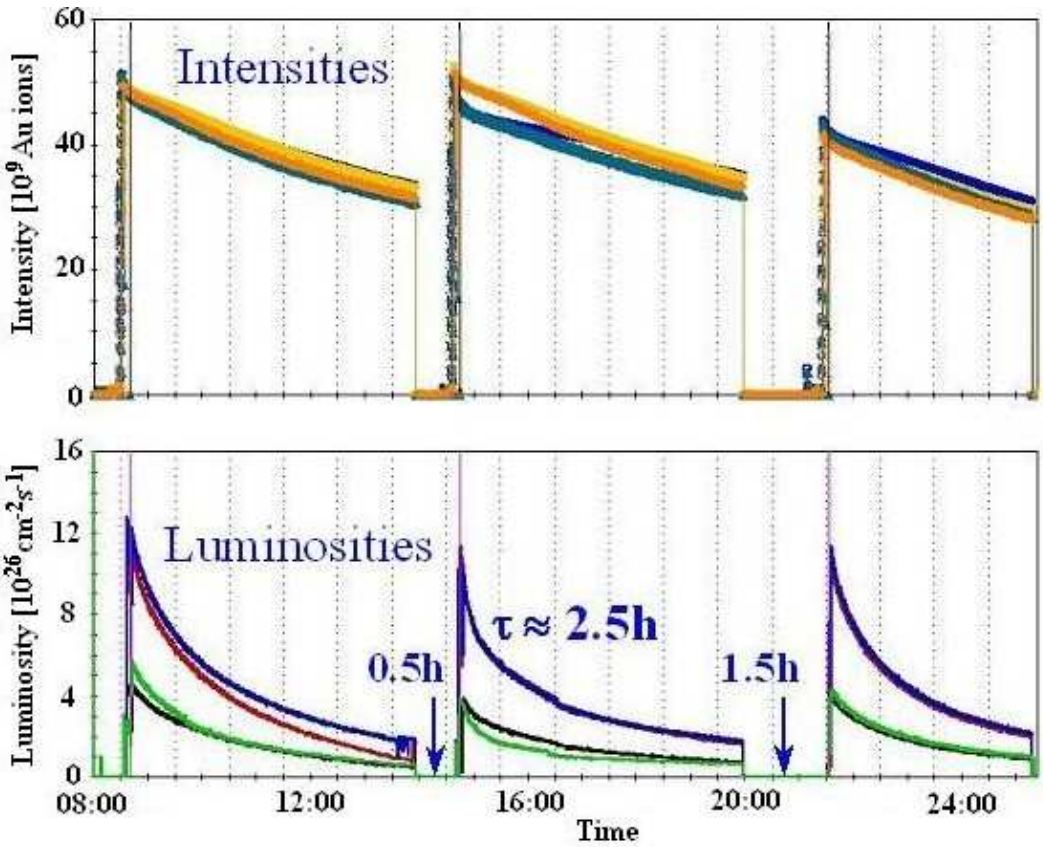

Figure 6.1: Typical RHIC stores and refill times with gold ions. The beam lifetime is limited by IBS leading to particle loss from the RF buckets. The luminosity lifetime is further reduced by transverse beam size growth from IBS. The luminosities are for the four RHIC experiments with β^*=1 m and β^*=3 m (courtesy W. Fischer).

6.2 Electron Cooling

Electron cooling is one of the key component in RHIC II, the next luminosity upgrade of RHIC aiming at a ten fold increase. Electron cooling, first proposed by G. I. Budker in 1965, is a technique to introduce low emittance electrons into the ion beam at the same average velocity (or $\langle\gamma\rangle$). Electron cooling can help increase the peak and average luminosity in several ways [62]:

- Energy exchange between ions to the electrons results in a decrease transverse emittance and momentum spread of the ion beam resulting in an increase in the luminosity.

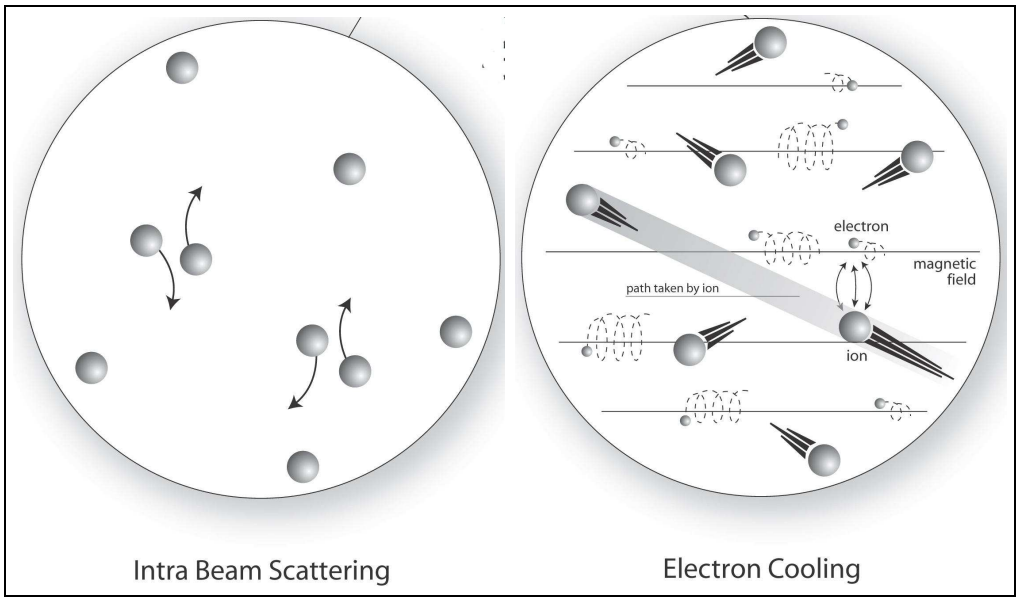

Figure 6.2: Graphical Representation of IBS with and without e^- cooling.

- The continuous cooling of ion beams may also help suppress non-linear resonances due to beam-beam interactions to achieve a higher beam-beam parameter and reduce emittance growth.
- The limitations imposed by the injectors to the high energy colliders can overcome accumulation of high intensity ion beams.
- Cooling of the large amplitude particles in the tail can result in a reduction of the experimental background.

The rate of cooling for a given transverse emittance scales as

$$\frac{1}{\tau_{cooling}} \sim \frac{Z^2 L_{cs}}{A\gamma^2}\left(\frac{\beta_x}{\gamma\epsilon_x}\right)^{3/2} \tag{6.3}$$

where Z and A are the ion charge and atomic number, L_{cs} is the length of the cooling section, and β_x beta function in the cooling section. For RHIC parameters with Au ions, the cooling time is estimated to be in the range of 15-30 min for a typical store of approximately 4 hrs. The ultimate goal of any collider is to reach particle burn-off limit which seems feasible at RHIC with e^- cooling.

Cooling Gold beams at 100 GeV/nucleon require an electron beam energy of approximately 54 MeV and a high average current in the range of 50-200 mA. The traditional e^- coolers are typically low energy DC accelerators. The energy of e^- beam for RHIC is quite high, and the only feasible option to generate high current high quality CW beam is via a superconducting energy-recovery linac (SC-ERL). Without energy-recovery, CW operation is prohibitive due to the large beam power. In this option, an e^- beam from the gun is accelerated using high gradient superconducting RF cavity ($\sim$ 15 MV/m) to match to the ion velocity and then injected into the colling section along with the ion beam for cooling. The e^-'s are returned back to the accelerating cavity with 180° phase shift to recover the energy back into the cavity before being dumped. A schematic of the proposed electron cooler with a $\sim$ 5 MeV SRF injector, a linac comprising of four five-cell SRF cavities, and a recirculation loop for energy recovery is shown in Fig. 6.3. Two variants of the e^- cooling, a non-magnetized version with a simple drift section, and a magnetized version with a 60 m solenoid are being considered as primary and secondary options for cooling sections respectively. Table 6.1 lists relevant beam parameters for both non-magnetized and magnetized versions. Future projects such as eRHIC (electron-ion collider) push the operational current to 300 mA-600 mA at 20 nC bunch charge or higher.

A prototype consisting of a $\frac{1}{2}$-cell SRF gun as an injector to a 20 MeV SRF linac comprised of a single five-cell SRF cavity, and a return loop back through the linac for energy recovery is being pursued as an initial R&D step towards the realization of high current e^- cooler and future SC-ERLs. Part II of thesis will focus on the design and development of SRF cavities in the ampere regime and their related challenges. The next section will introduce some relevant RF cavity basics, specifically related to SRF cavities. The following chapters will elaborate on the design of the five-cell SRF linac cavity followed by the $\frac{1}{2}$-cell SRF injector gun design for the SC-ERL prototype and some future developments.

Table 6.1: Parameters for the prototype SC-ERL used in simulations for optimization of the gun shape. A possible scenario with high charge and low repetition rate similar to the electron cooling case is also presented.

Parameter	Magnetized	Non-Magnetized
Injection energy [MeV]	5.2	5.2
Maximum energy [MeV]	20-40	20-40
Avg. beam current [mA]	200	50
Repetition rate [MHz]	9.4	9.4
Charge/Bunch [nC]	20	5
Norm. emittance [mm.mrad]	50	3
Bunch length [cm]	1.0	1.0
Energy recovery efficiency	> 99.95 %	> 99.95 %

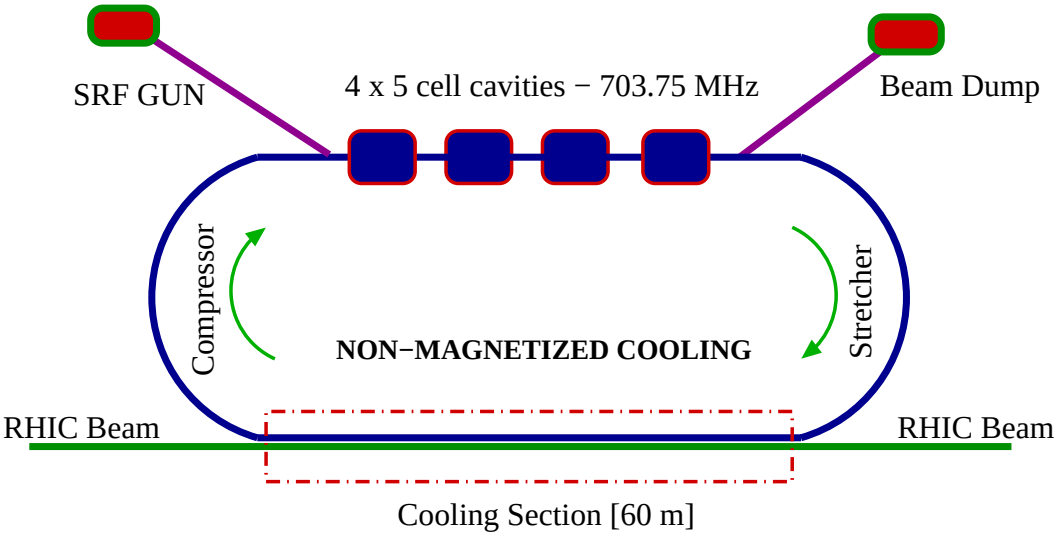

Figure 6.3: Electron cooling schematic for RHIC II upgrade (not to scale).

Chapter 7

Radio Frequency Basics and Superconductivity

7.1 Introduction

An radio frequency (RF) cavity is a resonant waveguide with closed boundaries. Microwave power in the RF cavity is coupled to the particle beam to accelerate the particles to high energies. It is of interest to find monochromatic waves propagating down the waveguide of the form

$$\vec{E} = \vec{E}_0 e^{i(kz-\omega t)} \tag{7.1}$$

$$\vec{B} = \vec{B}_0 e^{i(kz-\omega t)} \tag{7.2}$$

The $\vec{E}$ and $\vec{B}$ fields must satisfy Maxwell's equations inside the waveguide given by

$$\begin{array}{ll} \vec{\nabla} \times \vec{E} = -\frac{\partial \vec{B}}{\partial t}, & \vec{\nabla} \cdot \vec{B} = 0 \\ \vec{\nabla} \times \vec{B} = \frac{1}{c^2}\frac{\partial \vec{E}}{\partial t}, & \vec{\nabla} \cdot \vec{E} = 0 \end{array} \tag{7.3}$$

Combining Maxwell's equations, we arrive at two uncoupled wave equations

$$\nabla^2 - \frac{1}{c^2}\frac{\partial^2}{\partial t^2}\left\{ \begin{array}{c} \vec{E} \\ \vec{B} \end{array} \right\} = 0 \tag{7.4}$$

The $\vec{E}$ and $\vec{B}$ fields can be determined by solving the eigenvalue equation subject to boundary conditions

$$\hat{n} \times \vec{E} = 0, \quad \hat{n} \cdot \vec{B} = 0 \tag{7.5}$$

The solutions to the eigenvalue problem by substituting Eq. 7.1 and 7.2 form an orthogonal set of eigenvalues each with unique frequency and corresponding

field configuration. Since, the electric and magnetic fields are independent with different boundary conditions, they form two families of solutions which are classified as transverse magnetic (TM) and transverse electric (TE) modes.

7.2 Pill-Box Cavity

In a pill-box cavity the fields are additionally subject to Eq. 7.5 at $z = 0$ and $z = l$, where l is the length of the cylindrical cavity. Reflections at the z-boundaries create appropriate standing waves of the form

$$\vec{E} = \vec{E_0} \cos\left(\frac{p\pi z}{l}\right) e^{i\omega t}, \quad p = 0, 1, 2 \ldots \text{(TM Modes)} \tag{7.6}$$

$$\vec{B} = \vec{B_0} \sin\left(\frac{p\pi z}{l}\right) e^{i\omega t}, \quad p = 1, 2, 3 \ldots \text{(TE Modes)} \tag{7.7}$$

Substituting the above fields into the eigenvalue equation, two families of modes similar to a waveguide are obtained. These modes are classified as TM_{mnp} or TE_{mnp}, where m, n, and p are integers and describe the azimuthal, radial, and longitudinal periodicity. The resonant frequencies of TM or TE modes are given by

$$\omega_{mnp} = \frac{1}{\sqrt{\mu_0 \epsilon_0}} \sqrt{\left(\frac{p_{mn}}{r}\right)^2 + \left(\frac{p\pi}{l}\right)^2} \; - \; \text{(TM)} \tag{7.8}$$

$$\omega_{mnp} = \frac{1}{\sqrt{\mu_0 \epsilon_0}} \sqrt{\left(\frac{p'_{mn}}{r}\right)^2 + \left(\frac{p\pi}{l}\right)^2} \; - \; \text{(TE)} \tag{7.9}$$

where, p_{mn} and p'_{mn} are the nth zero of the Bessel function and its derivative respectively, and r is the radius of the cylinder. The mode frequencies as a function of cavity dimensions for a pill box cavity are shown in Fig. 7.1

To accelerate particles, a longitudinal $\vec{E}$ is required which is satisfied only by J_0. The lowest accelerating mode of the type TM_{0np} has fields of the form

$$E_z = E_0 J_0(\omega_0 r/c) \cos(\omega_0 t) \tag{7.10}$$

$$H_\phi = -\frac{1}{\mu_0 c} E_0 J_0(\omega_0 r/c) \sin(\omega_0 t) \tag{7.11}$$

with all other field components are zero. This mode is denoted as TM_{010} with fields similar to that shown in Fig. 7.2. The frequency of this mode in a pill-box cavity is independent of the cavity length and is given by

$$\omega = \frac{2.405\ c}{R} \tag{7.12}$$

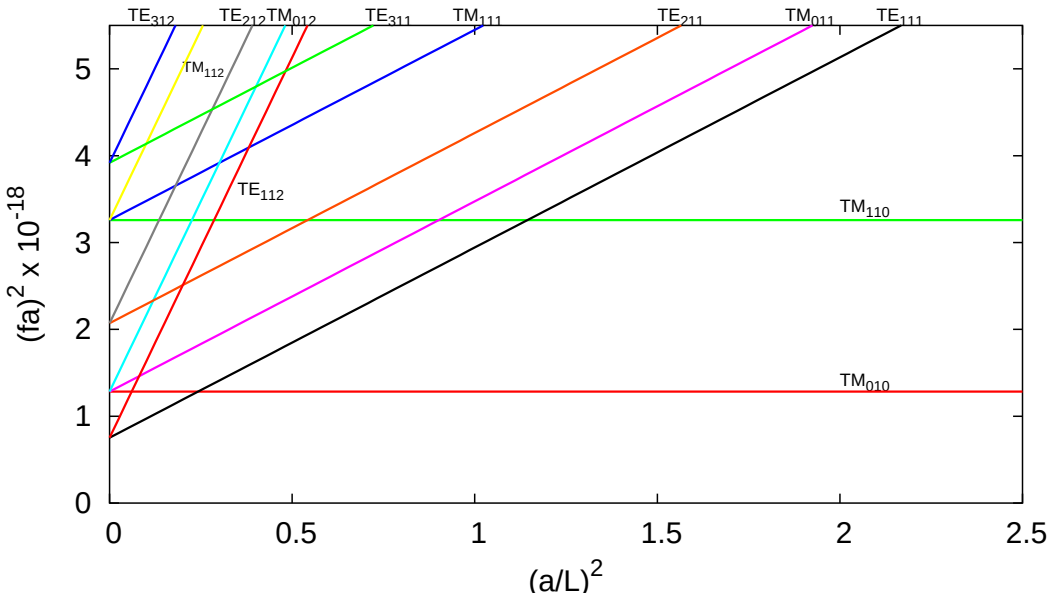

Figure 7.1: Mode frequencies as a function of cavity dimension for a pill box resonator.

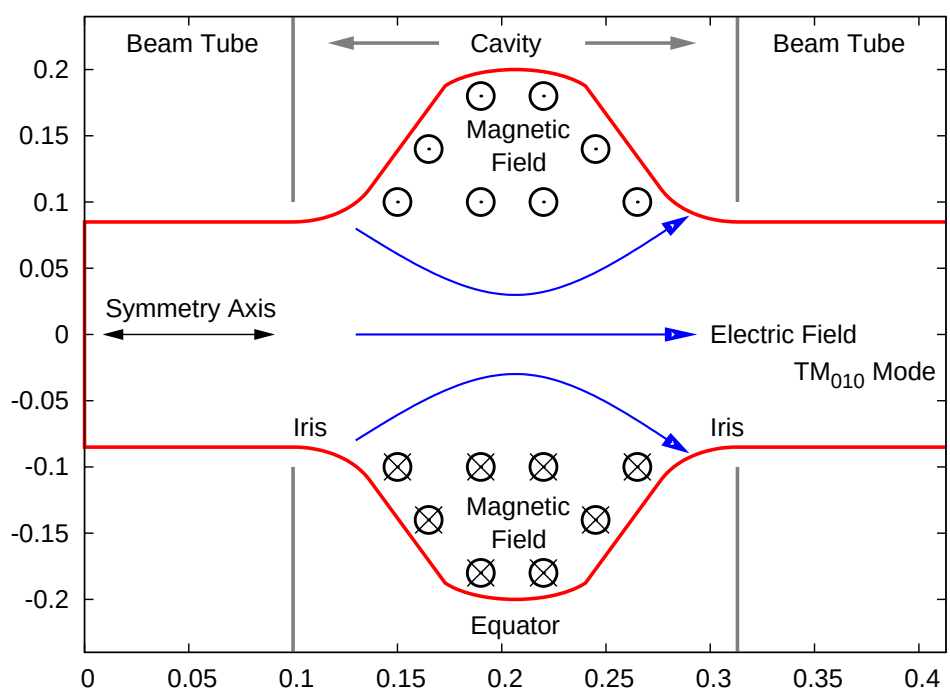

Figure 7.2: Schematic of an elliptical cavity with field lines of TM_{010} mode.

7.3 Characteristic Parameters

Some relevant figures of merit characterizing RF cavities are described in the following section.

7.3.1 Accelerating Voltage

The longitudinal electric field accelerates or decelerates a particle depending on the particle phase with respect to the RF. The voltage gained by the particle across the gap is given by

$$V_{acc} = \left| \int_{z=0}^{z=l} E_z e^{i\omega_0 z/c} dz \right| \tag{7.13}$$

where l is the cavity length, and ω_0 is the frequency of the mode. The particle takes a finite time to traverse the cavity, leading to a reduction in energy gain which is characterized by a transit time factor

$$T = \frac{\int_0^l E_0 e^{i\omega z/c}\ dz}{\int_0^l E_0\ dz} \tag{7.14}$$

7.3.2 Stored Energy

For each mode in the cavity, the time averaged energy in the electric is equal to that in the magnetic fields. The stored energy in the fields is given by a volume integral

$$U = \frac{1}{2}\epsilon_0 \int_V |\vec{E}|^2\ dv = \frac{1}{2}\mu_0 \int_V |\vec{H}|^2\ dv \tag{7.15}$$

7.3.3 Surface Resistance and Power Dissipation

Since, real metals have finite conductivity, RF fields at sufficiently high frequencies penetrates a finite depth into the conductor. The current density is exponentially decreasing into the metal. The surface impedance of the metal is given by

$$R_s = \sqrt{\frac{\mu\omega}{2\sigma}} \tag{7.16}$$

where, δ is known as the skin depth which is defined as

$$\delta = \sqrt{\frac{2}{\mu\omega\sigma}}. \tag{7.17}$$

The power dissipated in the cavity walls due to the surface resistance is given by the surface integral

$$P_d = \frac{1}{2} R_s \int_S |\vec{H}|^2 \, ds \tag{7.18}$$

7.3.4 Quality Factor

The stored energy in the cavity decays exponentially

$$U(t) = U_0 \; e^{-t/\tau} \tag{7.19}$$

where τ is the characteristic time constant dependent on the material. This figure of merit can also be expressed in terms of a quality factor

$$Q_0 = \frac{\omega_0 U(t)}{P_d(t)} \tag{7.20}$$

which characterizes the amount of stored energy dissipated in on RF cycle

7.3.5 Geometric Factor and Shunt Impedance

A product of the surface resistance and quality factor is geometric constant given by

$$G = R_s Q_0 = \frac{\omega_0 \mu_0 \int_V |\vec{H}^2 dv}{\int_S |\vec{H}|^2 ds} \tag{7.21}$$

Another figure of merit of a cavity which is the shunt impedance given by

$$R_{shunt} = \frac{V^2}{P_d} \tag{7.22}$$

which measures the efficiency the accelerating voltage for given dissipation. A more meaningful quantity is the ratio of shunt impedance to the quality factor

$$\frac{R_a}{Q_0} = \frac{V^2}{\omega U} \tag{7.23}$$

This quantity is independent of the cavity material and the field amplitude and is a measure of the efficiency of the accelerating voltage for a given stored energy.

7.4 RF Superconductivity

The two most important characteristics of superconducting RF (SRF) cavities are the high average gradient and cavity intrinsic Q_0. The fundamental advantage of superconducting materials is due to the extremely small surface resistance (< 10 nΩ) compared to conventional copper which is typically several orders higher ($\sim$ mΩ). Therefore, operation of cavities in CW mode or high duty factor become feasible due to significant reduction of power dissipation on the cavity walls. A simple example comparing the power consumption of SRF cavities to copper cavities is illustrated in Table 7.1 [63]

Table 7.1: AC power required to operate 500 MHz superconducting and normal conducting cavities at 1 MV/m

Option	SRF	Normal
Frequency [MHz]	500	500
Q_0	2×10^9	2×10^4
R_a/Q_0 [Ω/m]	330	900
P/L [W/m]	1.5	5.6×10^4
AC Power [kW/m]	0.54	112

Limitations on the maximum power dissipated on the cavity walls resulting in vacuum degradation, stresses, and metal fatigue puts an upper limit on the maximum gradient. In addition, SRF cavities also offer the option of having a larger beam pipe to reduce wakefield effects. However, this results in a drop in the R/Q_0, but the very large intrinsic Q_0 factor naturally helps to compensate for this drop compared to copper cavities.

7.4.1 Superconductivity

The unique properties of superconductors has been subject of scrutiny for several decades. A simplified two-fluid model proposed by London offers a phenomenological explanation of the field exclusion of below the critical temperature. The zero dc resistivity of a superconductor can be attributed to the fact that super-electrons carry the current while shielding the field from the normal electrons.

A more successfully microscopic theory to explain superconductivity was put forth by Bardeen, Cooper, and Schrieer (BCS) in 1957. At a temperature below the critical temperature (T_c), it is energetically favorable for a fraction of

the electrons to be paired into Cooper pairs. The number of unpaired electrons is

$$n_{normal} \propto e^{-\frac{\Delta}{k_B T}} \tag{7.24}$$

where, k_B is the Boltzmann factor. These pairs consist of opposite spin and momenta electrons which freely move without resistance. At $T = 0$ K, all charge carriers are condensed into a single state transforming the metal into an ideal superconductor.

7.4.2 Surface Resistance of Superconductor

Although, the dc resistivity is zero, there are small losses in the presence of RF currents. The Cooper pairs posses inertia and at microwave frequencies they are unable to screen the external fields completely from the normal electrons. Although, Eq. 7.24 predicts that the surface resistance goes to zero at $T = 0$ K, measurements reveal

$$R_s = A\frac{1}{T}f^2 e^{-\frac{\Delta(T)}{k_B T}} + R_0 \tag{7.25}$$

where Δ is the half the energy needed to break a Cooper pair, and A is a material dependent constant which is dependent on the penetration depth, coherence length, Fermi velocity, and the mean free path. R_0 is known as the residual resistance and can be affected by trapped flux and surface impurities. The operating temperature of the SRF cavities is usually chosen in the range where the BCS resistance dominates and the Carnot efficiency is tolerable.

7.4.3 Critical Fields

When considering superconducting materials for practical applications (for example SRF cavities), the maximum tolerable surface fields are of substantial interest. The ultimate theoretical limit is only posed by RF critical magnetic field beyond which the screening effect of the Cooper pairs is lost. Existing superconductors are classified as either Type I or II and differ in the surface energy between the normal and superconducting boundaries.

Type I superconductors have positive surface energy and remain in a Meisnner state up to a temperature dependent critical field H_c which is given by [64]

$$H_c(T) = H_c(0)\left[1 - \left(\frac{T}{T_c}\right)^2\right] \tag{7.26}$$

Type II superconductors such as niobium are different because of their negative surface energy of the interface. Therefore, it is energetically favorable for the flux to create an interface. Beyond a critical field H_{cl}, a mixed state of superconductor and normal conducting zones in periodic lattice is created which also referred to as vortices. The flux in the vortices is given by

$$\Phi_0 = \frac{hc}{2e} \tag{7.27}$$

The densities of the vortices increases with external magnetic field until the entire sample is normal conducting at a second critical field H_{c2}. For niobium, the choice of metal for SRF cavities, the theoretical critical field limit is approximately 2200-2400 Oe.

There are no theoretical limitations on the RF electric fields, but accelerating cavities are usually operated well below field level ($\sim$ 150 MV/m) to support the critical magnetic field. This is due to several reasons like thermal breakdown originating from surface defects, resonant electron multiplication or multipacting, field emission, and other phenomena which are studied in great detail in Refs. [63, 65].

7.4.4 Elliptical Multi-cell Cavities

The phenomenon of resonant electron multiplication in RF electric fields or multipacting results in absorption of RF power and eventually breakdown superconducting cavities. A more detailed treatment of multipacting can be found in Ref. [63]. The most successful solution proposed to reduce or eliminate multipacting was to use a spherical geometry to force the charges to drift to the equator [66]. At the equator, $E_\perp$ vanishes thereby reducing the number of secondaries and suppress multipacting. Modern SRF cavities are elliptical in shape due to mechanical stability requirements and ease of chemical treatment of the cavity surface compared to the spherical shape [67].

The quest for achieving higher gradients to maximize the "real-estate" gradient (or "MV/m") has lead to strongly coupled multi-cell cavities. These cavities can be viewed as coupled oscillators where each mode in a single cell cavity is split into a passband of normal modes. The length of each cell is chosen to be $\lambda/2$ so that the acceleration in the multi-cell cavity is maximized for the eigenmode in the TM_{010} passband with π phase advance between each cell.

Chapter 8

Ampere Class Energy-Recovery SRF Cavities

8.1 Introduction

Superconducting energy recovery linacs (SERLs) are increasingly becoming an attractive option for light sources, X-FELs, electron coolers and electron-ion colliders. SERLs show a potential to accelerate high current electron beams with high average current and brightness with ultra short bunches. The major challenge to accelerate high current beams is to overcome the dissipation of large amounts beam power into cavity modes making CW operation prohibitive. Fig. 8.1 shows a plot of average beam power deposited into an accelerating structure for some existing and future SERLs. The diagonal lines show contours of power normalized to a loss factor of 1 V/pC which is independent of accelerating structure used in the linac.

A five-cell superconducting cavity is under fabrication as a fundamental unit of the linac structure to accelerate the electron beam from 2.5 MeV to 54 MeV. This chapter focuses on the design and development of the first multicell cavity optimized for very high currents in an energy-recovery mode. HOMs excited by the beam can result in both single bunch (short range wakefields) and multi-bunch effects (long range wakefields) limiting the maximum charge per bunch and maximum current due to collective instabilities. The cavity design is optimized to suppress the effects of HOMs and increase the threshold currents beyond the ampere level. HOMs are studied in great detail to investigate their effects on the beam and the feasibility of accelerating high bunch charge ($>$ 20 nC) and high current ($>$ 1 A) beams. Measurements from a copper prototype of monopole and dipole modes are compared to simulations from numerical codes which show good agreement. Other important issues for superconducting cavities such as fundamental power coupler, multipacting, bellows shielding and Lorentz force detuning are also discussed.

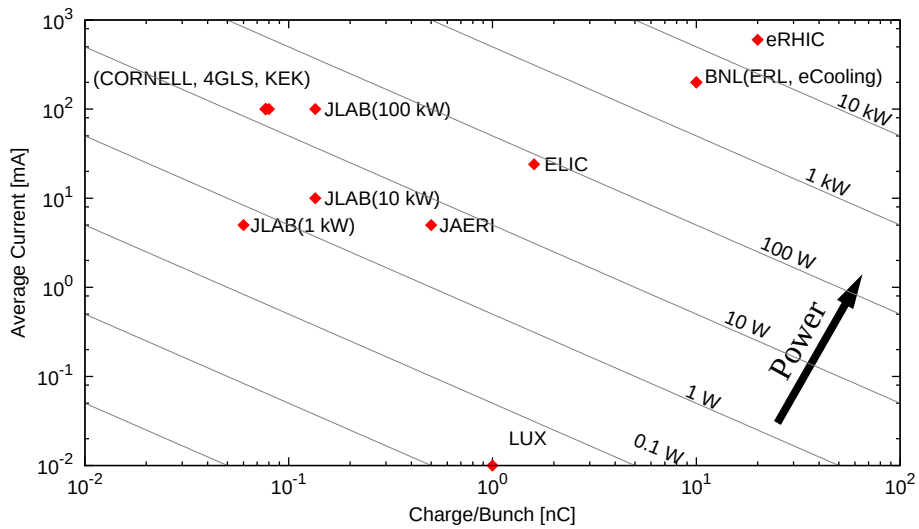

Figure 8.1: Average power dissipated due to single bunch losses in accelerating structures for exisiting and future SERLs. The diagonal lines represent the power contours normalized to a loss factor of 1 V/pC. Therefore, the power dissipated by the SERL facilities shown should be scaled to the actual loss factor of the accelerating structure used.

8.2 Cavity Design

The cavity design is greatly influenced by the operational modes of the linac. Several factors influenced the choice of key parameters of the cavity for high current energy recovery operation.

8.2.1 Frequency

A frequency choice of 703.75 MHz was made due to both physics and engineering issues. The precise frequency is the 25th harmonic of the RHIC bunch repetition frequency with 360 bunches. The power dissipated on cavity walls due to surface magnetic fields of the fundamental mode is proportional to

$$P \propto \frac{R_s}{\left(\frac{R}{Q}\right) G} \tag{8.1}$$

The surface resistance, $R_s = R_{BCS} + R_{res}$, where R_{BCS} is the BCS resistance of the superconductor ($\propto \omega^{1.8}$) and R_{res} is the residual resistance which is generally determined by the surface smoothness. Fig. 8.3 shows a plot of R_{BCS} as a function of temperature for three different frequencies that

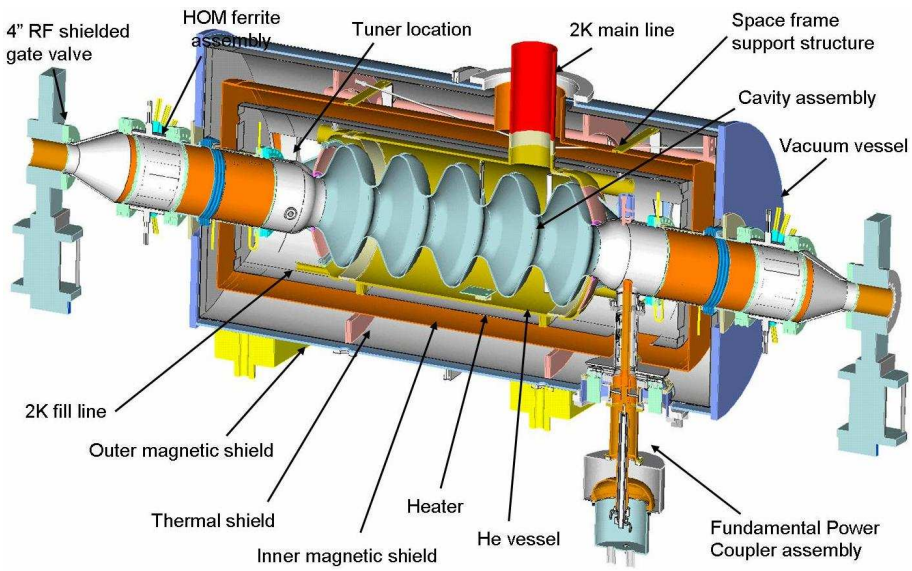

Figure 8.2: 3D cut away model of the five-cell cavity, cryostat, power coupler, ferrite absorbers, and feedthroughs (courtesy AES).

are widely used for superconducting linacs. If the R_{res} is sufficiently small ($\leq 1\ n\Omega$), a lower frequency significantly reduces cavity losses. If we assume that the cavity dimensions linearly scale with frequency, the factor $(R/Q)G$ is approximately constant for a constant number of cells, and therefore a lower frequency is preferable despite the increase in dimensions. However, the effective length of the linac decreases with increasing frequency which may help increase "real estate gradient" for long linacs.

A lower frequency allows a possibility of a large aperture resulting in a significant reduction of both longitudinal and transverse wakefields. This not only reduces HOM power deposited by the beam, but helps in raising the threshold current for the onset of multibunch instabilities in SERLs which are discussed in section 8.4 & 8.5. Availability of high power CW RF sources and compatibility with chemical cleaning facilities also played an important role to converge to 700 MHz region. A potential future use of this cavity in a linac-ring version of eRHIC was also considered.

8.2.2 Cavity Geometry

A parametrization developed in Ref. [68] for elliptical cavities to tune the shape for optimum electromagnetic and mechanical properties was used to design the cavity. The five-cell cavity is constructed from eight identical inner

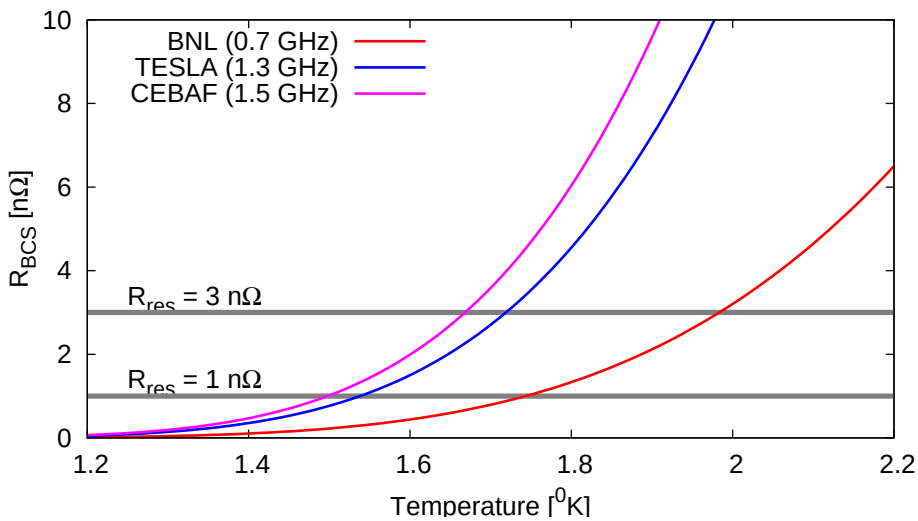

Figure 8.3: BCS surface resistance as a function of temperature for different operating frequencies. Here, the three frequencies correspond to the state-of-the-art SRF cavities being proposed or under operation in the energy recovery mode.

half cells and two end half cells. Each half cell can be described with the geometrical parameters shown in Fig. 8.4.

The geometrical parameters for the half cells were optimized using "Build Cavity", a graphics interface to Superfish [69]. The half-end cells are usually tuned separately for the freqency using the wall angle (α) or equator radius (D) to compensate for the beam tube. Several criteria like peak surface fields (E_{peak}/E_{acc}, B_{peak}/E_{acc}), shunt impedance (R/Q), cell-to-cell coupling (k_{cc}), and mechanical stiffness (dF/dR) were considered to optimize cell shape.

- Minimize peak surface fields, E_{peak}/E_{acc}, to avoid field emission at lower gradients and B_{peak}/E_{acc} to reduce surface losses or reach the magnetic breakdown limit. E_{peak}/E_{acc} is strongly dependent on the aspect ratio of iris ellipse (r), distance from cavity wall to iris plane (d), and iris radius (R_{iris}) as shown in Fig. 8.5(a), 8.5(b), and 8.5(c).

- A Large cell-to-cell coupling is important to avoid trapped HOMs especially in long structures. The coupling for the fundamental mode is mainly dependent on the iris radius (R_{iris}) as seen in Fig. 8.5(b), hence a large aperture is desirable. However, a larger iris does not always guarantee the best cell-to-cell coupling for all HOMs. Small irises should generally be avoided to reduce both the longitudinal and transverse loss

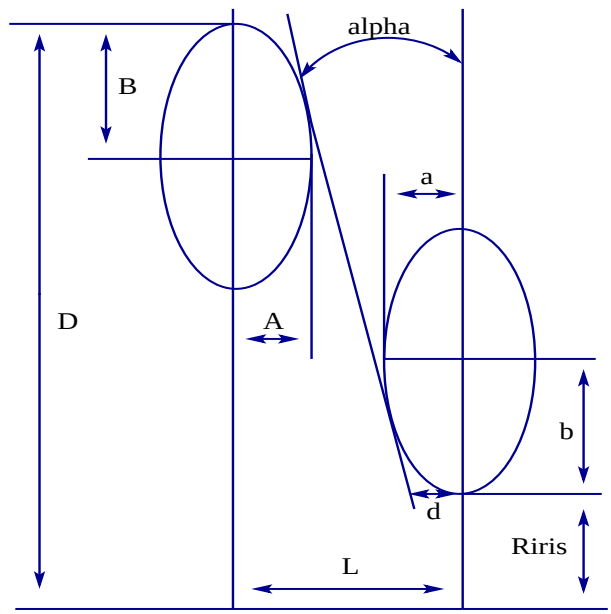

Figure 8.4: Parametrization of elliptical cavities.

factor. Other parameters like α, r, and d, were also optimized to maximize k_{cc}.

- Good mechanical stiffness to reduce the effects of microphonics and Lorentz force detuning while allowing a reasonable tuning capability. The equator aspect ratio (R_{eq}), α and d are dominating factors for mechanical stability. Larger α and d not only increase cavity stiffness but also helps in makes it easier for chemical treament of internal surfaces. However, larger wall angle also degrades k_{cc}, R/Q and H_{peak}/E_{acc} while improving E_{peak}/E_{acc} as seen Fig. 8.5(c).

- Minimize cavity wall losses by maximizing R/Q of the accelerating mode. R/Q decreases with a large aperture (Fig. 8.5 B), however extremely small surface resistance of SRF cavities allows one to significantly enlarge the aperture without much compromise. Therefore, HOMs are easily extracted through beam pipes even for multicell cavities.

The final optimized parameters describing the cavity geometry are listed in Table 9.4. An alternate design (BNL II) with modifications to α, d, and r is compared to the original design in Table 9.4. The main motivation for BNL II design was to reduce the cavity wall losses by increasing $\frac{R}{Q}G$. The cell-to-cell coupling and peak magnetic field were also improved at the cost of increasing

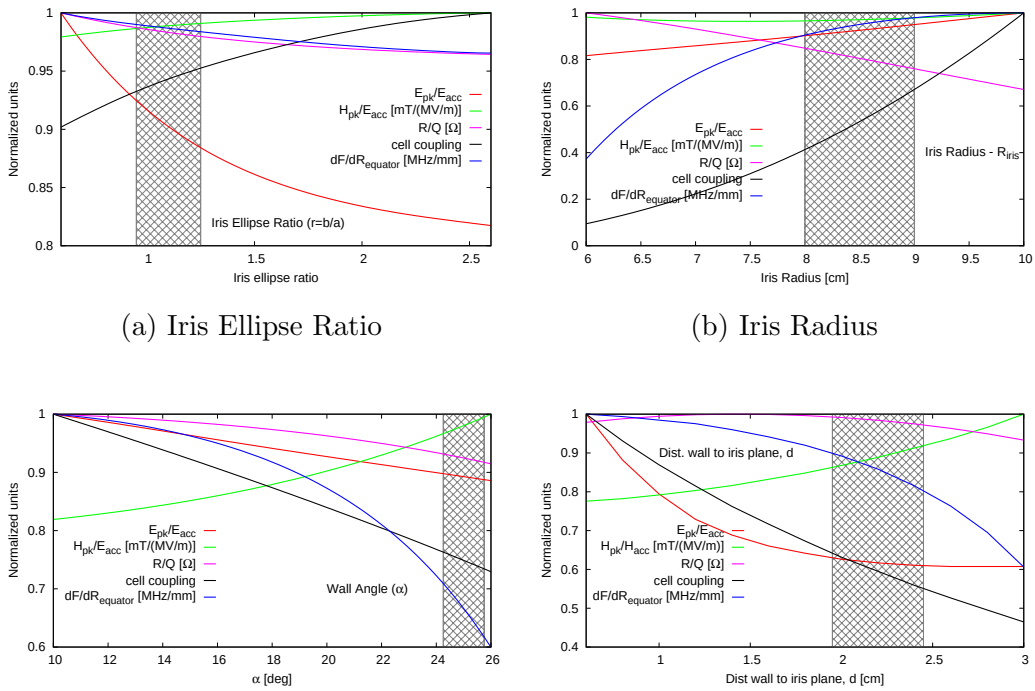

(a) Iris Ellipse Ratio

(b) Iris Radius

(c) Wall Angle

(d) Distance from wall to iris plane

Figure 8.5: Optimization of some relevant RF parameters as a function of each geomtrical tuning parameter. It should be noted that the tuning parameters are not completely independent of each other.

the peak electric field and reducing mechanical stiffness. Mechanical stiffners may become necessary to compensate the loss in stiffness for BNL II design. The inner half cell and half-end cell for BNL I & II are plotted in Fig. 8.6, and the relevant RF parameters are summarized in Table 8.2. A variant of BNL I design with the same middle cells and different end group is also shown in Fig. 8.6. The end group is tuned using the equator height (D) instead of the wall angle (α) unlike BNL I & II designs. Detailed analysis of these designs and some comparisons to the TESLA and CEBAF cavities are discussed in the follwing sections.

8.2.3 Number of Cells

Field flatness of the fundamental mode is an important factor to maximize the accelerating voltage and minimize surface fields for a given strored energy.

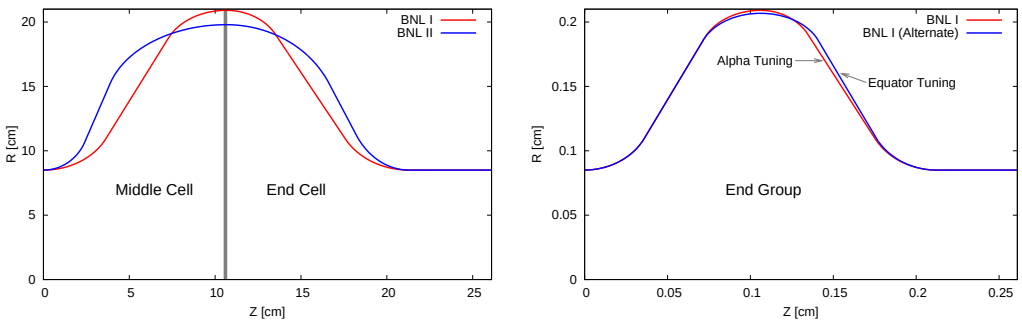

Figure 8.6: Final middle-cell and end-cell designs for five-cell cavity and an alternate design option, BNL II.

Table 8.1: Cavity geometrical parameters

Parameter	BNL I		BNL I-A	BNL II	
	Middle Cell	End Cell	Alt. End Group	Middle Cell	End Cell
Frequency [MHz]	703.75	703.75	703.75	703.75	703.75
Iris Radius, R_{iris} [cm]	8.5	8.5	8.5	8.5	8.5
Wall Angle, α [deg]	25	26.64	25	18	21.6
Equatorial Ellipse, $R = \frac{B}{A}$	1.0	1.1	1.0	0.9	1.2
Iris Ellipse, $r = \frac{b}{a}$	1.1	1.1	1.1	1.4	1.6
Dist. from cavity wall to iris plane, d [cm]	2.5	2.5	2.5	1.7	1.7
Half Cell Length, $L = \frac{\lambda\beta}{4}[cm]$	10.65	10.65	10.65	10.65	10.65
$H = D - (R_{iris} + b + B)[cm]$	4.195	4.160	3.792	1.254	-2.456
Cavity Beta, $\beta = \frac{v}{c}$	1.0	1.0	1.0	1.0	1.0

A figure of merit that determines the acheivable field flatness for multicell cavities can be expressed in terms of a field sensitivity factor given by

$$a = \frac{N^2}{\beta k_{cc}} \tag{8.2}$$

where N is the number of cells, $\beta = v/c$, and k is the cell-to-cell coupling. Larger a values limit the maximum achievable field flatness and make it more sensitive to mechanical tolerances. Table 8.2 shows a comparison of the field sensitivity factor for the BNL designs and are also compared to the TESLA and CEBAF cavity shapes.

Ampere class cavities require strong HOM damping ($Q_{ext} \leq 10^4$) due to large HOM power and multibunch effects that limit the maximum acheivable current. Since HOM extraction and damping in SRF cavities is constrained to the exterior of the structure, propagation of HOMs to the outside the cavity is imperative. Fig. 8.7 show an illustration of trapping an HOM in the interior cells as the number of cells is increased from 5 to 17. The increase in the number of cells gradually decreases the field in the end cells and beam pipe

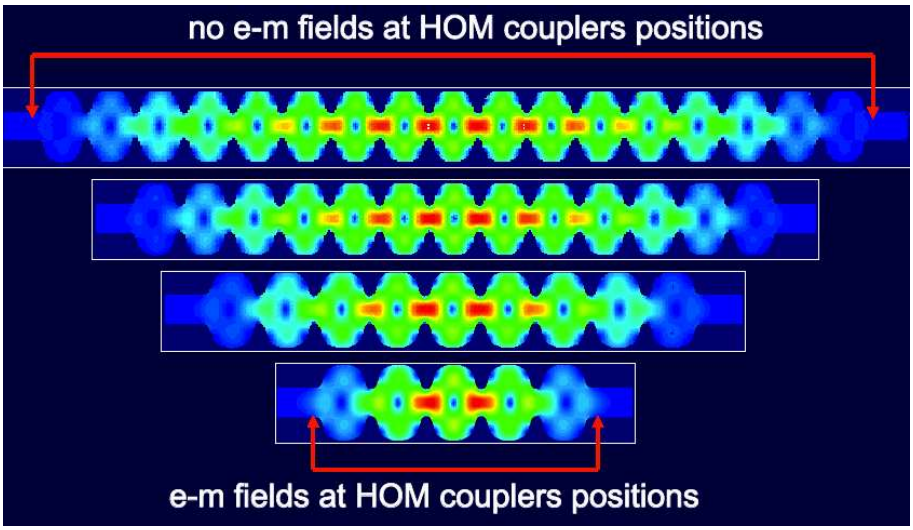

Figure 8.7: Effect of the number of cells on HOM propogation. Increase in number of cells causes the field of the HOM to be confined in the middle cells and makes it difficult to couple them out to a beam pipe load or HOM coupler.

making it impracticle to extract and damp the HOM. Fewer cells with large k_{cc} not only improves field sensitivity factor for the fundamental mode but also help in achieve strong HOM damping. However, the active length of the linac is reduced. Therefore, five cells were chosen to be an optimum number to able to achieve effective damping while maintaining a reasonable accelerating gradient.

8.2.4 Beam Pipe Ferrite Absorbers

The beam pipe is a natural high pass filter and can be efficiently used to propagate HOMs to a load outside the cryogenic environment. Ferrite absorbers were the choice of HOM load because of their capability to absorb large HOM power and effective broadband damping with a simple and robust design. These absorbers are placed in the warm section (300 K) to minimize cryogenic losses.

Several highly lossy materials like C-48, Ferrite-50, and TT2-111V have proven to be excellent microwave absorbing materials (0.01-10 GHz) [72, 73]. A ferrite layer on a section of the beam pipe acts as a broadband HOM load. These absorbers have proven to be very successful in storage rings with single cell cavities (CESR & KEK-B). Fig. 8.8 shows a picture of ferrite assembly with "porcupine like" protrusions for water cooling [74, 75]. These absorbers

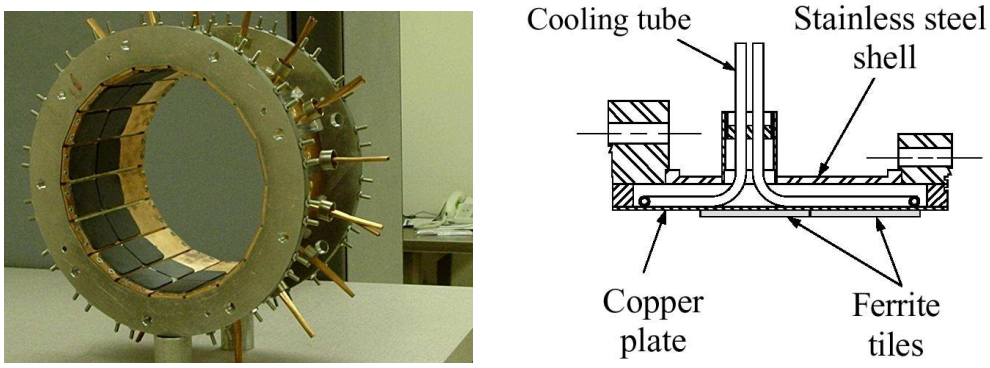

Figure 8.8: Ferrite absorber assembly [73]. The ferrite tiles are attached in copper plates provided with water cooling pipes. These plates are mounted on a stainless steel waveguide which is UHV compatible and assembled in class 100 clean room [74].

have been tested upto 15 kW or higher and may become the only viable and effective option for high power beams.

8.2.5 HOM Loop Couplers

A possibility of using TESLA type loop couplers for HOM damping was also considered in conjunction with the ferrite dampers. The loop couplers are required for TESLA type high "real-estate" gradient cavities with some HOMs that do not propagate along the beam pipe. They are placed very close to the cavity end-cell at superconducting temperatures to couple to the HOM fields in the end cell. However, they pose severe problems for high-current cavities due to extraction of large HOM power with a carefully tuned resonant circuit. Technical issues like the error in the notch frequency [76] and the temperature of the pick up probe [77] can lead to large cryogenic losses making it an undesirable candidate. Neverthless, a 3D model of the HOM loop coupler is designed for testing purposes in the five-cell cavity with the notch filter optimized for 703.75 MHz as shown in Fig. 8.9.

8.2.6 Beam Pipe Geometry

The damping of HOMs with ferrite absorbers require all mode frequencies above fundamental passband be sufficiently larger (> 20 MHz[1]) than cutoff

[1]The propagation (or attenuation) depends on the beam pipe length and diameter.

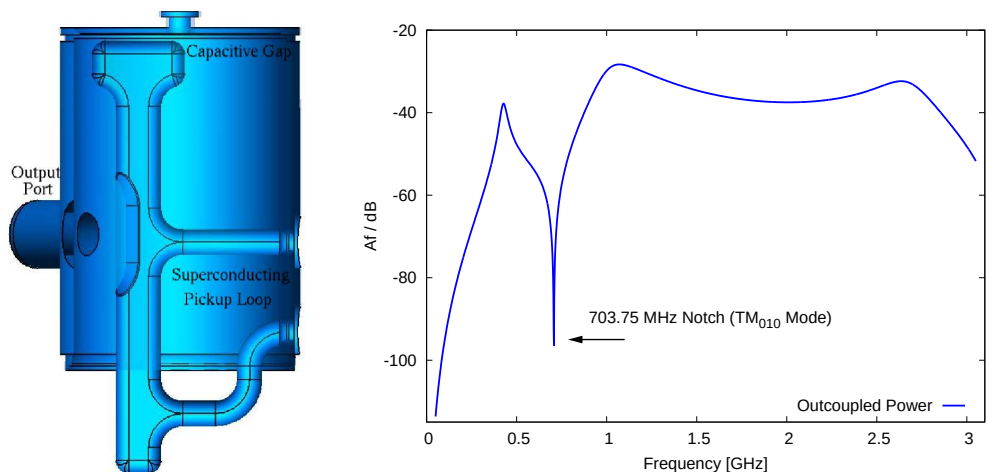

Figure 8.9: Cut away view of 3D model of the HOM loop coupler tuned for notch filter at 703.75 MHz (3D model courtesy AES).

frequency of the beam pipe. The cutoff frequency for a cylindrical waveguide is given by

$$f_c = \frac{c}{\pi D} X \tag{8.3}$$

where c is the speed of light, D is the diameter of the beam pipe, and X is the root of the Bessel function or its derivatives as appropriate. Fig. 8.10 shows plot of aperture size as a function of cutoff frequency for the first few monopole, dipole and quadrupole modes. For example, crossing of the vertical and horizontal line representing the frequency and beam pipe diamter is lower than the cut-off frequency line for TM_{011} implying that it is below cut-off. However, the crossing for TE_{111} is above the cut-off curve implying it is propagating into the beam pipe.

The beam pipe diameter was chosen such that the lowest monopole and dipole passband frequencies are well above their cutoff frequency. Fig. 8.11 shows a schematic of the end cell and beam pipe transition geometry. The transition consists of two elliptical sections of 5 cm each to gradually expand from a 17 cm iris to 24 cm beam pipe diameter. This enlargement causes an increase in the "leakage" of the fundamental mode field into the beam pipe, subsequently increasing cryogenic losses. A superconducting niobium transition is placed between cavity iris (2K) to the copper beam section ($\geq$ 5K) to minimize losses in normal conducting metals ($\leq$ 10 watts). A smooth transition of 10 cm from 17 cm to 24 cm aperture also reduces short range wakes from abrupt transitions. The cold to warm section of the beam pipe is equipped with a spiral channel for 5K helium gas flow to heat transfer the RF

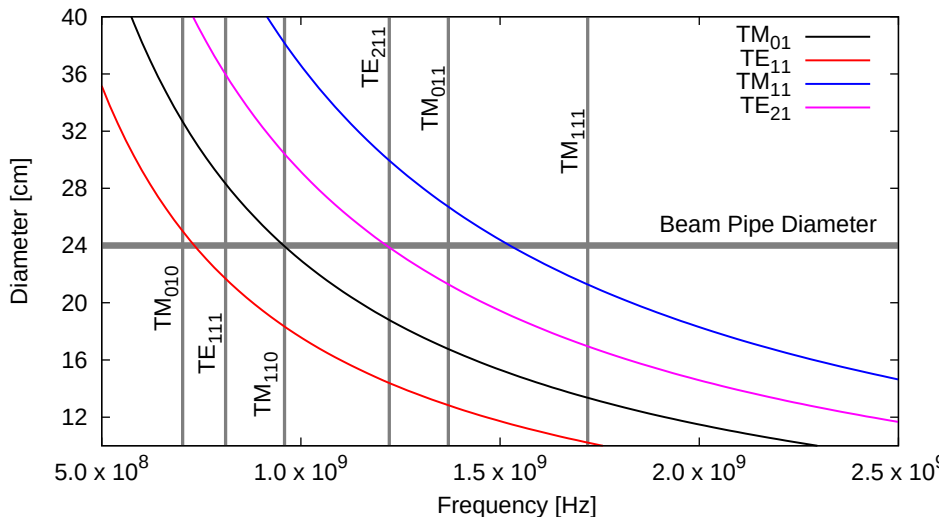

Figure 8.10: Cutoff frequencies of different types of modes in a cylindrical waveguide of a given diameter plotted as a function frequency. The vertical lines are frequencies of different modes for the five-cell cavity which may or maynot propogate depending on if they are above or below the cutoff.

losses in the beam pipe. Two sets of unshielded bellows (see Appendix D.3) are placed on the beam pipes to allow longitudinal and vertical motion during different phases of the cavity manufacturing and operation.

8.2.7 Final Design

A graphic of the final design of five-cell SRF cavity along with the coaxial fundamental power coupler (FPC) is shown in Fig. 8.12. Two full-size copper prototypes are manufactured to measure several properties of the cavity including field flatness, coupling, and most importantly HOM damping. Fig. 8.13 shows a comparison of calculated and measured field profile for the fundamental mode of the 5 cell cavity. The "moderatly" tuned copper prototype yields a field flatness of $96 \pm 1\%$ which agrees extremely well with electromagnetic (EM) codes giving 96.5%. The beam pipe enlargment causes additional leakage of the field resulting in a reduction in the field flatness. This reduction can be easily compensated by tuning the end cells. Some relevant RF parameters of the final design are listed in Table 8.2 and compared to BNL II, TESLA and CEBAF designs.

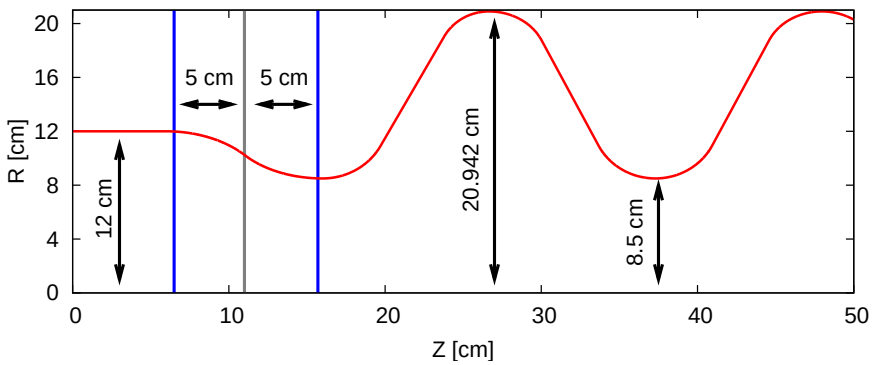

Figure 8.11: Beam pipe transition section consisting of two ellipses to transition from 17 cm iris diameter to a 24 cm beam pipe. The length of the transition section was determined to reduce the leakage of the fundamental into the beam pipe and also minimize the loss factor.

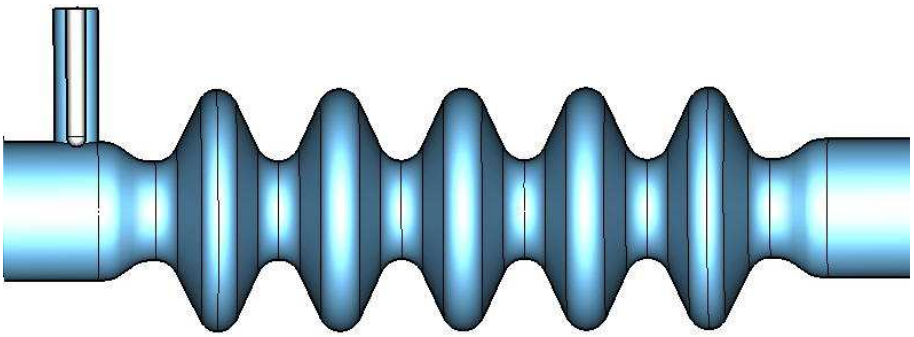

Figure 8.12: Graphic of the final design of the five-cell cavity, beam pipe transition and the coaxial FPC.

8.3 Higher Order Modes

The complex structure of multi-cell cavities can often lead to trapped modes which can be excited by the beam, leading to large HOM power and in some cases invoke beam instabilities. The three main causes of trapped modes are:

- Large number of cells trapping HOMs in the middle cells as discussed in section 8.2.3 and in Fig. 8.7.
- Small irises resulting in small cell-to-cell coupling thus trapping a mode. However, large irises can reduce R_a/Q_0 of the fundamental mode which is also undesirable (section 8.2.1).

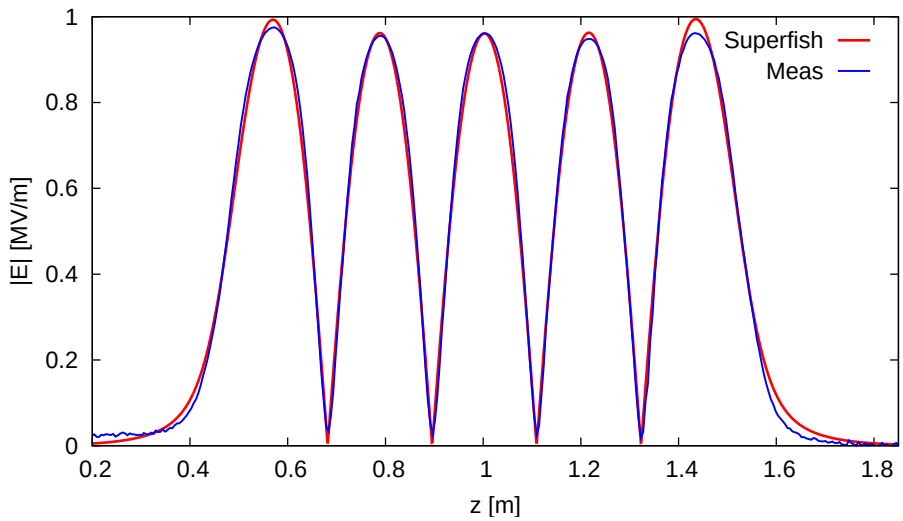

Figure 8.13: Field flatness of the fundamental mode peak-peak 96.5%.

- The presence of the beam pipe can result in an end cell geometry which significantly different from the middle cells. This can lead to a large deviation in the frequency of an HOM between the middle and the end cells. If this deviation is sufficiently large, the two cells are unable to resonate together thus trapping the mode. A simple example of an HOM in a TESLA cavity is compared to an HOM in BNL I cavity to illustrate the effect of a large frequency deviation.

- HOMs below the cut-off frequency of the beam pipe exponentially decay, and do not propagate into the beam pipe. The beam pipe diameter is enlarged to propagate all HOMs while staying sufficiently below the cutoff of the fundamental as illustrated in Fig. 8.10.

It is essential to study the behavior of HOMs and identify potentially trapped modes and damp them sufficiently. The following sections will focus primarily on the characteristics of monopole and dipole modes and their effects on the beam for the five-cell cavity. Comparisions to BNL II, TESLA, and CEBAF shapes are also made where appropriate.

8.3.1 Shunt Impedance and Quality Factor

Each HOM can be characterized by its shunt impedance R_a/Q_0 and a quality factor Q. R_a/Q_0 characterizes beam power deposited into a particular HOM excited by the beam. It is independent of the surface resistance of the

Table 8.2: RF Parameters for final design of BNL I cavity compared to an alternate BNL II, TESLA, and CEBAF cavities. NE - Not estimated.

Parameter	Unit	BNL 1(HC)	BNL 2 (HC)	CEBAF(HG)	TESLA(HG)
Frequency	[MHz]	703.75	703.75	1497	1300
Number of cells	-	5	5	7	9
$(R/Q) * G$	$[\Omega^2]$	9×10^4	9.58×10^4	2.1×10^5	2.8×10^5
E_p/E_a	-	1.97	2.25	1.96	1.98
H_p/E_a	$[mT/MV/m]$	5.78	4.88	4.15	4.15
Cell to cell coupling (k_{cc})	-	3%	4.45%	1.89%	1.87%
Sensitivity Factor ($\frac{N^2}{\beta k_{cc}}$)	-	8.3×10^2	5.6×10^2	2.6×10^3	4.1×10^3
Field Flatness	-	97.2%	97.3%	97.5%	95 %
Lorentz detuning coeff.	$[Hz/(MV/m)^2]$	1.28 (UnStiff)	NE	2	1

metals and is given by

$$\left(\frac{R}{Q}\right)_n = \begin{cases} \dfrac{|\int_0^d E_z e^{ik_n z} c dz|^2}{\omega_n U_n} & : \ monopole \ [\Omega] \\ \dfrac{|\int_0^d E_z(\rho{=}a) e^{ik_n z} c dz|^2}{(k_n a)^2 \omega_n U_n} & : \ dipole \ [\Omega] \end{cases} \tag{8.4}$$

where $k_n = \omega_n/c$ is the wave number of the mode with a frequency ω_n and stored energy U_n. Perturbation techinques can be used to measure R_a/Q_0, but numerical codes like MAFIA [78] are accurate and far less tedious. Fig. E.1 shows a computation of the $R/Q's$ for monopole and dipole modes upto 2.5 GHz. The R_a/Q_0 for just the fundamental mode is measured using the bead pull technique (see appendix D.1) using three different perturbing objects and results are compared to simulations in Table 8.3.

Table 8.3: Measurement of R_a/Q_0 using spherical beads. R/Q determined from MAFIA calculation is **403.5** Ω.

Material	R [mm]	R_a/Q_0 $[\Omega]$
Teflon	4.77 ± 0.02	474 ± 10
Steel	3.96 ± 0.01	532 ± 20
Aluminum	2.5 ± 0.01	370 ± 10

Microwave surface resistance of superconducting materials such as niobium are several orders of magnitude smaller than conventionally used copper. Therefore, the power dissipation in an SRF cavity wall is also small and can be

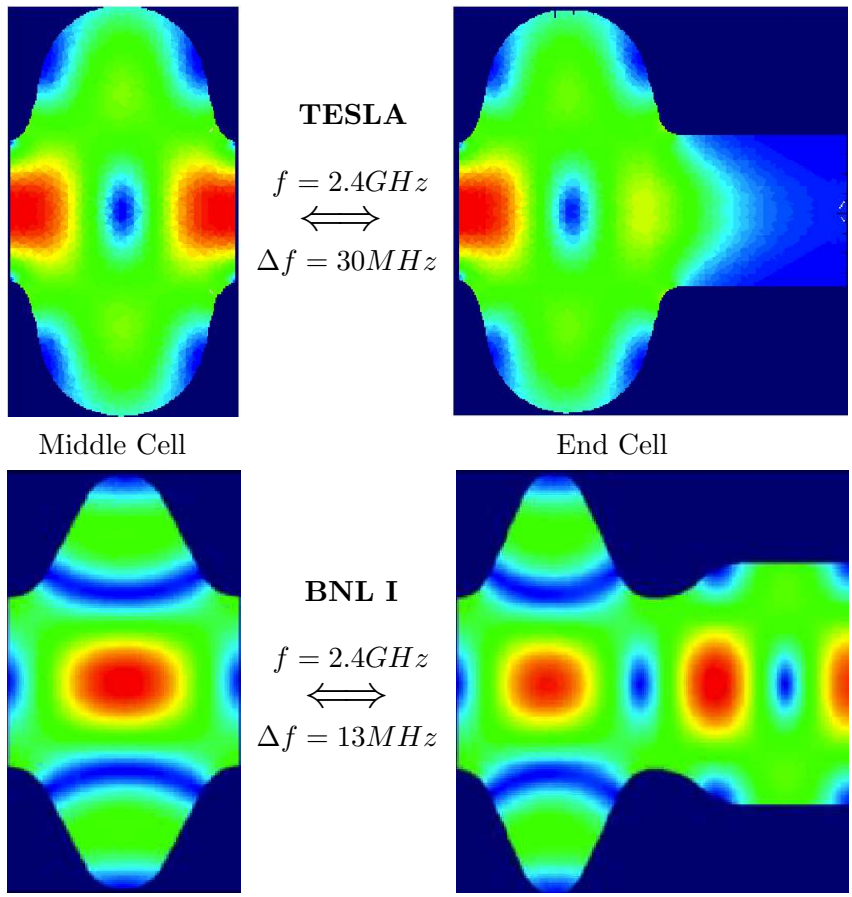

Figure 8.14: Illustration of trapped mode due to large difference in the frequency of the HOM between middle and end cell. The large difference prevents them from resonating together thus trapping the mode.

characterized by a high intrinsic quality factor, Q_0 given by Eq. 7.20. Typical Q_0 values of SRF cavities range anywhere between $10^9 - 10^{11}$. Since the power is dissipated partly in the cavity walls, and partly through beam pipe load, we define an effective Q_{tot} [2]

$$\frac{1}{Q_{tot}} = \frac{1}{Q_0} + \frac{1}{Q_{ext}} \tag{8.5}$$

For modes below the cutoff frequency the Q_{tot} is dominated by the cavity Q_0 (wall losses) and for modes propogating through the beam tube, Q_{ext} (load)

[2]Note that there is also power dissipated into the beam pipe walls and can be associated to Q_{ext} for modes below cut-off. For modes above cut-off, this can be neglected since the Q_{ext} is dominated by the external load.

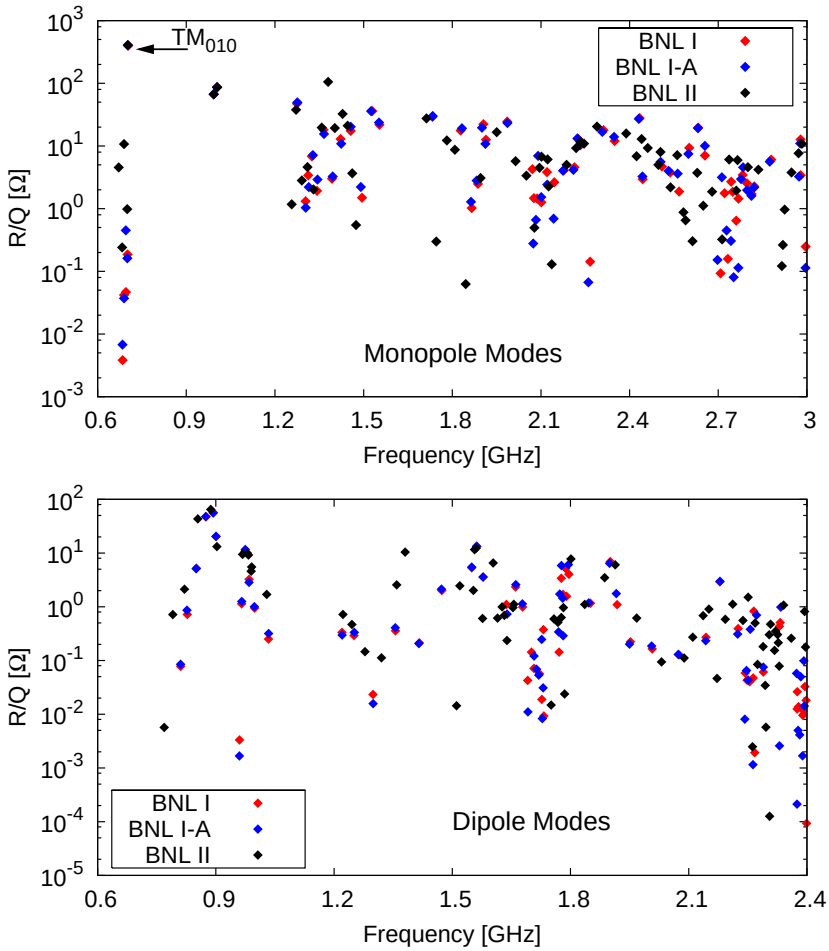

Figure 8.15: Shunt impedance (R/Q) calculated using MAFIA for monopole and dipole modes upto 2.5 GHz.

becomes the dominating factor. Numerical codes in frequecy and time domain are commonly used to estimate these high Q_0 factors of HOMs in superconducting cavities. However, numerical calculations are prone to errors and measurements can aid in benchmarking simulations. Boundary conditions play an important role in accurately determining HOM fields in a cavity and their propogation into beam pipe. Two different approaches will be discussed in detail and compared to measurements on a copper prototye.

8.3.2 HOMs: Frequency Domain

The conventional technique to identify possible trapped modes involves computation of the eigenmodes with two different boundary conditions at the beam tube termination [79]: electric wall or short-circuited transmission line ($\hat{n} \times \vec{E} = 0$) and magnetic wall or open-circuited transmission line ($\hat{n} \times \vec{H} = 0$). The influence of boundary conditions (BC) on the frequency can be used to infer the coupling of the mode to the beam pipe.

$$\kappa = 2\frac{|f_{mag} - f_{ele}|}{f_{mag} + f_{ele}} \tag{8.6}$$

$$\frac{1}{\kappa} \approx \begin{cases} 1 & : \quad untrapped \\ \infty & : \quad trapped \end{cases} \tag{8.7}$$

Fig. 8.16 shows a comparison of $\frac{1}{\kappa}$ as a function of frequency for the three designs for both monopole and dipole HOMs. For both longitudinal and transverse modes, BNL I and II show slightly different behavior but on average reveal coupling values of the same order of magnitude. For monopole modes, the $1/\kappa$ values are smaller than 10^3 with a majority of them below the 10^2 level. Therefore, we expect all the monopole HOMs to propogate through the beam pipe and be damped by the ferrite absorbers. Note that the fundamental mode is not shown in the plot since it is evanacent with $1/\kappa \approx \infty$. In the case of dipole modes, we see a few distinct bands with relatively higher values than the rest. BNL I show lower values for the 1st and 2nd passband, but have higher values for the $5^{th} - 7th$ pass band compared to BNL II design. It must be noted that lower frequency trapped modes are potentially more dangerous as the beam is more effective in exciting modes within its frequency spectrum ($\omega \sim \frac{1}{\sigma_z}$).

Another illustrative technique to study HOMs is to represent mode frequencies as a function of their phase advance per cell through dipersion curves. Although strictly valid for infinitely periodic structures, dispersion curves can also be calculated for finite structures by defining a corresponding function dependent on the longitunidal position to form a passband of modes. The slope of the dispersion curves represent the group velocity ($d\omega/dk$) of the passbands in an infinitely periodic structure. The dispersion curves can be calculated using numerical codes for a single cell with periodic boundary conditions

$$\hat{E}(r, z + L) = \hat{E}(r, z)e^{i\phi} \tag{8.8}$$

where $L = \lambda\beta/2$ is the cell length, and ϕ is the phase advance per cell. The dispersion curves for a periodic structure (BNL I) along with the dispersion

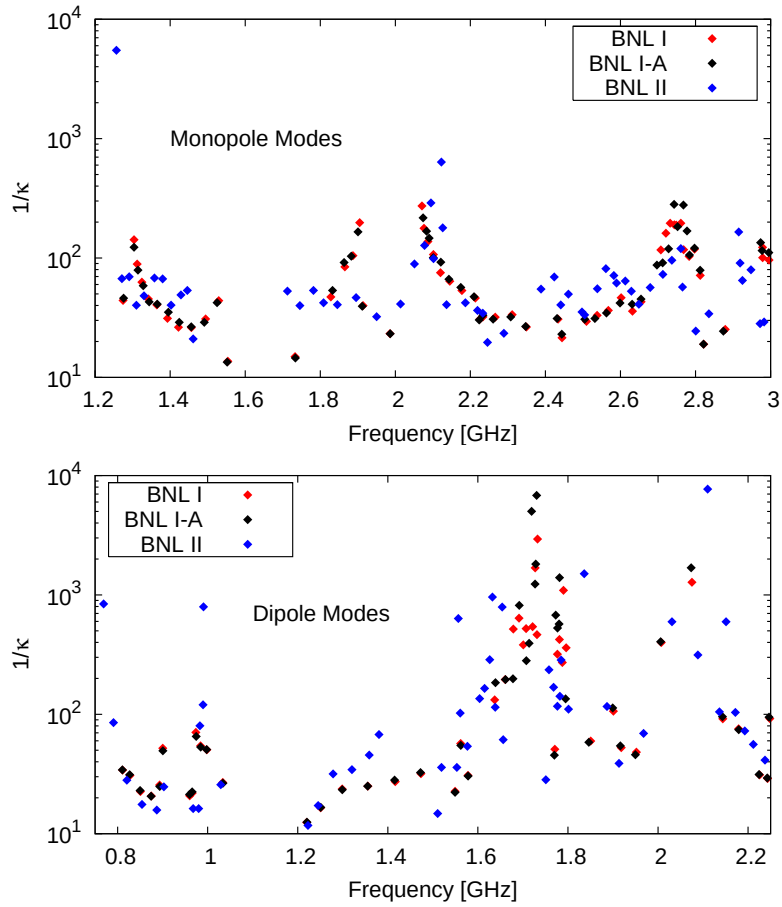

Figure 8.16: A coupling parameter κ shows the influence of the BC on the frequency of the mode. κ can be used identify possible trapped modes in the cavity.

curves for the five-cell cavity is shown in Fig. 8.17 for both monopole and dipole modes. The phase advance per cell for a finite number of cells can be determined from

$$\phi(z) = \arccos\left(\frac{E_z(r, z + L_{cell}) + E_z(r, z + L_{cell})}{2E_z(r, z)}\right). \tag{8.9}$$

The solid black line represents the light cone ($f_\phi = \frac{\phi c}{2\pi L}$) folded into the phase region between 0 to π.

The beam strongly excites modes that are synchronous to the beam, or simply modes with phase velocities equal to the speed of light ($v_\phi = c$). For monopole modes a select few in the $4^{th} - 8^{th}$ passbands are relatively close

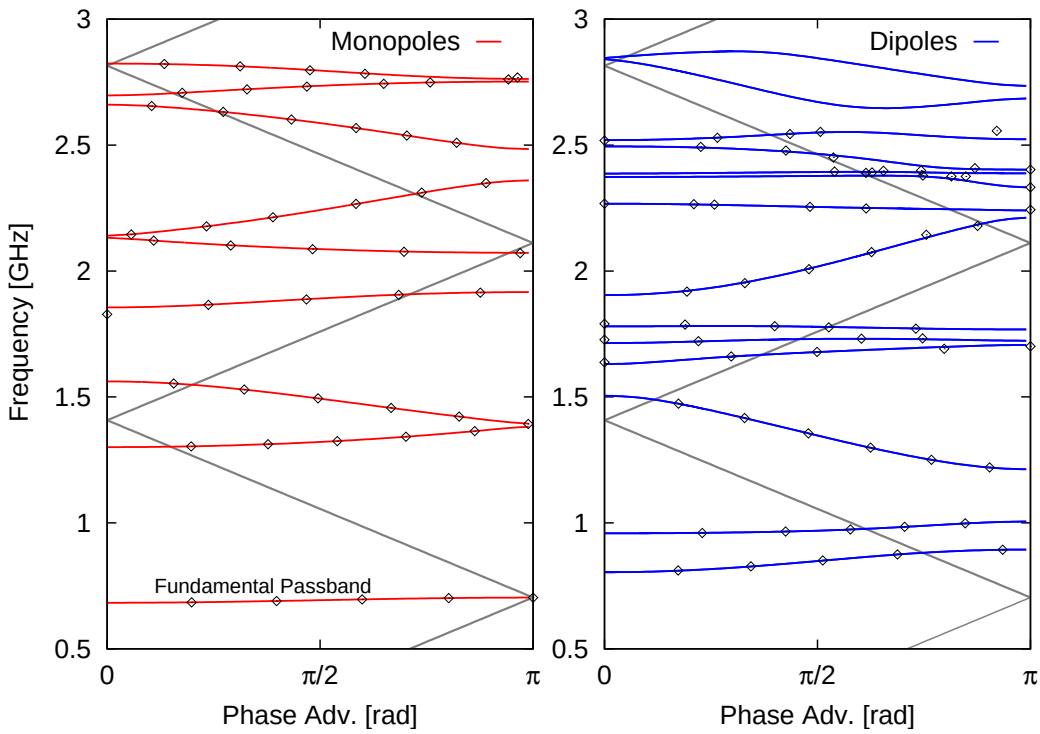

Figure 8.17: Dispersion curves of monopole and dipole modes for an infinite periodic structure along with the five-cell cavity (BNL I) for monopole (left) and dipole (right) modes. The black line is the light cone folded into the phase range from 0 to π.

to the light cone but none are exactly synchronous. It is interesting to note that successive passbands have alternating slopes and hence a symmetric beam pipe transition with ferrites on both sides of the cavity will be most effective in damping all higher order monopoles. In the dipole case, the 6th passband has a potentially synchronous mode with a frequency 1.78 GHz, and possibly some more modes above the 10th passband. A flat dispersion curve can make selective tuning of a single mode in the passband very difficult. This is particularly important for the fundamental passband where the accelerating modes is tuned continously to counteract Lorentz forces. The 5th and the 6th passbands have relatively flat dispersion curves, which may indicate to potentially trapped modes.

The most direct measure of a trapped HOM is to determine the external quality factor (Q_{ext}) of the mode which also ultimately sets the thresholds for the onset of beam instabilities. Numerical codes (like MAFIA) in frequency

domain formulated as a complex eigenvalue problem can be used to estimate $Q's$ of HOMs. The Q factor is given by [79, 78, 80].

$$Q_{ext} = \frac{1}{2}\frac{Re(f)}{Im(f)} \tag{8.10}$$

Since the damping is mainly due to beam pipe ferrites, it is important to include dissipative materials (complex ϵ and μ) in the simulation which are feasible in codes like MAFIA. However, highly dissipative materials like ferrites lead to long computational time and tend to cause the solutions to diverge or result in large errors. Therefore, calculations of Q_{ext} are restricted to small values of imaginary ϵ and μ (see Table 8.4). This approximation at worst should yield an upper limit to the Q_{ext} of HOMs. Although, numerical codes

Table 8.4: Lossy properties of ferrrite-50, C-48, and those used in MAFIA calculations. Note that values of the ϵ and mu are estimated from data in Refs. [73, 81]. The exact values are both both frequency and temperature dependent which are not taken into account in the calculation.

	C-48	Ferrite-50	MAFIA
ϵ_{Re}, ϵ_{Im}	(14.0, -1.5)	(12, -11.0)	(10.0, -1.0)
μ_{Re}, μ_{Im}	(2.0, -10.0)	(0.3, -1.0)	(2.0, -1.0)

have continually become better, it is customary to fabricate a copper prototype which is a useful tool to make several measurements and validate simulations. The prototype also aids as a learning tool in the fabrication process of complicated elliptical structures, and identify any pitfalls in the design of the cavity and its components. Fig. 8.18 shows the prototype of the five-cell cavity used to measure the Q_{ext} of HOMs upto 2.2 GHz. The cavity is placed in a tuning fixture which is used to tune individual cells for frequency and field flatness.

A comparison of simulations and measurments of Q_{ext} for modes upto 2.2 GHz is shown Fig. 8.19. In general the agreement between the simulations and measurements are quite good despite of the large difference in the lossy properties of ferrites in the simulations. The Q_{ext} for monopole modes are in the order of 10^3 or smaller. The agreement for dipole modes are exceptionally good, and in most cases the simulations show an upper limit as expected. The Q_{ext} values range between $10^2 - 10^4$ which are 2-3 orders of magnitude smaller than the currently state-of-the-art TESLA or CEBAF cavities. These small Q_{ext} values are needed to raise instability thresholds from milli-ampere to the ampere level and beyond. It must be noted that the measurements were done

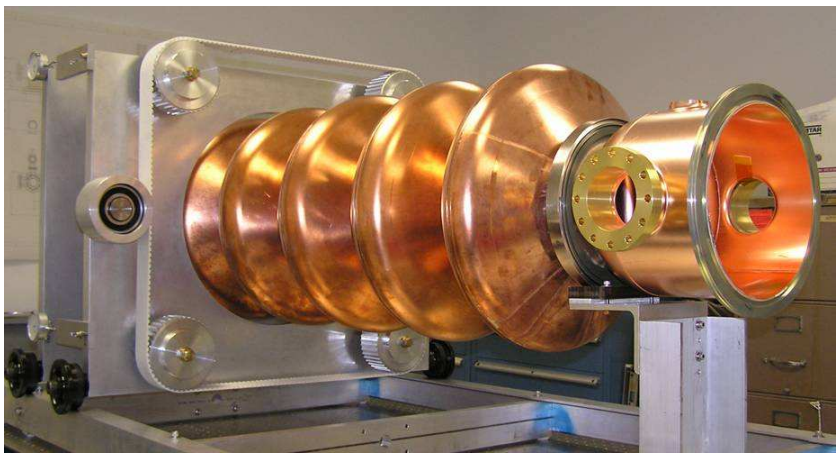

Figure 8.18: Full scale copper prototype used to measure Q_{ext} of HOMs the prototype ferrites (Fig. 8.8). The outer frame setup is the tuning fixture which will also be used to tune the final Nb cavity to 703.75 MHz.

using a single ferrite placed on either side and Q_{ext} was determined using

$$\frac{1}{Q_{ext}} = \frac{1}{Q_{left}} + \frac{1}{Q_{right}} \tag{8.11}$$

For modes with $Q_{L/R}$ in the noise level due to an asymmetric field distribution with respect to the cavity center, the Q from the side with the higher value was used as a pessimistic upper limit. Hence, a few measurements show larger values than the simulation, but in actuality are significantly smaller with symmetric ferrites on both ends.

More detailed simulations comparing an earlier geometry to BNL I design, and several numerical aspects such as mesh size, lossy properties of the ferrite, and comparison to other numerical codes were discussed in [111].

8.3.3 HOMs: Time Domain Method

In the frequency domain, one is limited to analyzing cavity modes with closed boundary conditions. This constrains one to rely on techniques described above to study HOMs and their effects. However, finite difference (or finite integration) time domain techniques allow one to simulate a real beam traversing any arbitary structure and the possibility of an infinite waveguide. The boundary is defined as perfectly matched layer with

$$\vec{\nabla} \times \vec{E} = -i\omega\mu\vec{H} - \sigma_M\vec{H} \tag{8.12}$$

$$\vec{\nabla} \times \vec{H} = -i\omega\epsilon\vec{E} - \sigma_E\vec{E} \tag{8.13}$$

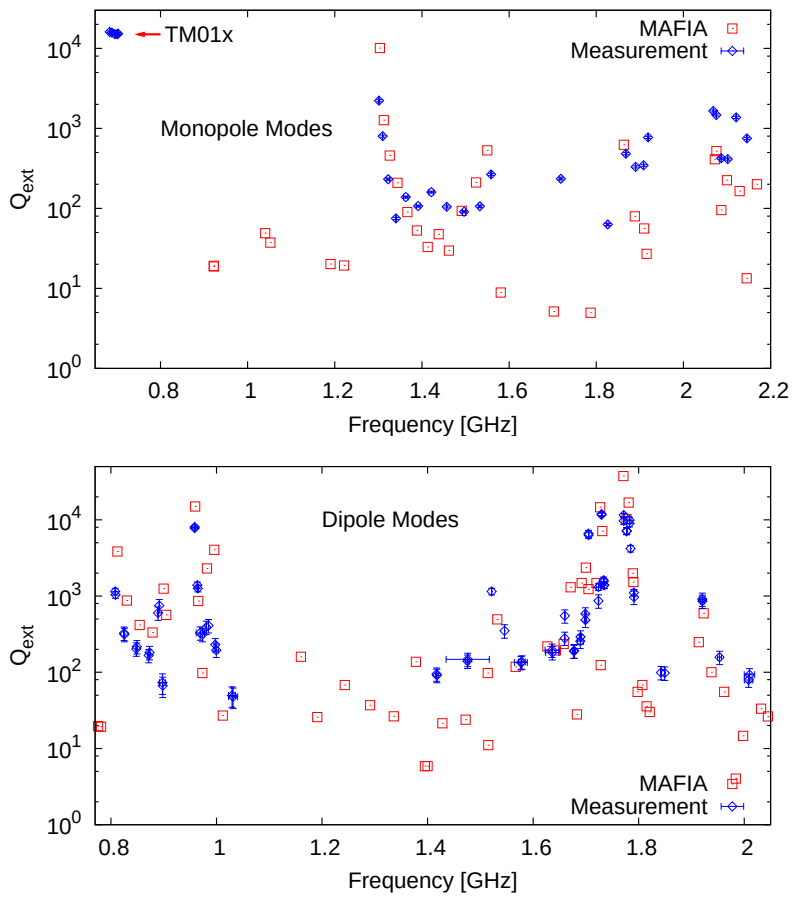

Figure 8.19: Top: Comparison of calculated and measured values of Q_{ext} for monopole modes (top) and dipole modes (bottom) upto 2.2 GHz.

where σ_E and σ_M are the electrical and magnetic conductivity and

$$(\vec{\epsilon}, \vec{\mu}) = (\epsilon_0, \mu_0) \left[\Lambda_{(\epsilon,\mu)} + \frac{\Sigma_{(E,M)}}{i\omega} \right] \tag{8.14}$$

are complex 3×3 matrices of permittivity, permeability and conductivity in the three dimensions [82]. These layers (or ports) allow waves above the cut-off frequency of the waveguide to propagate without any reflections at all incident angles. It is usually of interest to study the effect of the fields generated by a leading charge on a trailing particle which is commonly refered to as wakefields. The integrated effect of fields gives the longitudinal or transverse

wake potentials which are given by [83, 84]

$$W_{||}(\vec{r},s) = -\frac{1}{q}\int_{-\infty}^{\infty}[E(\vec{r},z,(s+z)/c)dz \tag{8.15}$$

$$W_{\perp}(\vec{r},s) = \frac{1}{q}\int_{-\infty}^{\infty}[\vec{E}_{\perp}+c\ (\hat{e}\times\vec{B})]dz \tag{8.16}$$

The broadband impedance spectrum of the structure can be directly obtained from a Fourier transform of the wake potential normalized by the bunch spectrum $\rho(\omega)$ which is given by

$$Z_{||}(\omega) = \frac{1}{c\rho(\omega)}\int_{-\infty}^{\infty}W_{||}(\vec{r},s)e^{-i\frac{\omega}{c}s}ds \tag{8.17}$$

$$Z_{\perp}(\omega) = -\frac{i}{c\rho(\omega)}\int_{-\infty}^{\infty}W_{\perp}(\vec{r},s)e^{-i\frac{\omega}{c}s}ds \tag{8.18}$$

Since, the longitudinal and transverse wake potentials are related by the Panofsky-Wenzel theorem [85], the impedances are also related in the frequency domain as

$$\frac{\omega}{c}\ Z_{\perp}(\vec{r},\omega) = \nabla_{\perp}\ Z_{||}(\vec{r},\omega) \tag{8.19}$$

where $\nabla_{\perp} = \frac{\partial}{\partial r}\hat{r} + \frac{1}{r}\frac{\partial}{\partial\phi}\hat{\phi}$. In numerical codes like MAFIA, a Gaussian bunch with a charge density

$$\rho(s) = \frac{1}{\sqrt{2\pi}\sigma}e^{-\frac{(s-s_0)^2}{2\sigma^2}} \tag{8.20}$$

and length σ_z traveling at the speed of light can be launched in the cavity center or off-axis with appropriate boundary conditions to excite longitudinal (monopole like) or transverse (dipole like) modes respectively. MAFIA computes the longitudinal wake potential as a function of bunch coordinate (s = ct) which can then be Fourier transformed to calculate the impedance spectrum. Since, trapped HOMs in SRF cavities can have high Q factors, long-range wake potential computations are usually required to estimate the impedance accurately. If Q factors are extremely high, the spectrum of that mode is artificially broadened due to the truncation of the wake. In such cases the impedance can be better approximated using two different long-range computations [96]. To investigate high Q modes in the five-cell cavity, wake computations upto 300 m were performed. Fig. 8.20 shows broadband impedance spectrum of longitundinal modes compared to measurements performed on the copper prototype. It should be noted that the impedance measurements are a product of the shunt impedance of each individual mode with the measured external Q from

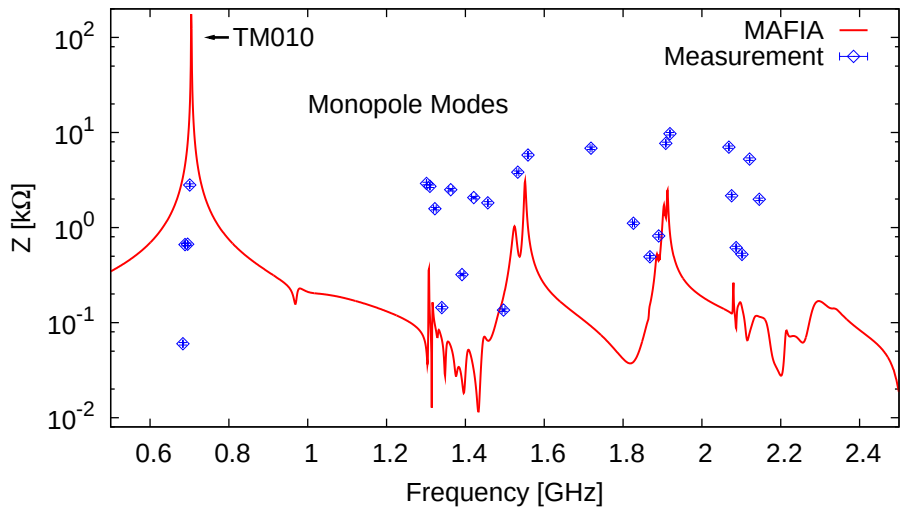

Figure 8.20: Impedance spectrum and wake function for azimuthally symmetric modes

the prototype and hence can be different from the beam coupling impedance as calculated using the wake potential. The spectrum is dominated by the fundamental mode as expected and all other monopole modes with rather small impedances. There is only partial agreement with simulation and measurements due to the measurement technique for modes in the noise level giving an upper limit as described in section 8.3.2. Neverthless, we do not find any high Q trapped monopole modes.

A similar calculation for transverse deflecting modes was performed by displacing the bunch by 3 cm from the cavity center with appropriate boundary conditions to selectively excite dipole modes. Fig. 8.21 shows impedance spectrum for the dipole modes compared to measurements performed using the prototype. The agreement for the relatively higher Q modes are very good. The spectrum shows two distinct bands of interest: 1st and 2nd passband in the 0.9 GHz region and $4^{th} - 6^{th}$ passband near the 1.7 GHz region similar to that of the frequency domain results. Both regions yield external Q factors smaller than the 10^4 and are sufficiently damped to suppress both single bunch and multibunch effects which are studied in the following sections.

8.4 Single Bunch Effects

A beam traversing a structure losses energy into the structure dominated by single bunch losses primarily from longitudinal modes. The power lost is

given by

$$\frac{dE}{dt} = \frac{c^2}{2\pi R} \int_{-\infty}^{\infty} |\rho(\omega)|^2 \; Z_{||}(\omega) d\omega \tag{8.21}$$

where R is the aperture radius, $\rho(\omega)$ is the bunch spectrum, and $Z_{||}$ is the longitudinal impedance. For a Gaussian bunch of RMS length σ_z, the power lost can be expressed as

$$P_{lost} = k_{||} q_b^2 f_b \tag{8.22}$$

where Q_b is the bunch charge, f_b is the beam repetition frequency, and $k_{||}$ is the longitudinal loss factor which is given by [86]

$$k_{||}(\sigma) = \frac{1}{2\pi} \int_{-\infty}^{\infty} Z_{||}(\omega) f(\omega, \sigma) d\omega \tag{8.23}$$

where $f(\omega, \sigma) \approx e^{-\omega^2 \sigma^2}$ is the spectral power density of a Gaussian bunch. For a cavity with discrete modes, the longitudinal loss factor for a given mode can be expressed as

$$k_{||}(n) = \frac{1}{2\pi} \int_{-\infty}^{\infty} Re Z_{||}(\omega) d\omega. \tag{8.24}$$

In the high Q regime and in the neighborhood of the resonance,

$$\mathrm{Re}(Z_{||}) = \frac{Z_n}{1 + [2Q(\omega - \omega_n)/\omega_n]^2}. \tag{8.25}$$

Therefore, the loss factor integral simplifies to

$$k_{||}(n) \approx \frac{\omega_n}{4} \left(\frac{R}{Q} \right)_n \tag{8.26}$$

where $(R/Q)_n$ is the accelerator physics definition of the shunt impedance of the nth mode. The longitudinal short range wake excited by the beam induces an energy spread in the beam which can be calculated using [86]

$$\frac{\delta E}{E} = \frac{2 Q_b k_{||}}{E_{acc}}. \tag{8.27}$$

Therefore, $k_{||}$ has to be minimized especially for high charge scenarios.

A beam off-axis can excite deflecting modes (dipole like) and generate transverse wakefields. These transverse wakefields in turn act back on the

beam and give an effective kick which can be characterized by analogous transverse loss factor given by [86]

$$k_{\perp}(\sigma) = \frac{1}{2\pi} \int_{-\infty}^{\infty} Z_{\perp}(\omega) f(\omega, \sigma) d\omega \tag{8.28}$$

where $Z_{\perp}$ is the transverse impedance of the structure. The transverse wake gives rise to kick thus displacing the tail with respect to the head and resulting in an emittance growth which can estimated from [63]

$$\frac{\Delta x}{x} = \frac{Q_b k_{\perp}}{2E_{acc}} \langle \beta \rangle \; ln \frac{\gamma_f}{\gamma_i} \tag{8.29}$$

where, E_{acc} is the accelerating gradient, $\langle \beta \rangle$ is the average beta function.

The loss factor for the five-cell cavity was calculated using ABCI [87], a numerical code for azimuthally symmetric structures. Fig. 8.22 shows the integrated loss factor as a function of frequency for a gaussian bunch of RMS length of 1 cm traveling through the cavity for BNL, TESLA and CEBAF deisgns. The integrated loss factors and the corresponding power dissipated for electron cooling scenario with 5 nC bunch charge and 50 mA beam current are listed in Table 8.5. The loss factors per single cell of the BNL, TESLA and CEBAF designs are plotted in Fig. 8.23 as a function of bunch length for comparison. For bunch lengths of 1 cm or smaller, the BNL design has clearly much smaller $k_{||}$ and $k_{\perp}$ and hence better suitable in high current high bunch charge regime. In addition the lower BNL's lower frequency allows the possibility of longer bunches. Estimates for the energy spread and the emittance growth induced by the corresponding accelerating structures are shown in Table 8.5 for nominal bunch length ($\sigma = 1\ cm$), bunch charge ($Q_b = 5\ nC$) and an energy gain of 20 MeV through the accelerating structure.

Table 8.5: Longitudinal and transverse loss factors for final design (BNL I). Loss factors for an alternate design (BNL II), TESLA and CEBAF cavities are also listed for comparion (σ_z = 1 cm, Q_b = 5 nC, and E_{gain} = 20 MeV). NE - Not Estimated

Parameter	Unit	BNL I (HC)	BNL II (HC)	CEBAF(HG)	TESLA(HG)
$k_{\|\|}$ (σ_z - 1 cm)	[V/pC]	1.07	1.18	2.84	3.56
$k_{\perp}$ (σ_z - 1 cm)	[V/pC/m]	3.19	3.37	48.84	45.71
$\delta E/E$ (Q - 5 nC)	-	0.05 %	0.06 %	0.14 %	0.18 %
$(\Delta\epsilon)/\epsilon_0$ (Q - 5 nC)	-	NE	NE	NE	NE

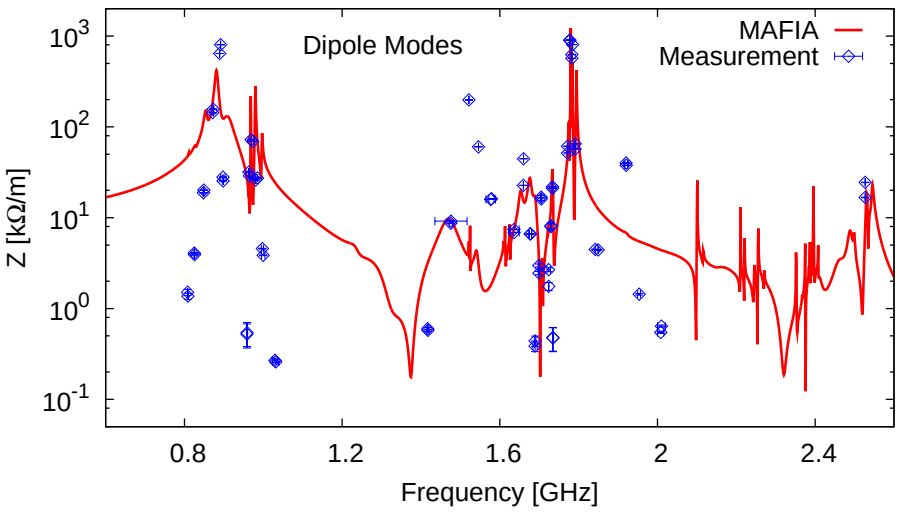

Figure 8.21: Impedance spectrum and wake function for transverse dipole modes

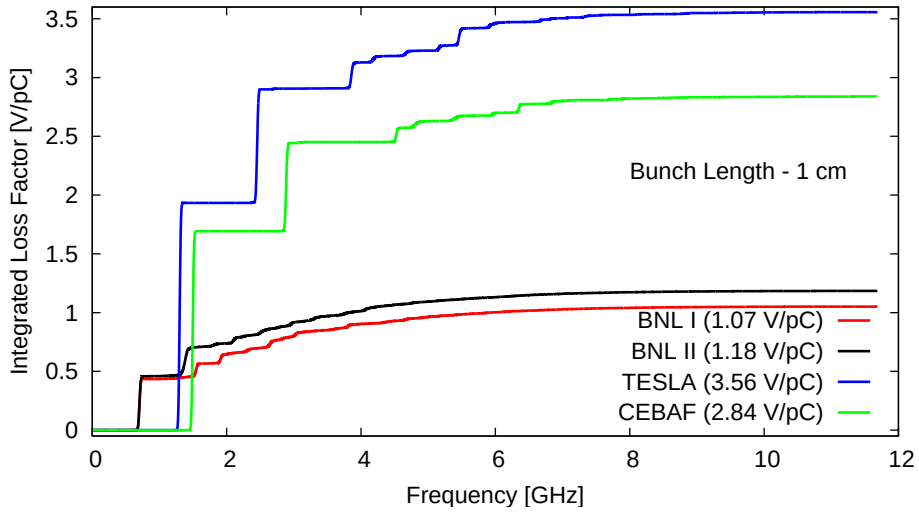

Figure 8.22: Integrated loss factor for BNL I geometry

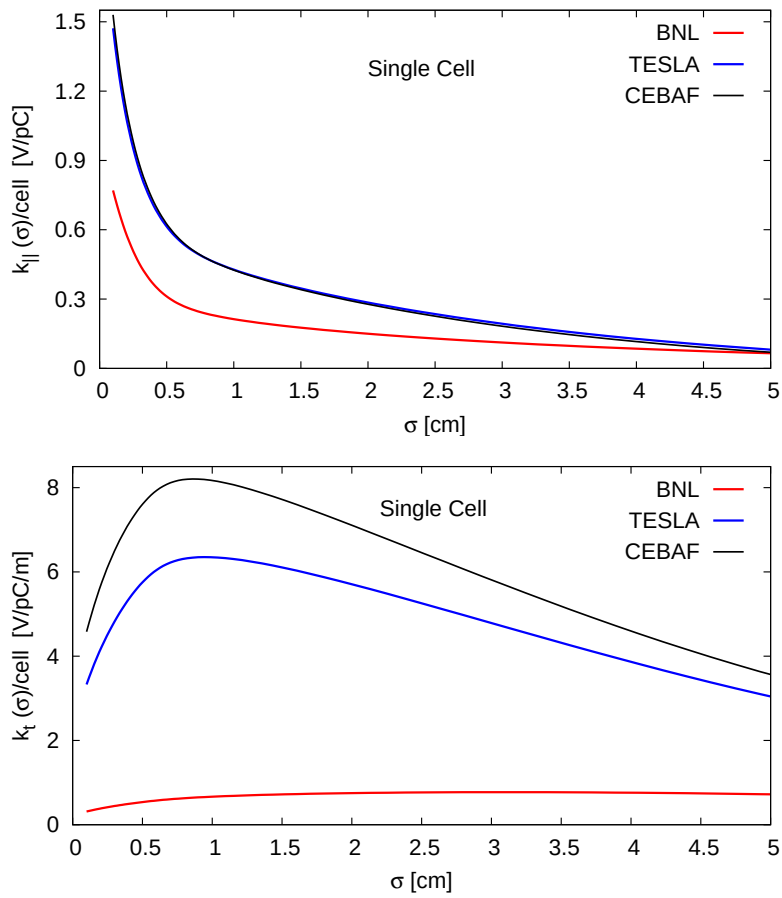

Figure 8.23: Logitudinal and transverse loss factors as a function of bunch length.

8.5 Multipass Multibunch Instabilities

In addition to the average HOM power, energy spread, and emittance growth, individual HOMs interacting with the beam beyond certain thresholds can cause instabilities. In SERLs, transverse multibunch beam breakup (BBU) is one of the main limiting factor primarily driven by high Q dipole modes. A bunch traveling through the cavity with an offset can excite a transverse HOM (mainly dipole) and the subsequent bunch will exprience a momentum kick

$$\delta p = \frac{q}{c} W(\tau) \tag{8.30}$$

where, $W(\tau) = \frac{cZ_\perp}{2Q} \sin(\omega\tau) e^{-\omega\tau/2Q}$.

The bunch returns back to the cavity on its recirculation path with the momentum kick translated to a transverse displacement through the M_{12} component of the recirculated matrix. If the bunch returns back "in-phase" with the HOM, it can form a closed feedback loop between the beam and cavity. If the Q_{ext} is sufficiently large, the induced voltage in the HOM grows exponentially and leads to beam breakup. An analytical expression was developed for a single dipole HOM with a single recirculation pass which is given by [97]

$$I_{thr} = \frac{-2p_r c}{e\left(\frac{R}{Q}\right) Q_e k_m M_{12} sin(\omega_m t_r)} \tag{8.31}$$

where p_r is the momentum of the recirculating beam, c is the speed of light, $Q_e \frac{R}{Q}$ is the impedance of the HOM, k_m is the wave number, M_{12} is the transport matrix of the recirculation path and t_r is the recirculation time.

Threshold current calculations for cavities with a train of bunches through N cavities, each with several HOMs are usually carried out with numerical methods. Several numerical codes have been developed to simulate multibunch BBU and estimate threshold currents for SRF cavities with high Q deflecting modes [91, 92, 93, 94]. Simulations can be performed in both time domain (for example TDBBU [91]) and frequency domain (for example MATBBU [92]). In time domain the transverse phase space of the bunches is calculated through each RF cycle and the cavity excitation levels is correspondingly updated. This procedure is iterated through several RF cycles either to reach a steady state or beam break up for given threshold current. In the frequency domain a steady state solution can be formulated into a system of linear equations. The eigenvalues for each coherent frequency can be computed which are simply the inverse of the complex currents. The values corresponding to the positive real axis are physically realizable currents which determine the threshold for that frequency. A sample computation of complex currents as the frequency is stepped through region of interests is seen in Fig 8.24. Both numerical techniques usually treat a cavity as a drift space with an accelerating gap and an impulse kick at the center of the cavity to represent the effect of the deflecting mode.

Simulations were performed for an electron cooling scenario shown in Fig. 6.3 with four cavities to accelerate the electron beam from 2 MeV to 54 MeV. A threshold current of 2 Amps show no growth of multibunch BBU with a unit recirculating tranfer matrix. Due to manufacturing errors the HOM frequencies exhibit a random spread for different cavities. The reasonable HOM frequency spread ($\delta f \sim Q_{ext} f_{HOM}$) reduces the effective Q_{ext} of the mode and as a result increases the threshold current. Fig. 8.25 shows a simulation for a threshold

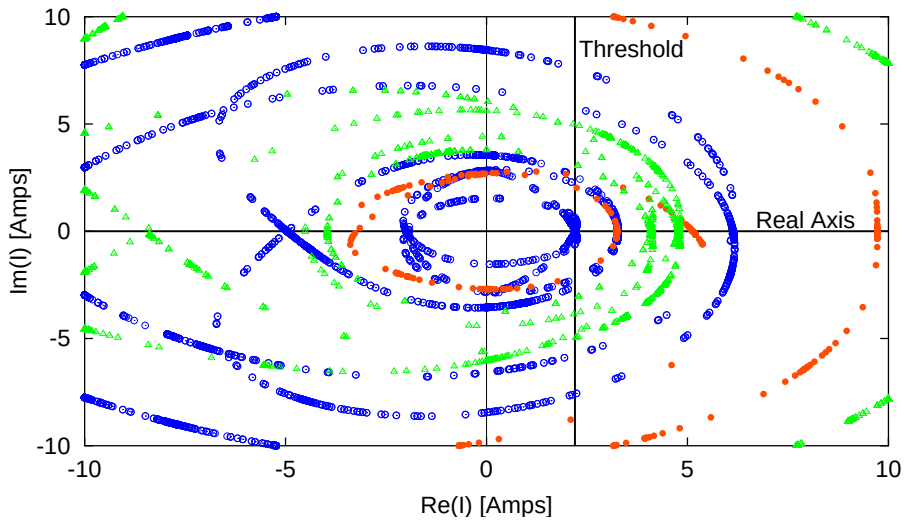

Figure 8.24: A computation of complex eigenvalues for each frequency sample from 0.8 to 1.8 GHz.

current of 2 Amps with different HOM frequency spread ranging from 3-10 MHz. A simulation using the same cavity and lattice parameters in MATBBU confirms the threshold current. Fig. 8.26 shows threshold current as a function of frequency and the limiting modes are mainly between 850-950 MHz and 1.7-1.8 GHz. This is consistent with the impedance measurements of the modes in these regions ($Q_{ext} \approx 10^4$). The case with no HOM spread shows a slightly smaller threshold current as expected and the simulations results are within the discrepancies expected between the two codes [98]. Since the threshold current is also dependent on M_{12}, lattice techniques such as reflection and rotation can be employed to further supress multibunch BBU in recirculating linacs [94].

8.6 Power Coupler Kick

The fundamental power coupler (FPC) is a co-axial antenna with a rounded tip placed on the 24 cm beam pipe as shown in Fig. 8.12. The design is adapted from an SNS FPC [101] due to the proximity of frequency (805 MHz). The average input power is approximately 25 kW which requires a Q_{ext} of approximately 3×10^7. Fig. 8.27 shows a plot of the Q_{ext} as a function of the penetration depth of the inner conductor of the coaxial line. The required Q_{ext} can be achieved without any penetration into the beam pipe. Note that the Q_{ext} was calculated using the 3 db bandwidth of the transmission coefficient

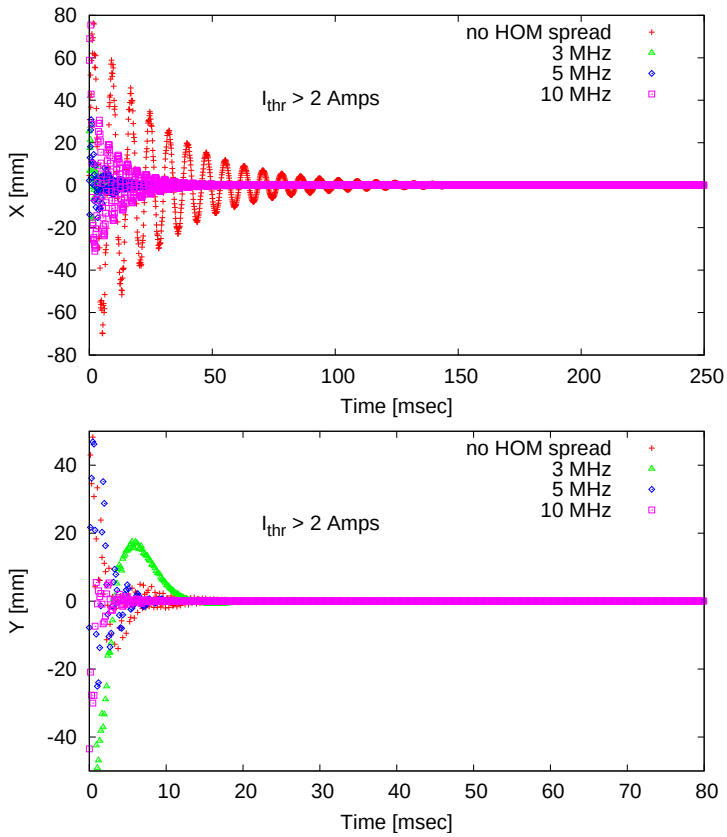

Figure 8.25: Time domain simulation using TDBBU for an electron cooling scenario with four five-cell cavities to accelerate the beam from 2 MeV to 54 MeV. The threshold current was set at 2 Amps with 40 dipole HOMs with both polarizations and show no growth of multibunch BBU for an arbitrary M_{12}.

S_{21} in the frequency domain of Microwave Studio [102].

The presence of single FPC can lead to a non-zero transverse field on-axis resulting in a kick to a bunch traversing the structure. The FPC is placed at the exit of the linac to alleviate the effect of the tranverse kick so that beam experiences the kick at a higher energy. In the absence of a symmetric coupler to cancel the effect, a symmetric stub can be placed to reduce the transverse kick. Also, the large beam pipe and relatively weak coupling are natural remedies to help minimize the transverse kick. The transverse fields for the case of a single coupler with and without a symmetrizing stub and a symmetric coupler with a 1 mm relative offset is shown in Fig. 9.22 and the respective transverse kicks are computed using a similar approach described

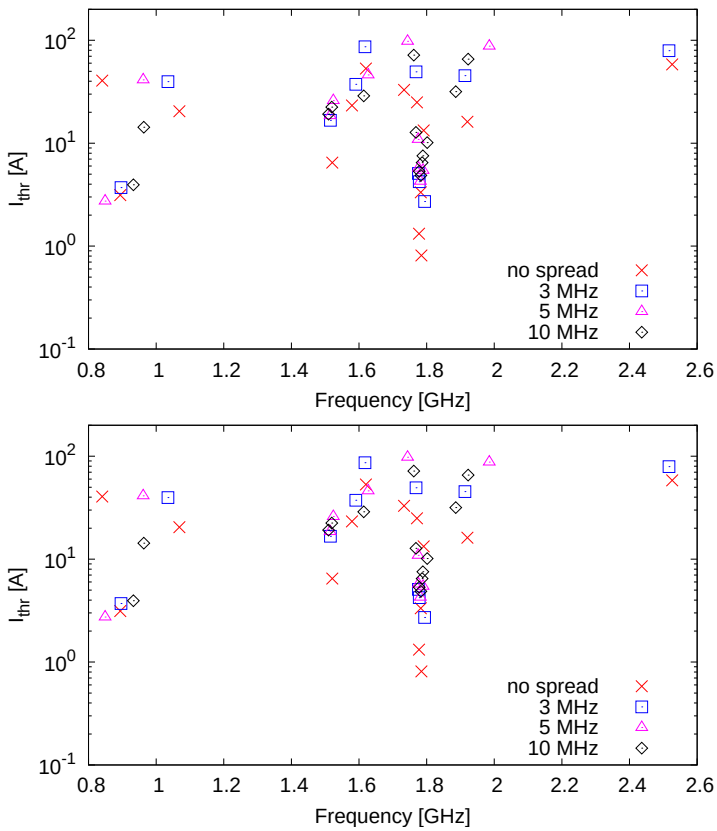

Figure 8.26: Frequency domain simulation using MATBBU for the same electron cooling scenario. The threshold current are above 2 Amps for three different frequency spreads. The limiting modes are mainly near two different regions (850-950 MHz and 1.7-1.8 GHz) as expected. 40 dipole HOMs with both polarizations were used in the simulation for an arbitrary M_{12}.

in [103, 104].

The transverse "kick factor" is simply given by

$$\delta_t = \frac{\int (E_y + cB_x)dz}{\int E_z dz} \tag{8.32}$$

which can be numerically evaluated. The kick received by the bunch passing through is dependent on the relative phase between bunch and the RF and is given by

$$\frac{p_t}{p} = \frac{eV_{acc}}{pc}\mathrm{Re}\left(\delta_t e^{i\phi_0}\right) \tag{8.33}$$

where ϕ_0 is the bunch phase with respect to the RF, and V_{acc} is the voltage

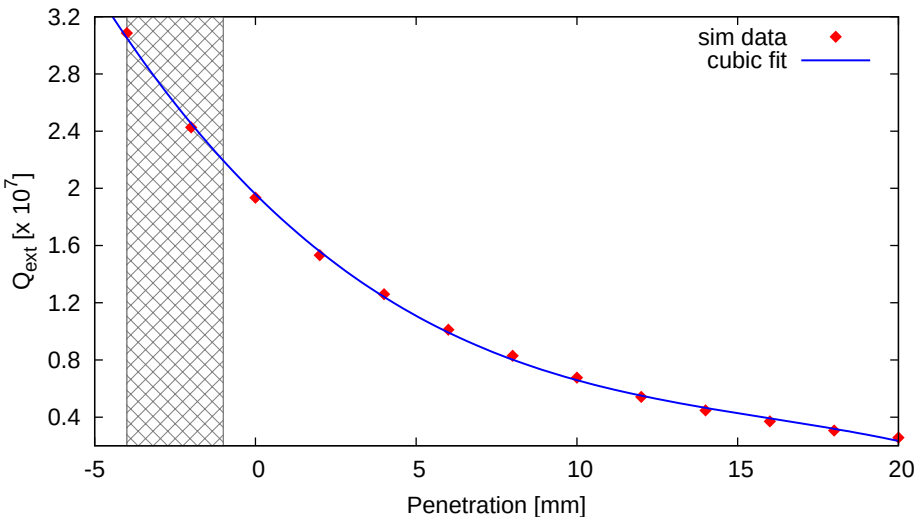

Figure 8.27: A scan of Q_{ext} as a function of the penetration of the tip into the beam pipe. The solid line is a quadratic fit to the calculated Q_{ext} points. The shaed region shows the expected penetration to achieve the required Q_{ext} of approximately 3×10^7.

of the accelerating gap. The normalized emittance growth due to the time dependent RF kick can be estimated using the formula derived in Ref. [105] which is given by

$$d\epsilon_n = \sigma_t \frac{2\pi\sigma_z}{\lambda_{RF}} \frac{eV_{acc}}{E_0} |\delta_t e^{\phi_0}| \tag{8.34}$$

where σ_t and σ_z are the transverse and longitudinal beam sizes, and E_0 is rest energy of the e^-. Table 9.5 shows the kick factors, transverse kicks, and the corresponding emittance growth for three cases with transverse RF fields. In all three cases, the kicks received are quite small and amount to negligible emittance growth compared to the growth induced by space charge.

Table 8.6: Transverse kick and normalized emittance growth for a single coupler,dual coupler with 1 mm asymmetry, and a single coupler with a symmetrizing stub, both with a $Q_{ext} \approx 3 \times 10^7$.

Scheme	$\delta_t \times 10^{-4}$	Kick
Single Coupler	(-9.3 + 1.2i)	0.85 mrad
Single Coupler + Stub	(3.0 - 3.8i)	0.27 mrad
Dual Couplers (offset)	(0.6 - 0.6i) mm^{-1}	50 μrad

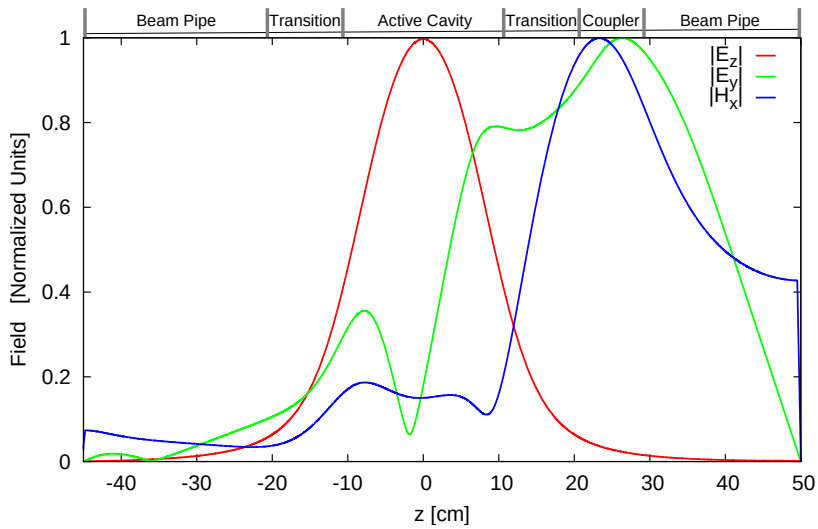

Figure 8.28: Longitudinal and transverse fields on-axis of the SRF cavity due to transverse coaxial coupler. The calculations were carried out using a single cell with the same transition sections as the five-cell cavity and normalized to 15 MV/m for the kick calculations.

8.7 Multipacting

Multipacting in RF structures is a resonant electron multiplication caused by secondary electrons emitted from the cavity surface. Primary electrons emitted from the surface impact back in an integer number of RF cycles causing emission of secondary electrons. If the secondary electron yield (SEY) of the surface is greater than 1, the resonant emission can lead to an avalanche, absorbing RF power and also lead to loss of superconducting properties locally, and sometimes result in thermal breakdown.

The Helsinki code, MultiPac 2.1 [99, 100], is used to calculate the field levels at which multipacting can be onset. Since the five-cell design is made of identical $\frac{1}{2}$ cells, it is sufficient to perform a simulation for single cell. Fig. 8.29 shows the counter function representing the total number of electrons (primary and secondary) and the corresponding impact energies as a function of peak surface field for BNL I and II designs. The total number of electrons after a given number of impacts normalized to the average secondary emission coefficient corresponding to the impact energy (enhanced counter function) is shown in Fig. 8.30 as a function of peak electric field.

An enhanced counter function (ECF) larger than 1 represents an onset of multipacting at that field level. Fig. 8.30 shows a region of interest at high

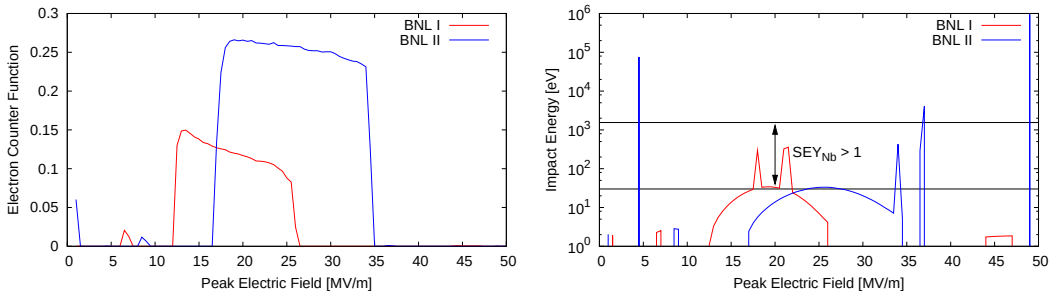

Figure 8.29: Top: The electron counter function representing the total number of free electrons after a given number of impacts (20) as a function of peak electric field. Bottom: The final impact energy of the electrons surviving the maximum number of impacts (20) as a function of peak electric field.

surface fields (15-40 MV/m). The impact energies between 15-40 MV/m are quite low (< 30 eV) and the the corresponding SEY for niobium is smaller than 1. Therefore, the ECF is much smaller than 1 therefore making multipacting very unlikely for both BNL I and II designs. It is interesting to note that peak of the ECF for BNL I is located at 20 MV/m which is approximately a factor of 2 smaller than expected surface field ($E_{peak} > 40$ MV/m). BNL II design has more peaks which are located closer to the operating surface fields.

The electron trajectory for BNL I (also similar to BNL II) near field region of ≈ 20 MV/m is shown in Fig. 9.6 which exhibits stable two point multipacting.

8.8 Lorentz Force Detuning

The surface fields on the cavity exerts a force on the walls which are non-negligible at high gradients. The radiation pressure due to Lorentz force is given by

$$P_{rad} = \frac{1}{4}\left[\mu_0|\vec{H}|^2 - \epsilon_0|\vec{E}|^2\right] \tag{8.35}$$

where $\vec{H}$ and $\vec{E}$ are the magnetic and electric fields on the surface. Fig. 8.32 shows a plot of the surface fields and radiation pressure for BNL I.

The radiation pressure deforms the cavity and results in a frequency shift which is expressed as

$$\delta f \propto \frac{f_0}{4U}\int_{\delta V}\left(\epsilon_0|\vec{E}|^2 - \mu_0|\vec{H}|^2\right)dV \tag{8.36}$$

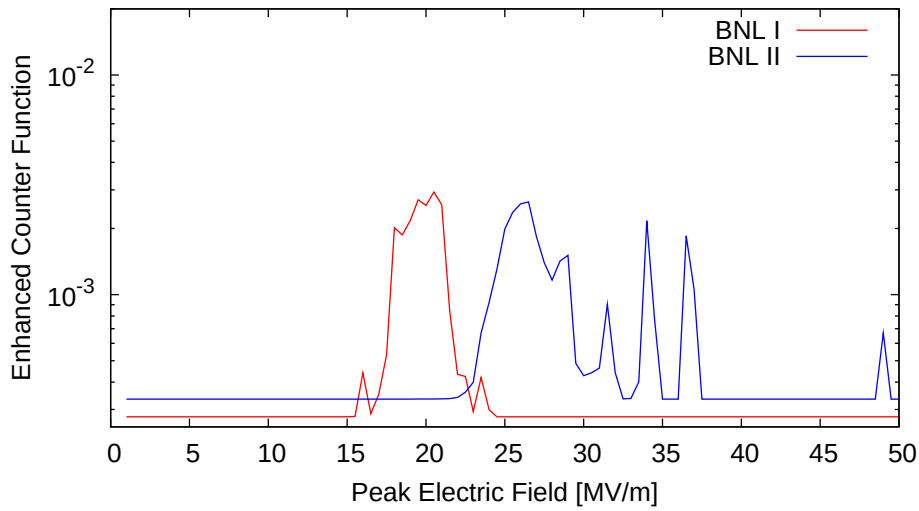

Figure 8.30: The enhanced counter function which represents the number of secondary electrons after a given number of impacts normalized to the secondary emission coefficient corresponding to the impact energies plotted as a function of peak electric field.

where f_0 is the resonant frequency, U is the stored energy, and δV is the fractional change in volume. Assuming that change in volume is small compared to the cavity and scales linearly with pressure, the static frequency shift for a given E_{acc} is given by

$$\delta f = -K_L E_{acc}^2 \tag{8.37}$$

where, K_L is the Lorentz detuning coefficient which is a figure of merit of the stiffness. Fig. 8.33 shows the effect of radiation pressure on the cavity shape for an $E_{acc} = 1$ MV/m with a wall thickness of 3 mm. The Youngs modulus and the Poisson's ratio were taken to be 103 GPa and 0.38 respectively.

Due to the high Q (3×10^7) operation, a small coeffecient is necessary. K_L for the BNL I cavity was calculated to be 1.28 Hz/(MV/m)^2 and is compared to the stiffened TESLA and CEBAF cavities in table 8.5. An independent calculation carried by AES [107] determined K_L to be 1.2 Hz/(MV/m)^2. Due to inherent stiffness of the cavity shape, no special stiffening rings are required. The simulations were performed using ANSYS [108] with fixed ends on both sides. The tuner end of the cavity is not absolutely fixed which may result in slightly larger K_L.

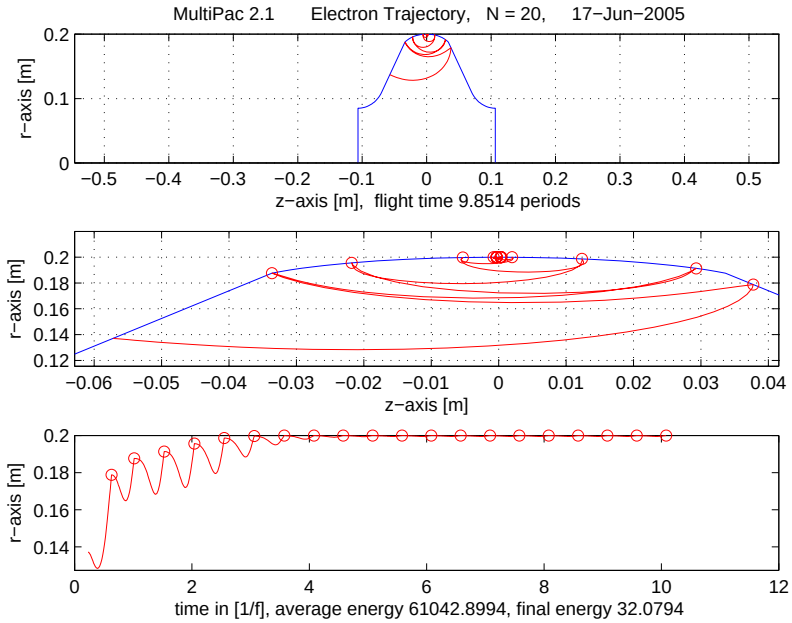

Figure 8.31: Electron trajectory calculated for a peak field of approximately 20 MV/m which shows a stable two point trajectory but no multipacting is expected due to impact energies smaller than 30 eV.

8.9 Conclusion

A five-cell SRF linac cavity has been designed to operate at 703.75 MHz to accelerate ampere class beams in an energy-recovery mode. The design is optimized to propagate the large HOM power through the beam pipe to an external ferrite load operating at room temperature. Several aspects of the cavity design and HOM characteristics have been simulated and benchmarked with measurements on a copper prototype. Extensive comparisons have also been made to the other existing SRF cavities being proposed for SC-ERLs. Multipass multibunch simulations have been carried out and the threshold currents for the onset of the instabilty is set at ~ 2 Amps. Issues relating to fundamental power coupling, transverse kicks, multipacting, bellows shielding, and Lorentz force detuning have also been addressed.

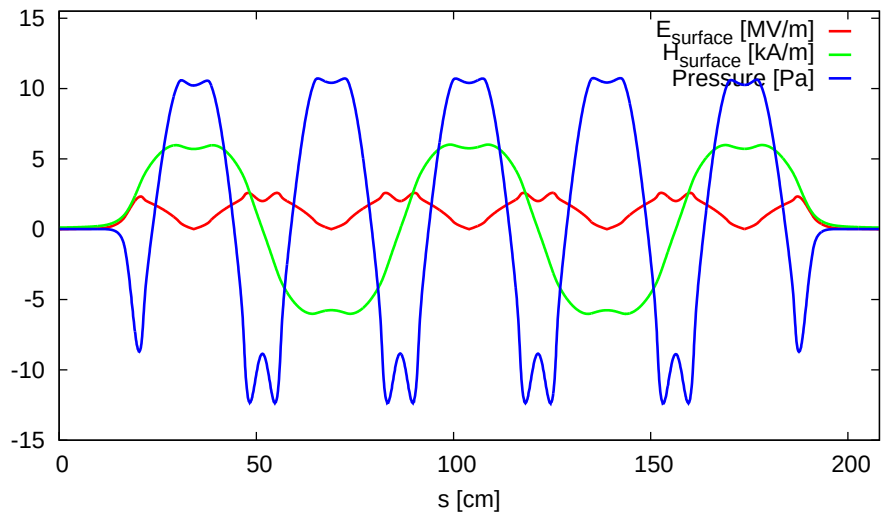

Figure 8.32: Electric and magnetic fields on the surface of the five-cell BNL I design and the corresponding radiation pressure as a function of longitudinal position.

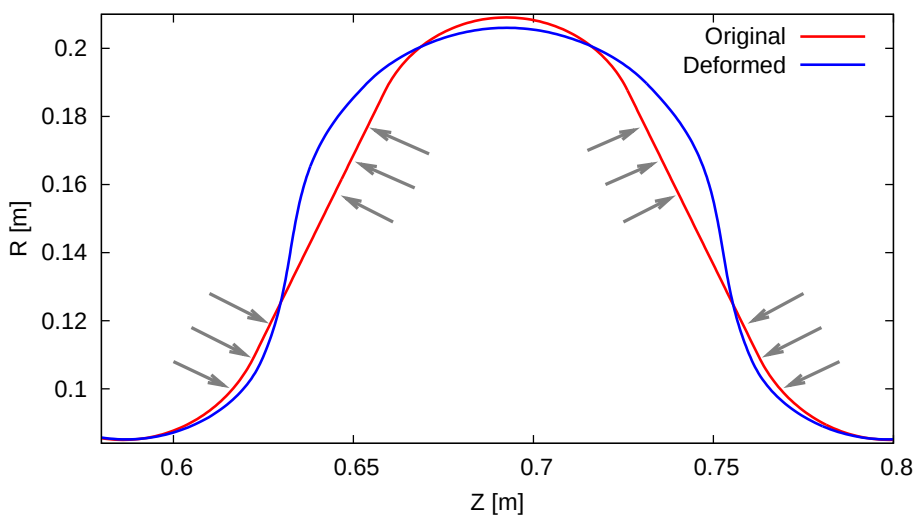

Figure 8.33: Deformation of the cavity walls due to Lorentz forces. The surface magentic field at the equator pushes the walls outward and surface electric fields at the iris pushes the walls inward. The deformation has been magnified to illustrate the effect.

Chapter 9

High Current Superconducting $\frac{1}{2}$-Cell Gun

9.1 Introduction

A superconducting energy recovery linac (SC-ERL) has been identified as the most efficient choice to generate and accelerate high current, high charge electron beam for the electron cooling project at RHIC. Electron cooling of ion beams is the main component of the next luminosity upgrade of the Relativistic Heavy Ion Collider (RHIC). Cooling ions (gold) at 100 GeV/nucleon requires very high average current (> 200 mA) electron beam. A 20 MeV prototype SC-ERL is under construction as an initial R&D step towards the realization of the e^- cooler and future high current SC-ERLs. The prototype will consist of a $\frac{1}{2}$ cell SRF gun shown in Fig. 9.1 as an injector to the 20 MeV SRF linac comprised of a five-cell SRF cavity [111, 112], and a return loop back through the linac for energy recovery before the beam dump. This paper will focus on the design and optimization of the $\frac{1}{2}$ cell gun based on both RF issues and preservation of small transverse and longitudinal emittances. Table 9.1 shows some relevant parameters for the prototype SC-ERL which were used as inputs for the optimization procedure.

9.2 SRF Gun Design

Like any SRF cavity, the design of the gun is affected by the peak surface fields, avoidance of multipacting, access to efficient surface chemistry, minimization of welds at critical points, mechanical stiffness and complexity of manufacturing. High current beams along with high bunch charge pose a significant challenge in suppressing HOM wakefields and extraction of the large HOM power. Accelerating ampere CW class beams also require high power fundamental couplers (FPC) capable of delivering megawatts (MW) of power

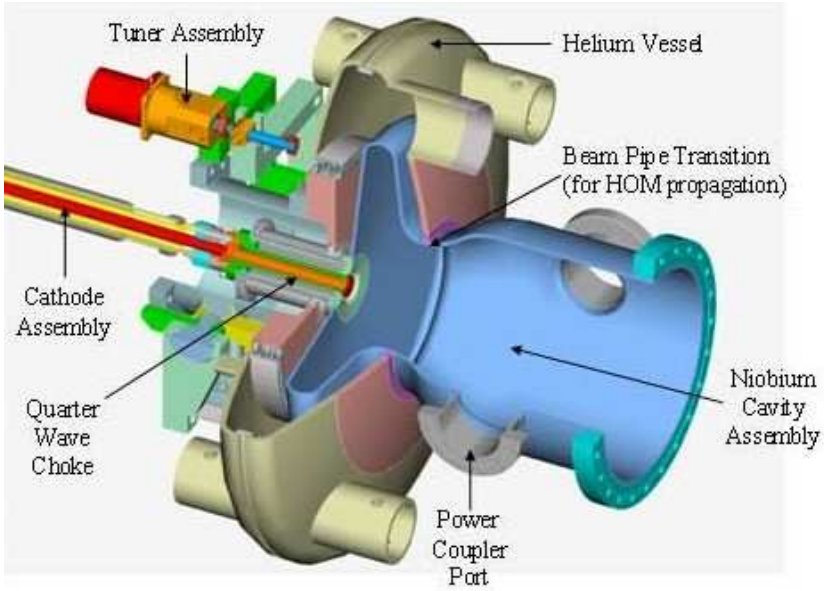

Figure 9.1: Conceptual 3D Graphic of $\frac{1}{2}$ cell SRF gun at 703.75 MHz with helium vessel, cathode insertion and tuner assembly (Courtesy AES).

which is non-trivial.

9.2.1 Cavity Shape

An initial design (1) was first proposed from the Rossendorf $\frac{1}{2}$ cell gun scaled to 703.75 MHz [113]. The cavity to beam pipe transition was enlarged to propagate all the lowest frequency HOMs. However, this design was inadequate to provide the required longitudinal focusing and emittance at the exit of the gun. A re-entrant shape (design 2) resulted from the modification of design 1 (right half-cell) to increase the longitudinal focusing and improve the overall emittance at the exit of the gun. This was achieved by shortening the effective cell length by reducing the beam pipe aperture and the wall angle and tuning for the frequency using the equator radius. However, coupling strongly to the fundamental mode ($Q_{ext} \sim 4 - 5 \times 10^4$) with a small beam pipe radius of 4 cm was not a viable option. The re-entrant shape may also pose problems relating to effective chemical treatment of the surface, multipacting issues and mechanical stability.

Several other designs (3-6) were developed as a result of shape optimization to reduce the effective cell length while keeping the beam pipe aperture $\geq 5cm$ and the wall angle $\geq 6.5^0$. The six different shapes that were considered are

Table 9.1: Parameters for the prototype SC-ERL used in simulations for optimization of the gun shape. A possible scenario with high charge and low repetition rate similar to the electron cooling case is also presented.

Parameter	High Current	High Charge
Injection energy [MeV]	2.5	2.5
Maximum energy [MeV]	20-40	20-40
Avg. beam current [A]	0.5	0.2
Repetition rate [MHz]	703.75	9.4
Charge/Bunch [nC]	1.4	10-20
Norm. emittance [mm.mrad]	1-3	30
Bunch length [cm]	1.0	3.0
Energy recovery efficiency	> 99.95 %	> 99.95 %

shown in Fig. 9.2, and detailed comparisons will be made in the following sections. Table 9.2 shows a comparison of some relevant RF parameters (peak fields and R/Q values) for the six designs.

Table 9.2: Comparison of RF parameters for the six different cavity shapes. The R/Q values are calculated using the accelerator definition. Note that the active cavity length is chosen from the cathode wall to the iris plane of the right half-cell of the gun.

Shape	R_{iris} [cm]	L_{cav} [cm]	R/Q [Ω]	E_p/E_a	B_p/E_a [$\frac{mT}{(MV/m)}$]
Design 1	7	10.1	100.0	1.20	2.88
Design 2	4	9.5	106.0	1.47	3.15
Design 3	6	10.0	102.4	1.27	2.96
Design 4	6	10.0	102.8	1.33	2.69
Design 5	5	9.5	95.0	1.43	2.96
Design 6	6	9.5	92.1	1.42	2.88

9.2.2 HOM Power

High current along with high bunch charge beams dissipate large amount of power into HOMs, which has to be extracted outside the cryogenic envi-

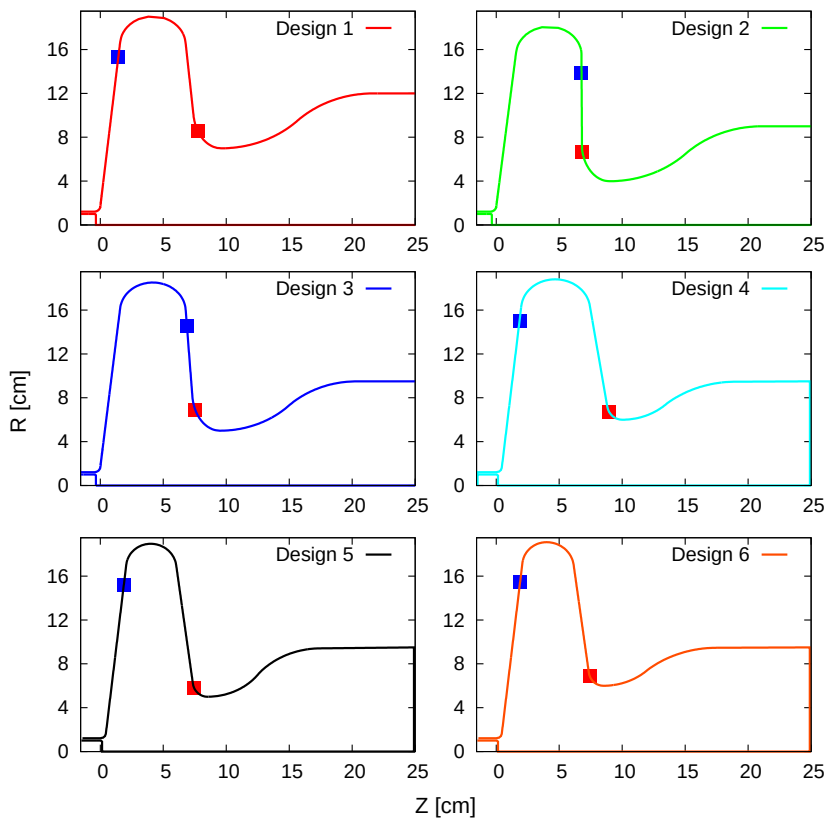

Figure 9.2: Six different cavity shapes used for comparison based on both RF and beam dynamics issues for the 703.75 MHz SRF gun. The red and blue solid squares represent the location of the peak electric and magnetic fields in the cavity respectively.

ronment. Beam pipe ferrite absorbers will be placed in the warm section to absorb this HOM power for modes above the cut-off frequency of the beam pipe. The average power dissipated by a beam traversing a structure is given by

$$P_{HOM} = k_{||} Q_b I_b \tag{9.1}$$

where $k_{||}$ is the geometrical loss factor of the structure. The loss factors for the six designs are calculated using ABCI [87, 88] and are shown in Fig. 9.3. The loss factors are quite similar ($\sim 0.7\ V/pC$), and the total HOM power dissipated is approximately 0.5 kW for a 500 mA beam current and 1.4 nC bunch charge.

Note that the loss factors shown in Fig. 9.3 were calculated for ultra relativistic particles ($\beta = 1$) and are assumed as the upper limits for the case with

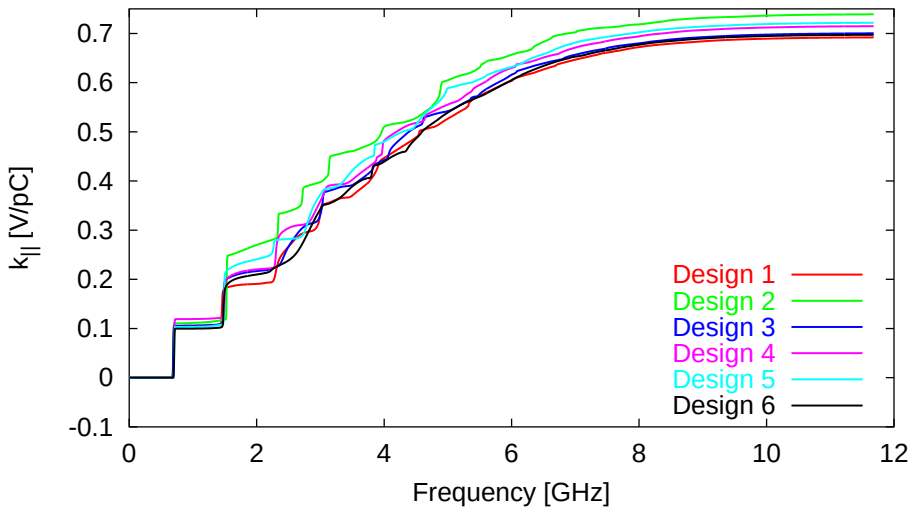

Figure 9.3: Integrated longitudinal loss factor calculated by ABCI for the six different designs under consideration.

$\beta < 1$ (see appendix A).

9.2.3 Multipacting

As any RF cavity the gun also is prone to multipacting, a resonant electron multiplication caused by electrons emitted from the surface. The primary electrons impact back on the surface emitting secondary electrons. If they satisfy the resonant condition with a secondary electron yield (SEY) larger than 1, it can lead to an avalanche. This will lead to absorption of RF power and thermal breakdown of the superconducting surface.

The Helsinki 2D code, MultiPac 2.1 [99, 100] is used to calculate the field levels at which multipacting can be onset for the six designs. Fig. 9.4 shows the counter function representing the total number of electrons (primary and secondary) and corresponding impact energies as a function of peak electric field. The total number of electrons after a given number of impacts normalized to the average secondary emission coefficient corresponding to the impact energy (enhanced counter function) is shown in Fig. 9.5 as a function of peak electric field. An enhanced counter function larger than 1 represents an onset of multipacting at that field level. Fig. 9.5 shows two main regions of interest, one at low surface fields ($< 5MV/m$), and the other at high surface fields ($>$ 30 MV/m). The impact energies near 0.5 MV/m are considerably high ($\gg$ 2 keV) and the impact energies near 33 MV/m are very low ($<$ 30 eV).

For both impact energies, the corresponding SEY for niobium is smaller than 1. Therefore, the enhanced counter function is much smaller than 1 as seen from Fig. 9.5, thus making multipacting very unlikely. The electron trajecto-

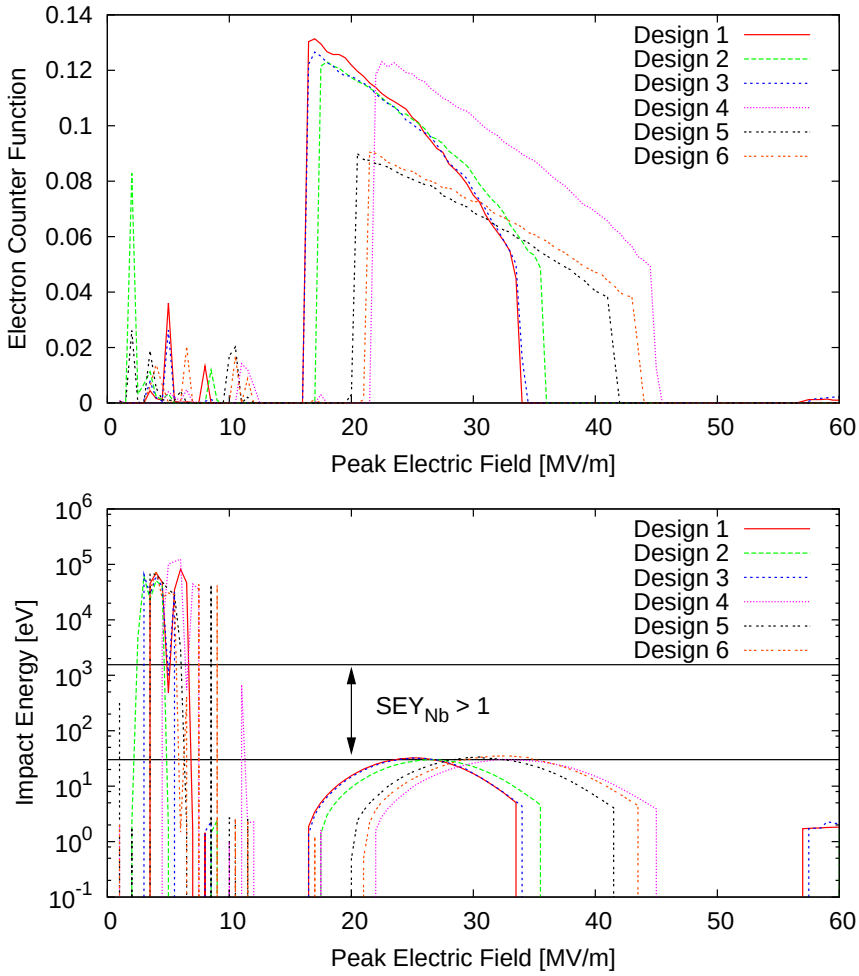

Figure 9.4: Top: The electron counter function representing the total number of free electrons after a given number of impacts (20) as a function of peak electric field. Bottom: The final impact energy of the electrons surviving the maximum number of impacts (20) as a function of peak electric field.

ries for the two field regions are shown in Fig. 9.6. The trajectory in the low field region (∼5 MV/m) does not stabilize and drifts radially. The electrons are lost after approximately 40 impacts. The trajectory at high field region (∼33 MV/m) exhibits stable two point multipacting.

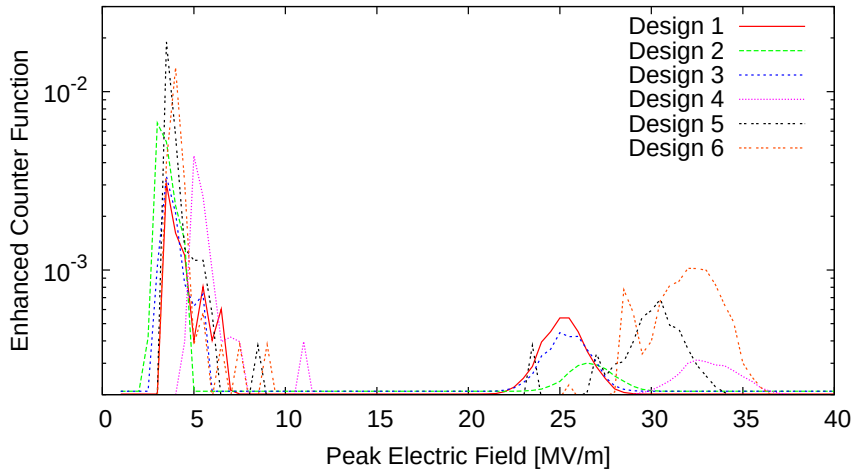

Figure 9.5: The enhanced counter function which represents the number of secondary electrons after a given number of impacts normalized to the secondary emission coefficient corresponding to the impact energies plotted as a function of electric field.

9.3 Beam Dynamics

In addition to RF and mechanical requirements, the preservation of very low emittances and energy spread due to space charge forces puts strict constraints on the gun shape. For meaningful calculations of longitudinal and transverse beam emittances, simulations for the six designs are preformed using PARMELA [114, 115] for a prototype ERL system comprising of a 2 MeV SRF gun, a Z-bend injection merging optics [116], and a 20 MeV linac [111, 112]. The longitudinal electric field of the gun for beam simulations are calculated using SUPERFISH [117].

9.3.1 Longitudinal Focusing

The beam acquires an energy spread due to longitudinal space-charge forces giving the head of the bunch a higher energy relative to the rest of the bunch. A large energy spread can lead to adverse affects on the beam quality. To counter this energy spread, the bunch phase is placed before the peak in the energy-phase curve to achieve longitudinal focusing. This curve is dependent on the effective length of the gun (including the field penetration into the beam pipe), the electric field intensity, and the degree to which the cathode is recessed. The energy vs. initial phase of the emitted electrons calculated for

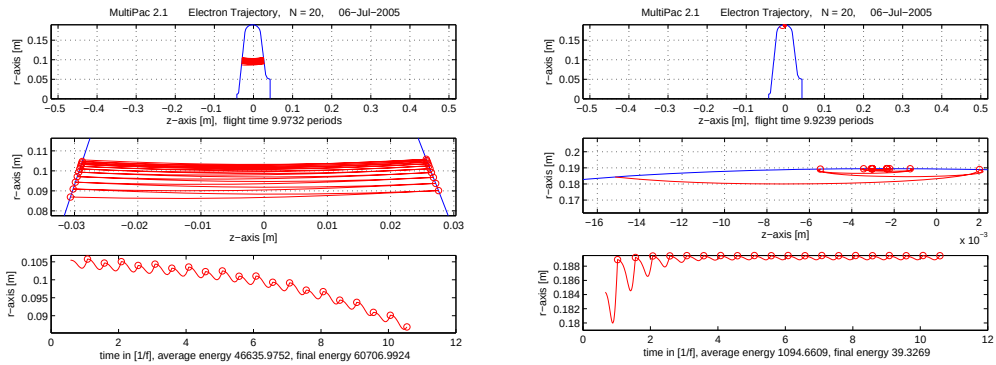

Figure 9.6: Left: Electron trajectory calculated for a peak electric field of approximately 5 MV/m. The trajectory drifts radially and does not stabilize. The electrons are lost after approximately 40 impacts. Right: Electron trajectory calculated for a peak field of approximately 33 MV/m which shows a stable two point trajectory but no multipacting is expected due to impact energies smaller than 30 eV.

the six designs is shown in Fig. 9.7. Design 2 & 5 show a significant positive slope compared to the others, thus providing a larger phase window for placing the bunch and provide effective longitudinal focusing to achieve the smallest energy spread.

The beam dynamics calculations in the following were made with a bunch charge of 1.4 nC, emitted from a cathode spot size of 5.0 mm diameter. The launch phase was chosen to be 25° as a result of optimization of the beam dynamics of photoinjectors with space charge [118]. A sufficiently large initial phase is required to provide adequate field on the cathode for electron emission and acceleration. Furthermore, to minimize chromaticity, the launch phase should be placed before the maximum energy gain on the positive slope of the energy-phase curve. For designs 2 and 5 the initial phase of 25° results in a minimum energy spread. The bunch distribution was uniform in both transverse and longitudinal directions. Fig. 9.8 shows the energy spread as a function of longitudinal position for the different gun shapes.

The electrons start from the cathode from rest. Therefore, a high field on the cathode is necessary to rapidly accelerate the high charge bunches to avoid emittance dilution due to space charge forces. Fig. 9.9 shows a schematic of two cases with a recessed cathode (left) and a cathode inserted 3mm towards the cavity wall (right). From Fig. 9.10 one can see that ratio of E_{cath}/E_{acc} is significantly larger when the cathode is not recessed with respect to the

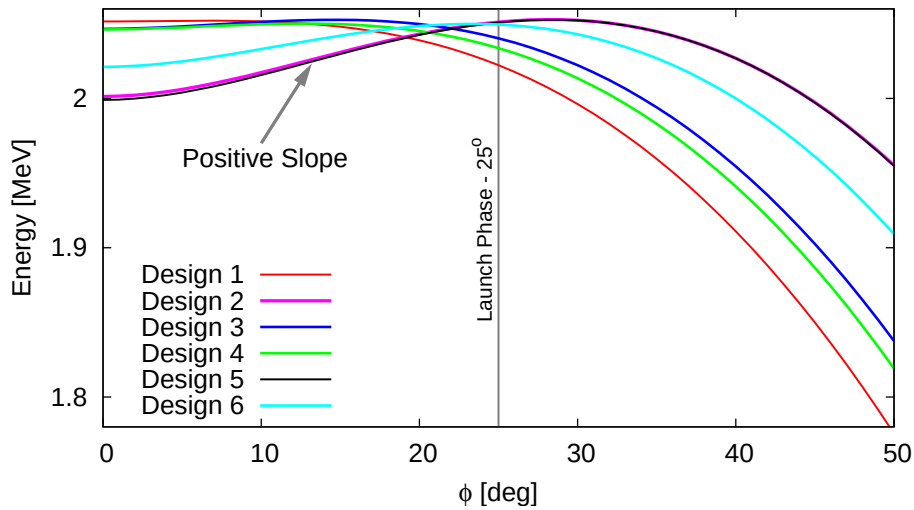

Figure 9.7: Energy of the electrons plotted as a function of initial phase for the six designs. Positive slope indicating an effective longitudinal focusing required for maintaining a small energy spread.

cavity wall. This high field near the cathode region is crucial to accelerate the electrons immediately after leaving the cathode to counteract space charge effects.

9.3.2 Transverse Emittance

Transverse focusing of the high-charge electron bunch and matching it to the invariant beam envelope [119, 120] is critical to achieve extremely small transverse emittance from the gun. This requires under certain conditions a recessed cathode, a solenoidal magnetic field or combination of the two. The evolution of vertical emittance through the SRF gun (recessed cathode), a nominal merging system, and a 20 MeV linac is seen in Fig. 9.11. Although, all guns show small emittances, designs 2 & 5 are significantly better. Table 9.3 lists loss factors, transverse emittances and energy spreads for the six designs.

The actual amount of recess must be determined by optimizing the effects of the larger electric field on the cathode which favor no recess, and transverse focusing which favors a recess. Fig. 9.12 shows the longitudinal and transverse emittances through the same prototype system, but with a simplified injection system (without bends). For each recess position of the cathode, the initial spot size, bunch length, and the solenoids were adjusted to minimize

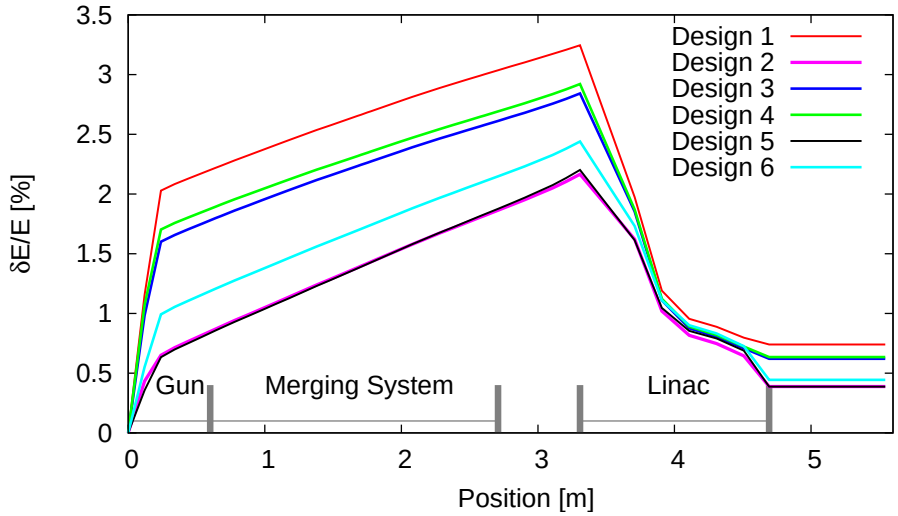

Figure 9.8: Energy spread of the electron beam calculated by PARMELA for a system with the gun, merging system, and a 20 MeV linac for the six different designs.

emittance at the exit of the Linac. It can be seen from Fig. 9.12 that position of the cathode with respect the cavity wall has a strong influence on both longitudinal and transverse emittances. Therefore, the cathode positions of -1 ± 0.5 mm with respect to a cavity wall seems to be an optimal region, and an adjustable cathode stalk is proposed for the prototype design to determine the best insertion length with beam. The launch phase for a fixed recess was varied $\pm$ 5° which had a weak effect on the final emittances.

9.4 Final Design and Issues

All six designs exhibit similar RF characteristics, but designs 2 and 5 show significantly better emittances in both longitudinal and transverse planes. Design 5 is prefered for its better mechanical properties, and its accessibility for a more effective surface treament due to larger wall angles. Additionally, a larger iris radius in design 5 is preferable to achieve strong FPC coupling. The geometrical parameters for design 5 are shown in Table 9.4. Issues relating to HOM damping and the FPC coupler will be discussed using design 5 in the following sections.

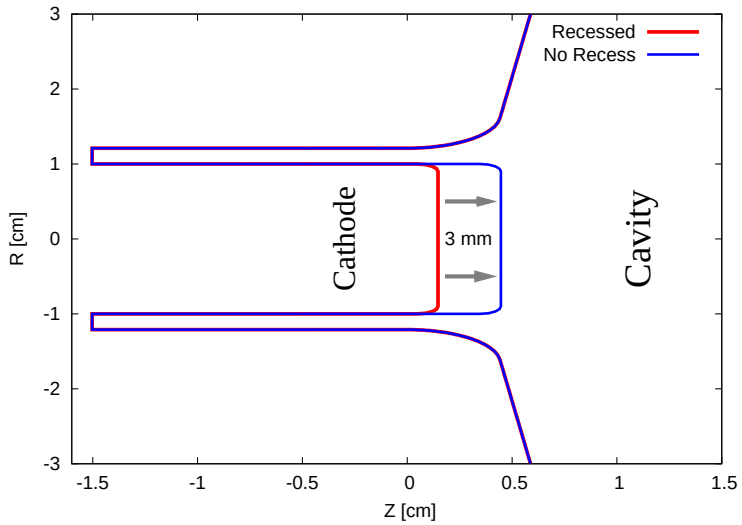

Figure 9.9: Graphic of the recessed and non-recessed cathode with the $\frac{1}{4}$ wave choke for RF isolation near the cathode region. The choke will be at an elevated temperature compared to the SRF gun.

9.4.1 Transition Section

It is important to damp all HOMs to avoid single bunch and multi-bunch effects which can degrade the beam quality and possibly lead to instabilities. It was initially proposed to enlarge the beam aperture similar to the five-cell linac cavity [112] to propagate all HOMs down to the lowest frequency, and damp them using beam pipe ferrites. HOM loop couplers were unfavorable due to their low power handling capability and their resonant nature leading to a high probability of failure for high current operations. The impedance spectrum of monopole and dipole modes are shown in Fig. 9.13 for the SRF gun and is compared to the case with the enlarged beam pipe. Fig. 9.14 shows a schematic of the gun with and without an enlarged beam pipe aperture of 19cm. The density of HOMs is quite small below 6 GHz beyond which the cavity modes are above the beam pipe cut-off. Also, the increase in the beam pipe aperture to 19 cm is only effective in propagating a subset of the trapped modes. Further increase in aperture may not be feasible without compromising beam emittances. Therefore, the choice of an enlarged beam pipe was avoided at the cost of having a few extra undamped modes. This allows one to bring the FPC closer to the cavity and couple strongly without requiring to penetrate deep into the beam pipe. The straight beam pipe also allows one to bring the first solenoid closer to the gun to improve the beam emittances, as well as

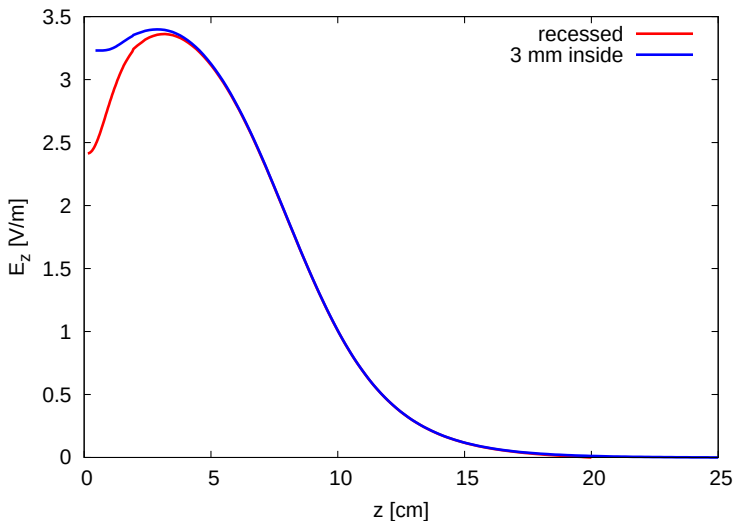

Figure 9.10: The magnitude of the electric field plotted a function of longitudinal position for the recessed and non-recessed cathode cases. The non-recessed cathode shows a field enhancement in the proximity of the cathode which is important to accelerate the electrons immediately to counteract space charge effects.

simplify several engineering issues.

Fig. 9.13 also shows a train of Dirac-δ functions (black spikes) representing the harmonics of the bunch repetition frequency of 703.75 MHz. The harmonics are well separated from the high Q undamped modes which allievates the need for damping. However, if the repetition rate is much smaller than 703.75 MHz, the number of harmonics will consequently become large. This may cause an inevitable overlap with one or more of the cavity resonances and dissipate large amounts of beam power into the HOMs. A tuning mechanism (possibly a HOM tuner) may become necessary to detune the HOM frequencies to avoid resonant excitation for lower repetition rates.

The bunches emitted from the cathode can also exhibit variation in amplitude and timing jitter caused by the amplitude and timing jitter of the laser. The modulation is usually random in nature and will induce a change in the frequency spectrum of the harmonics. It is important to understand the spectral behavior of the beam harmonics in the presence of the modulation to avoid any overlap with the cavity resonances. The spectral power density of a modulated current of pulse shape $p(t)$ is derived in appendix B for general uncorrelated variables. For simplicity, we will assume that the harmonics represent a infinite train of Dirac δ functions ($\hat{p}(\omega) = 1$) separated by T_0. The

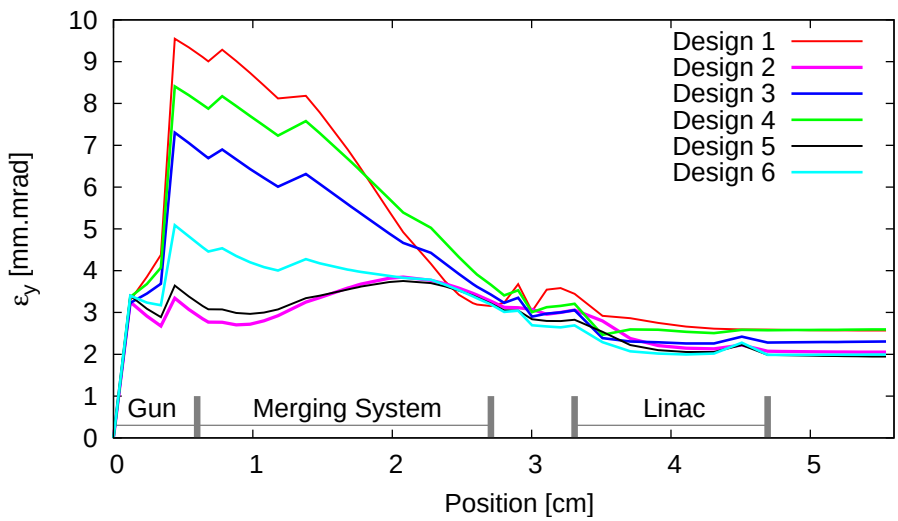

Figure 9.11: Vertical emittance calculated by PARMELA for the six designs in a beam line with the gun, merging system and 20 MeV linac.

amplitude modulation and time jitter can be included into the beam current as

$$I(t) = \sum_{n=-\infty}^{\infty} a_n \delta(t - nT_0 - \epsilon_n) \tag{9.2}$$

where a_n and ϵ_n are random uncorrelated variables. Assuming that a_n and ϵ_n have uniform distributions with rms σ_a and σ_ϵ respectively, the spectral power can be calculated from Eqs. E.13 and E.14 and is given by

$$\begin{aligned} P(\omega) &= \frac{2\pi}{T_0^2} \underbrace{\left[\frac{\sin(\sqrt{3}\omega\sigma_\epsilon)}{(\sqrt{3}\omega\sigma_\epsilon)}\right]^2}_{envelope} \sum_{m=-\infty}^{\infty} \underbrace{\delta\left(\omega - \frac{2\pi m}{T_0}\right)}_{harmonics} \\ &\quad + \frac{1}{T_0} \underbrace{\left[\left(1 - \left[\frac{\sin(\sqrt{3}\omega\sigma_\epsilon)}{(\sqrt{3}\omega\sigma_\epsilon)}\right]^2\right) + \sigma_a^2\right]}_{baseline} \end{aligned} \tag{9.3}$$

From Eq. 9.3, it can be seen that the power spectrum has two components. The first component represents the harmonics of the bunch repetition frequency given by a Dirac comb suppresed by a sinc envelope. The second component is a "baseline" sinc function independent of the harmonics and can result in large HOM power for large σ_ϵ and σ_a. Fig. 9.15 shows a simulation

Table 9.3: Beam dynamics parameters for the six designs under consideration as shown in Fig. 9.2.

Shape	$k_{\|\|}$ [V/pC]	$k_{\perp}$ [V/pC/m]	ϵ_y [mm.mrad]	$\delta E/E$
Design 1	0.692	49.1	2.569	7.4 %
Design 2	0.7397	31.42	2.053	3.9 %
Design 3	0.7011	31.62	2.306	6.2 %
Design 4	0.7155	32.3	2.595	6.3 %
Design 5	0.7225	31.74	1.944	3.86 %
Design 6	0.6981	32.25	1.993	4.4 %

Table 9.4: Cavity geometrical parameters using the parametrization decribed in Ref. [68] of the right half-cell for design 5. The left wall angle of the gun was maintained at 6.5° with a cathode radius of 1.46 cm.

Parameter	Right Half-Cell
Frequency	703.75 MHz
Iris Radius, R_{iris}	5.0 cm
Wall Angle, α	6.5°
Equatorial Ellipse Ratio, $R = \frac{B}{A}$	1.1
Iris Ellipse Ratio, $r = \frac{b}{a}$	1.2
Dist. from cav. wall to iris plane,	1.0 cm
Active cavity Length, L	8.5 cm
Dist. from center to equator end	18.95 cm
Avg. Beta, $< \beta = \frac{v}{c} >$	0.587

of the effect of amplitude modulation (10%) and timing jitter (10 ps) with uniform random distributions and is compared to the analytical expression. The finite number of frequency samples in the simulation result in the sinc like behavior of the harmonics (see Eq. E.12).

It is of interest to estimate the additional voltage induced in a given trapped mode due to the beam fluctuations. An approximate expression for the induced voltage for a simple statistical model for the fluctuations is derived in appendix C. Assuming a bunch length of 1 cm, $\sigma_a = 1\%$, $\sigma_\epsilon = 1$ps, and a $Q_{ext} \approx 10^8$, the ratio of the voltage induced due to fluctuations to the accelerating voltage ($\sim$ 2 MV) for the first longitudinal trapped HOM (TM_{011}) is approximately 9×10^{-3}. These modulation criteria for σ_a and σ_ϵ are easily feasible with

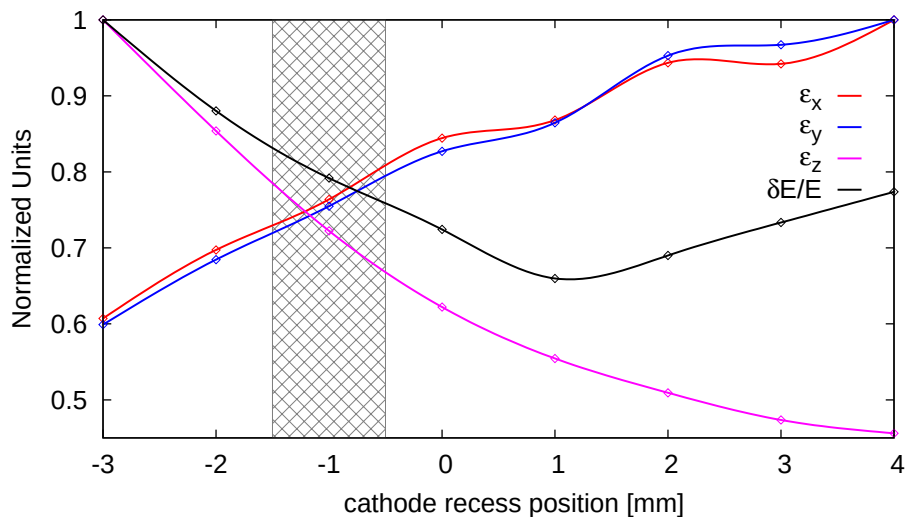

Figure 9.12: Longitudinal and transverse emittances at the end of a 20 MeV Linac for different positions of the cathode in SRF gun (results of PARMELA simulations). The energy of the e^- at the exit of the gun was fixed. Note that all emittances are normalized and the solid lines are spline fits to the simulation points.

current technologies. However, the induced parasitic voltage is significant, and the contribution to the energy spread is comparable to that of space charge effects. Therefore, tighter tolerences will be required to suppress the effects of laser fluctuations. Furthermore, the presence of a strongly coupled FPC, although not matched to HOM frequency, is expected to damp the HOMs ($Q_{ext} \ll 10^8$), and therefore relax the modulation criteria.

9.4.2 Fundamental Power Coupler

Another critical component of the SRF gun is the design of FPC. The SRF gun is being designed to generate a 2 MeV beam with an average current of 500 mA or larger. Therefore, the average RF power required is ≥ 1 MW, thus requires very strong coupling ($Q_{ext} \sim\ 4-5\times10^4$). Several options of electrical and magnetic coupling were considered, and a coaxial coupler with a "pringle" shaped electrical tip was found to be an effective choice. The pringle shape (originally designed for the Cornell ERL injector [103]) with a contour radius of the beam pipe is used to maximize coupling while minimizing wakefield effects. Fig. 9.16 shows a graphic of the SRF gun with the dual fundamental couplers (FPCs) to couple RF power into the gun.

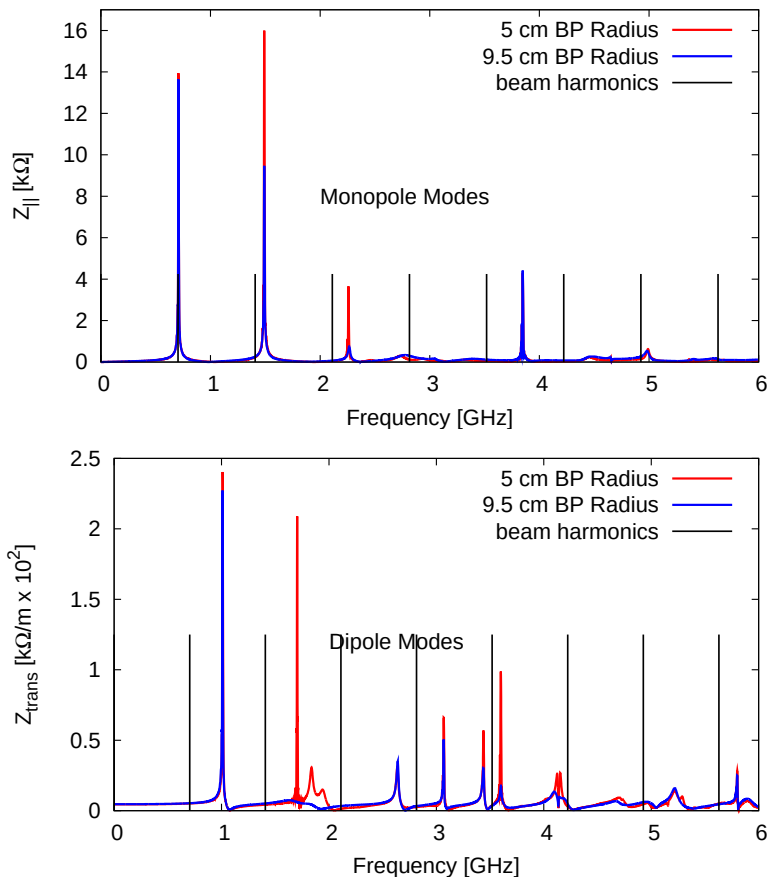

Figure 9.13: Broadband impedance spectrum calculated using ABCI [87, 88] for longitudinal (monopole like) and transverse (dipole like) modes for the two different beam pipe transitions. The black δ functions represent the harmonics of the bunch repetition frequency.

The beam pipe radius and the distance of the FPC to the cavity is fixed due to beam dynamic issues and engineering constraints. Therefore, the following geometrical aspects of the coupler were studied to increase coupling while minimizing the penetration of the inner conductor to reduce coupler kicks and wakefields. Note that the Q_{ext} for the optimization scans were calculated from the 3 db bandwidth of the transmission coeffcient (S_{21}) using the frequency domain of Microwave studio [102, 121].

- The intersection of the outer conductor and beam pipe was blended as shown in Fig. 9.17. A scan of Q_{ext} as a function of the blend radius is plotted in Fig. 9.17. The two curves represent scans performed with

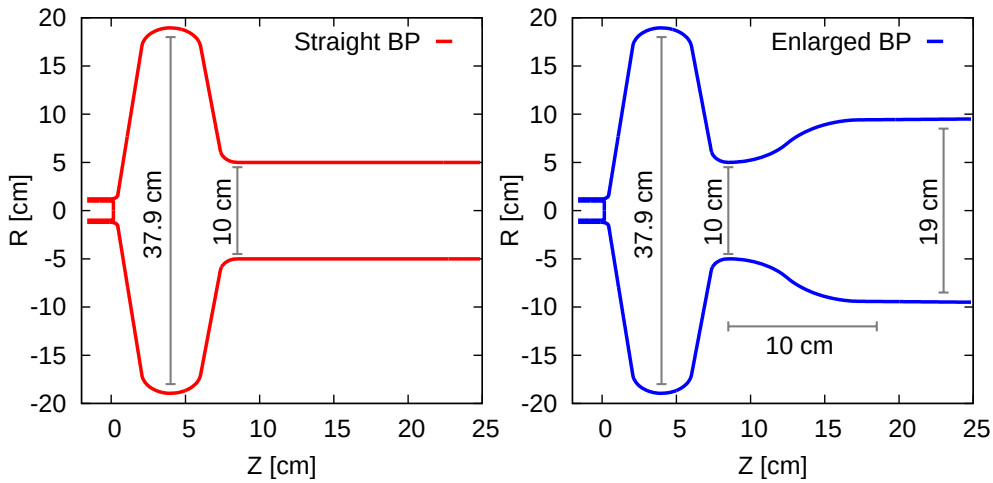

Figure 9.14: Graphic of the two different transition sections considered for the SRF gun. The straight beam pipe without enlargement is preferred due to the simplicity in manufacturing at the cost of a few undamped modes.

two different pringle radii (25 cm, 30 cm) which exhibit approximately linear behavior. A larger radius is prefered, but the actual radius will be constrained by the helium vessel and tuning fixtures.

- An elliptical pringle was found to provide larger coupling than a circular pringle. This is partially due to the geometry of the outer conductor and the beam pipe intersection. The optimized semi-major ($x_r \approx 36$ mm) and semi-minor ($y_r \approx 27$ mm) axes of the pringle cross section and the contour of the elliptical pringle are shown in Fig. 9.18. A scan of Q_{ext} as a function of the transverse dimensions of the pringle is shown in Fig. 9.19. A larger x_r is prefered, but it cannot exceed the radius of the outer conductor due to clearance for assembly of the FPC in clean room conditions.

- The thickness of the pringle tip was also varied to study the effect on coupling. Fig. 9.20 shows scans of Q_{ext} as a function of the tip thickness for two different pringle radii (25 mm and 30 mm). The thickness has a stronger influence on Q_{ext} for a larger pringle radius. A thinner pringle is prefered, but it should be mechanically rigid.

- With the most optimized geometry of the coupler, the penetration of the inner conductor into the beam pipe was varied to achieve the required coupling. Fig. 9.21 shows a a scan of the Q_{ext} as a function of

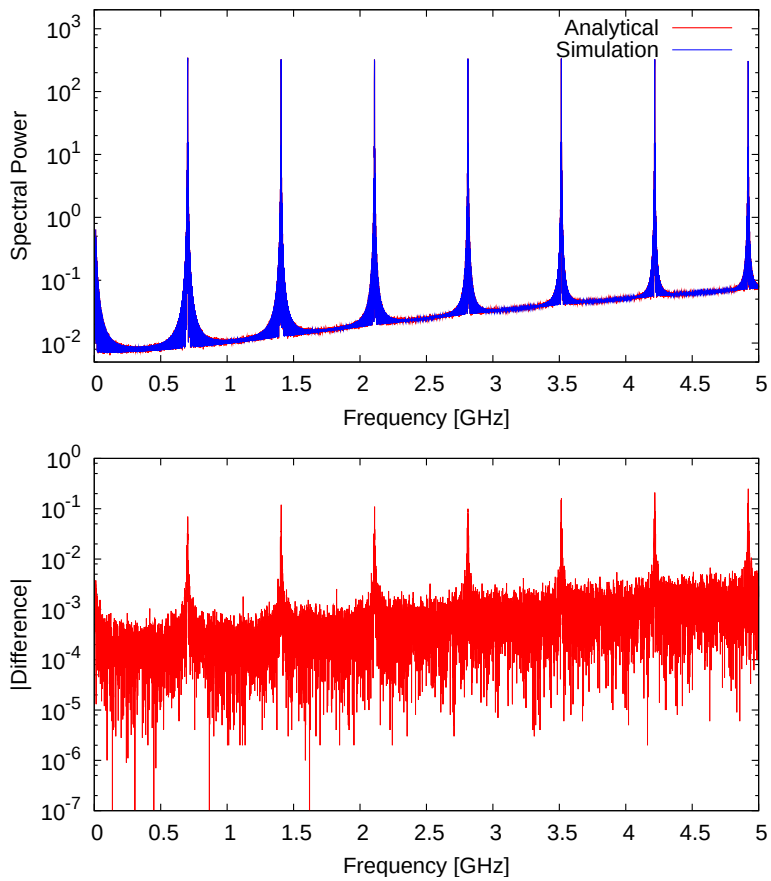

Figure 9.15: Top: Simulation of the frequency spectrum of the harmonics of the bunch repetition frequency in the presence of timing jitter ($\sigma_\epsilon = 10$ ps) and amplitude modulation ($\sigma_a = 10$ %) compared to Eq. E.12. Bottom: Absolute value of the difference between analytical formula and simualtion.

the penetration depth. With the geometric modifications, the required $Q_{ext} \sim 4 - 5 \times 10^4$ can be achieved with penetration of $\leq$ 2mm which is significantly less than previously required 10 mm [107].

The presence of a FPC can lead to a non-zero transverse field on-axis resulting in a kick to a bunch traversing the structure. Since, the energy of the beam is relatively low ($\sim$ 2 MeV), the effect of the kick on the bunch can be significant. One of the remedies to minimize the transverse kick is to add a symmetric coupler to cancel the effect. On top of minimizing the kick, the average power through coupler would be also halved, thus relaxing the power handling of the FPCs. However, symmetric couplers are prone to

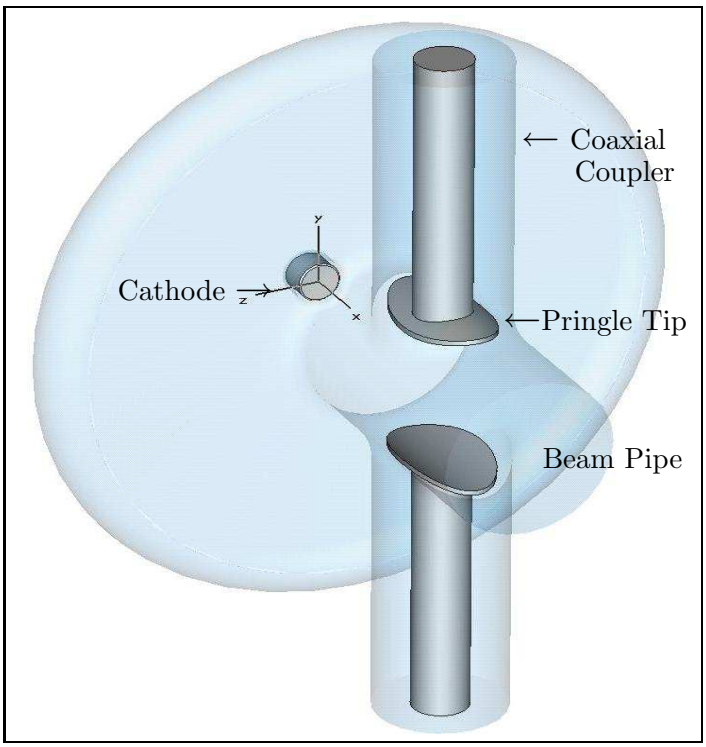

Figure 9.16: 3D graphic of the 703.75 MHz SRF gun with the dual FPCs with an optimized "pringle" tip.

manufacturing and alignment errors, but the transverse kick is significantly smaller compared to a gun with a single coupler. For a dual coupler geometry, an asymmetry in the penetration or a phase mismatch between the coaxial lines can result in a transverse kick. The transverse fields for both cases are shown in Fig. 9.22 and the respective transverse kicks are computed using an approach similar to described in Ref. [103].

The transverse "kick factor" is simply given by

$$\delta_t = \frac{\int (E_y + v_z B_x) dz}{\int E_z dz} \tag{9.4}$$

which can be numerically evaluated. The normalized emittance growth due to the time dependent RF kick can be estimated using the formula derived in Ref. [105] which is given by

$$d\epsilon_n = \sigma_t \frac{2\pi\sigma_z}{\lambda_{RF}} \frac{eV_{acc}}{E_0} \left|\mathrm{Re}(\delta_t)\sin\phi_0 + \mathrm{Im}(\delta_t)\cos\phi_0\right| \tag{9.5}$$

where ϕ_0 is the bunch phase with respect to the RF, E_0 is the rest mass of

the e^-, σ_t and σ_z are the transverse and longitudinal beam sizes, and V_{acc} is the voltage of the accelerating gap. Table 9.5 shows the kick factors and relative emittance growths for the two cases with transverse RF fields. In both cases, the emittance growth estimates are quite small compared to space charge induced growth.

Table 9.5: Transverse kick and normalized emittance growth for a two-coupler scheme with an asymmetry in penetration depth and phase offset respectively.

Asymmetry	Kick	$d\epsilon_n/\epsilon_n$
Tip Penetration (1 mm)	(-6.1 - 5.0i)$\times 10^{-5}$	$< 3\%$
Phase Offset (1 deg)	(8.4 - 5.9i)$\times 10^{-5}$	$< 3\%$

9.4.3 Cathode Isolation & Design Issues

The addition of a replaceable and variable laser photo-cathode (for example cesium potassium antimonide) in ultra clean superconducting environment adds to the overall complexity of design. Some of the main issues are as follows

- Providing a demountable joint that is thermally isolated from the cavity to minimize heat load into the liquid helium environment.
- The demountable joint also carries a large RF current which must be prevented from developing large losses in the normal-conducting joint.
- Avoid strong multipacting in the cathode stalk
- A separate liquid nitrogen channel is required to remove the heat generated in the cathode.
- The cathode material should be replaceable without breaking the vacuum while keeping the gun at superconducting temperature.

A simple approach involving a multiple quarter wave choke joint is being designed for RF isolation of the demountable cathode insertion. Triangular groves on the choke joint are under investigation to suppress multipacting by effectively reducing the SEY by geometric means. Initial tests on a copper prototype show no evidence of strong multipacting for the proposed design [123].

The structure of the cathode current stimulated by the laser also can be a source of abundant harmonics causing extra losses in the choke. Since, the

choke is only a short for the fundamental mode (703.75 MHz), it must be designed carefully to avoid any resonances that will coincide with the harmonics of the bunch repetition frequency and result in large losses [124].

9.5 Ideas for a $1\frac{1}{2}$-Cell Gun for e^- Cooling

For e^- cooling, the injection energy is set at ∼5 MeV. The beam requirements are outlined in Table 6.1. The injector gun for e^- cooling will also be a all niobium SRF gun with $1\frac{1}{2}$ cells. Under the assumption of high gradient (25-50 MV/m), it was shown that a longer first $\frac{1}{2}$ cell ($\sim 0.6\lambda/2$) was optimum for final longitudinal and transverse emittances [125, 126]. Similar to the $\frac{1}{2}$-cell gun for the prototype, an optimization of the cell shape is underway for the $1\frac{1}{2}$ cell gun. This is an iterative procedure to optimize both RF issues and final beam emittance. A few initial designs with a half-cell length of $\lambda/2$ and different iris radii were developed as a starting point as shown in Fig 9.23.

The presence of a second cell with only one beam pipe opening poses a challenge of possible trapped HOMs which are now twice as many compared to the $\frac{1}{2}$-cell gun. However, the addition of the second cell relaxes the need for having a small iris, and allows one to use this as tuning parameter for better HOM damping. The goal of the iterative procedure is to arrive at a final iris radius and cell lengths of the two cells to have the best possible HOM damping as well as the small final beam emittances. The general procedure will follow the steps outlined below:

- Iris radius optimization
  - Study of HOM spectrum and impedances as function of R_{iris}
  - Frequecies of HOMs and respective cut-off frequecies for different radii
- Beam pipe transition
  - Propagate of modes below cut-off of the final R_{iris}
  - Strong fundamental power coupling without large penetration of coaxial attenna
- Determine optimum length of cell lengths (l_1 and l_2)
  - Maximize the positive slope on the energy-initial phase curve for longitudinal focusing

  - Minimize transverse emittances

- Determine optimum cavity geometrical parameters using peaks field, R/Q, mechanical stability and other relevant issues [1].

Other issues like fundamental power coupler and cathode stalk design can be directly adapted from the $\frac{1}{2}$-cell design.

9.6 Conclusion

A prototype SC-ERL is underway to test various components and physics issues to demonstrate the feasibility of ampere class ERLs. A $\frac{1}{2}$ cell SRF gun with diamond amplified photo-cathode is chosen as the injector to the SC-ERL. Six potential designs for the $\frac{1}{2}$ cell gun have been presented and several RF, mechanical and beam dynamics issues were used in the optimization of the final choice of the gun shape. Design 5 was found to adequately satisfy RF and mechanical constraints as well as provide longitudinal and transverse focusing to combat space charge forces thus resulting in a low emittance beam with a small energy spread. Issues related to multipacting, cathode insertion, and laser stability were also presented. A general procedure for the development of a $1\frac{1}{2}$-cell for e^- cooling is outlined with some initial designs under progress.

[1] The cavity geometrical parameters like the ellipse ratios have been determined from an intial optimization run.

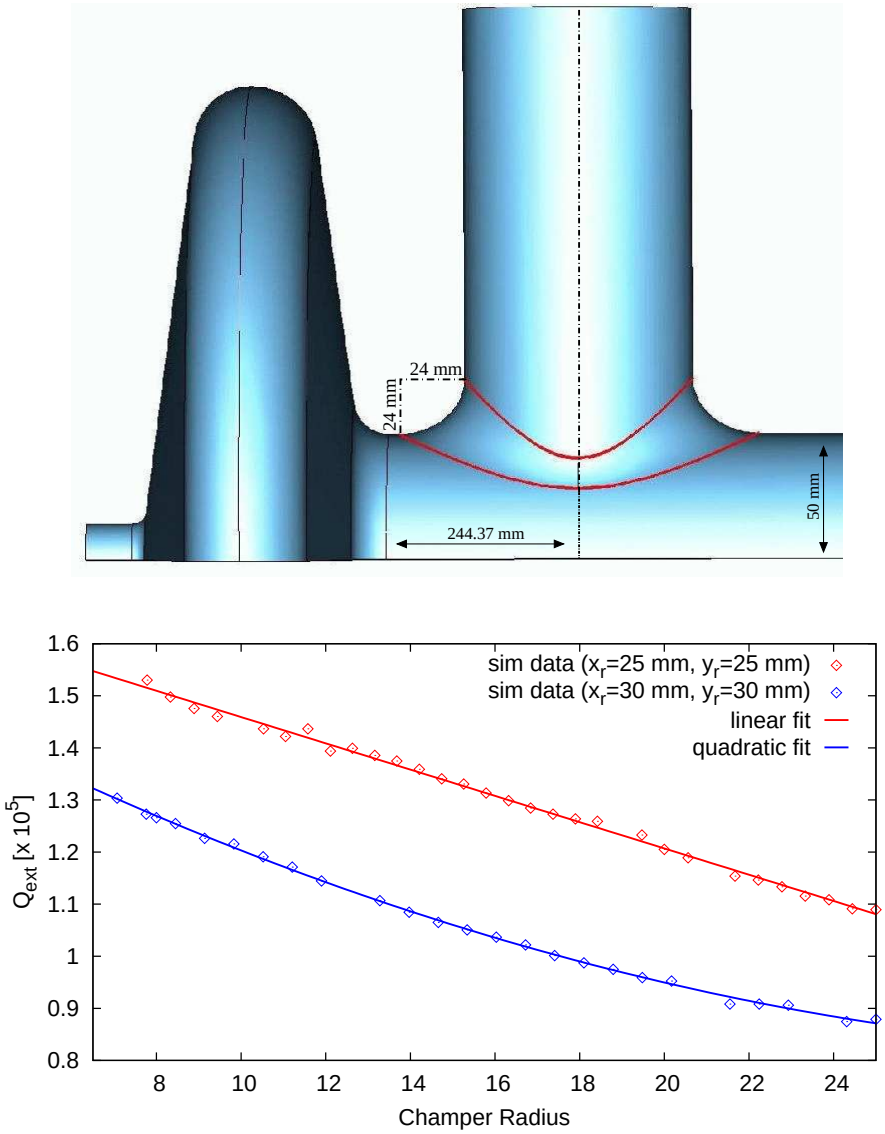

Figure 9.17: Top: Graphic of the symmetric top-half of the SRF gun with the FPC outer conductor intersection to the beam pipe. This intersection is blended using an arc to couple stronger to the fundamental mode without increasing the entire beam pipe radius. Bottom: Q_{ext} plotted as a function of the blend radius of the edge between FPC and the beam pipe. The two curves represents the scan with two different pringle radii.

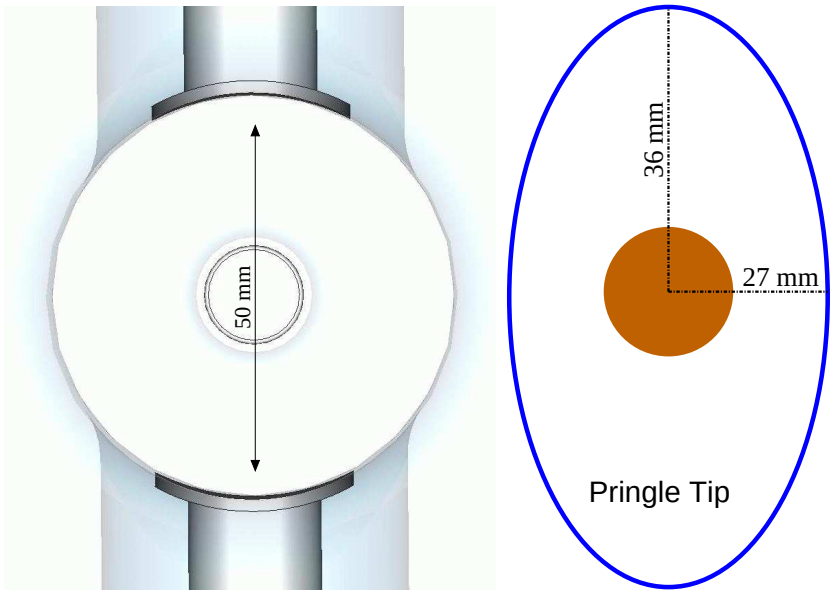

Figure 9.18: Left: A longitudinal cross section of the SRF gun and the coupler which shows the contour of the pringle tip. Right: The transverse dimensions of the elliptical pringle optimized for maximum coupling.

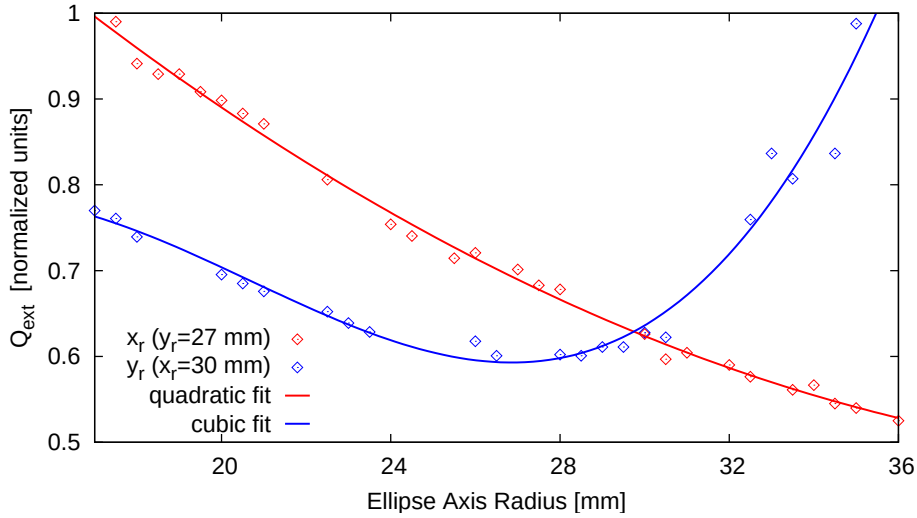

Figure 9.19: A scan of Q_{ext} as a function of the transverse dimensions of the elliptical pringle. The solid lines are quadractic and cubic fits for x_r and y_r respectively. The y-axis is normalized to compare the effect of both transverse dimensions on the same scale.

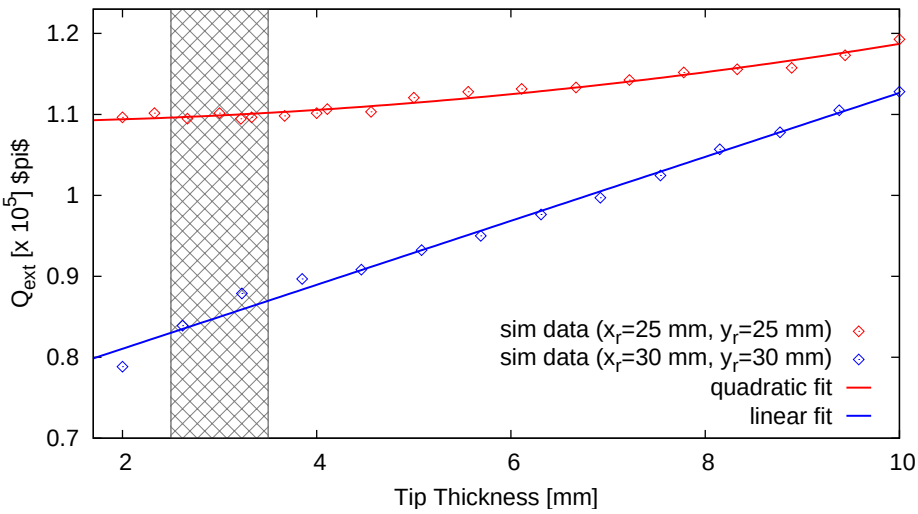

Figure 9.20: A scan of Q_{ext} as a function of the thickness of the tip for two different pringle radii. The solid lines are fits to the the calculated Q_{ext} points which are approximately linear.

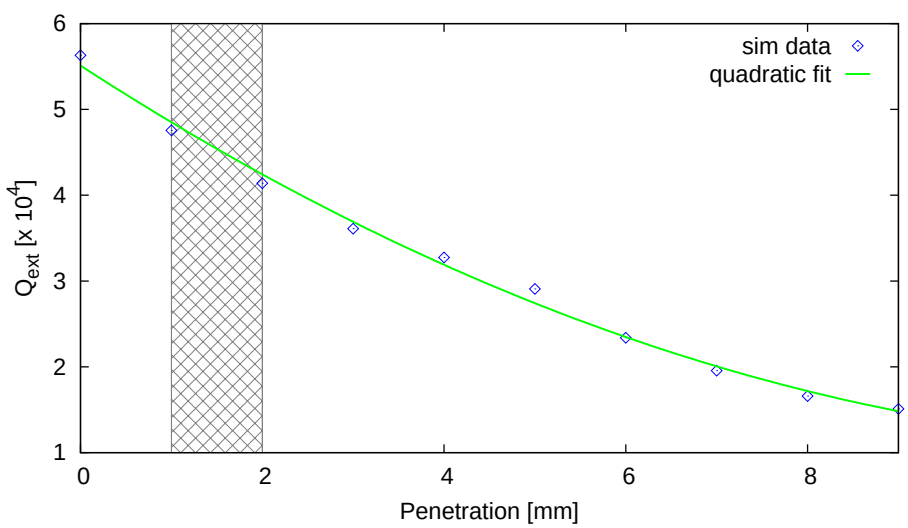

Figure 9.21: A scan of Q_{ext} as a function of the penetration of the tip in to the beam pipe. The solid line is a quadratic fit to the the calculated Q_{ext} points. The shaded area shows the expected penetration to achieve the required Q_{ext}.

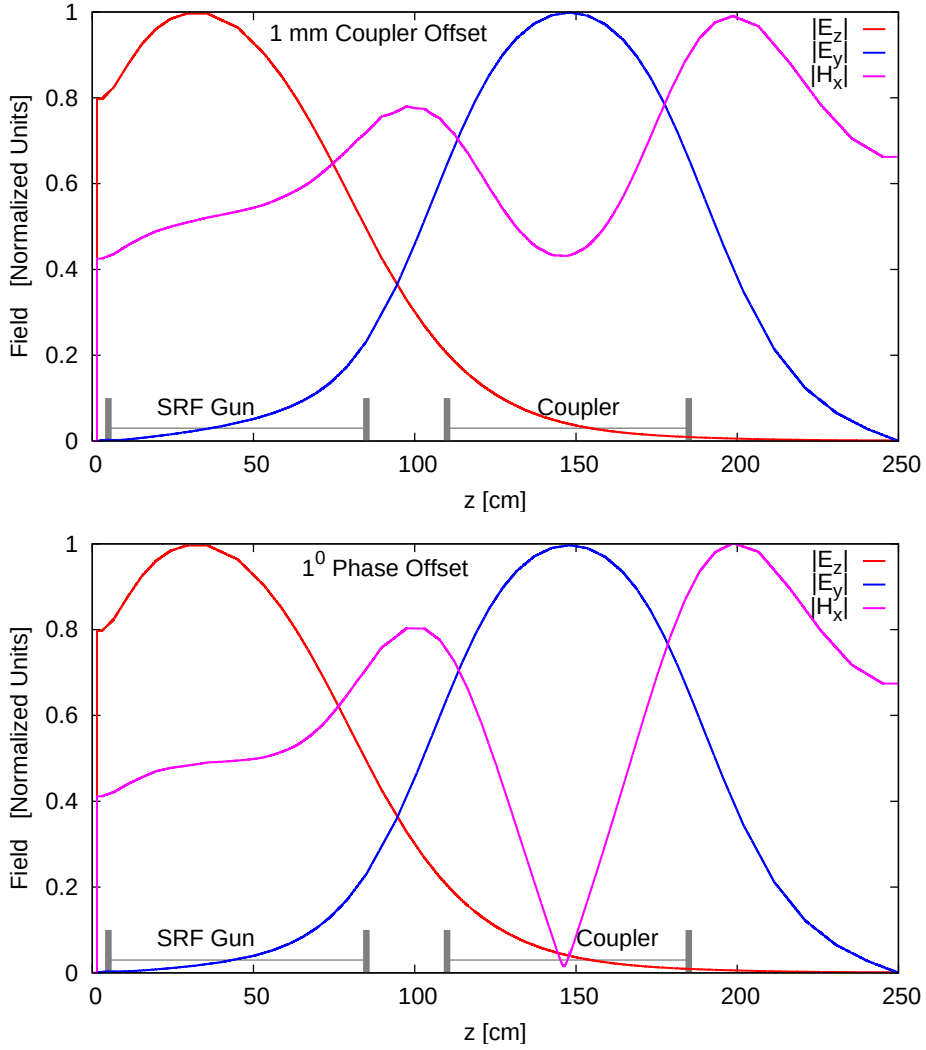

Figure 9.22: Longitudinal and transverse fields on-axis of the SRF gun due to 1 mm asymmetry in the coupler penetration between the dual couplers (top) and 1^0 phase offset between the dual couplers (bottom) [104].

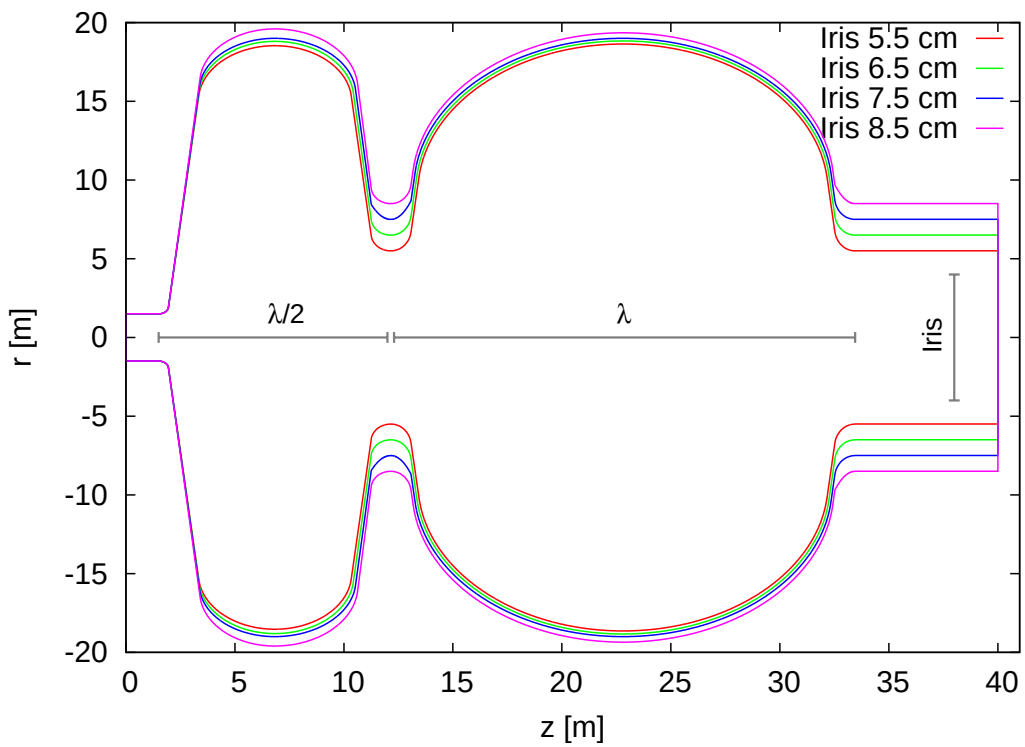

Figure 9.23: Initial design of the $1\frac{1}{2}$-cell gun designs with half-cell length of $\lambda/2$, and different radii (5.5-8.5 cm) for e^- cooling injector.

Chapter 10

Conclusions

10.1 Part I: Linear Optics and Coupling

The knowledge of accurate linear optics and coupling and appropriate lattice corrections are fundamental to the RHIC collider performance and sustain stable operation. An approach using SVD technique on BPM data with coherent betatron oscillations driven by ac dipoles has been discussed in detail. Optics measurement during a tune scan experiment during Run 2004 is presented and no significant effect on machine tunes were found on global β-beat which was approximately 15%. Two approaches using a global correction and local three β-bump have been outlined. Simulations on LHC lattice to keep the β-beat level under a strict aperture limitation of 20% are underway.

The SVD approach has been extended to fully coupled system and relevant parameters characterizing coupling parameters in the lattice have been derived. A comparison of different formalisms were made and numerical techniques to determine the coupling terms have been discussed. Detailed measurements from ac dipole driven data have been analyzed for RHIC at injection and top energies. A possible corrector scan strategy was implemented due to several constraints imposed by the BPM system. The nominal IR corrector settings are clearly not the most optimum and suggested settings for improvements are presented. An anomalous slope phenomena observed is under investigation and fitting techniques are being implemented to identify the sources for this behavior.

10.2 Part II: SRF Cavities

A SC-ERL has been identified as the most viable technology for generating and accelerating ampere class CW electron beams to $\sim$54 MeV. These high

energy electrons low emittance electrons are introduced into RHIC to cool the ion beams and combat intra-beam scattering resulting in an increase of both the peak and average luminosity. The two fundamental components of the SC-ERL, the $\frac{1}{2}$-cell SRF gun and a five-cell SRF cavity, are the central focus of part II of this thesis. A detailed design and development of the two components with comparisons to some existing and future SRF facilities are discussed. The optimization of the elliptical cell shape and the cavity structure along with strong HOM damping makes the five-cell cavity the first of its kind in the high current regime. Extensive simulations and measurements on copper prototypes have been carried and beam breakup thresholds beyond 2 Amps was calculated for the electron cooling scheme. The fabrication of the cavity is complete and chemical treatment of the cavity surface is underway. Extensive testing at 2 K and cryostat assembly will follow the chemical surface treatment.

The $\frac{1}{2}$-cell gun will be the first step to develop an all niobium SRF gun with a diamond amplified photo-cathode. A detailed study of both RF and beam dynamics issues lead to a final optimized gun shape. Several major challenges including an intricate power coupler, cathode stalk, laser stability issues have been overcome. A conceptual $1\frac{1}{2}$-cell design has been developed for the electron cooling scheme, and further optimization is required to arrive at the final design.

Appendix A

Perturbative View of BPM data Decomposition

Taylor expanding 'b' over all physical variables:

$$\begin{aligned} b - \langle b \rangle &= \sum_{v} \left.\frac{\partial b}{\partial v}\right|_{v=\overline{v}} (\Delta v - \langle \Delta v \rangle) \\ &+ \frac{1}{2} \sum_{v_1, v_2} \left.\frac{\partial^2 b}{\partial v_2 \partial v_1}\right|_{v=\overline{v}} (\Delta v_1 \Delta v_2 - \langle \Delta v_1 \Delta v_2 \rangle) \\ &+ \ldots \end{aligned}$$

where b is a function of $\overline{x}, \overline{x}', \overline{\delta}, \overline{\sigma}_z$ and other physical physical variables.

Treating 1st and 2nd order terms the same (higher-order negligible):

$$b - \langle b \rangle = \sum_{(q)} q f_q \tag{A.1}$$

where

$$q = \frac{\Delta v - \langle \Delta v \rangle}{std(\Delta v)} \tag{A.2}$$

$$= \frac{\Delta v_1 \Delta v_2 - \langle \Delta v_1 \Delta v_2 \rangle}{std(\Delta v_1 \Delta v_2)}, \tag{A.3}$$

and

$$f_q = \left.\frac{\partial b}{\partial v}\right|_{v} std(\Delta v) \tag{A.4}$$

$$= \left.\frac{\partial^2 b}{\partial v_2 \partial v_1}\right|_{v_1 v_2} std(\Delta v_1 \Delta v_2) \tag{A.5}$$

Eq. A.1 in matrix notation is simply

$$B = W V^T \tag{A.6}$$

Appendix B

Geometric view of coupled SVD modes

Since, the SVD modes are approximately linear combinations of the spatial eigenmodes, it is interesting to view the evolution spatial vectors for each axes in terms of a parametric plots as shown Fig. B.1 In the absence of coupling,

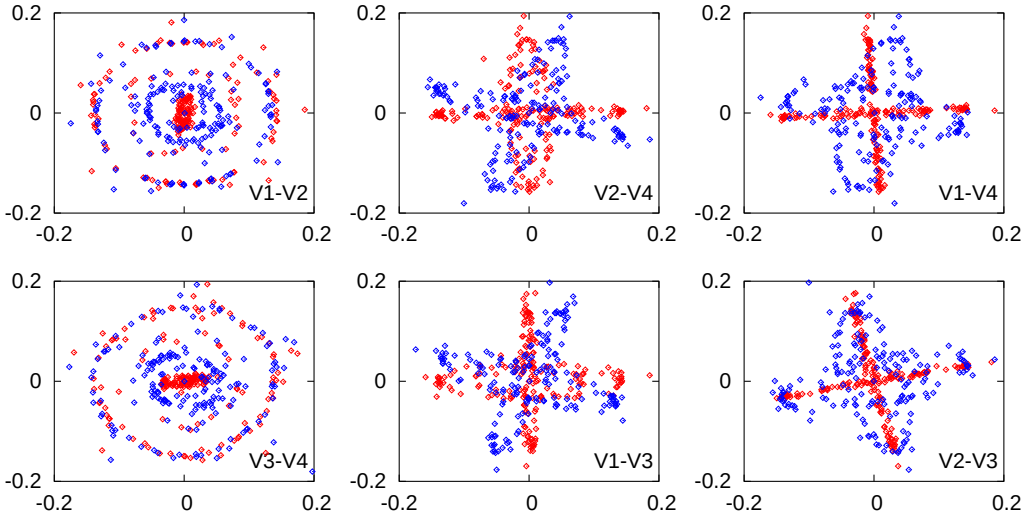

Figure B.1: Parametric plots of SVD modes of BPM data from each plane (x-red, y-blue). Data taken using ac dipoles during Run-2004.

parametric plots should simply exhibit orthogonal lines lying on the coordinate axes. The rotation with respect to the coordinate axes and the finite width to the ellipses point to non-zero coupling present in the lattice.

A simple inference from these plots can be made that there are approximately two angles of rotation (ϕ_1 and ϕ_2) by which the spatial vectors are rotated w.r.t to each other. One can construct a simple orthogonal rotation

matrix $O_{4\times 4}$ given by

$$\begin{bmatrix} \cos\phi_1 & 0 & -\sin\phi_1 & 0 \\ 0 & \cos\phi_2 & 0 & -\sin\phi_2 \\ \sin\phi_1 & 0 & \cos\phi_1 & 0 \\ 0 & \sin\phi_2 & 0 & \cos\phi_2 \end{bmatrix} \tag{B.1}$$

which will rotate the SVD modes into the physical eigenmodes Although, this approach maybe more intuitive, one has to rely on fitting techniques to accurately determine these angles. The harmonic projection is in the frequency domain is far simpler and probably yield a numerically more accurate O matrix. Nevertheless, the outcome of this parametric plots are interesting.

Appendix C

Coupling Matrix

C.1 Propagation of the $\overline{\mathbf{C}}$ matrix

In a coupler free region $\overline{\mathbf{C}}$ matrix is simply propagated by an arbitrary phase advance in both modes which is given by [40]

$$\overline{\mathbf{C}}_{\mathbf{2}} = \mathbf{R}_x(\phi_x)\overline{\mathbf{C}}_{\mathbf{1}}\mathbf{R}_y^{-1}(\phi_y) \tag{C.1}$$

where $\mathbf{R_{x,y}} = \begin{pmatrix} \cos\phi_{x,y} & \sin\phi_{x,y} \\ -\sin\phi_{x,y} & \cos\phi_{x,y} \end{pmatrix}$.

If coupling is small and couplers modeled as thin skew quadrupoles, the $\overline{\mathbf{C}}$ is propagated to first order given by [47]

$$\overline{\mathbf{C}}_{\mathbf{2}} = \overline{\mathbf{C}}_{\mathbf{1}} - \overline{\mathbf{k}} \tag{C.2}$$

where

$$\overline{\mathbf{k}} = \begin{pmatrix} 0 & 0 \\ \overline{k} & 0 \end{pmatrix} \tag{C.3}$$

with $\overline{k} = \sqrt{\beta_a^{skew}\beta_b^{skew}}k$ and k is the strength of the coupler. Here γ is assumed to be 1.

C.2 Normalized momenta

The normalized momenta $\hat{p}_{x,y}$ are given by the normalized positions at a location $\pi/2$ apart. This location does not have to correspond to any physical location. To compute $\hat{p}_x$ the $\overline{\mathbf{C}}$ matrix is propagated by $\pi/2$ in the horizontal mode and an arbitrary ϕ_y in the vertical mode

$$\begin{aligned} \overline{\mathbf{C}}' &= \mathbf{R}_x(\pi/2)\mathbf{C}\mathbf{R}_y^{-1}(\phi_y) \\ &= \begin{pmatrix} \overline{C}_{21}c\phi_y + \overline{C}_{22}s\phi_y & -\overline{C}_{21}s\phi_y + \overline{C}_{22}c\phi_y \\ -\overline{C}_{11}c\phi_y - \overline{C}_{12}s\phi_y & \overline{C}_{11}s\phi_y - \overline{C}_{12}c\phi_y \end{pmatrix} \quad . \end{aligned} \tag{C.4}$$

where $c\phi = \cos(\phi)$ and $s\phi = \sin(\phi)$. Therefore, $\hat{p}_x$ is obtained by using $\hat{x}$ and $\overline{\mathbf{C}}'$ as the $\overline{\mathbf{C}}$ matrix at the new location,

$$\begin{aligned}
\hat{p}_x &= \gamma A_x \cos(\psi_x + \pi/2) + \\
&\quad A_y\Big((\overline{C}_{21}\cos\phi_y + \overline{C}_{22}\sin\phi_y)\cos(\psi_y + \phi_y) - \\
&\quad (-\overline{C}_{21}\sin\phi_y + \overline{C}_{22}\cos\phi_y)\sin(\psi_y + \phi_y)\Big) \\
&= -\gamma A_x \sin\psi_x + \\
&\quad A_y\Big(\overline{C}_{21}\cos\psi_y - \overline{C}_{22}\sin\psi_y\Big) \ . \qquad \text{(C.5)}
\end{aligned}$$

Note that the arbitrary ϕ_y has canceled out and $\hat{p}_x$ only depends on parameters evaluated at the initial physical location. Similarly for $\hat{p}_y$,

$$\begin{aligned}
\hat{p}_y &= -\gamma A_y \sin\psi_y + \\
&\quad A_x\Big(\overline{C}_{21}\cos\psi_x + \overline{C}_{11}\sin\psi_x\Big) \ . \qquad \text{(C.6)}
\end{aligned}$$

C.3 $\overline{C}_{21}$ in coupler free region

Using Eq. (C.1), $\overline{\mathbf{C}}$ matrix elements at two locations are related in terms of the phase advance alone which is expressed as,

$$\begin{pmatrix} C_{11}^{(2)} \\ C_{12}^{(2)} \\ C_{21}^{(2)} \\ C_{22}^{(2)} \end{pmatrix} = \begin{pmatrix} c\phi_x c\phi_y & c\phi_x s\phi_y & s\phi_x c\phi_y & s\phi_x s\phi_y \\ -c\phi_x s\phi_y & c\phi_x c\phi_y & -s\phi_x s\phi_y & s\phi_x c\phi_y \\ -s\phi_x c\phi_y & -s\phi_x s\phi_y & c\phi_x c\phi_y & c\phi_x s\phi_y \\ s\phi_x s\phi_y & -c\phi_x c\phi_y & -c\phi_x s\phi_y & c\phi_x c\phi_y \end{pmatrix} \times \begin{pmatrix} C_{11}^{(1)} \\ C_{12}^{(1)} \\ C_{21}^{(1)} \\ C_{22}^{(1)} \end{pmatrix} , \qquad \text{(C.7)}$$

where $c\phi = \cos(\phi)$ and $s\phi = \sin(\phi)$. Given two BPM locations at which turn-by-turn data is recorded, $\overline{C}_{12}/\gamma$, $\overline{C}_{11}/\gamma$, and $\overline{C}_{22}/\gamma$ are calculated as illustrated in section 4.3.1. The phase advances between the two locations can also be determined using SVD techniques from the same turn-by-turn data [25]. Rearranging the second row of Eq. (C.7), $\overline{C}_{21}/\gamma$ is exactly calculated

in a coupler free region which is given by

$$\begin{aligned}\overline{C}_{21}^{(1)} &= \Big(-\overline{C}_{11}^{(1)} \cos\phi_a \sin\phi_b + \overline{C}_{12}^{(1)} \cos\phi_a \sin\phi_b \\ &\quad + \overline{C}_{22}^{(1)} \sin\phi_a \cos\phi_b - \overline{C}_{12}^{(2)} \Big) / (\sin\phi_a \sin\phi_b)\end{aligned} \tag{C.8}$$

C.4 Skew quadrupole strength from two BPMs

Using Eq. (C.1) and (C.2), $\overline{\mathbf{C}}$ matrix is propagated between two observation points with one skew quadrupole between them given by

$$\begin{aligned}\overline{\mathbf{C}}_{\mathbf{2}} &= \mathbf{R}_x(\phi_x^{skew+l}) \\ &\quad \times \Big[\mathbf{R}_x(\phi_x^{skew-l}) \overline{\mathbf{C}}_{\mathbf{1}} \mathbf{R}_y^{-1}(\phi_y^{skew-l}) - \overline{\mathbf{k}} \Big] \\ &\quad \times \mathbf{R}_y^{-1}(\phi_y^{skew+l})\end{aligned} \tag{C.9}$$

where $\phi_{x,y}^{skew\mp l}$ are the phase advances between the skew quadrupole and locations 1 and and 2 respectively. Determinants are distributive ($|\mathbf{AB}| = |\mathbf{A}| \times |\mathbf{B}|$), therefore

$$|\overline{\mathbf{C}}_{\mathbf{2}}| = |\mathbf{R}_x(\phi_x^{skew-l}) \overline{\mathbf{C}}_{\mathbf{1}} \mathbf{R}_y^{-1}(\phi_y^{skew-l}) - \overline{\mathbf{k}}| \tag{C.10}$$

since, $|\mathbf{R}_x(\phi_{x,y})| = 1$. Using Eq. (C.7) and (C.10) $\bar{k}$ is expressed as

$$\bar{k} = -\frac{|C^{(2)}| - |C^{(1)}|}{C_{12}^{skew}} \ , \tag{C.11}$$

which is equivalent to Eq.(4.42) derived from RDT's given that $\gamma = 1$.

Appendix D

Five-Cell SRF Cavity

D.1 Bead Pull for Fundamental Mode

In this technique, a small bead (radius $<< \lambda$) is introduced in the cavity to perturb the field which changes the resonant frequency proportional to the fields [110]. The frequency of a mode is commonly measured from scattering parameter S_{21} with a network analyzer. An equivalent and sometimes more sensitive measurement would be the phase shift of S_{21} at the unperturbed resonant frequency. The S_{21} is given by

$$S_{21} = \frac{2\sqrt{\beta_1\beta_2}}{(1+\beta_1+\beta_2) + iQ_0\left(\frac{\omega}{\omega_0} - \frac{\omega_0}{\omega}\right)} \tag{D.1}$$

where β_1 and β_2 are the coupling coefficients of input and output probes. If coupling is weak ($\beta_1, \beta_2 << 1$) and $\Delta\omega/\omega << 1$. then the change in frequency can be expressed as

$$\frac{\delta\omega}{\omega_0} \approx -\frac{1}{2Q_L} tan(\phi) \tag{D.2}$$

For spherical bead:

$$\frac{\delta\omega}{\omega_0} = \begin{cases} -\frac{\pi r^3}{U}(\epsilon_0 \frac{\epsilon_r+2}{\epsilon_r-1} E_0^2) & : \ dielectric \\ -\frac{\pi r^3}{U}(\epsilon_0 E_0^2 - \frac{\mu_0}{2} H^2) & : \ metal \end{cases} \tag{D.3}$$

By mapping the longitudinal electric field and using Eq. E.1, the shunt impedance can be calculated using

$$\frac{R}{Q}_{sphere} = -\frac{1}{2\pi\omega_0 r^3 \epsilon_0}[\int \sqrt{\frac{\delta\omega}{\omega_0}} \cos(kz) dz]^2 \tag{D.4}$$

D.2 BNL II - Alternate Design

A comparison of the broadband impedance spectrum for both longitudinal and transverse modes calculated using ABCI are shown in Fig. D.1 for BNL I, I-A and II designs as listed in Table 8.2. BNL I and I-A are essentially similar in geometry accept for subtle change in the end cell. Therefore, the impedance spectrum correspondingly looks similar. The spectrum for BNL

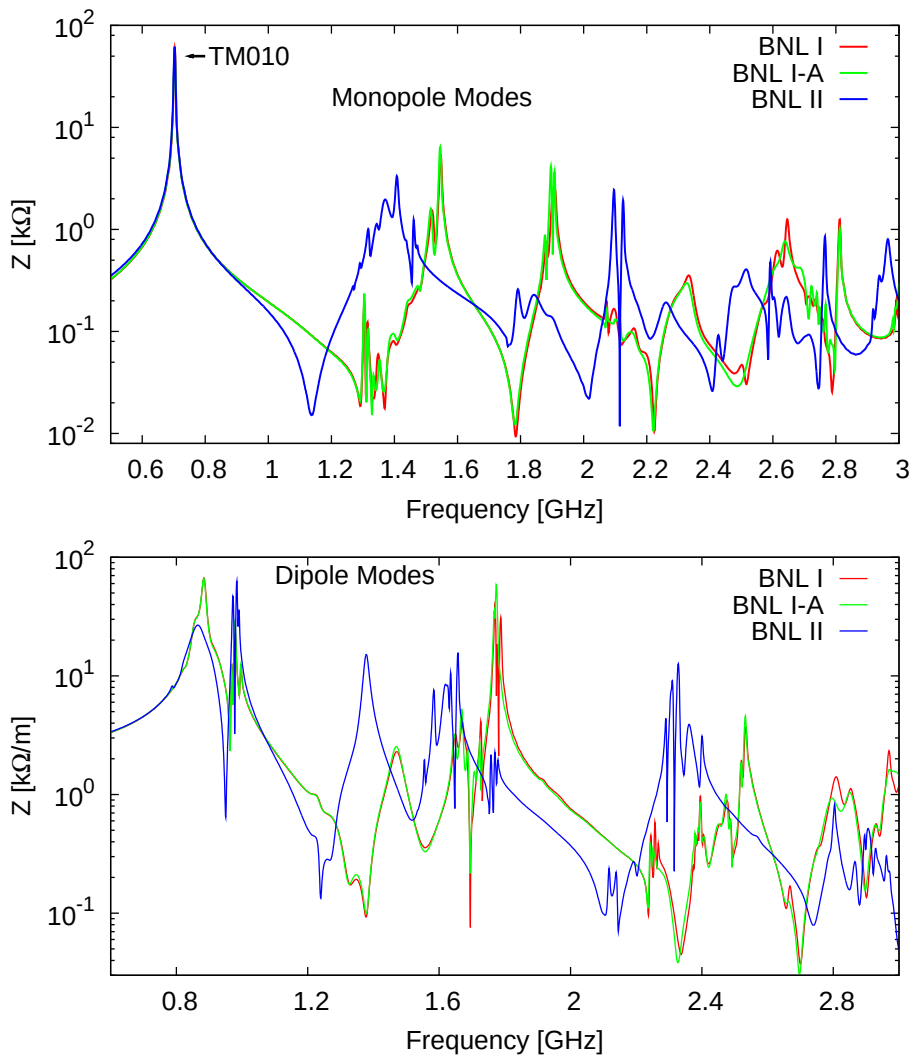

Figure D.1: Broadband impedance for monopole and dipole modes computed by ABCI for BNL I, I-A, and II designs.

II looks quite different for both monopole and dipole modes. For monopole

modes, the impedance peaks seems to have shifted to a lower frequency but the amplitude is similar to that of BNL I. In the case of dipole modes, the spectrum for BNL II shows smaller impedance values for the $5^{th} - 6^{th}$ passbands, but the larger for $2^{nd} - 3^{rd}$ and $8^{th} - 10^{th}$ passbands.

D.3 Bellow Shielding

Bellows are added on the beam pipe section of the five-cell cavity to allow longitudinal and transverse motion during cool down, warm up, alignment and transportation. The bellows are made of copper plated stainless steel. The primary power losses in these bellows can occur from surface currents of the fundamental mode and single bunch losses induced by the passage of beam. The beam pipe transition and the cold to warm transition section is designed to allow no more than 10 W of fundamental power being dissipated in bellow section. A counter flow of He gas on the beam pipe acts as a heat exchanger which is extracted out at 300 K.

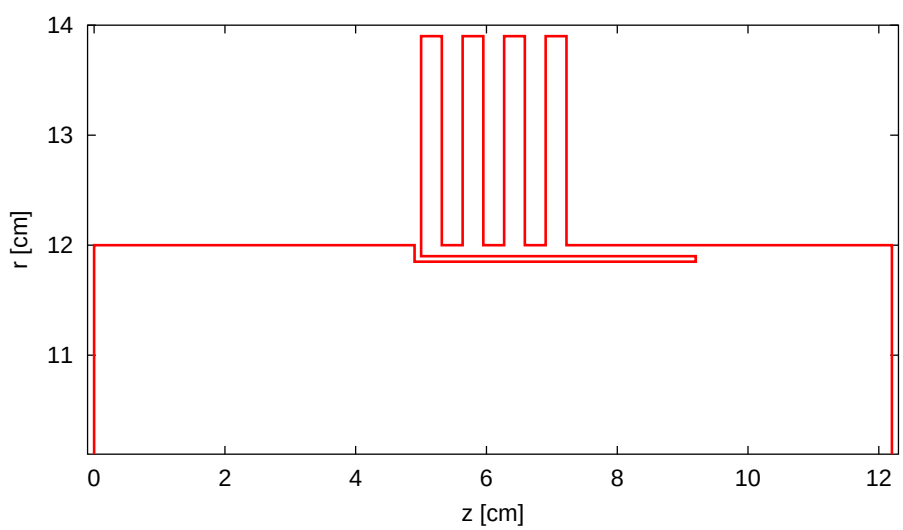

Figure D.2: A simple shielding mechanism for the bellows in the 5 K helium region.

Two sets of bellows, one right after the Niobium-Stainless Steel transition (5 K) with and one before the transition to room temperature (300 K). Several shielding mechanisms including capacitive finger were considered if shielding was necessary to reduce further losses. Fig. D.2 shows a simple shielding mechanism and a comparison of integrated loss factor is shown in Fig. D.3.

Note that the rectangular bellows were taken as an approximation to the elliptical bellows used in the cryomodule. It is clear that shielding suppress the overall power loss by an order of magnitude, but the unshielded bellows only contribute $k_{||} = 3.8 \times 10^{-2}$ which amounts to ≈ 10 W of power which is quite small. To further reduce He losses, the bellow section in the 5 K region maybe reduced to two convolutions.

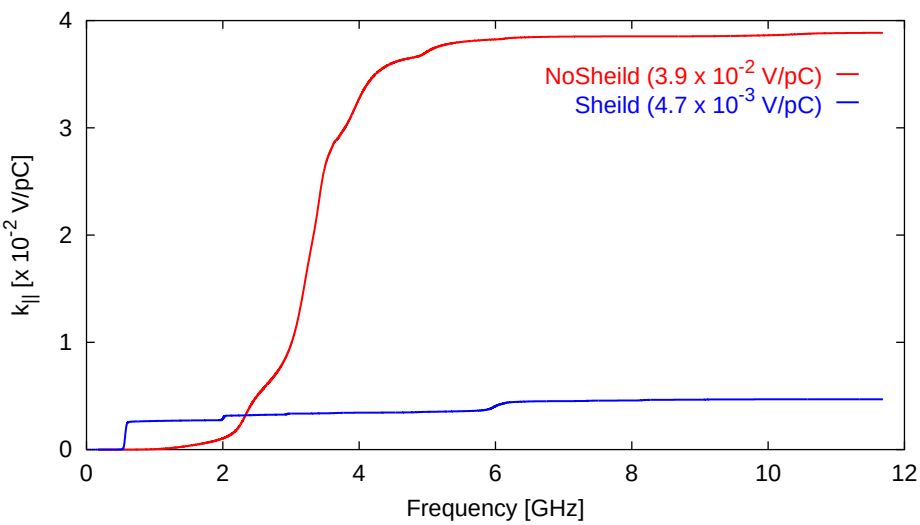

Figure D.3: A simple shielding mechanism for the bellows in the 5 K helium region.

Appendix E

$\frac{1}{2}$-Cell SRF Gun

E.1 Loss Factor Correction for $\beta < 1$

The loss factors in section II B has been calculated for ultra relativistic bunches through the gun. Since the gun will accelerate relatively long bunches (1 cm) and has a fairly large beam pipe aperture (5 cm), the loss factors were assumed to be an upper limit. Modal loss factors for $\beta < 1$ and $\beta = 1$ were calculated using the analytical expression derived in Ref. [127] given by

$$k(\beta, \sigma) = \sum_{n=1}^{n} \frac{\omega_n R_s(\beta)}{4Q_n} \; e^{-(\frac{\omega_n \sigma}{\beta c})^2}. \tag{E.1}$$

where ω_n and R_s/Q_n are the frequency and the shunt impedance (accelerator definition) of the nth mode respectively and σ is the bunch length. Fig. E.1 shows a comparison between analytical expression ($\beta < 1$, $\beta = 1$) and numerical calculation ($\beta = 1$) using ABCI [87, 88] for modes below the cut-off frequencies of the beam pipe for a bunch length of 1 cm. The loss factors are clearly over estimated for $\beta = 1$ compared to $\beta < 1$. However, we use the total loss factor calculated by ABCI as the upper limit since it is difficult to analytically estimate the loss factor for modes above cut-off.

E.2 Amplitude and Phase Modulation

The effects of random fluctuations have been extensively studied in signal processing theory. Several interesting models for random processes and its effects can be found in Ref. [128]. We will assume that the beam harmonics can be represented by an infinite train of pulses with a pulse shape $p(t)$. Any modulation of the laser amplitude and/or phase will manifest itself as a

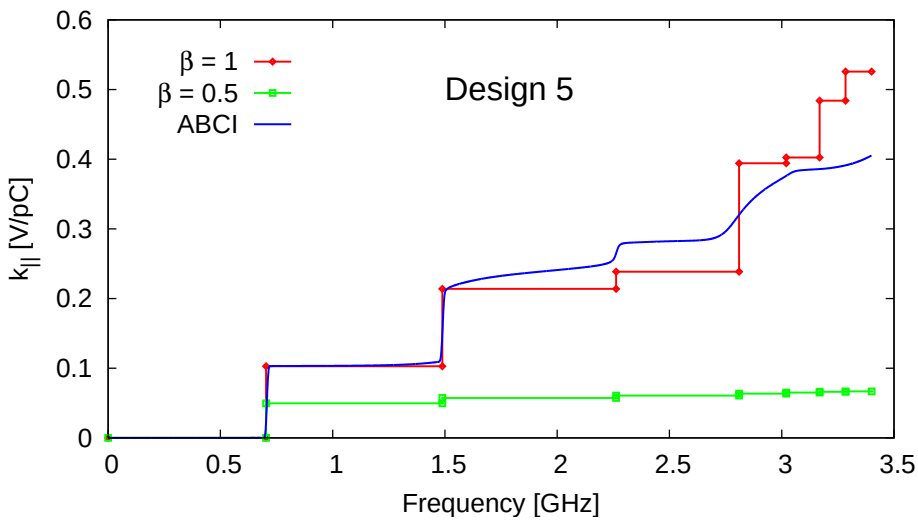

Figure E.1: Longitudinal loss factors computed for the first nine monopole modes in the gun using Eq. E.1 for both $\beta = 1$ and $\beta = 0.5$. The analytical calculation is also compared to the numerical calculation using ABCI.

modulation of the pulse train which can be expressed as

$$I(t) = \sum_{n=-\infty}^{\infty} a_n \, p(t - nT_0 - \epsilon_n) \tag{E.2}$$

where T_0 is the average separation between the pulses. We will also assume that the random variables a_n and ϵ_n are uncorrelated and follow some arbitrary distribution function.

It is of interest to calculate the spectral power density (SPD) to determine the characteristics of the modulated pulse train in the frequency domain. The SPD along with the impedance spectrum of the cavity can be used to estimate the HOM losses induced as a result of the modulation. The SPD can be

Table E.1: Frequencies and R/Q values (accelerator definition) for the first few monopole and dipole modes in the SRF gun.

Monopole Modes		Dipole Modes	
Freq [GHz]	R/Q [Ω]	Freq [GHz]	R/Q [Ω]
0.703	96.5	1.01	53.8
1.49	55.8	1.71	10.7
2.25	8.4	1.88	11.7
2.34	48.7	2.05	2.1
2.56	10.3	2.44	0.4
2.80	13.0	2.64	6.3
2.99	33.1	3.06	0.05
3.13	2.2	3.08	3.5
3.36	19.2	3.43	2.2

determined from amplitude of the Fourier transform given by

$$\mathcal{P}(\omega) = \lim_{T\to\infty} \frac{1}{2T} \langle \, | \int_{-T}^{T} I(t)\ e^{i\omega t} dt|^2 \, \rangle \tag{E.3}$$

$$= \lim_{N\to\infty} \frac{|\hat{p}(\omega)|^2}{2T_0 N} \langle \, | \sum_{n=-N}^{n=N} a_n\ e^{i\omega(nT_0+\epsilon_n)}|^2 \, \rangle \tag{E.4}$$

$$= \lim_{N\to\infty} \frac{|\hat{p}(\omega)|^2}{2T_0 N} \times \sum_{n,m} \langle a_n a_m\ e^{i\omega[(n-m)T_0+(\epsilon_n-\epsilon_m)]} \, \rangle \tag{E.5}$$

where $\hat{p}(\omega)$ is the Fourier transform of the pulse shape. Since, a_n and ϵ_n are uncorrelated

$$\langle a_n a_m\ e^{i\omega(\epsilon_n-\epsilon_m)} \rangle = \langle a_n\ a_m \rangle \langle e^{i\omega(\epsilon_n-\epsilon_m)} \, \rangle \tag{E.6}$$

For general uncorrelated amplitude modulation and time jitter, the char-

acteristic functions can be evaluated as

$$\begin{aligned}
\langle a_n \; a_m \rangle &= a_0^2 \; + \; \delta_{n,m}\sigma_a^2 && \text{(E.7)}\\
\langle \; e^{i\omega(\epsilon_n - \epsilon_m)} \; \rangle &= \delta_{n,m} + (1-\delta_{n,m}) \\
&\quad \times \; \Big| \int_{-T_0/2}^{T_0/2} d\epsilon f(\epsilon) e^{i\omega\epsilon} \Big|^2 && \text{(E.8)}\\
&= \; |\hat{f}(\omega)|^2 + \delta_{n,m}(1 - |\hat{f}(\omega)|^2) && \text{(E.9)}
\end{aligned}$$

where $\hat{f}(\omega)$ is the integral in Eq. E.8.

Using change of variables ($k = n - m$), we can rewrite

$$\begin{aligned}
\sum_{n=-N}^{n=N} \sum_{m=-N}^{m=N} F(n-m) &= \sum_{k=-2N}^{k=2N} F(k) && \text{(E.10)}\\
&\quad \times \; (2N + 1 - |k|) && \text{(E.11)}
\end{aligned}$$

Therefore, using Eqs. E.5, E.7, and E.9, we can express the SPD in the new variable as

$$\begin{aligned}
\mathcal{P}(\omega) \;\; &= \;\; \lim_{N\to\infty} \frac{a_0^2 |\hat{p}(\omega)|^2}{2T_0 N} \left| \hat{f}(\omega) \frac{\sin\left[(N+1/2)\omega T_0\right]}{\sin\left(\omega T_0/2\right)} \right|^2 \\
&\quad + \; \frac{|\hat{p}(\omega)|^2}{T_0} \left[a_0^2 (1 - |\hat{f}(\omega)|^2) + \sigma_a^2 \right] && \text{(E.12)}
\end{aligned}$$

Taking the limit, we find that

$$\begin{aligned}
\mathcal{P}(\omega) \;\; &= \;\; \frac{2\pi a_0^2 |\hat{p}(\omega)|^2}{T_0^2} |\hat{f}(\omega)|^2 \sum_{k=-\infty}^{\infty} \delta\left(\omega - \frac{2\pi k}{T_0}\right) \\
&\quad + \; \frac{|\hat{p}(\omega)|^2}{T_0} \left[a_0^2 \left(1 - |\hat{f}(\omega)|^2\right) + \sigma_a^2 \right] && \text{(E.13)}
\end{aligned}$$

If the probability distribution $f(\epsilon)$ for the timing jitter is uniform or Gaussian, the characteristic function can be easily evaluated and is given by

$$|\hat{f}(\omega)|^2 \;\; = \;\; \begin{cases} \left[\frac{\sqrt{3}\sin(\omega\sigma_\epsilon)}{(\sqrt{3}\omega\sigma_\epsilon)} \right]^2, & \text{Uniform} \\ \\ e^{-(\omega\sigma_\epsilon)^2}, & \text{Gaussian.} \end{cases} \qquad \text{(E.14)}$$

where σ_ϵ is the rms of ϵ.

E.3 Voltage Estimates for Parasitic Modes

Let the longitudinal wake potential for the parasitic mode be $W(t)$ with $W = 0$ for $t < 0$. Any dependence on the beam's transverse coordinates are assumed to be included. Model the beam as a sequence of pulses with normalized shape $p(t)$, arrival times $nT_0 + \epsilon_n$ and charges $(1 + a_n)q$. The voltage on the beam due to this mode is then

$$\begin{aligned} V(t) &= -q \sum_{n=-\infty}^{\infty} (1 + a_n)\hat{W}(t - nT_0 - \epsilon_n), && \text{(E.15)} \\ &\approx -q \sum_{n=-\infty}^{\infty} (1 + a_n)\hat{W}(t - nT_0) \\ &\quad -\epsilon_n(1 + a_n)\frac{d\hat{W}}{dt}(t - nT_0), && \text{(E.16)} \end{aligned}$$

where it has been assumed that the arrival time variation is short compared to the time scale (oscillation period) of the wake field and we have defined

$$\hat{W}(t) = \int d\tau W(t - \tau)p(\tau)d\tau, \tag{E.17}$$

as the smoothed wake potential for a single bunch.

Assume the simplest statistical model with $\langle \epsilon_n \rangle = \langle a_n \rangle = 0$, $\langle a_n a_m \rangle = \sigma_a^2 \delta_{m,n}$, $\langle \epsilon_n \epsilon_m \rangle = \sigma_\epsilon^2 \delta_{m,n}$, and $\langle \epsilon_n a_m \rangle = 0$. Also, assume a resonant wake field with a large quality factor Q_r, resonant frequency ω_r with $\omega_r \sigma_\tau \ll 1$, and shunt impedance R_r. Then the expectation value of the voltage is

$$\begin{aligned} \langle V(t) \rangle &= -\sum_{n=-\infty}^{\infty} q\hat{W}(t - nT_0), \\ &= -\sum_{k=-\infty}^{\infty} (q/T_0)Z(\omega_k)\tilde{p}(\omega_k)e^{-i\omega_k t}, && \text{(E.18)} \\ &= -\sum_{k=-\infty}^{\infty} \frac{q}{T_0} \frac{R_r}{1 - iQ_r\left(\frac{\omega_k}{\omega_r} - \frac{\omega_r}{\omega_k}\right)} \\ &\quad \times \tilde{p}(\omega_k)e^{-i\omega_k t/T_0}, && \text{(E.19)} \end{aligned}$$

where $\omega_k = 2\pi k/T_0$,

$$\hat{p}(\omega) = \int_{-\infty}^{\infty} p(t)e^{i\omega t}dt$$

is the Fourier transform of the pulse shape and $Z(\omega)$ is the impedance of the mode. The average voltage modifies the RF bucket and is a type of static beam loading.

Now consider the variance of this parasitic voltage,

$$\begin{aligned}\langle (V(t) - \langle V(t)\rangle)^2\rangle &\approx q^2 \sum_n \sigma_a^2 \hat{W}^2(t - nT_0) \\ &\quad + \sigma_\epsilon^2 \left\{ \frac{d\hat{W}}{dt}(t - nT_0) \right\}^2 \qquad \text{(E.20)} \\ &\approx q^2 \left(\sigma_a^2 + \omega_r^2 \sigma_\epsilon^2\right) \left(\frac{R_r \omega_r}{Q_r}\right)^2 \\ &\quad \times \frac{Q_r}{2\omega_r T_0} |\tilde{p}(\omega_r)|^2 \qquad \text{(E.21)}\end{aligned}$$

where we have ignored terms proportional to $\sigma_a^2 \sigma_\epsilon^2$ and assumed that the bandwidth of the parasitic resonance is narrow compared to the bunching frequency. For a Gaussian pulse of rms duration σ_t one finds $\tilde{p}(\omega) = \exp(-\omega^2 \sigma_t^2/2)$ so Eq. E.21 predicts that high frequency parasitic modes are suppressed. It is worthwhile to note that the dependence on the bunching frequency in equation (E.21) is fairly weak. For $T_0 \omega_r \gg 1$ the variance of the parasitic voltage is unaffected by a detuning of order $1/T_0$.

Bibliography

[1] M. Harrison, S. Peggs, and T. Roser, The RHIC Accelerator, Annu. Rev. Nucl. Part. Sci. 2002. 52:425 69 (2002).

[2] H. Hahn (Ed.). RHIC design manual, October 2000, available at http://www.agsrhichome.bnl.gov/NT-share/rhicdm/00 toc1i.htm.

[3] T. Suzuki, General Formulae of Luminosity for Various Types of Colliding Beams Machines, KEK-76-3, 1976.

[4] M. A. Furman, Hourglass effect for asymmetric colliders, in the proceedings of the particle accelerator conference (PAC91), San Francisco, California, 1991.

[5] P. C. Garcia, Luminosity and beta function measurement at the electron-positron collider ring LEP, Ph.D. Thesis, 1996.

[6] This information is compiled and maintained by W. Fischer and more details can also be found at http://www.agsrhichome.bnl.gov/RHIC/Runs

[7] R. Tomás *et al.*, Quest for a new working point in RHIC, in the proceeding of European particle accelerator conference (EPAC04), Lucerne, Switzerland, 2004.

[8] E. D. Courant and H. S. Snyder, Ann. Phys. (Paris) 3, 1 (1958).

[9] S. Y. Lee, Accelerator Physics, World Scientific, Singapore, 1999.

[10] A .Chao, M. Tigner, *Handbook of Accelerator and Engineering*, World Scientific Publishing Co. Pte. Ltd., Singapore, 1999, p. [263-264].

[11] http://www2.slac.stanford.edu/vvc/accelerators/bpm.html

[12] P. Cameron etal, Overview of RHIC beam instrumentation and first experience from operation, in the proceedings of DIPAC, Grenoble, 2001.

[13] http://www.rhichome.bnl.gov/RHIC/Instrumentation/Systems/IPM/IPMdayOne.html

[14] http://www.rhichome.bnl.gov/RHIC/Instrumentation/Systems/WCM/WCM.html

[15] S. Peggs and C. Tang, BNL Report No. RHIC/AP/159, 1998.

[16] M. Bai *et al.*, Experimental test of coherent betatron resonance excitations, PRE 56 (1997.)

[17] M. Bai, Overcoming intrinsic spin resonances by the use of of an RF dipole, Ph.D. thesis, University of Indiana (1999).

[18] R. Tomás, Normal Form of Particle Motion under the Influence of an AC Dipole, Phys. Rev. ST Accel Beams, volume **5** 54001 (2002).

[19] R. Tomás *et al.*, Measurement of global and local resonance terms", Phys. Rev. ST Accel. Beams **8**, issue 2, 024001 (2005).

[20] K. Pearson, "On Lines and Planes of Closest Fit to Systems of Points in Space". Philosophical Magazine 2(6):559-572 (1901).

[21] H. Hotelling, Analysis of a complex of statistical variables into principal components, Journal of Educational Psychology, 24:417-441,498-520 (1933).

[22] I. T. Jolliffe, Principle Component Analysis, Springer series in statistics, 2nd Edition, NY, 1986.

[23] G. H. Golub, and V. Loan, Matrix Computations, 3rd ed., Johns Hopkins University Press, Baltimore, 1996.

[24] G. W. Stewart, Introduction to Matrix Computations, SIAM, 1973.

[25] J. Irwin, C. X. Wang, Y. T. Yan, K. L. F. Bane, Y. Cai, F. J. Decker, M. G. Minty, G. V. Stupakov, and F. Zimmermann,Phys. Rev. Lett. 82(8), 1684(1999).

[26] C. X. Wang, V. Sajaev, C. Y. Yao, Phys. Rev. ST Accel. Beams 6,104001(2003).

[27] C. X. Wang, Model independent analysis of beam centroid dynamics in accelerators, Ph.D. Thesis, Stanford Univerisity (1999).

[28] X. Huang, Application of Independent Component Analysis to Beam Diagnosis, Ph.D. Thesis, Indiana University, 2005.

[29] H. Wiedemann. Particle Accelerator Physics I, Springer-Verlag, New York, 1998.

[30] R. Calaga and R. Tomás, Statistical analysis of RHIC beam position monitors performance, Phys. Rev. ST Accel. Beams **7**, 042801 (2004).

[31] J. van Zeijts, Transverse Optics Improvements for RHIC Run 4, this proceedings.

[32] Y. Chang, G. Decker, K. Evans Jr., in the proceedings of PAC 93, p.2263.

[33] A. Friedman, E. Bozoki, NIM A344, 1994, p.269.

[34] R. Calaga, O. Bruning, Y. Papaphilippou, S. Peggs, R. Tomas, Procedures and accuracy estimates for beta-beat correction in the LHC, to be submitted to EPAC06.

[35] T. Satogata, M. Bai, P. Cameron, P. Ceniglia, R. Connolly, J. Cupolo, C. Degen, A. Drees, R. Fliller, D. Gassner, J. Mead, V. Ptitsyn, T. Shea, R. Sikora, P. Thompson, R. Witkover, RHIC beam instrumentation, NIM Physics Reasearch A. 499, 372(2003)

[36] R. Tomás, "Direct measurement of resonance driving terms in the super proton synchrotron (SPS) of CERN using beam position monitors" Ph.D. Dissertation, University of Valencia, Spain, ISBN:84-370-5724-8, 2003.

[37] C. X. Wang, M. Borland, V. Sajaev, K. Kim, BPM System Evaluation using Model Independent Analysis, PAC2001, p.1354(2001).

[38] T. Satogata, private communication(2004).

[39] D. Edwards and L. Teng, IEEE Trans. Nucl. Sci. **20**, 3 (1973).

[40] D. Sagan and D. Rubin, "Linear analysis of coupled lattices", Phys. Rev. ST Accel. Beams volume **2**, 074001 (1999).

[41] P. Bagley and D. Rubin, "in Proceedings of the 1997 Particle Accelerator Conference", Chicago (IEEE, Piscataway, NJ, 1989), pp.874.

[42] D. Sagan, R. Meller, R. Littauer, and D. Rubin, "Betatron phase and coupling measurements at Cornell Electron/Positron Storage Ring", Phys. Rev. ST Accel. Beams volume **3**, 092801 (2000).

[43] C. X. Wang, R. Calaga, "Transverse Coupling Measurement using SVD Modes from Beam Histories", EPAC 2004, Lucerne, Switzerland.

[44] L. Schachinger and R. Talman, "Manual for the Program TEAPOT, Non-interactive FORTRAN Version", Appendix G, 1996.

[45] W. Fischer, "Robust linear coupling correction with N -turn maps" Phys. Rev. ST Accel. Beams volume **6**, 062801 (2003).

[46] R. Bartolini and F. Schmidt, "Normal Form via tracking or Beam Data", Part. Accelerators. **59**, pp. 93–106, (1998).

[47] D. Sagan, "Betatron phase and coupling correction at the Cornell Electron/Positron Storage Ring" Phys. Rev. ST Accel. Beams volume **3**, 102801 (2000).

[48] F. Schmidt, "MAD-X User's guide, Version 2.12", CERN, 2003.

[49] C .X. Wang, "Untangling mixed modes in model-independent analysis of beam dynamics in circular accelerators", Phys. Rev. ST Accel. Beams 7, 114001 (2004).

[50] R. Tomás, M. Bai, W. Fischer, A. Franchi, G. Rumolo, "Measurement of multipole strengths from RHIC BPM data", EPAC 2004, Lucerne, Switzerland.

[51] A. Franchi, T. Beier, M. Kirk, P. Moritz, G. Rumolo, R. Tomás, "A method to measure the skew quadrupole strengths in the SIS-18 using two BPMs", EPAC 2004, Lucerne, Switzerland.

[52] M. Bai, F. Pilat, T. Satogata, F. Schmidt and R. Tomás "Measurement of Linear Coupling Resonance in RHIC" presented in the the 2003 Particle Accelerator Conference, May 2003, Portland, Oregon.

[53] Y. Luo et al., "Measurement of global betatron coupling with skew quadrupole modulation", Phys. Rev. ST Accel. Beams **8**, 014001 (2005).

[54] R. Calaga, R. Tomás, and A. Franchi, "Betatron coupling: Merging Hamiltonian and matrix approaches", Phys. Rev. ST Accel. Beams **8**, 034001 (2005)

[55] M. Bai et al., "Measuring Beta Function and Phase Advance in RHIC with an ac dipole", The proceedings of the 2003 Particle Accelerator Conference, Portland (May 2003).

[56] R. Calaga et al., "RHIC Optics Measurement with Different Working Points", The proceedings of the 2004 Particle Accelerator Conference, Lucerne (May 2004).

[57] R. Tomás, "Normal form of particle motion under the influence of an ac dipole", Phys. Rev. ST Accel. Beams **5**, 054001 (2002).

[58] A. Piwinski, Int. Conf. on High-Energy. Acc., Stanford (1974).

[59] Generalization to include variation of lattice functions was done by Sacherer, Mohl and Piwinski and summarized by M. Martini (1984).

[60] Bjorken and Mtingwa, Particle Acc., V. 13, p.115 (1983).

[61] A. Fedotov, Comments on Simplified Treatment of Intrabeam Scattering, Internal Note: C-A/AP/168 (2004).

[62] V. Parkhomchuk, I. Ben-Zvi, Electron Cooling for RHIC, Internal Note: C-A/AP/47 (2001).

[63] H. Padamsee, J. Knobloch, and T. Hays, RF Superconductivity for Accelerators, Wiley and Sons, New York, 1998.

[64] M. Tinkham, Introduction to Superconductivity, Krieger, Malabar, Florida, 1975.

[65] J. Knobloch, Advanced Thermometry Studies of Superconducting RF Cavities, Ph.D. Thesis, Cornell University, 1997.

[66] U. Kelin and D. Proch, in the proceedings of the Conference of Future Possiblities for Electron Accelerators, Charlottesville, pp. N1-17 (1979).

[67] P. Kneisel *et al.*, Nucl. Instrum. Methods Phys. Res., **188** :669 (1981)

[68] C. Pagani, D. Barni, A. Bosotti, P. Pierini, G. Ciovati, "Design criteria for elliptical cavities", 10th Workshop on RF Superconductivity, Tsukuba, Japan (2001).

[69] Paolo Pierini, Build Cavity Manual, Milan, Italy.

[70] D. Wang et. al., PAC 2003, Portland, May 2003.

[71] R. Calaga et. al., SRF 2003, Travemunde/Lubeck, Germany.

[72] D. Moffat et al., Proceedings of the 1993 Particle Accelerator Conference, IEEE Publishing, Piscataway, New Jersey, 1993.

[73] W. H. Hartung, Ph.D. thesis, Cornell Univeristy, Ithaca, NY (1996).

[74] ACCEL Instruments GmbH, D-51429 Bergisch Gladbach, Germany.

[75] The prototype ferrite tiles were provided by ACCEL (M. Pekeler) as a part of HOM damping measurements.

[76] Y .Zhao, H. Hahn, HOM Coupler Measurement and Simulation, C-AD/AP Note 161, 2004.

[77] P. Kneisel, private communication.

[78] The MAFIA Collaboration, MAFIA Version 4.0, CST GmbH, Darmstadt, Germany.

[79] R. Schuhmann, T. Weiland, PRST-AB, Vol. 3, 122002(2000).

[80] R. Schuhmann, M. Clemens, P. Thomas, and T. Weiland, *in the proceedings of the 12th Annual Review of Applied Computational Electromagnetics Conference*, Monterey, 1996 (p. 1295).

[81] J. Mouris and R. M. Hutcheon, Measurements of complex microwave permeability of un-biased ferrite C-48 and Ferrite-50, Internal Note, Microwave Properties North, Canada, 2000.

[82] J. Berenger, "A perfectly matched layer for absorption of electromagnetic waves",J. Comput. Phys., Vol. 114, 185-200, 1994.

[83] P. B. Wilson, Introduction to wakefields and wake potentials, SLAC-PUB-4547, 1989.

[84] T. Weiland, R. Wanzenberg, Wakefields and impedances, in the proceedings...

[85] W. K. H. Panofsky and W. A. Wenzel, Rev. Sci. Instrum. 27, p. 967 (1956).

[86] A. W. Chao, Physics of Collective Beam Instabilities in High Energy Accelerators, Wiley (1993).

[87] Y. H. Chin, Advances and Applications of ABCI, Proceedings of the 1993 Particle Accelerator Conference, Vol. 2, pp. 3414-3416, Washington, D.C., May 1993.

[88] Y. H. Chin, ABCI Version 8.7, CERN, Geneva.

[89] T. 0. Raubenheimer, Estimates of emittance dilution and stability in high-energy linear accelerators, Phys. Rev. ST Accel. Beams, Vol. 3, 121002(2000).

[90] High Frequency Structure Simulation (HFSS), ANSOFT Co., Pittsburgh, PA, USA.

[91] TDBBU was written by G.A. Krafft at Jefferson Laboratory.

[92] MATBBU was written by G.A. kraft at Jefferson Laboratory.

[93] G. Hoffstaetter, I. Bazarov, Beam-breakup instability theory for energy recovery linacs, Phys. Rev. ST Accel. Beams, Vol. 7, 054401 (2004).

[94] E. Pozdeyev, Regenerative multipass beam breakup in two dimensions, Phys. Rev. ST Accel. Beams, Vol. 8, 054401 (2005).

[95] Advanced Energy Systems, USA.

[96] D. Li and R.Rimmer, Beam Impedance Calculations and Analysis of HOMs using MAFIA in Time Domain, PAC 2001, Chicago.

[97] J. Bisognano and R. .L. Gluckstern, *in the proceedings of the Particle Accelerator Conference*, 1987 (p. 1078).

[98] K. Beard, *Private Communication*.

[99] P. Ylä-Oijala, J. Lukkarinen, S. Järvenpää, M. Ukkola, MULTIPAC - "Multipacting simulation package with 2D FEM field solver," in the proceedings of the 10th workshop of RF superconductivity, Tsuchiura, Tokyo, 2001.

[100] P. Ylä-Oijala, J. Lukkarinen, S. Järvenpää, M. Ukkola, MultiPac 2.1 users manual, *http://www-mhf.desy.de/ brinkma/multipac/*, 2001.

[101] I. E. Campisi et al., The Fundamental Power Coupler Prototype for the Spallation Neutron Source (SNS) Superconducting Cavities, PAC 2001,Chicago,IL,June 2001.

[102] Computer Simulation Technology, Microwave Studio Manual Verion 5.0, CST GmbH, Darmstadt, Germany.

[103] V. Shemelin, S. Belomestnykh, H. Padamsee, *Low-Kick Twin-Coaxial and Waveguide-Coaxial Couplers for ERL*, Cornell LEPP Report: SRF 021028-08, 2002.

[104] Note that the fields were computed in frequency domain simulating the FPC as a coaxial line with perfect transmission unlike in [103].

[105] S. Belomestnykh, et al., "High average power fundamental input couplers for the Cornell University ERL: requirements, design challenges and first ideas," Cornell LEPP Report ERL 02-08.

[106] J. C. Slater, Microwave Electronics, D. Van Nostrand Company, Princeton(1950).

[107] M. Cole, *Private Communication.*

[108] ...

[109] J. Sekutowicz, PRST-AB, Vol.2, 062001 (1999).

[110] L. C. Maier, J. C. Slater, J. App. Phys., Vol. 23, No. 1 (1952) 68.

[111] R. Calaga, I. Ben-Zvi, Y.Zhao, J. Sekutowicz, *Study of Higher Order Modes in High Current Multicell SRF Cavities*, in the proceedings of the 11th workshop of RF superconductivity, Travemunde/Lubeck, 2003.

[112] R. Calaga, I. Ben-Zvi, J. Sekutowicz, *High current energy-recovery superconducting linacs* (to be submitted to PRST-AB).

[113] J. Lewellen, *Private communication.*

[114] J. Billen, L. Young, *PARMELA version 3.36 Users Manual*, LANL,*laacg1.lanl.gov/laacg/services/parmela.html.*

[115] Beam dynamics PARMELA simulations for each design was carried out by D. Kayran.

[116] D. Kayran, V. Litvinenko, *Novel Method of Emittance Preservation in ERL Merging System in Presence of Strong Space Charge Forces*, in the proceeding of the particle accelerator conference (PAC05), Knoxville, 2005.

[117] J. Bellen, L. Young, *SUPERFISH version 6.0 Users Manual*, LANL, *laacg1.lanl.gov/laacg/services/superfish.html*.

[118] X. Chang, I. Ben-Zvi, J. Kewisch, "Emittance compensation of compact superconducting guns and booster linac system (submitted to PRST-AB)".

[119] L. Serafini, J. Rosenzweig, *Envelope analysis of intense relativistic quasilaminar beams in rf photoinjectors: A theory of emittance compensation*, Physical Review E, V55, 7565).

[120] X. Chang, I. Ben-Zvi, J. Kewisch, *Design Considerations for Low Field Short Photo-Injected RF Electron Gun with High Charge Electron Bunch*, in the Proceedings of the 11th Advanced Accelerator Concepts Workshop, June 21-26, 2004, Stony Brook NY. AIP Conference Proceedings 737 page 462, 2004.

[121] Note that $Q_L \sim Q_{ext}$ since $Q_0/Q_{ext} \gg 1$.

[122] M. Cole, *Private communication.*

[123] J. Preble, *private communication.*

[124] Y. Zhao, *private communication.*

[125] M. Ferrario *et al.*, An ultra-high brightness, high duty factor, superconducting RF photoinjector, in the Proceedings of European Particle Accelerator Conference (EPAC04), Lucerne, Switzerland, 2004.

[126] J. Rosenzweig, E. Colby, Charge and wavelength scaling of RF photoinjectors: a design tool, in the proceedings of Particle Accelerator Conference, Dallas, Texas, 1995.

[127] S. Kurennoy, Dependence of bunch energy loss in cavities on beam velocity, Phys. Rev. ST Accel. Beams 2, 032001 (1999).

[128] L. Franks, Signal Theory, Prentice-Hall, Inc. Englewood Cliffs, N.J., 1969.